

Proyecto de Investigación del Programa de Doctorado en:
Métodos Matemáticos y Simulación Numérica en Ingeniería y
Ciencias Aplicadas

**DEVELOPMENT OF A MULTIDISCIPLINARY AND OPTIMIZED
DESIGN METHODOLOGY FOR SURFACE PERMANENT
MAGNETS SYNCHRONOUS MACHINES**

Doctorando

Alejandro L. Rodríguez González

Director

Alfredo Bermúdez de Castro López-Varela

Co-director

Irma Villar Iturbe



Facultad de Matemáticas

03/07/2014

Contents

1	Introduction.....	11
1.1	Thesis Objectives.....	13
1.2	Background: The Permanent Magnet Synchronous Machine.....	14
1.2.1	Operating Principle.....	15
1.2.2	Permanent Magnets: Features and Evolution.....	17
1.2.3	PMSM Structure and Classification.....	20
1.3	Radial SPMSM Design: The Starting Point.....	24
1.4	Outline of the Document.....	27
2	Design and Modelling of PMSM: Optimized-Multiphysical Study.	29
2.1	Towards a Design Methodology: State of the Art.....	31
2.1.1	From a Magnetic to a Multiphysical Approach.....	33
2.1.2	From a Sizing to an Optimized Approach.....	35
2.1.3	The Global Picture.....	39
2.2	State of the Art in PMSM Modelling.....	40
2.2.1	Electromagnetic Modelling.....	41
2.2.2	Thermal Model.....	48
2.2.3	Vibro-acoustic Model.....	50
3	Electromagnetic Characterization.....	55
3.1	Introduction: Between Mechanical and Electric Power.....	57
3.1.1	Relation between Mechanical and Electrical Domains.....	57
3.2	Winding Layout: the Star of Slots.....	61
3.3	Magnetic Domain.....	65
3.3.1	Rotor Magnetic Field.....	65
3.3.2	Slotting Effect: Relative Permeance Function.....	67
3.3.3	Electro-Motive Force and Stator Flux Induced by the Magnets....	71
3.3.4	Armature Reaction and Total Magnetic Field.....	78
3.3.5	Radial Stator Force and Cogging Torque Calculus.....	85
3.4	Electric Domain.....	90
3.4.1	PMSM Coil Inductance.....	91
3.4.2	PMSM resistance.....	101
3.5	Results and Conclusions.....	105
4	Efficiency and Losses Estimation.....	109
4.1	Copper and Iron Losses.....	111
4.2	Magnet losses.....	113
4.2.1	Eddy Current Loss Estimation Method.....	113
4.2.2	Magnetic Induction in the Rotor Frame.....	115
4.2.3	Total Current Density in the Magnets.....	117

4.3	Efficiency and other Quality Parameters.....	118
4.3.1	Power, Torque and Efficiency.....	118
4.3.2	Electric Quality Parameters.....	119
4.4	Results and Conclusions.....	120
5	Thermal Approach	121
5.1	Heat Transfer: Basic Principles.....	123
5.1.1	Conduction	123
5.1.2	Convection.....	124
5.1.3	Radiation.....	125
5.2	Introduction to Lumped Thermal Models	126
5.3	Simplified Thermal Network for a SPMSM	128
5.3.1	Housing and Stator Yoke	129
5.3.2	Stator Teeth.....	131
5.3.3	Stator Coils.....	132
5.3.4	End-Winding Region	136
5.3.5	Airgap.....	138
5.3.6	Rotor.....	138
5.4	Thermal-Electromagnetic Coupling	140
5.5	Results and Conclusions.....	142
6	Structural and Vibratory Behaviour	145
6.1	Classic Vibratory Theory: d'Alembert Principle and Hooke Law	147
6.2	Dynamic of a Thin Ring	150
6.2.1	Breathing Mode.....	151
6.2.2	Bending Modes without Elongation.....	153
6.3	Dynamic of a Stator.....	156
6.4	Results and Conclusions.....	159
7	Optimized Methodology Proposal	161
7.1	The optimization process: A Global View	163
7.1.1	Design and Status Variables	163
7.1.2	Objective and restriction functions.....	165
7.1.3	The DMS Algorithm	167
7.2	The Proposed Methodology	168
8	Conclusions and Future Work	171
8.1	Conclusions	173
8.2	Future Work.....	174
9	Bibliographic references	175

Figure index

Figure 1.1. ABB motors. Left, DC motor. Right, stator and rotor of an induction motor.	14
Figure 1.2. Comparative between an induction motor and a PMSM for similar power.	15
Figure 1.3. Motors basic principles (a) basic case with magnets, (b) with a rotor electromagnet.....	16
Figure 1.4. PMSM configuration. (a) example with one coil, (b) example of a three-phases configuration. Figure from [Hanselman 2012].	17
Figure 1.5. Hysteresis loop of permanent magnet material. Figure adapted from [Hanselman 2003].	17
Figure 1.6. Demagnetization curves for N40H magnets at different temperatures. (Arnold® Magnetic Technologies).	18
Figure 1.7. Characteristic demagnetization curve, operation line segment and BH curve. Adapted from [Pyrhönen 2008].	19
Figure 1.8. Evolution timeline of the permanent magnet maximum energy product during the last decades [Rahman 2013].	19
Figure 1.9. (a) Schematic of a 2-D slice of a radial PMSM. (b) Typical radial PMSM.	21
Figure 1.10. (a) External rotor configuration, (b) Internal rotor configuration.	22
Figure 1.11. (a) SPMSM rotor, (b) IPMSM rotor (from [Rahman 2013]).	22
Figure 1.12. Comparison of distributed (a) and concentrated (b) windings. [Photo: University of Bundeswehr].	23
Figure 1.13. Example of the main PMSM topologies. (a) Radial flux, (b) axial flux, (c) transversal flux [Anyuan 2010].	24
Figure 1.14. Block diagram of the proposed multiphysics linked models.	25
Figure 1.15. (a) Main dimensions of the SPMSM motor, (b) detail of a slot.	27
Figure 2.1. Classical two-stage flowchart in recent machine design approaches.	32
Figure 2.2. Example of electromagnetic-thermal loop in PMSM design [Kazmin 2008-a].	34
Figure 2.3. Physical domains and main possible objectives of a multiphysical design methodology. Adapted from [Muetze 2008].	35

Figure 2.4. Proposed classifications of the main optimization algorithms applied to PMSM design methodologies. Adapted from [García 2014].	38
Figure 2.5. Different model approaches for electromagnetic characterization of PMSM.	42
Figure 2.6. Geometry simplification done in order to obtain airgap flux density. Adapted from [Hanselman 2012].	43
Figure 2.7. Interaction forces between slots and magnets. The forces acting on the magnets cause the cogging torque.	44
Figure 2.8. 6 th mode force on the stator. This is the fundamental mode induced by the magnets if $p=3$.	46
Figure 2.9. Deformation caused by an unbalanced force distribution.	46
Figure 2.10. Lumped thermal networks. (a) Model proposed by [Mellor 1991], (b) SPMSM network model in Motor-CAD [®] .	49
Figure 2.11. Noise sources and sound propagation in electrical machines. Figure adapted from [Yang 1981].	51
Figure 2.12. Electromagnetic sound genesis in electrical machines.	52
Figure 2.13. 2 nd to 5 th stator radial modes calculated with ANSYS [®] . Deflections have been scaled for visual purposes.	53
Figure 3.1 Modules within the electromagnetic model block.	57
Figure 3.2 Single coil in a magnetic core with equivalent circuit model. Figure adapted from [Hanselman 2012].	59
Figure 3.3 Interaction between a coil and a magnet sharing a core. Figure adapted from [Hanselman 2012].	60
Figure 3.4. Equivalence between a stator slotting and its star of slots.	63
Figure 3.5. Star of slots method applied to a single and a double layer layout.	64
Figure 3.6. Angle covered by a single magnet with respect to the slot pitch.	67
Figure 3.7. Geometry considered for the calculus of the relative permeance function.	69
Figure 3.8. Radial component of the magnet flux density in the airgap. The PMSM simulated is a Q3p1 (3 slots and just one pole pair)	70
Figure 3.9. Flux paths simulated in FEM with FLUX2D [®]	71
Figure 3.10. Equivalent reluctance circuit for stator yoke magnetic flux calculus.	75
Figure 3.11. Example of phase A winding in a fractional slot machine.	77
Figure 3.12. Armature reaction caused by one coil in the adjacent teeth.	79

Figure 3.13. Spatial distribution of the MMF per current unit caused by a single coil. Example from [Almandoz 2008].	79
Figure 3.14. Spatial distribution of the MMF per current unit caused by a phase conformed by two coils. Example from [Almandoz 2008].	80
Figure 3.15. Spatial distribution of the radial magnetic field and the generated force density in the stator boundaries.	85
Figure 3.16. Radial force density over a tooth during an electrical period.	88
Figure 3.17. Detail of the slot opening surfaces where the forces are applied. Adapted from [Almandoz 2008].	89
Figure 3.18. Phase A PMSM electric model including iron losses effect.	91
Figure 3.19. Magnetic energy stored in a PMSM due to the armature reaction. FEM simulation in FLUX®.	92
Figure 3.20. (a) Example of phase A winding for a Q12p2 machine, (b) equivalent reluctance circuit.	93
Figure 3.21. Example of the two main cases of slot windings types.	94
Figure 3.22. Example of magnetic field intensity due to armature reaction.	96
Figure 3.23. Axial cut of a PMSM generated with MotorCAD®.	99
Figure 3.24. (a) Flux generated in the end-winding region, (b) Top view of a coil inserted in the stator slots.	100
Figure 3.25. Graphic representations of the skin effect and the proximity effect.	102
Figure 3.26. Wires distribution within a slot.	103
Figure 3.27. Flowchart of the RFe calculus algorithm.	104
Figure 3.28. Rotor flux density in the airgap at a time instant.	106
Figure 3.29. Armature reaction in the airgap at a time instant.	106
Figure 3.30. Total flux density in the airgap at a time instant.	106
Figure 3.31. EMF induced by the magnets in phase A.	107
Figure 3.32. Mutual torque ripple	107
Figure 3.33. Cogging torque	108
Figure 4.1. 2-D section of the PMSM geometry under study. Both angular references respect to the stator and the rotor have been included.	114
Figure 4.2. One pole geometry with three axial slices, eddy current paths are represented.	115

Figure 4.3. Current density in one of the magnets. Current is nearly constant in r	117
Figure 4.4. Phase A PMSM electric model.	118
Figure 5.1. Example of an electrical machine thermal network [Kylander 1995].	126
Figure 5.2. SPMSM small thermal network model proposed.	128
Figure 5.3. Motor 2-D section geometry. Figure from Motor-CAD®	130
Figure 5.4. Stator teeth and slots typical geometry.....	132
Figure 5.5. Relation between λ_{slot} and λ_{imp} as a function of the slot fill factor and the manufacture technique [Kylander 1995].	133
Figure 5.6. Slot geometry equivalence used in the thermal modelling [Lindström 1999]......	134
Figure 5.7. Thermal model of a coil. Adapted from [Lindström 1999]......	135
Figure 5.8. Global thermal resistance between embedded coils and end-winding Adapted from [Lindström 1999].	136
Figure 5.9. Equivalent end-wind thermal network in its Y and Δ forms. [Kylander 1995]......	136
Figure 5.10. Electromagnetic-thermal coupling algorithm flowchart.....	141
Figure 5.11. PMSM temperatures calculated by Motor-CAD®.....	142
Figure 6.1. Stresses on a differential element in polar coordinates. Figure adapted from [Timoshenko 1951].	149
Figure 6.2. Example of a stator breathing mode.....	151
Figure 6.3. (a)Strain and dimensions in a ring element (b)stresses in a ring.....	151
Figure 6.4. Stator seen as a ring (mean radius R_c and thickness h) loaded with teeth.....	156
Figure 6.5. 1 st to 4 th stator axial modes calculated with ANSYS®. Deflections have been scaled for visual purposes.....	159
Figure 7.1. PMSM model flowchart.....	165
Figure 7.2. PMSM design methodology flowchart.....	169

Table index

Table 2.1. Classification of the PMSM design proposals found in the literature.....	39
Table 3.1. Scale factor for the example shown in Figure 3.11	76
Table 3.2. Two phases slots distribution in a thriphasic PMSM.....	97
Table 3.3. Classification of the PMSM design proposals found in the literature.....	98
Table 3.4. PMSM main parameters.....	105
Table 3.5. PMSM calculated resistance and inductance	108
Table 4.1. PMSM quality parameters	120
Table 5.1. Analogy between electrical and thermal circuit.....	127
Table 5.2. Estimated PMSM temperatures	142
Table 6.1. Simulated and estimated modal static displacements and natural frequencies.....	160
Table 7.1. Design variables	164
Table 7.2. State variables.....	164
Table 7.3. Design restrictions	166
Table 7.4. Geometric restrictions	166
Table 7.5. Magnetic restrictions	167
Table 7.6. Electric restrictions	167
Table 7.7. Thermal and acoustic restrictions	167

1

Introduction

1.1 Thesis Objectives

Nowadays, most of electrical machines design methodologies applied in the industry are based on empirical and semi-heuristic rules that require a lot of personal experience and whose accuracy strongly depends on previous available data, often considered being property of large motors manufacturers [Amrhein 2013]. Moreover, most of the models are only focused on the electromagnetic performance and other important physical fields such as thermal or vibro-acoustics are taken into account through very rough “rules of thumb” or directly treated as an afterthought in best cases.

On the other hand, only a small amount of academic literature devoted to machine methodological design exists, and typically it presents incomplete and partial approaches, difficult to apply and more focused on the improvement of a previous design than in the development of a new, complete and optimized machine [Goss 2013-a].

Both approaches provide a first approximation that needs to be fulfilled with trial and error methods usually supported by time consuming numerical calculus. So, these design methodologies are only suitable for very well-known applications or low-performance machines but they are unsystematic by nature and present serious difficulties to extrapolate the obtained results to a new set of specifications or to more exigent applications where more physical domains, such as vibro-acoustics, must be taken into account.

Since electrical machines are complex systems where a great amount of physical phenomena are produced simultaneously a detailed multidisciplinary approach taking into account the coupling between different physical fields is needed in order to implement a fast, accurate, reliable and optimized design methodology.

Therefore, the main goal of the thesis, where this investigation project is a first stage, is to aid to fill the detected gap, developing a multidisciplinary and optimized design methodology for Permanent Magnet Synchronous Machines (PMSM).

In order to achieve the proposed aim the next objectives must be fulfilled:

- 1) Review and summarize the state of the art in the design methodologies and modelling strategies of PMSM, paying particular attention to the optimized and multidisciplinary approaches.
- 2) Implement a multiphysical modelling of a PMSM including electrical, magnetic, thermal, structural and vibro-acoustics domains. The key feature of the model is to be completely analytical and based on Fourier series, this permit to obtain a model not only multidisciplinary but modular and fast, especially suitable to be used it in a subsequent optimized methodology. A summary of the proposed model is going to be presented in the upcoming conference ICEM 2014 [Rodríguez 2014-a].

- 3) Develop a new, improved, multidisciplinary and optimized design methodology for PMSM coupling the aforementioned models.
- 4) Perform a case of study completely by designing a machine in order to validate the proposed methodology with both, numerical simulations and experimental tests.

During the first two years of the thesis the first and the second goals were accomplished, while the third is in progress. Therefore, this project comprises the state of the art in PMSM design, the developed models and the major lines of the proposed design methodology. The fulfilment of the third and fourth objectives will be presented in the final thesis document.

1.2 Background: The Permanent Magnet Synchronous Machine

Electric energy is one of the supports of modern civilization. In the actual context, the electrical machines are of capital importance since most of power plants, from nuclear plants to wind turbines, need an electrical machine working as a generator. Moreover, it is estimated that, nowadays, the 65% of the total energy supplied by the grid is consumed by electric motors [Rahman 2013].

The widespread use in industry of electrical machinery all over the 20th century has lead to a great investigation and improvement of its technology. Until the 50's the DC motors were the only available option at a competitive cost, because of the possibility of a simple and precise control, but it has many drawbacks such as high maintenance, big size and limited reliability.

The electronic advancements permitted, during the eighties, a precise control of induction AC machines. In a decade they substituted the DC machines in most of industrial applications due to their smaller size, more robust construction and, overall, their lower maintenance caused by the absence of brushes and commutator [Novotny 1996]. Figure 1.1 shows an example of an induction AC and a DC machine.

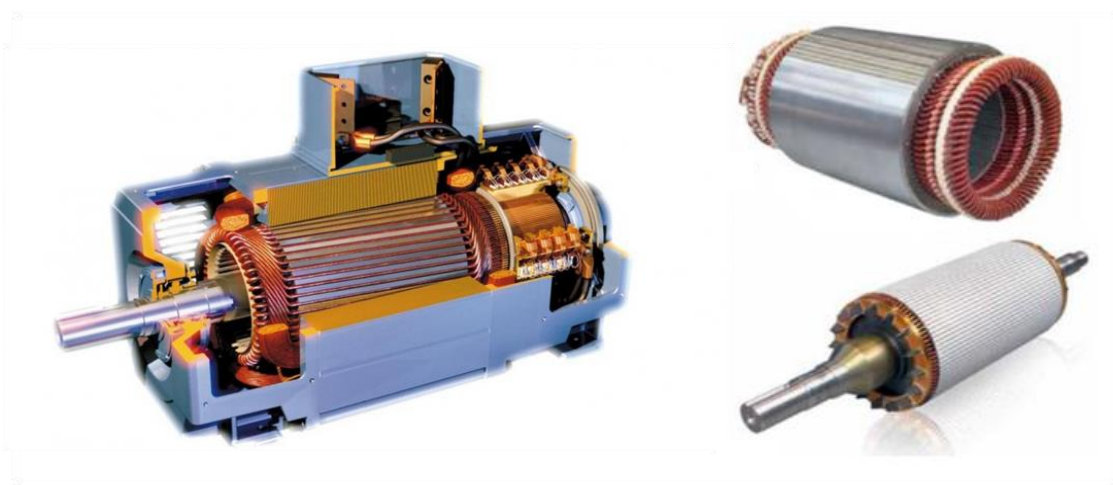


Figure 1.1. ABB motors. Left, DC motor. Right, stator and rotor of an induction motor.

In spite of the fact that PMSM technology is well known since the thirties and the presence of practical designs in the literature in dates as early as 1953 [Ginsberg 1953], is in the nineties when the commercialization of Neodymium Iron Boron (NdFeB) magnets permits to the PMSM to penetrate into the industry as a suitable choice.

Compared with the induction machine the PMSM has good amount of advantages such as compactness, no rotor losses, higher power factor, higher power density and better efficiency [Islam 2009]. Like induction machines, PMSM do not need brushes. Due to these attractive features PMSM are widely employed in high power applications such as aircraft industry, elevation, electric vehicle or power generation where they are a competitive alternative to induction machines, a visual size comparative between the two technologies is shown in Figure 1.2.

Two main PMSM drawbacks are the reason that the induction machines continue being the preferred choice in most of the industrial application: high magnet cost and the risk of permanent magnet demagnetization that supposes less reliability than induction machines.

However, a clear trend towards an increasing presence in both, industrial and domestic applications, makes the PMSM an emerging technology and a very active field of study, as it is highlighted by the great amount of publications devoted to that topic in the last years.

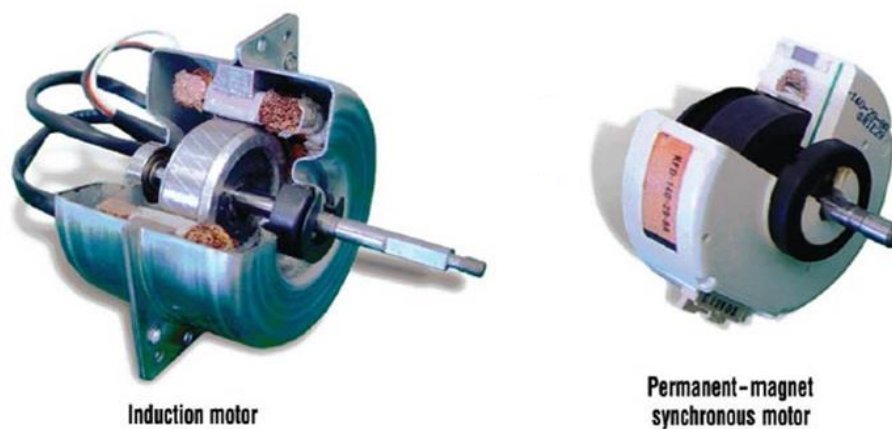


Figure 1.2. Comparative between an induction motor and a PMSM for similar power.

The aforementioned reasons are the cause that the PMSM is the chosen topology to perform the design methodology proposed in this thesis. In this section a brief summary of PMSM operating principles, classification, challenges and evolution is included.

1.2.1 Operating Principle

All electrical motors and generators operate with the same principle: the interaction between magnetic fields. In most cases (except in some reluctance machines) there

exist two magnetic fields whose interaction transform the electrical energy into mechanical one or vice versa, by means of storing it in magnetic fields.

The simplest kind of motor is formed by two external permanent magnets which remain fixed (stator) and an internal one which is free to rotate about its centre (rotor), see Figure 1.3 (a). Of course, the internal magnet tries to align itself with the others generating a torque, as far as different poles attract each other and equal poles experiment a repulsion force. The motion will end when the internal magnet is aligned with the other two in an equilibrium position.

If the internal magnet is substituted by an electromagnet its polarity can be reversed inverting the DC current direction through it, in that way it is possible to change the polarity when the electromagnet reaches the equilibrium point, so the motion will continue indefinitely. Figure 1.3 (b) shows an electromagnet under the aforementioned conditions. It is interesting to notice the presence of the brushes and the commutator that permits to propagate the current to the rotor during its motion and invert the current direction, respectively.

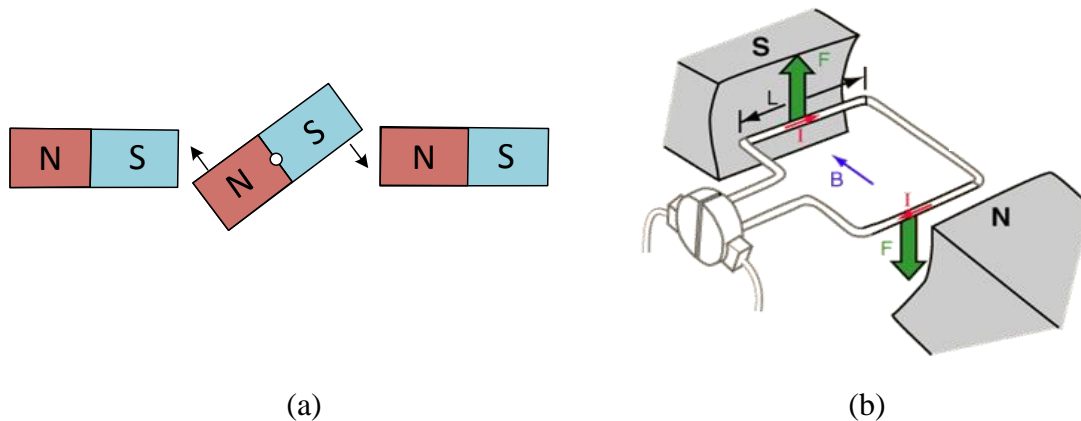


Figure 1.3. Motors basic principles (a) basic case with magnets, (b) with a rotor electromagnet.

In the case of a PMSM the principles are the same that in the example presented but some important changes are introduced: usually there are a higher number of magnets (called poles) and they are usually placed not in the stator but in the rotor, in order to avoid the faults caused by the brushes. On the other hand, the current source is a polyphase AC with one or many coils in each phase as Figure 1.4 shows, rather than a DC one.

As a general principle, during a normal motor operation, the magnetic field caused by the stator coils (that can be seen as an equivalent electromagnet) leads the rotor motion, causing the magnets to rotate while the rotor magnetic fields is lagging the stator one by a constant angle φ that is usually near 90° in order to transfer the maximum energy between the stator and the rotor, i.e. to have the higher possible torque.

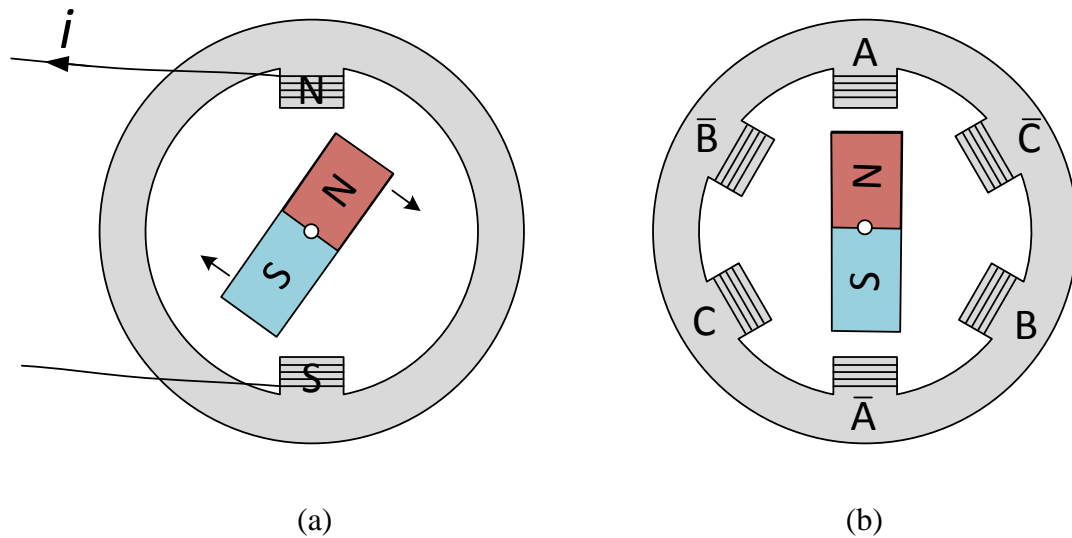


Figure 1.4. PMSM configuration. (a) example with one coil, (b) example of a three-phases configuration. Figure from [Hanselman 2012].

1.2.2 Permanent Magnets: Features and Evolution

The history of the PMSM is undeniable linked with the features and technical evolution of the permanent magnets. In essence, permanent magnets are magnetic materials with very large hysteresis loop [Hanselman 2012], see Figure 1.5. In order to create a new magnet from an unmagnetized sample of a magnetic material (e.g. ferrite, samarium-cobalt, neodymium-iron-boron, etc.) very large magnetic field intensity is applied by means of external electromagnets and then it is removed. Thus, the relaxed material goes from its unmagnetized point 1 to 2, once the external magnetic field is switched off the newly created magnet reach point 3, going through a demagnetization curve different from the magnetization one.

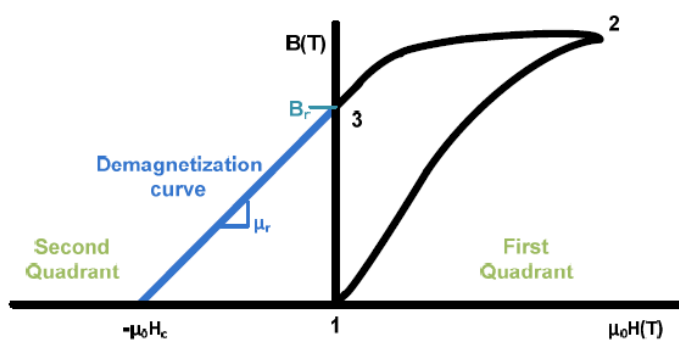


Figure 1.5. Hysteresis loop of permanent magnet material. Figure adapted from [Hanselman 2003].

Once the magnet has been created, it is expected that its normal operation is not in the first but in the second quadrant, where its operating point depends both, on the reluctance path that the PMSM offers to the magnetic flux and on the external magnetic field caused by the stator coils. Generally, three data define the magnet behaviour in a practical motor design: first, its residual induction B_r , second its relative

permeance μ_r which, generally, is very close to unity and third. The first is the origin ordinate and the second the line slope. The third important data is the dependence of B_r with temperature, because real magnets decrease its residual induction with temperature as it is shown in Figure 1.6. This loss is reversible and B_r is recovered once the temperature returns to its original value.

Figure 1.6 shows another important characteristic of the permanent magnets; its real demagnetization curve presents a knee in the second quadrant. If the external field intensity H_g is large enough to operate beyond the knee an irreversible demagnetization will occur. Once H_g is removed the residual induction is not the original one B_r and the recovery line is different to the demagnetization curve leading to a new point B_r' lower than B_r (see Figure 1.7). So it is very important to ensure that the magnets do not reach that operation point, not even if a short circuit in the PMSM coils is produced.

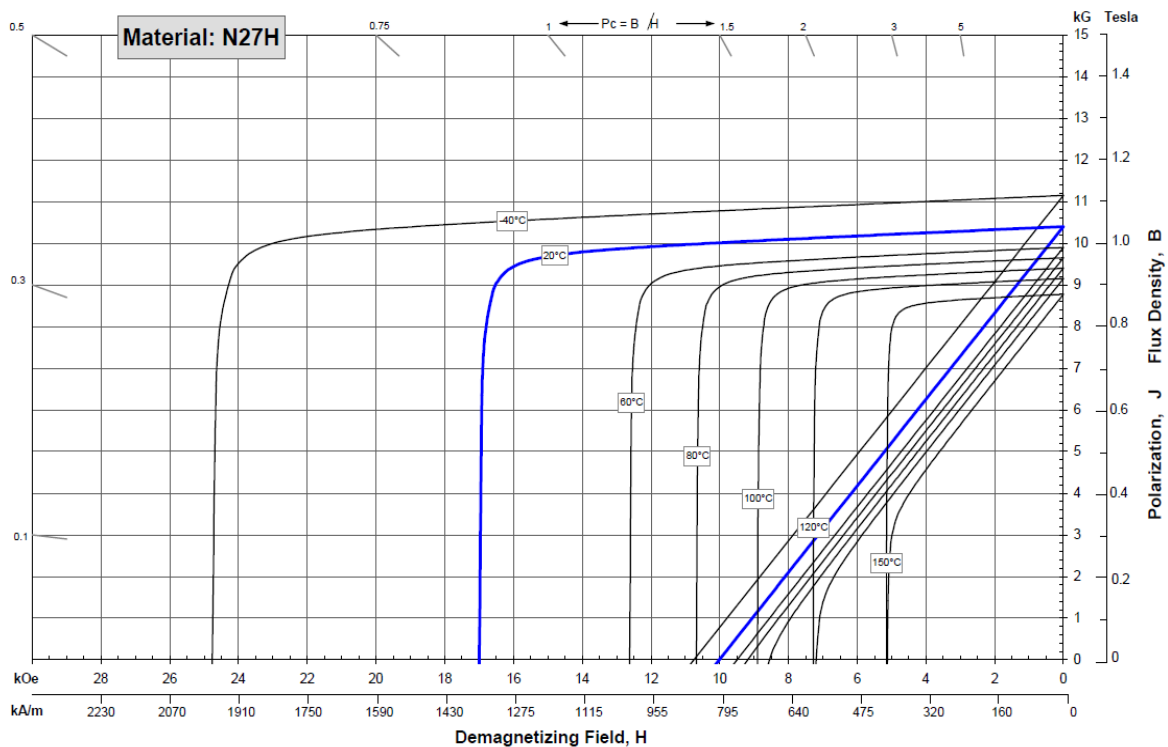


Figure 1.6. Demagnetization curves for N40H magnets at different temperatures. (Arnold® Magnetic Technologies).

Another interesting feature of the magnets related with their hysteresis loop is the maximum energy product, which is defined as the maximum achieved BH value. Although this magnitude is a typical figure of merit in magnets comparisons and it has units of energy it is not, in fact, the stored magnetic energy but rather a qualitative measure of the magnets general performance in a motor [Hanselman 2012]. Figure 1.7 shows an example of this concept. It is important to notice that, though $BH|_{max}$ is the point of maximum efficiency in order to exploit the magnets properties it is unusual that the PMSM magnets work in that point because of the high risk of demagnetization if the knee is reached.

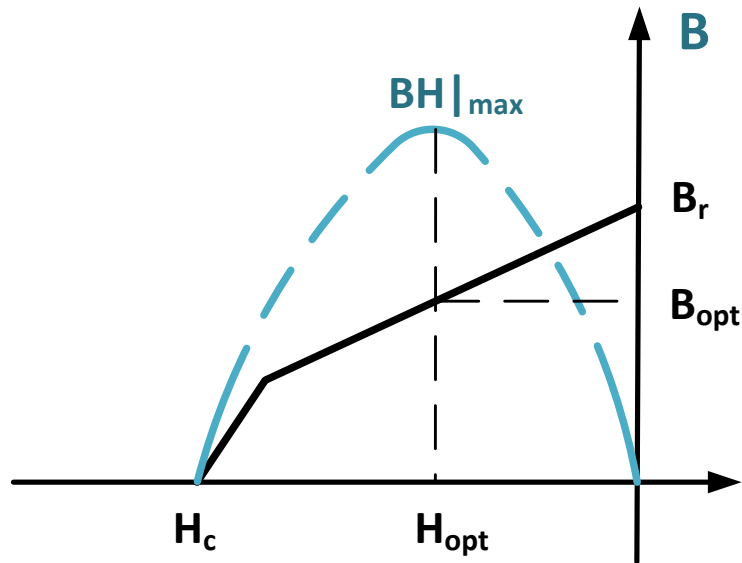


Figure 1.7. Characteristic demagnetization curve, operation line segment and BH curve. Adapted from [Pyrhönen 2008].

The general features of the permanent magnets have been introduced in the previous paragraphs but each permanent magnet technology has its own advantages and drawbacks related to its BH product, features variation with temperature, external field dependence and cost.

Over the past century great improvement of high-energy permanent magnet materials has been done. Figure 1.8 shows the maximum energy product achieved for each magnet technology during the last years.

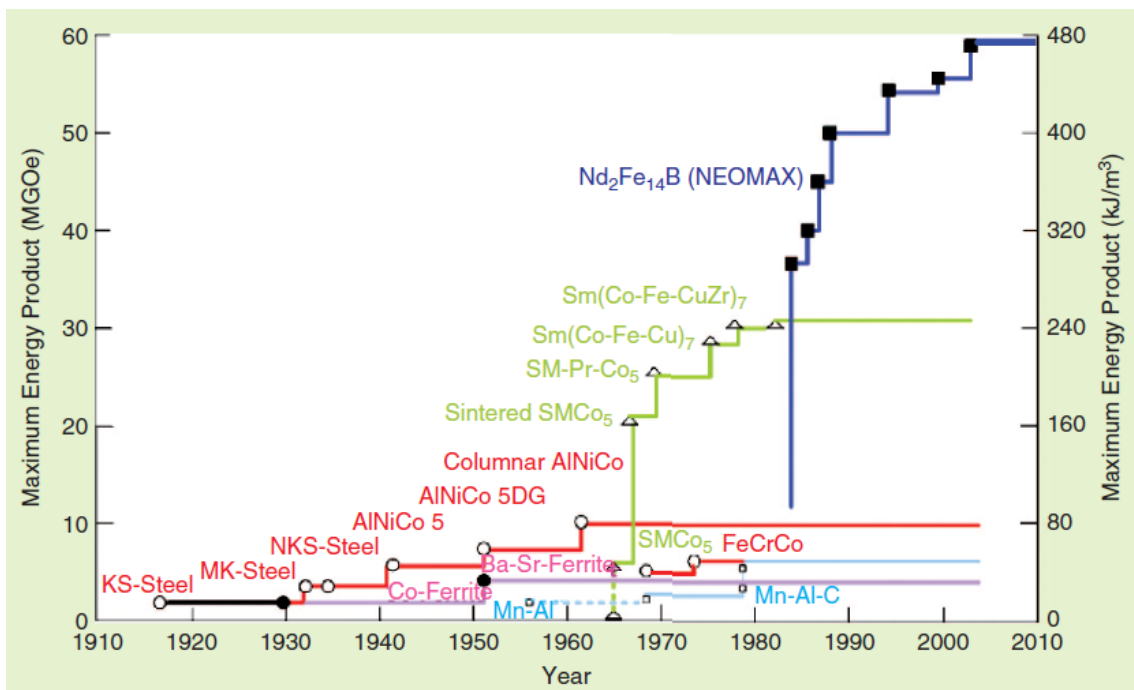


Figure 1.8. Evolution timeline of the permanent magnet maximum energy product during the last decades [Rahman 2013].

In the fifties, ferrite and barium ferrite magnets were the favourite choice for PMSM construction, with energy products from 8 to 30 kJ/m³ [Rahman 2013]; even nowadays ferrite magnets are a suitable option in PMSM of low power and performance, due to their low market price.

In the late fifties aluminium nickel cobalt magnets (AlNiCo) reached energy products of 40 kJ/m³ and became the best choice for PMSM until rare-earth magnets appeared in the sixties with samarium cobalt alloys [Rahman 2013].

But it is in the late eighties when the discovery of NdBF_e magnets enables the popularization of the PMSM and a higher integration of this kind of machines in industrial and transport environments due to their good features. These magnets present the higher energy product available in the actual market [Islam 2009], reaching 480 kJ/m³ with a residual induction of 1.2 T.

In spite of that fact, the NdBF_e magnets present some important drawbacks, like their high temperature dependence, their poor cooling capabilities and their relative low electrical conductivity that causes higher eddy current losses [Pyrhönen 2012]. However, their main disadvantage is their high and changing price.

The main cause of this high price is that most of the operating rare-earth metals mines are in China (e.g. China controls the 75% of the NdBF_e magnet production), which has the ability to modify their market price according to their own needs. For example, in 2010 Chinese government limited to a 60% the rare-earth metal exportation respect to previous years, causing a high increase in their price. Eventually, this fact makes that other potencies, such as the US, are opening new rare-earth mines in their own territory, trying to avoid the excessive dependence from China [Sirvent 2012].

NdBF_e magnet cost is the main reason for the PMSM high price that is, in fact, its main drawback when compared with other possibilities such as induction machines. If the NdBF_e magnets price was lower it is quite likely that PMSM overcomes competing technologies in most of the industrial sectors, but while China has the control over NdBF_e magnet markets this is a remote possibility.

1.2.3 PMSM Structure and Classification

Classical PMSM structure consists of a mobile part or rotor where the permanent magnets are glued or inserted, and a fixed part or stator where the coils are wound, generally in slots situated between teeth. Both, the stator and the rotor are constructed with some type of ferromagnetic material in order to conduct and lead the magnetic flux in the appropriate direction. Between the rotor and the stator there is a slight layer of air called airgap, where most of the magnetic energy is stored.

The aforementioned components establish the machine magnetic circuit. Figure 1.8 (a) shows a 2D representation of a radial, superficial PMSM, whose magnetic flux flows

radially through the airgap and it is only dependent on the circumferential coordinate, so just a 2D slice of the PMSM can be used in order to study its magnetic behaviour. This scheme represents accurately a real PMSM, as it is shown in Figure 1.8 (b), where more important machine parts can be seen, such as the coils end-windings, the housing with its fins or the rotor shaft, all of them playing a major role in the mechanical, thermal, electrical and structural machine features.

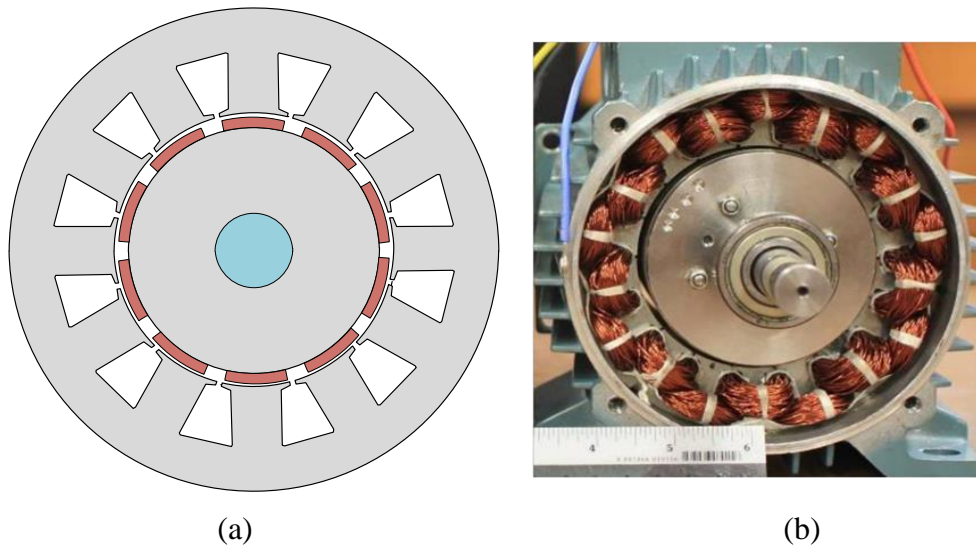


Figure 1.9. (a) Schematic of a 2-D slice of a radial PMSM. (b) Typical radial PMSM.

The example presented in Figure 1.8 (a) is a radial, superficial, exterior rotor, concentrated winding PMSM, which is one of the commonest PMSM topologies. In this section other possible PMSM topologies will be introduced.

There exist a lot of PMSM valid topologies that can be classified according to the magnets situation in the rotor, the rotor relative position, the wound stator coils or the main direction of the flux through the airgap. The classification presented in this section is the most common but it is far from being an exhaustive one, mainly because some PMSM topologies were invented in recent dates, changing old classifications and generating new ones, because many of their properties are still unknown.

1.2.3.1 Rotor Relative Position

Two options exist related to the rotor position: internal or external rotor. Figure 1.9 shows both alternatives.

The main advantage of the exterior rotor is that the motor could be designed with larger airgap diameter for the same volume, as far as the magnets height is less than the total stator height, usually determined by the slots. Since the total PMSM power is roughly proportional to the squared airgap diameter, this leads to a design with more power density [Kazmin 2008-b]. Another advantage is that the magnets are closer to the motor surface, being able to evacuate the heat more easily and avoiding the risk of permanent demagnetization due to high temperatures.

On the other hand, the rotor is more exposed in that configuration; this fact can lead to operation failures. Moreover, the stator is known to be the PMSM part where most of the losses are concentrated. Indeed, both iron losses in the core and copper losses in the winding are concentrated in the stator. Due to the stator enclosure in external rotor machines most of the generated heat must be evacuated through the hub which has much less surface than that available for dissipation purposes in an internal rotor configuration.

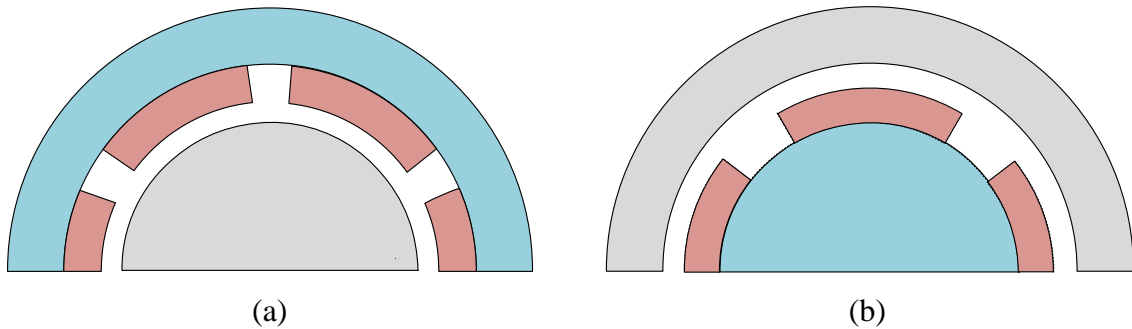


Figure 1.10. (a) External rotor configuration, (b) Internal rotor configuration.

Because of these disadvantages internal rotor configuration is the most common in practical applications.

1.2.3.2 Magnets Situation in the Rotor

Three main configurations can be found in the literature: superficial PMSM (SPMSM), internal PMSM (IPMSM) and inset PMSM. In the latter, the magnets are embedded in the rotor, but very near of the airgap. In practical terms, inset PMSM are more similar to IPMSM and their features are very close. An example of an IPMSM rotor and a SPMSM rotor can be seen in Figure 1.11.

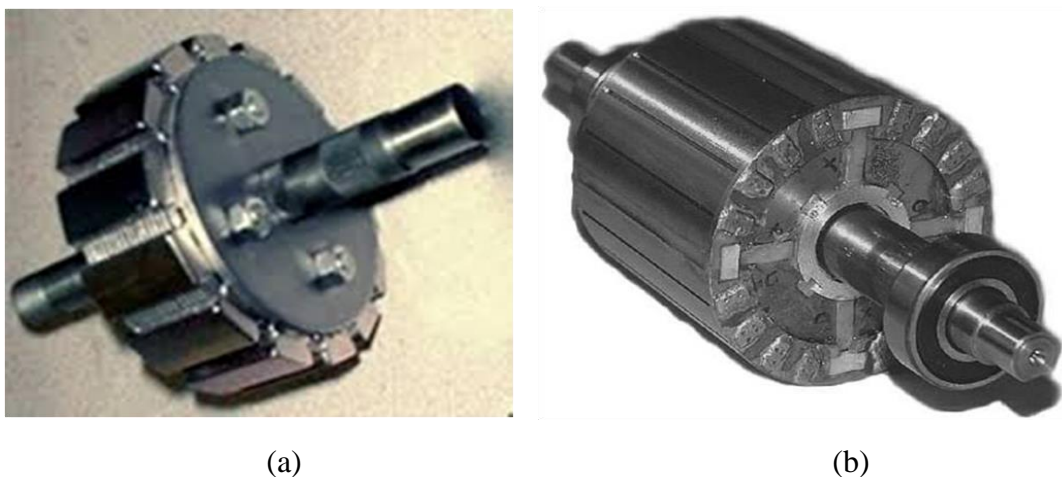


Figure 1.11. (a) SPMSM rotor, (b) IPMSM rotor (from [Rahman 2013]).

The main feature of an IPMSM is that it presents an additional source of torque called reluctance torque, that it is not caused by the rotor and the stator magnetic fields interactions, but just for the interest of the stator electromagnets to align

themselves with the lowest reluctance path. This effect will be highlighted in Chapter 3. The obvious conclusion is that the IPMSM has more torque density and, thus, more power density than a SPMSM.

Another important consequence of having the magnets inside the rotor is that the airgap could be much shorter, since the magnets are no longer a part of it [Kazmin 2008-b]. This means that the magnetic induction is higher than in a SPMSM design, causing higher rotor saturation and a higher risk of magnets demagnetization in case of stator coils short circuit.

As a summary, compared with SPMSM, IPMSM topology presents higher power density and, because of their enclosure, the magnets are more protected from mechanical stress, but it has the drawbacks of more complicated rotor manufacture process, higher level of torque ripple, higher rotor core losses, higher magnet heating and presence of local rotor saturations.

Therefore, the best choice between an IPMSM and a SPMSM mainly depends on the application.

1.2.3.3 Stator Coils Winding

There are two main options when a stator winding is chosen: concentrated or distributed winding. In concentrated windings the coils are wound in consecutive slots, while in distributed ones they are wound in order to maximize the rotor flux linkage, no matter the distance between consecutive connected slots.

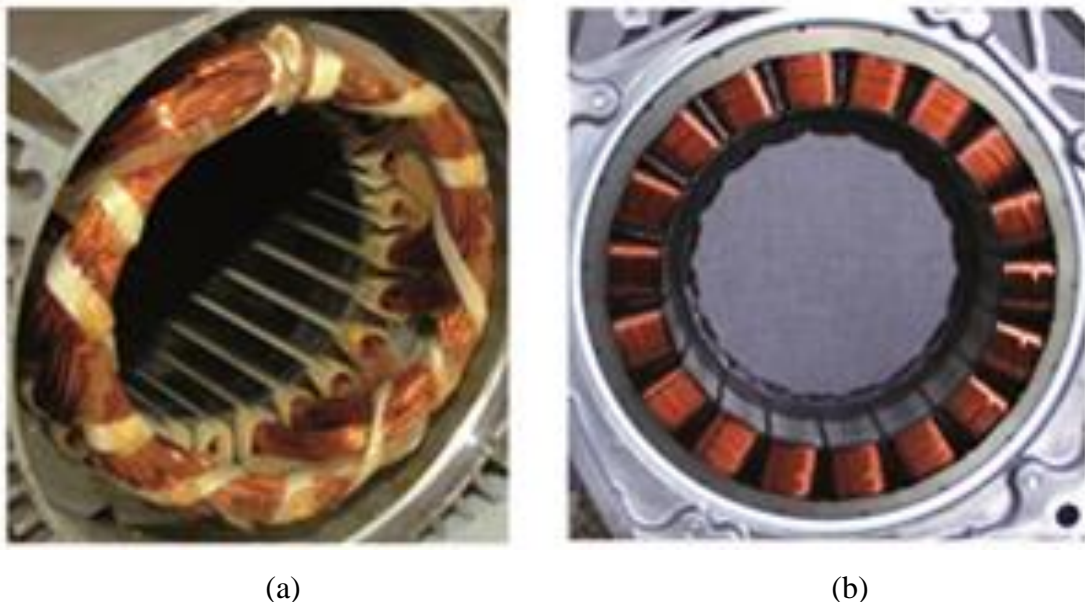


Figure 1.12. Comparison of distributed (a) and concentrated (b) windings. [Photo: University of Bundeswehr].

The main advantages of concentrated windings over the distributed ones are related with their shorter end-winding. In fact, less end-winding means lower copper losses, less total PMSM volume and more effective automated manufacturing.

However, the voltage induced by the magnets in the coils, i.e. the electromotive force (EMF), has more harmonic components, so current and torque ripples are generally higher than those caused by a distributed winding [Lee 2009, Patel 2013].

1.2.3.4 Flux Direction

One of the main fields of investigation of PMSM concerns new topologies where the classical airgap magnetic induction orientation in the radial direction is changed in order to achieve better machine performance.

The main flux path in an axial machine is in axial direction, while in transversal one the flux is directed in both, axial and radial directions. A representation of the three mentioned topologies is shown in Figure 1.13.

Transversal and axial machines are expected to have better performance than classical radial ones. For example, transversal PMSM present a very high power density due to the fact that they are able to increase their power with their pole number but without increasing the ferromagnetic material volume. Another of their features is less copper losses and high efficiency in applications with low speed and high torque.

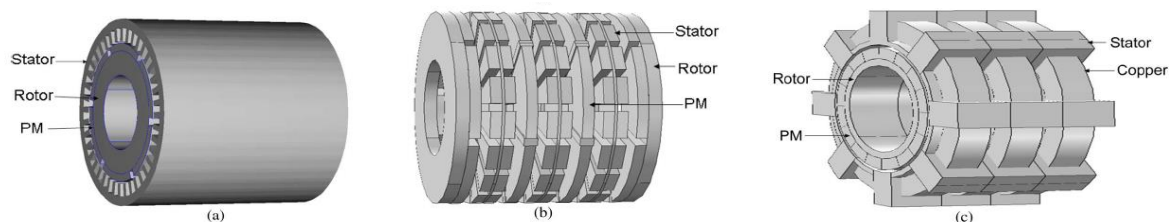


Figure 1.13. Example of the main PMSM topologies. (a) Radial flux, (b) axial flux, (c) transversal flux [Anyuan 2010].

In spite of the aforementioned reasons, radial flux machines are, by far, the most common among PMSM, because of its simpler manufacture process and the much more mature technology.

1.3 Radial SPMSM Design: The Starting Point

The PMSM topology selected in order to implement a complete analytical and multiphysical modelling and a subsequent design methodology is an internal rotor, radial, superficial PMSM because it is the more frequent PMSM topology and,

therefore, the most used for industrial applications, with good features and a well-established manufacture process.

The main features and advantages of this topology in particular and of PMSM in general with respect to other machines are summarized below.

- High compactness.
- High torque and power densities.
- Very low rotor losses. High efficiency.
- No need of brushes or commutator that other machines require.
- Higher power factor than induction machines.
- Simple and robust rotor construction, no need of internal holes or rotor bars.
- Lower noise and vibration with respect to induction or switched reluctance machines.

For the aforementioned characteristics, radial SPMSM was the final election to perform an improved design methodology useful to accomplish a real, complete industrial machine design.

In this section a brief summary of the multiphysics models used to support the optimized design methodology is introduced in order to achieve the necessary overview of the whole process that will be explained in detail during the rest of the document. Figure 1.14 shows the general diagram that will be the backbone of the proposed modelling.

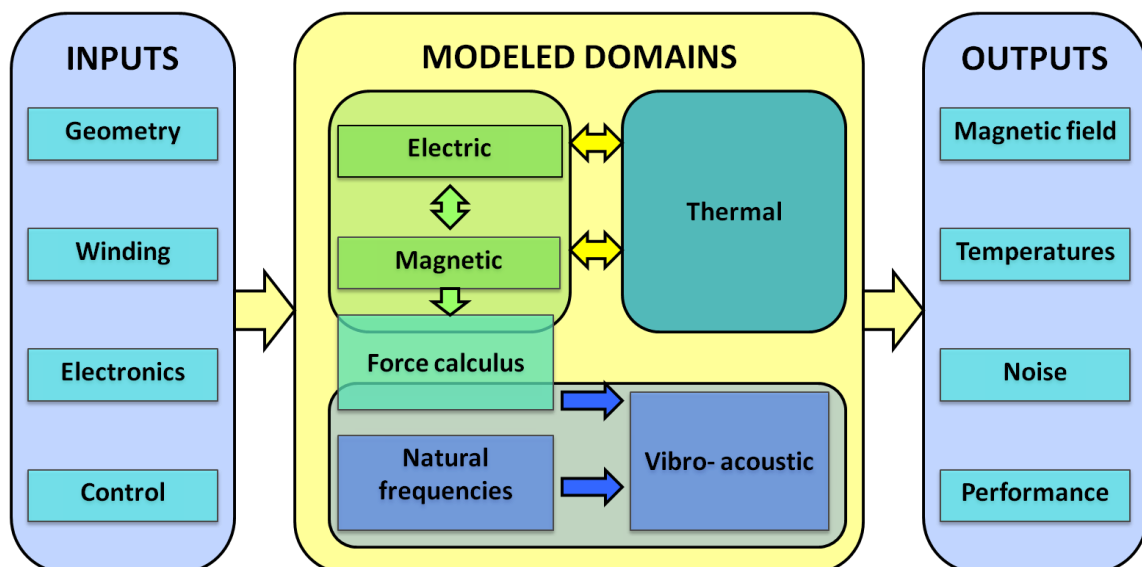


Figure 1.14. Block diagram of the proposed multiphysics linked models.

As it was introduced before, the implemented models are analytical, in order to save computation time. Such analytic methods require the simplifications and assumptions listed below:

- 1) It is assumed that the ferromagnetic material in the rotor and stator cores is infinitely permeable.
- 2) The magnetization profile of the magnet must be radial or parallel.
- 3) The machine has m phases without neutral with a balanced winding spatial distribution.
- 4) It is considered that the motor is rotating anticlockwise, so the teeth and the slots are numbered from 1 to Q in this direction. See Figure 1.15
- 5) No skew is considered.

The first simplification is especially important because it can lead to a considerable accuracy loss if the ferromagnetic core is saturated. In fact, this entails the main disadvantage of the analytic methods, but the error can be minimized ensuring that the ferromagnetic material is not in the saturated region during the PMSM normal operation mode.

Another important remark is the different nature of the input variables that the model needs in order to achieve the motor behaviour and performances. They can be classified by their origin as geometrical variables, winding and other configuration variables (such as number of poles or slots) or in electronics and control variables, the latter having a major influence in the motor feed current harmonics. All of them are required by the model and must be established by an external algorithm.

These input variables can also be classified in a more interesting way by their nature. They are divided into three groups:

Design specifications: initially established by the user as a requisite of the desired PMSM. Once the optimization software is running they cannot be changed, not even between different iterations of the model. Examples of design specifications are the revolutions per minute, the objective mechanical power or the number of the motor phases.

Physical constants: They are established by the program itself and cannot be modified, either by the user or the optimization program. Two examples can be the copper conductivity at 20°C or the void magnetic permeability.

Design variables: They are fundamental variables that cannot be modified in an iteration of the model but they are changed between iterations. They are used by the external optimization algorithm in order to find the best solution in terms of an objective function. Geometric variables (number and dimension of the slot in the stator, motor radial dimensions, etc...), configuration variables and most features of the used materials are included here.

Prior to the execution of physical models, a set of secondary variables is obtained from the aforementioned main variables. They can be calculated by direct operation and will not change during an iteration of the code. A good example is the rotor radius R_r which is obtained from the inner stator radius R_s , the magnet length l_m and the airgap g from.

$$R_r = R_s - g - l_m. \quad (1.1)$$

For a clear understanding of the geometric variables used during this thesis work Figure 1.15 is included, showing a radial section of the PMSM and a detailed view of a slot.

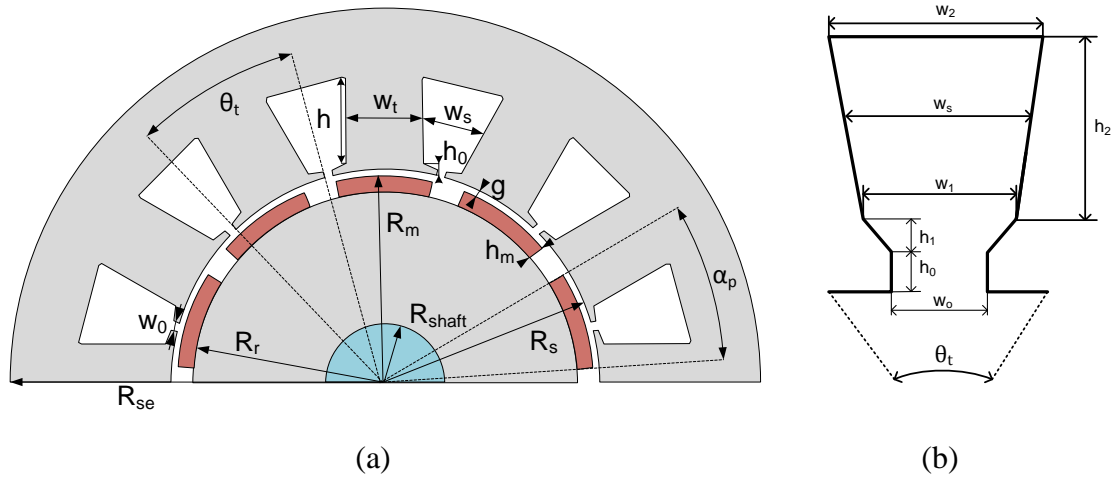


Figure 1.15. (a) Main dimensions of the SPMSM motor, (b) detail of a slot.

In order to validate the developed models and therefore design methodology, a tool was programmed in Matlab®, the results obtained will be compared with those achieved using commercial Finite Element Method (FEM) software.

1.4 Outline of the Document

The document contents are summarized as follows:

In this first chapter the objectives of the work, the general context of the problem and the starting point of the thesis is highlighted. Moreover, a brief introduction to the PMSM is included, explaining its operating principle, its different topologies and its historical evolution.

Chapter 2 shows the state of the art and the main technical and scientific contributions in PMSM design and modelling published in the past years, paying an especial attention to the optimized and multiphysical approaches that include two or more of the physical domains of interest, i.e. magnetic, electric, thermal, structural or vibro-acoustic.

Chapters from 3 to 6 explain the physical models implemented, showing the achieved results and proving their accuracy, usefulness and precision through the comparison between the developed tool and commercial FEM software (FLUX2D®, ANSYS® and Motor-CAD®).

Specifically, Chapter 3 is devoted to electromagnetic models and its linkage with main mechanical aspects, such as torque and mechanical power generation, Chapter 4 explains the losses and quality parameters estimation, Chapter 5 introduces a thermal approach based on lumped thermal network and Chapter 6 exposes the structural, vibratory and acoustic features of a PMSM.

Chapter 7 explains the synthesis and implementation of an improved, original, optimized, holistic and fully analytical design methodology and its associated software.

Finally, Chapter 8 shows the conclusion of this document and the proposal of the next future lines to be studied during this thesis work.

2

Design and Modelling of PMSM: Optimized-Multiphysical Study

SPMSM design is a complex matter, so the development of an extensive state of the art is a difficult task, as far as many criteria and different approaches should be taken into account. In this chapter, a brief global picture in PMSM design will be presented in order to achieved a summarized but a complete insight in the recent developments and global trends in the subject.

The chapter is divided into two main sections, corresponding to the parts of a complete design implementation: the first one introduces the state of the art in PMSM design methodologies and the second one is devoted to the main modelling approaches used in the aforementioned methodologies.

2.1 Towards a Design Methodology: State of the Art

Nowadays, in the technical literature many papers and related publications about PMSM design can be found. In spite of this fact, most of them only take into account partial aspects of the global problem and offers unclear and opaque methodologies that are hardly replicable at the best.

Moreover, these approximations are not only incomplete but, generally, use optimization tools and algorithms as a black box, trying to achieve just a satisfactory rather than an optimal design [Goss 2013-a].

In this context, it is common to find methodologies just based on a basic electromagnetic initial sizing, where the main contribution presented is the link of FEM calculus with a blind use of an optimization algorithm which slightly improves a pre-existing design.

On the other hand, in industrial design, most of the used methodologies are focused only on the electromagnetic performance and they estimate the most important features of the machine, such as efficiency, power, and volume to mass ratio, only considering its electromagnetic characteristics [Boglietti 2009]. Thermal sizing is usually reduced to some empirical rules and key aspects, such as maximum winding current density, which provides a first approximation that can be accurate enough in some low-performance, very well-known applications [Amrhein 2013]. Other important physical domains such as mechanics and vibro-acoustics are treated as an afterthought if needed.

This kind of “industrial methodologies”, labelled “sizing models” in [Carlson 2012], is based in basic electromagnetic equations without any optimization process and usually needs a great deal of approximations and “rules of thumb”. This fact supposes that, in a complete design process, many interesting machine possibilities are directly discarded and are never modelled at all.

Sizing models are fast and reliable if very similar machines have been previously studied and correct empirical parameters obtained. However, they are unsystematic

by nature and present serious difficulties to extrapolate the obtained results to a new set of specifications or to more exigent applications.

In recent years, especially in the last decade, a different methodological approach based on a deeper insight in the physical PMSM behaviour has been developed. This new modelling allows for the implementation of design methodologies which are less dependent on designer experience or empiric rules and, therefore, are much more reliable for high-performances and new applications.

The interest in these new design methodologies in the academic, and even in the industry world, is endorsed by recent publications, such as [Agamloh 2013], which explains in detail the multiphysical challenges of a holistic induction machines design, [Ombach 2007] which deals with the manufactured tolerances during an industrial design process, [Tsampouris 2013] which develops a software capable of coupling the design and control stages or [Favi 2011] which proposes an online design tool in order to shorten the development time. These works try to bring closer that new methodology approach from a more academic context to the industry, where its practical implementation can suppose more efficient machines at lower cost.

Despite their many advantages these methodologies are far from being widely used in industry because of their novelty and the specific knowledge necessary to analyse the different aspects of a PMSM. Because of the aforementioned drawbacks only some research groups are focusing on the multiphysics machine modelling and design, but the great accuracy and high integration levels of their results explain the increasing interest in these approaches.

Many of these methodologies present a double loop structure, where a first design stage is done with fast analytical sizing equations and a second one with numerical approaches, more accurate but more time consuming, in order to combine the advantages of both techniques. The general flowchart shown in Figure 2.1 is shared with slight modifications by many recent publications [Makni 2007, Elosegui 2008, Tutelea 2010, Wang 2012, Goss 2013-b].

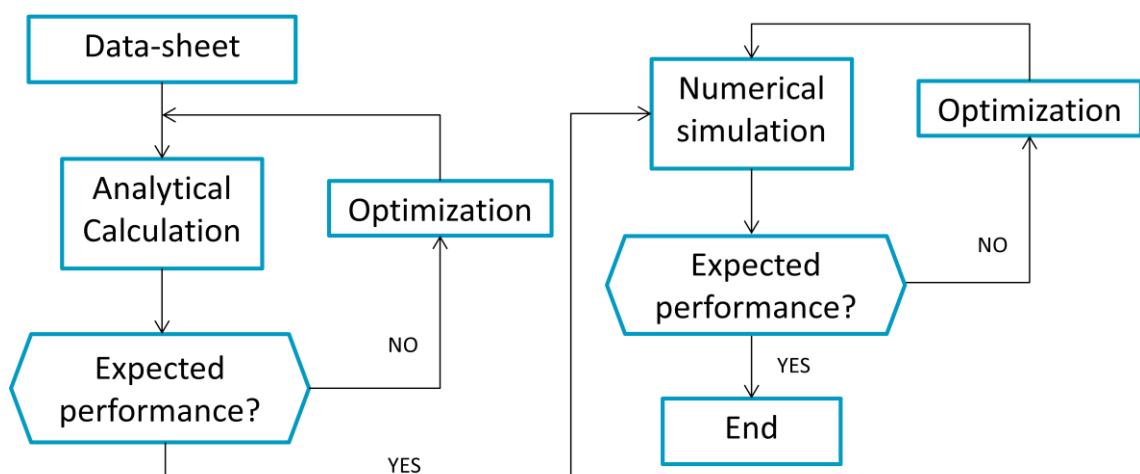


Figure 2.1. Classical two-stage flowchart in recent machine design approaches.

Most of the recent published design methodologies have nearly the presented flowchart; one of the differences is the specific weight of the numerical and analytical calculus (even some of them include only one of the two stages) and the presence or not of an optimization algorithm closing the loop. According to the design criteria the aforementioned methodologies can be classified as follows:

- **Design type:** Two main designs can be performed: the first is a global one, taking into account a high number of design variables and seeking for a holistic and new design; the second is a local one, varying a limited number of design parameters and generally starting from a previous design in order to improve some key features. Examples of global designs are [Bracikowski 2012, Hecker 2013], and local designs are [Mi 2006, Lee 2009].
- **Operation range:** Another major concern is the torque-speed PMSM operation range, some publications deal with the design problem just in nominal operation conditions [Hecker 2013, Duan 2013-b], i.e. at rated speed and torque, while others are centred in applications such as electric vehicle which demands a design centred in all the operation range and not just in nominal conditions [Hafner 2011, Wang 2013].
- **Physical domains:** In function of the number of physical domains studied the design methodologies can be classified in electromagnetic ones [Elosegui 2008, Tutelea 2010], magnetic-thermal [Kazmin 2008-a, Legranger 2008] or multiphysics [Semidey 2011, Jannot 2011].
- **Modelling:** According with the kind of modelling used a methodology can be analytic [Kazmin 2008-a], lumped parameter oriented [Bracikowski 2012], numeric [Giurgea 2008, Van der Giet 2010] or hybrid [Makni 2007, Goss 2013-a].
- **Optimization process:** Another major concern is the use or not of an optimization algorithm in the design process. The methodologies can be optimized [Iles-Klumpner 2004, Sarikhani 2012] or no optimized [Kazmin 2008-a, Saito 2010], the latter are the so called sizing models. Within the optimized methodologies a new classification according to the algorithm used and the proposed variables and objectives can be performed.

Between all the aforementioned features of these design methodologies, two are selected as the key features: their multiphysics nature and the possibility to run optimization algorithms as a part of an eventual design process. Since this state of the art will be specially focused in this kind of design, the global classification of different design methodologies proposed in the literature will be performed in function of two parameters: their optimization procedure and their multiphysical approach.

2.1.1 From a Magnetic to a Multiphysical Approach

When a new PMSM design must be done electromagnetic criteria are the major concern, since the machine main features depend on its electromagnetic behaviour.

Although the final performance and even the safety and reliability of the proposed design are heavily conditioned by thermal considerations, many designs only take into account the electromagnetic domain, oversizing the machine according to heuristic or empirical rules in order to ensure a correct temperature operation in the magnets and in the windings. Some very recent approaches are only focused in partial or global aspects of the electromagnetic design, ignoring the thermal effect in the design process.

A second kind of design methodology is an electromagnetic-thermal approach; this is a great improvement over the classical design methodology, as far as the thermal behaviour of the machine has a great influence over its electromagnetic performance. In fact, not only the electromagnetic features determine the temperatures in the PMSM through copper and iron losses but those temperatures vary the physical characteristic of the magnets and the copper wires, modifying the operating point and, thus, the performance. An example of flowchart that contains an iteration loop in order to calculate the thermal and electromagnetic behaviour is shown in Figure 2.2.

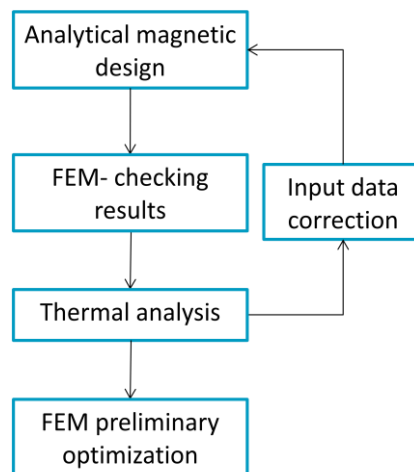


Figure 2.2. Example of electromagnetic-thermal loop in PMSM design [Kazmin 2008-a].

The third and most complete approach is the multiphysical design methodology, which takes into account not only the electromagnetic and thermal features but also the electric, mechanical and vibratory ones. This is a much more complete design method since it permits to modelled the PMSM from a global point of view, achieving an optimum which takes into account much more design goals and features. This is important since the global optimum is not the sum of the partial optima in each discipline. Moreover, it permits to apply optimization algorithms in a more useful sense, since the results obtained by the physical models can be used not only in the objective functions but also as restrictions, for example achieving efficient PMSM designs with restrictions in their interior temperatures, maximum converter voltage required or the radiated noise.

Figure 2.3 shows a graphical representation of the physical domains that a multiphysical design should take into account and the possible goals than can be achieved with this methodological approach.

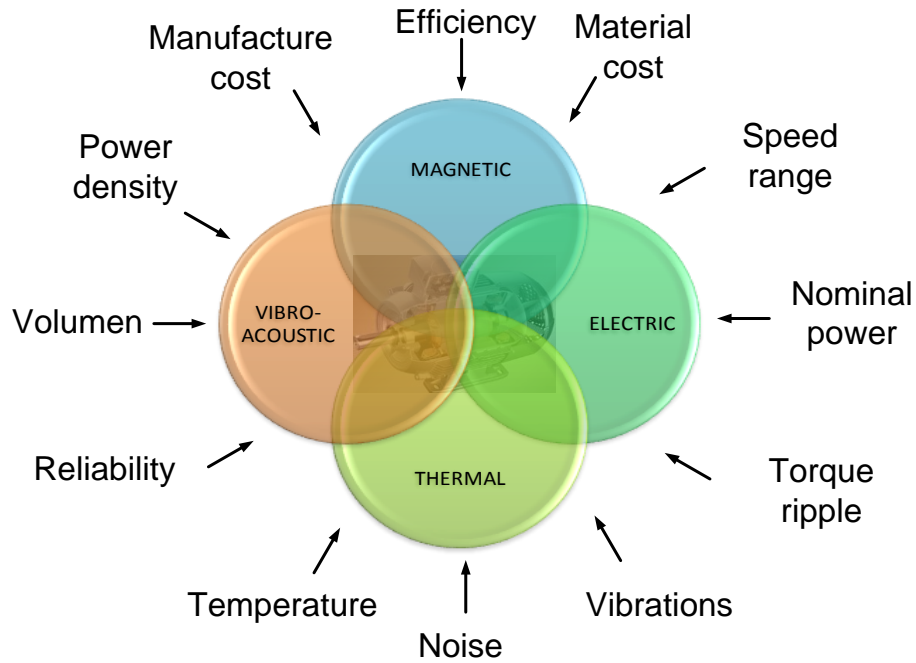


Figure 2.3. Physical domains and main possible objectives of a multiphysical design methodology. Adapted from [Muetze 2008].

2.1.2 From a Sizing to an Optimized Approach

From a mathematical point of view an optimization process can be defined as a problem where, from an input vector called design variables:

$$X = [x_1, x_2, \dots, x_n] \in \mathbb{R}^n \quad (2.1)$$

and a set of estate variables, calculated from the design ones,

$$Y = [y_1, y_2, \dots, y_m] \in \mathbb{R}^m \quad (2.2)$$

it is possible to define one or more objective functions such that

$$\begin{aligned} f: \mathbb{R}^n &\rightarrow \mathbb{R} \\ X &\rightarrow f(X), \end{aligned} \quad (2.3)$$

and a set of restriction functions:

$$\begin{aligned} g_i(X, Y) &\leq 0 \quad i = 1, \dots, k \\ h_j(X, Y) &= 0 \quad j = 1, \dots, s \end{aligned} \quad (2.4)$$

that must be satisfied.

The optimization problem is then to find a vector X such as $f(X)$ is a minimum (ideally the global minimum) of f verifying the restrictions imposed by $g_i(X, Y)$ and $h_j(X, Y)$.

The external users of any optimization algorithms have the main task to define the design variables X , the state variables Y , and also the objective function f and the

restriction functions g_i and h_j , and then the more adequate optimization algorithm to the proposed problem. In the studied design process the design variables usually are the motor dimensions and materials and the objective functions the maximum efficiency, minimum cost or minimum weight.

The different optimal design methodologies applied to PMSM design can be studied and classified according to their objective functions, design variables and restrictions, taking into account the optimization algorithm used.

2.1.2.1 Objective Functions and Design Variables

Many objective functions must be satisfied in a complete PMSM design, amongst them the more common are highest efficiency, lowest cost, minimum use of ferromagnetic material or minimum magnets weight. Since many of these objectives can be conflicting a compromise must be achieved. In recent optimized methodologies multiobjective optimizations with efficiency and cost [Muntenau 2012] or efficiency and weight [Jannot 2011] objectives are very usual.

Other approaches try to optimize more concrete motor features, such as the cogging torque [Cassimere 2009, Wang 2012], the stator structural characteristics, the noise emission [Lee 2009] or the amount of needed magne material [Wrobel 2006].

One important trend in the last years is the step from just one objective function in which all the proposed goals are contained, to a real multiobjective approach, with various objective functions and a Pareto-frontier oriented design. These new approaches have the advantage to provide, not just a single solution but an optimal set of them in order to let the designer to choose the most suitable for its application.

The choice of design variables is another major concern in optimization process. In that sense a clear evolution was performed during the present decade. Ten years ago, only a few geometrical continuous variables are taken into account in the design process, leading to very local approaches that generate designs very close to a proposed initial prototype. An example of that is [Iles-Klumpner 2004] with only needs seven variables in order to perform the electromagnetic design.

Nowadays, the global trend is to define a big set of design variables, usually more than ten, taking into account both continuous and discrete values and allowing a much more global design, varying not only the physical PMSM dimensions but the number of pole pairs, number of slots or the ferromagnetic and magnets materials. This evolution is possible since the powerful software and optimization algorithms developed in the last decades are starting to be applied in the machine design context. Good examples of this trend are [Cassimere 2009] which takes into account seventeen variables, including different core materials and [Kreuwawan 2007] which uses twelve variables, including the number of poles and slots.

2.1.2.2 Optimization Algorithm

An important decision in every optimized design methodology is the correct selection of the optimization algorithm. In order to do so, a first step is to know the particularities of the proposed problem. A lot of different optimization algorithms have been used in machine design methodologies and the main features of the problem are listed in the literature. A global review of the subject can be found in [Duan 2013-a].

To generate an optimal PMSM design it is necessary to take into account that it is a nonlinear and multiobjective optimization problem which involves not only closed-form equations but several estimations and possible lookup tables and iterative loops where a correct estimation of a derivative function is quite troublesome. These particularities imply that only certain types of optimization algorithms are suitable.

Two different approaches can be done in order to perform a design methodology:

- The first one is the use of surrogate models that capture the relationship between design objectives and inputs. These models are not exactly optimization algorithms but a possible initial step that consists in the reduction of the input vector X by means of mathematical approximations and screening techniques. These methods are very popular because they drastically reduces the number of model evaluations needed, a capital advantage when numerical calculus must be performed. Examples of this approach are the response surface method (RSM) or the Taguchi methods. Many authors apply surrogate models in electrical machine design [Giurgea 2008, Amdouni 2012, Duan 2013-b, Hwang 2013].
- The second is the use of a proper optimization algorithm, further explained in the present section.

Optimal search algorithms can be divided into several categories, so different classifications have been proposed in the literature. Figure 2.4 shows a possible one adapted from [García 2014] which includes the main algorithms used in PMSM design methodologies.

Exhaustive or grid-search methods are the simplest design methodologies, as far as they are based on performing a discretization of the variables, evaluating the objective functions in every selected point and choosing the best value as the global optimum. In the beginnings of the use of optimization algorithms for electrical machine designs some exhaustive methods were implemented but soon they proved to be unaffordable in that type of methodologies, as far as many variables are involved and the problem complexity scales exponentially with the number of variables. A comparative example between a grid-search algorithm and other types of optimization approaches can be found in [Iles-Klumpner 2004].

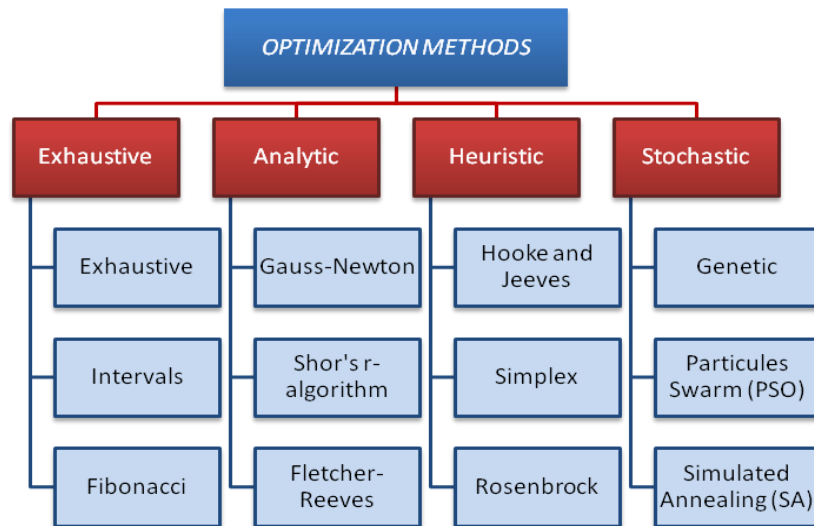


Figure 2.4. Proposed classifications of the main optimization algorithms applied to PMSM design methodologies. Adapted from [García 2014].

The analytical methods calculate or estimate the derivatives of the objective functions in order to change the design variables in the direction of their gradient. Their main advantage is that they are the faster optimization algorithms but firstly they can be caught in local minima and secondly, in some problems, the derivatives are very difficult to obtain. During the nineties, sequential unconstrained minimization techniques (SUMT), an analytical algorithm, were used in order to perform electrical machine design optimization [Wurtz 1996]. Some authors still use that kind of approaches [Wang 2012] but now they are mostly out of use since the advent of more powerful stochastic approaches, such as genetic algorithms (GA) or Particular Swarm Optimization (PSO), where no derivatives are needed.

Heuristics methods have some similarities with the analytical ones but the former are based in the gradient calculus, while in this case the search algorithm is based on performing pattern movements from one or various initial points, and on travelling from these initial points to another one if the objective functions improve. They are slower than the analytical algorithms and equally can be caught in local minima but they have the great advantage of their robustness, as far as no derivatives are needed, so they are a very suitable choice to be applied in design methodologies. One heuristic method, the Hooke and Jeeves, is usually applied in machine design [Iles-Klumpner 2004, Tutelea 2010, Amdouni 2012] but it is less popular than stochastic methods.

Both, the analytical and heuristic algorithms are encompassed in a more general classification called the deterministic algorithms, as far as they find the optimum algorithmically [Duan 2013-a]. In this work, it is considered more useful to divide them in the aforementioned categories, as far as their application in design methodologies is very conditioned by the use or not of derivatives.

The stochastic methods are based on the inclusion of some stochastic operation in order to improve the global search, escaping from local minima and becoming more independent respect to the starting points. Most of them are based on biological or

physical principles, such as natural evolution (GA), the movements of an insect swarm searching for nectar (SPO) or the particular behaviour within a heating solid (simulated annealing). These methods are very robust and especially suitable in searching global optima in complex problems where they can be easily used as black boxes. Thus, they became very popular in electrical machine design methodologies. In PMSM design GA is the most common choice [Cho 1999, Kreuawan 2007, Jannot 2011, Hecker 2013] but, in recent years, SPO is becoming very popular [Wrobel 2006, Sarikhani 2012]. Other stochastic methods, such as differential evolution [Duan 2013-b] or ant colony [Tsamouris 2013], have only a minor use.

Some comparative studies between different optimization algorithms applied to machine design methodology were performed, for example between GA and SPO [Cassimere 2009, Sarikhani 2012] and between GA and Hooke and Jeeves [Tutelea 2010].

2.1.3 The Global Picture

A summary of the studied methodologies is presented in Table 2.1 where the different PMSM design approaches published in the literature are classified according to their multiphysical approach, the used optimization algorithm and the developed type of design (a local or a global one).

Table 2.1. Classification of the PMSM design proposals found in the literature.

		No-optimized	Analytical optimized	Heuristics optimized	Stochastic optimized
Magnetic	Local	[Mi 2006] [Saito 2010]	[Wang 2012]	[Iles-Klump 2004]	[Wrobel 2006]
	Global	[Comanescu 2003] [Elosegui 2008]	[Muetze 2008]	[Tutelea 2010]	[Cassimere 2009] [Sarikhani 2012]
Magnetic-thermal	Local	[Dorrell 2006]	[Legranger 2008]	-	[Cho 2000]
	Global	[Kazmin 2008-a]	-	-	[Goss 2013-a]
Multiphysics	Local	[Marignetti 2006]	-	[Makni 2007]	[Jannot 2011] [Semidey 2011]
	Global	-	-	Proposed methodology	[Bracikowski 2012]

Next, the main conclusions achieved in this state of the art are presented.

From the point of view of the models used in design methodologies two different trends can be found in the literature: on one hand, the development of complex and accurate analytical models is performed by an increasing number of researchers. On the other hand, FEM calculus is the most popular option frequently combined with a stochastic optimization algorithm. In order to link the time-consuming FEM model with a GA or PSO algorithms, a surrogate model is usually applied.

Nowadays, it is evident the increasing trend in the use of optimization algorithms in the PMSM design methodologies, specially the stochastic ones. Some research groups go a step forward combining different types of optimization algorithms in order to take

advance of the benefits of a hybrid approach. For example [Amdouni 2012] applies RMS in order to reduce the problem size, then finds the optimum region by means of a GA and, finally, performs a local search using a Hooke-Jeeves algorithm.

Another major evolution in PMSM design is the increasing number of multiphysical approaches developed. Moreover, most of the multiphysical design methodologies are optimized, in order to maximize the inherent benefits of a multidisciplinary approach. They use their much more powerful insight in the machine behaviour in order to improve several objective functions by means of the optimization algorithm. In fact, in recent publications, the implementation of a multiphysical design without any optimization process is very odd.

Taking into account the aforementioned design approaches, the methodology developed in this work is a multiphysical, global and optimized one. The optimization algorithm used will be the direct multi-search (DMS), a novel multiobjective derivative-free heuristics algorithm developed and first presented by [Custódio 2011]. To the best knowledge of the author of this report, this new algorithm, based in the Hooke and Jeeves one, will be used by the first time in electrical machine design.

As far as it was investigated, no other PMSM multiphysical, global design methodology using heuristics algorithm could be found in the literature, in spite of the fact that the Hooke and Jeeves method obtains very good results in machine design [Tutelea 2010]. This is one of the reasons why it is considered that this new approach is a very interesting path to investigate in.

2.2 State of the Art in PMSM Modelling

As it was explained before, one of the main requirements for the implementation of an optimized design methodology is to develop a model which can represent the complexity of the physical system under study.

This is especially important for a device as complex as a PMSM whose design involves a multidisciplinary approach, including electromagnetic, mechanical, thermal and even structural and acoustical considerations [Bracikowski 2012].

Though many of the aforementioned publications develop multiphysical models in order to include them into different design methodologies, very few explain the correct coupling between physical models, remaining many of the interaction variables and coupling mechanisms unknown. A notable exception to this fact is provided in [Bracikowski 2012], where a complete dissertation about multiphysical coupling in PMSM modelling is performed.

Due to this lack in the consulted literature, this section will be divided into three separate parts, each one concerning to a specific physical field applied to the PMSM modelling.

2.2.1 Electromagnetic Modelling

It is well known that electromagnetic characterization is of critical importance in the design of electric machines. Moreover, most of the industrial models are focused only on the electromagnetic performance and they estimate the most important features of the machine only considering its electromagnetic features.

Thus, huge amount of literature have been written about both, the complete electromagnetic modelling of PMSM and the specific aspects of it, such as cogging torque [Zarko 2008], force density [Zhu 2010] or losses in the rotor permanent magnets [Markovic 2007]. Moreover, a lot of studies are focused on the influence of very concrete modifications in a PMSM, such as dovetails [Kolehmainen 2010] or arbitrary magnet shapes [Wu 2014].

All these models, both the particular and the global ones, can be classified by its method of calculus in three categories, as shown in Figure 2.5.

- Numerical methods: they are based in numerical calculus of the magnetic flux in several points of the machine geometry. Although they reach the most accurate results they are also the most time consuming. The most important methods are the Boundary Elements Methods (BEM) and the FEM ones; the seconds are, by far, the most common in PMSM electromagnetic modelling. An example of FEM modelling is [Giurgea 2008].
- Lumped parameters: this technique is based on a simplification of the motor geometry, represented by a grid of discrete reluctances, i.e. an equivalent magnetic circuit. It can be quite accurate and it is much faster than FEM approach but a very good initial knowledge of the magnetic flux distribution in the machine is required in order to obtain a good reluctance grid which takes into account the geometrical particularities without incur in prohibitive computation times. Examples of lumped parameters designs can be found in [Lu 2013, Gómez 2014].
- Analytical: based on geometrical and physical approximations which permit the simplification of the problem, its formulation in analytical equations can be solved in a short time, but it presents an accuracy loss respect to the previous methods. In spite of that, several researches [Zhu 1993-a, Proca 2003, Zarko 2006, Liu 2008] had shown that its precision is good enough for a first design stage. Moreover, they have very good accuracy if the ferromagnetic cores are unsaturated or only slightly saturated. An example of recent and complete analytical approach is [Liu 2008].

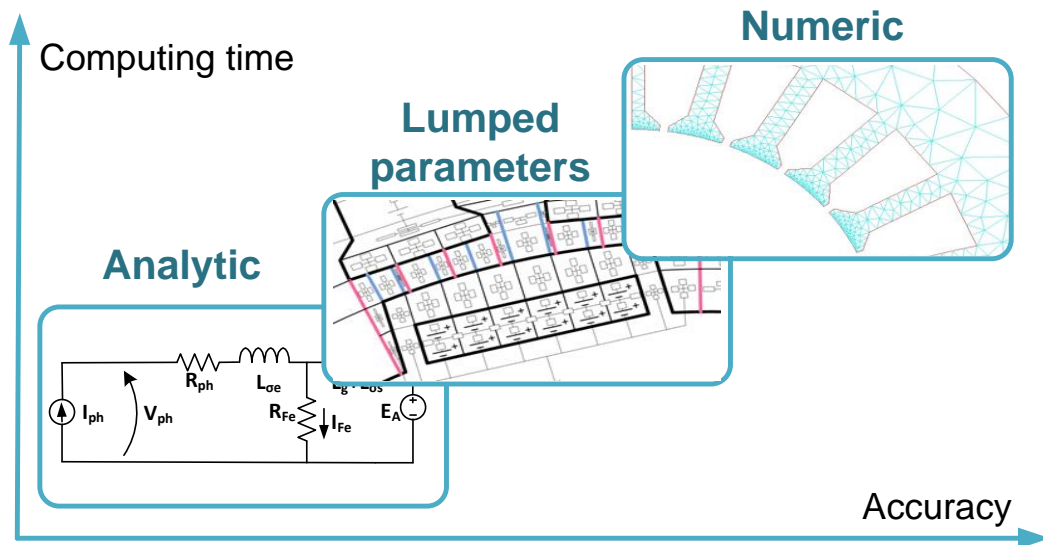


Figure 2.5. Different model approaches for electromagnetic characterization of PMSM.

As it was explained before, in this thesis an analytical approach is used due to its lower computing time. This is a critical advantage in order to implement an optimized methodology, which usually requires running the model many times. This is the main reason why this state of the art will be specially centred in the analytical modelling.

In the literature it is usual to divide the analytical modelling into two main groups: one related to simple and direct size equations and another one based on advanced approaches, which generally used Fourier Series (FS) [Almandoz 2008]. Obviously, the former methods are more straightforward and easier to implement but they are only useful for very rough calculi, so they are usually combined with a lumped parameter models or a FEM calculations in order to do most of the dimensioning process [Comanescu 2003, Mi 2006, Kazmin 2008-a].

The direct size equation modelling is only useful in the framework of a sizing model design methodology, so the presented work is centred in FS methods, due to their better accuracy, their good equivalence with FEM results and the robust and reliable Fast Fourier Transform (FFT) algorithm that the Matlab toolbox offers.

Next, a brief description of the advanced analytical modelling in the last years, both related to global modelling and to particular aspects, will be included.

2.2.1.1 Global Modelling

Global advanced analytical models are usually centred in the magnetic domain and more precisely in the correct calculus of the magnetic induction in the airgap. That is for a double reason: first, the airgap is the region where most of the energy is magnetically stored during its conversion between the electrical and the mechanical domains; and second, the airgap magnetic induction is the most critical parameter

which establishes the flux density in the stator core and, thus, PMSM performance and ferromagnetic core saturations [Makni 2007].

One of the capital contributions in the airgap magnetic induction estimation was done by [Zhu 1993-a] which solved the Maxwell equations in a simplified problem, modelling the PMSM as three concentric cylinders: the rotor, the magnet annulus and the stator (see Figure 2.6). In this way, the magnetic induction in both, the magnets and the airgap regions was calculated in a close analytical solution for a slotless PMSM.

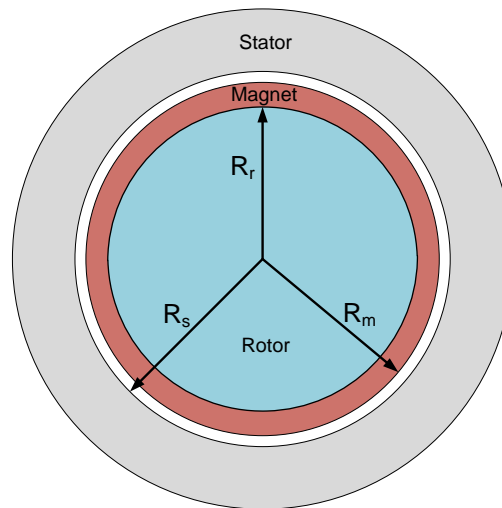


Figure 2.6. Geometry simplification done in order to obtain airgap flux density. Adapted from [Hanselman 2012].

Another of the major concerns about airgap magnetic intensity calculus is the accurate modelling of the stator slotting effect. Two different approaches can be found in the literature, both based on the concept of relative permeance.

Carter's coefficient theory is the backbone of the relative permeance concept; it is based on the fact that the magnetic flux has a lower reluctance path under the teeth than under the slots. Hence, it can be established that the equivalent airgap is higher in the circumferential points where the rotor faces a slot. Thus, an equivalent relative permeance θ -function can be defined, where θ represents the angular coordinate [Hanselman 2012, Pyrhönen 2012]. This theory will be further explained in Chapter 3.

The basic Carter's theory is unable to characterize some important aspects of the slotting effect, such as the higher magnetic induction at both sides of a slot opening. Those induction peaks appear because of the accumulation of electric charges in the teeth ends. In order to model this effect a conformal transformation can be used; one of the most complete explanations of this approach applied to a PMSM is found in [Zarko 2006], but many other studies also apply this mathematical technique [Proca 2003].

The conformal transformation method has high accuracy but it is very time consuming as far as some of the required equations do not have a closed form solution and hence must be solved applying numerical methods, such as Newton-Raphson algorithm.

2.2.1.2 Magnetic Forces and Cogging Torque

During the conversion of electric energy into mechanical one or vice versa many parasitic effects occur. As a consequence, not only the rotor magnets experience a force which causes torque and, therefore, the desired motion but a lot of additional and undesired forces arise both in the rotor and in the stator. Moreover, it has been calculated that the radial forces over the stator are an order of magnitude higher than those causing the motion (the tangential ones) [Weidong 2007].

The estimation methods used in order to calculate and minimize the problems caused by these effects will be further developed in Chapter 3. In this section the causes and main implications will be summarized.

The most important parasitic forces are the stator ones, both in the radial and in the tangential directions. Rotor forces are usually neglected because their enclosure greatly limits the undesired vibrations and noise that they can produce.

The parasitic tangential force component generates the so called cogging torque. As it was previously introduced, the cogging torque is caused by the interaction between the magnets and the slots, as far as the magnets try to align themselves with the maximum amount of ferromagnetic material, i.e. they seek the flux path with least reluctance.

In other words, when a magnet is “leaving” a slot it experiences a positive torque in the direction of the motion, as far as the magnet is decreasing its reluctance path. On the other hand, if a magnet is “entering” into a slot it undergoes a negative torque (opposite to the motion direction) because it is increasing its reluctance path, (see Figure 2.7). It is important to notice two important features of the torque ripple: the first one is that it has a null average and the second that it will exist as far as the PMSM is rotating, even if there is no load and no feed current, because it is a consequence of the interaction of the stator and the magnets.

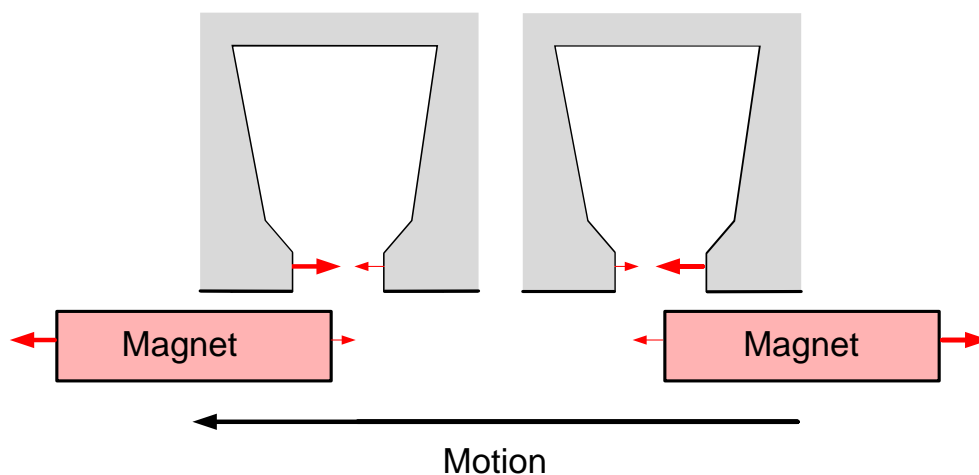


Figure 2.7. Interaction forces between slots and magnets. The forces acting on the magnets cause the cogging torque.

In spite of the null average of the cogging torque, it greatly contributes to the total torque ripple and, in many applications strict limits to that ripple are established.

The estimation of the cogging torque can be performed as any other magnetic force calculus. There are two ways in order to do so: the virtual work method, based on the principle of energy and co-energy [Lu 2006] and the Maxwell stress tensor method [Zhu 1992, Zarko 2008].

Both principles have similar results. For the sake of simplicity, the second method will be adopted. In this case the total force on a tooth face is estimated as:

$$f_t = L_e R_s \int_0^{\alpha_0/2} \frac{(B_g^m(\theta_m))^2}{2\mu_0} d\theta_m, \quad (2.5)$$

where f_t is the total force on a tooth face, B_g^m the airgap flux density due to the magnets, μ_0 the void permeability, L_e the effective PMSM length, α_0 the slot opening angle and θ_m the tangential coordinate. The calculated force is normal and outgoing from the tooth face.

By means of the second Newton law, the cogging torque generated by a single slot (taking into account the two faces of the slot opening) is

$$T_{\text{cog t}} = L_e R_s^2 \left(\int_0^{\alpha_0/2} \frac{(B_g^m(\theta_m))^2}{2\mu_0} d\theta_m - \int_{-\alpha_0/2}^0 \frac{(B_g^m(\theta_m))^2}{2\mu_0} d\theta_m \right) \quad (2.6)$$

where $T_{\text{cog t}}$ is the cogging torque measured in the motion direction.

Another major issue is the normal force applied on the stator teeth, caused by the magnets attraction on the stator core ferromagnetic material. That force can be calculated using the Maxwell stress tensor [Timar 1989]:

$$P_M(\theta_m) = \frac{(B_g^m(\theta_m))^2}{2\mu_0} \quad (2.7)$$

where $P_M(\theta_m)$ is the Maxwell force density as a function of the tangential coordinate.

The mentioned forces are the main cause of the external stator surface radial vibration, which moves the air and emits unpleasant sound. The vibration, and thus the noise, is especially high if the force spatial and temporal frequencies are equal to the structure natural frequencies, called resonance frequencies.

Reduction of noise emission is an important goal in many applications, such as elevation, railway traction or electric vehicle, as far as the PMSM is in close contact with passengers, and a quiet machine is necessary in terms of final users comfort.

The main component of the exposed force density has a temporal frequency equal to twice the electrical frequency (i.e. $2f_e$) and a spatial frequency (or mode) of π/p mechanical radians (the so called $2p$ mode), where p is the number of rotor poles (i.e.

magnets). However, the most important components in terms of noise emission are caused by lower modes produced by the interaction of the magnet poles and the stator slots [Zhu 2010]. An example of a force of a 6th mode is shown in Figure 2.8.

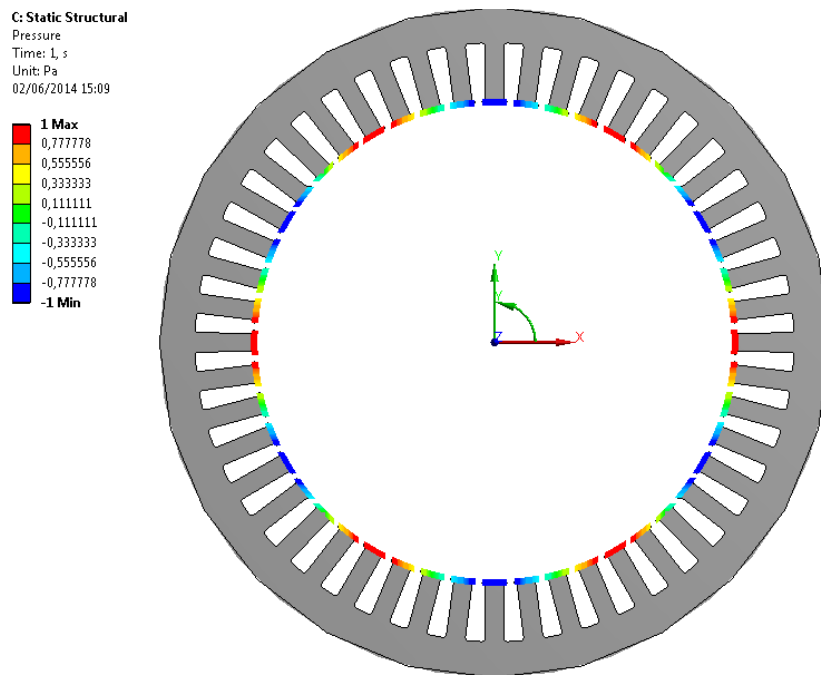


Figure 2.8. 6th mode force on the stator. This is the fundamental mode induced by the magnets if $p=3$.

Many studies have been carried out in order to do the best choice of the relation number of poles (p) / number of slots (Q) in order to achieve a noiseless machine by means of a correct selection [Besnerais 2009].

Another important problem caused by the stator radial forces is their possible unbalanced distribution, i.e. the total force tries to move the complete stator, which is kept at rest due to the shaft. This force is associated with the first mode and causes a bending deformation (see Figure 2.9). Its effect on a PMSM is especially harmful and should be minimized as far as possible [Islam 2009].

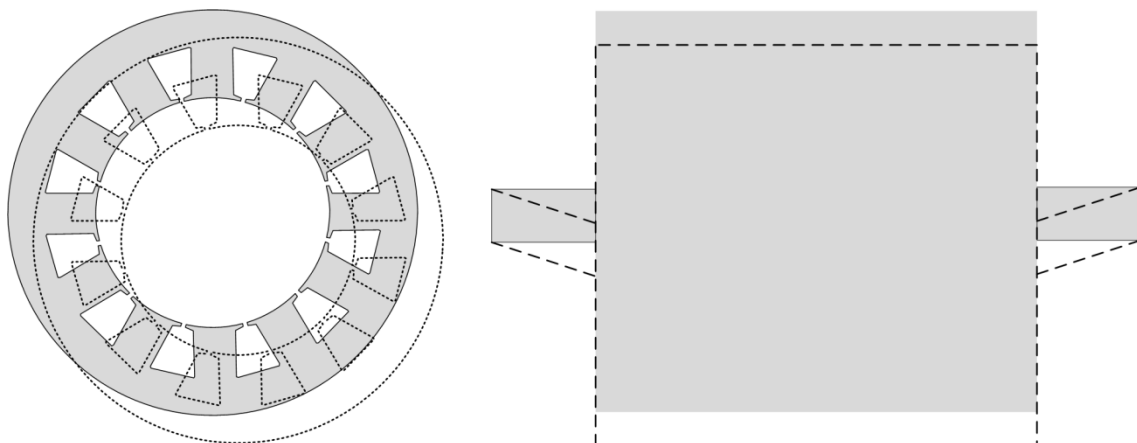


Figure 2.9. Deformation caused by an unbalanced force distribution.

2.2.1.3 Rotor Losses

One of the many advantages of PMSM topology is that the fundamental spatial component of the armature reaction (the magnetic induction generated by the stator coils) rotates in synchronism with the rotor which implies that rotor magnetic losses are negligible compared with the stator ones. The reason for this effect is that the rotor eddy current losses are proportional to the square derivative of the magnetic induction (this can be shown by using Faraday's law and a constitutive equation).

However, the presence of stator slotting and the spatial and temporal harmonic in armature reaction yields to induction components that rotate at different speeds and are reflected in the rotor with non-null frequency, causing losses that are especially important in the case of high speed and fractional slot machines (machines where the number of slots divided by the number of poles and phases is not an integer) [Nipp 1999, Ishak 2005].

Within rotor losses, eddy currents are especially relevant in NdFeB magnets which present a moderate conductivity [Pyrhönen 2012]. Although these losses are usually negligible in terms of efficiency, they are of great importance because of their contribution to the magnet heating and the difficulties to evacuate heat through the airgap; in most severe cases they produce magnet demagnetization [Wu 2012].

For the aforementioned reasons the analytical correct estimation of PMSM magnet losses is an important topic that has generated several publications in the last years.

First studies deal with the problem of estimating the losses in a simple manner, supposing the induction on the magnets is spatially constant and proposing formulas to extend a 2D-approximation into a 3D one [Nipp 1999]. Nowadays some papers propose new methods to estimate 3D eddy currents from 2D analytic methods [Ruoho 2009, Bettayeb 2010, Fadriansyah 2012], and others are centred in the 2D calculus of armature reaction harmonics, both in resistance limited problems [Atallah 2000, Ishak 2005, Ede 2007, Wu 2012] and skin limited problems which involve high frequency harmonics in the armature reaction, typically caused by a PWM supply [Zhu 2004, Markovic 2007].

Traditionally, induction harmonics causing eddy current losses in the rotor are divided into two groups: permeance harmonics caused by the stator slotting and winding harmonics caused by the armature reaction [Pyrhönen 2012]. In turn, the latter are divided into temporal and spatial ones. Usually, the losses due to each group are calculated separately and some of them, especially the permeance ones, are neglected. Since magnet losses are a non-linear phenomenon in its nature, these superposition techniques could yield to large errors [Tessarolo 2012].

In this thesis, a complete, straightforward and analytical model based on Fourier temporal and spatial series, which integrates all the losses in a single formula will be presented in Chapter 4, allowing for a simple and accurate way to estimate magnet losses.

2.2.2 Thermal Model

A proper thermal modelling of the PMSM is critical because of the great influence of the temperature in the machine performance and operation life. Especially, an accurate estimation of magnets and winding heating is of capital importance. Heating the magnets over their Curie temperature will cause their permanent demagnetization and an excessive temperature in the stator coils can damage their insulation, leading to a remarkable reduction of the PMSM operation life. To be more specific, it is estimated that every ten degrees over the insulation class temperature the life time is halved.

Due to the aforementioned reasons the classical empirical rules based on some key parameters, like maximum current density in the coils, are inadequate for high-profile designs and complete thermal models should be used, especially when the machine total size or its efficiency must be optimized [Nerg 2008].

Nowadays, the electrical machine thermal modelling can be divided into three different approaches: analytical lumped circuits, FEM and computational fluid dynamics (CFD), the two last having some common properties as far as both are numerical methods [Boglietti 2009]. The main properties of the three thermal approaches are listed below.

- Lumped thermal circuit: similar to a reluctance grid, a lumped thermal circuit is developed as an analogy of an electric network, where losses are treated as current sources and temperatures as voltages. The concepts of thermal resistance for conduction, convection and radiation process are established. Lumped parameter models have proven to be fast and accurate approaches and they have reached a high reliability level after decades of successful use. Moreover, they can be developed only taken into account geometrical and material features and new designs can be easily carried out once the basic geometry circuit is implemented [Mellor 1991]. As usual in lumped methods, its main disadvantages are the troubles associated with the generation of an accurate initial thermal circuit, as far as some thermal resistances are difficult to know, due to geometry and material uncertainties, such as the gaps across components interfaces or coolant flows over PMSM surfaces; most of these parameters must be obtained from direct measures or designer previous experience.
- FEM: the main advantage of FEM is its high accuracy obtaining the heat conduction paths in complex geometries. However, it suffers from the same uncertainties as the lumped circuits, needing experimental measures or rough approximations in order to estimate convection and radiation effects. Moreover, FEM is much more time consuming than a thermal network. For these reasons the role played by FEM techniques is to obtain the equivalent thermal conduction resistance of complex geometries in order to use these data in a lumped model [Boglietti 2009, Bermúdez de Castro 2011].
- CFD: computational fluid dynamics is a relative new technique in thermal modelling developed in order to calculate the coolant flow rate, speed and

distribution through the different machines surfaces and passages. It is very useful in the estimation of the convection process but it has some important disadvantages, such as its high computing time, the high developer previous experience needed to obtain accurate results, the difficulties in defining a suitable mesh and its relative technical immaturity. In spite of the exposed drawbacks, CFD use shows an evident growing trend because of the increasing demand of more compact, higher power density machines with special coolant necessities.

As it was exposed, lumped-parameter thermal models suppose a reliable, effective and short-time consuming thermal approach whose accuracy, in most cases, will be enough to estimate the temperature at the critical points of the PMSM.

Thermal network modelling was a common practice even before the advent of computers, when some designers developed simple thermal circuits in order to obtain a rough approximation of the temperature rise in some critical machine parts, namely, the windings [Boglietti 2009].

In more recent dates some authors have begun to implement new thermal network models representing the machine geometrical paths through which the heat flows. These studies started with the application in a machine thermal analysis of the heat equation in both, the axial and radial directions of a cylinder (see Pérez and Kassakian [Pérez 1979]). Based on this work Mellor et al. developed one of the first thermal networks calculated using a computer, its circuitual representation is shown in Figure 2.10 (a) [Mellor 1991]. Since then many other authors have tried, with good results, a small thermal-network as a suitable compromise between computation speed and accuracy [Kylander 1995, Lindström 1999].

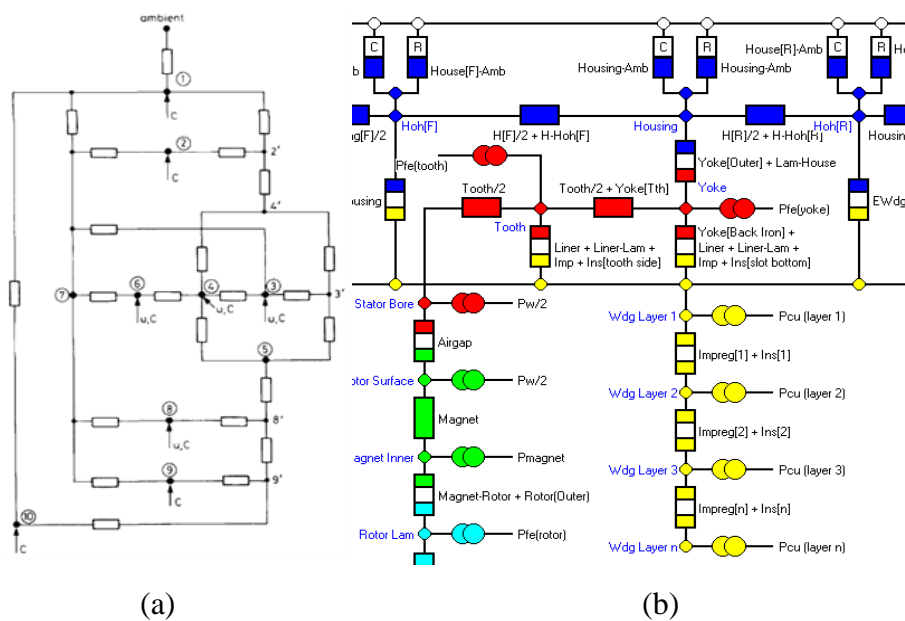


Figure 2.10. Lumped thermal networks. (a) Model proposed by [Mellor 1991], (b) SPMSM network model in Motor-CAD®.

The small thermal-networks developed in the nineties are still used, becoming one of the most popular methods to estimate the temperature rising in the machine during the design stage. Numerous PMSM thermal models use slight variations of the thermal circuits developed by the aforementioned authors [Hafner 2008, Vese 2010, Jannot 2011, Bracikowski 2012].

Nowadays improvements to these classical approaches still are done, but the basis of the theory and the main contributions in the modelling of most of the known machines topologies are well established in the literature, as it is proved by the existence of very accurate lumped parameter commercial programs, with a lot of machine topologies implemented and the empirical parameters well-known through years of experimentation. One of the most popular of these software packages is Motor-CAD®; one of its equivalent circuit networks is shown in Figure 2.10 (b).

In the last years, the literature about PMSM lumped thermal models has been devoted to the study of particular aspects, such as the thermal influence of the magnets positions in an IPMSM [El-Refaire 2004], the particularities of high speed operation [Saari 1998] or the determination of critical parameters that are usually very difficult to estimate without experimental measures [Boglietti 2008].

2.2.3 Vibro-acoustic Model

Noise has become a major factor in the ambient quality, so a lot of laws and normative have been written in order to limit the total amount of noise to a safe and comfortable level. This is not surprising, as far as nowadays there is a high consciousness about the need to keep a non-polluted environment and noise can become an important part of ambient pollution.

This is especially true in an urban context, where people live in close contact with noisy machinery that has greatly increased its presence during the last decades. Among these machinery are the electrical machines and the PMSM, whose application in railway traction and in hybrid and electric vehicles (EV) implies that a careful vibratory and acoustical design must be performed in order to avoid passengers and residents annoyance.

Vibro-acoustic modelling is traditionally neglected during the design process and noise problems are only treated like an afterthought, if needed. For the aforementioned reasons this classical approach is no longer efficient and desirable in many applications.

Sound emitted by electrical machines has different sources that are classified by classical literature in the next three types [Timar 1989, Gieras 2006]:

- Magnetic source: directly caused by the magnetic field effect on the machine materials. The Maxwell forces on the ferromagnetic cores and the magnetostriction effects are included in this group.

- Mechanical sources: associated with the mechanical assembly and mechanical energy transmission, the generated noise is mainly due to bearings, sliding contacts, gears, etc.
- Aerodynamic source: noise related to the air flow in the machine. It is mainly caused by the airstream produced by the cooling fan and flowing through the machine surfaces or structure vent holes.

Figure 2.11 graphically shows this classification and the acoustic energy propagation process.

The previous sources can generate air-born sound or structure-born sound, more precisely mechanical and magnetic noise sources produce vibrations that, through the housing, propagate their energy into the air, causing noise.

The magnetic noise plays a major role in many PMSM, especially for low and medium-power designs, whereas aerodynamic noise is the main contribution to total sound in high-power machines cooled by air requiring large fans and multiple vent conducts. In most cases, mechanical sound sources are negligible compared with the magnetic and aerodynamic ones and usually they are not taken into account [Besnerais 2008].

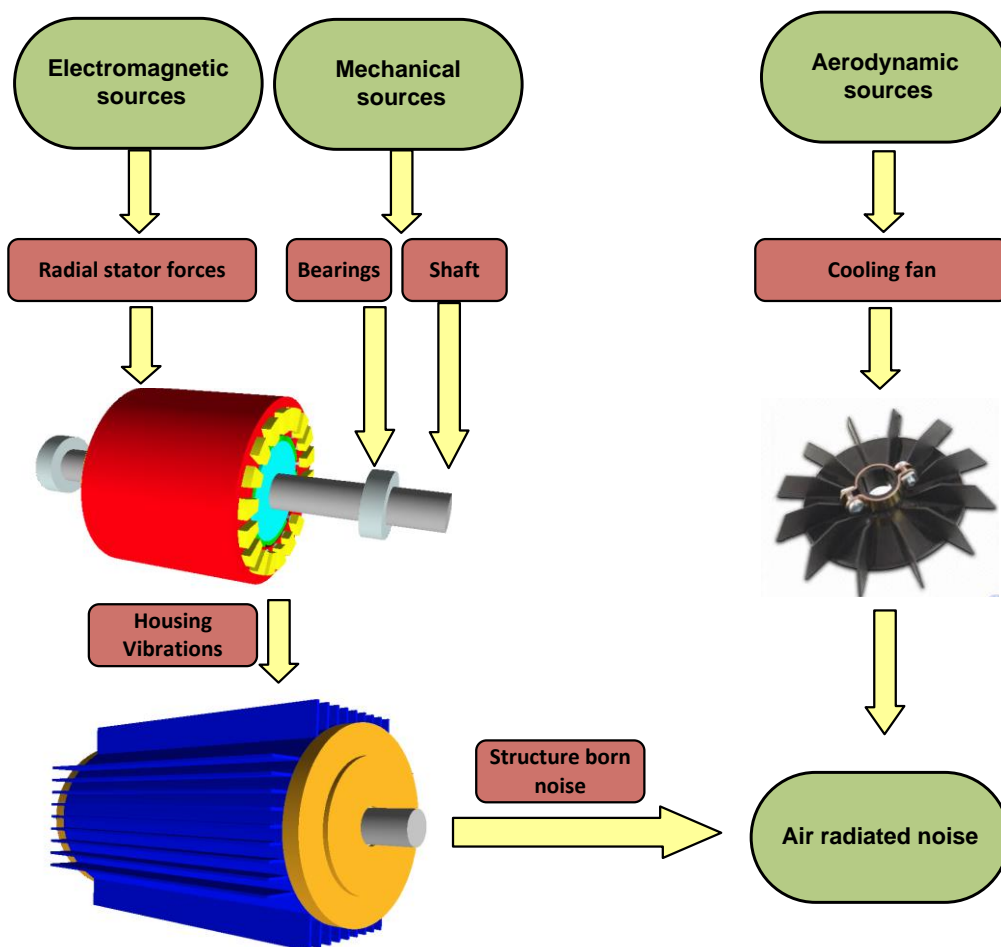


Figure 2.11. Noise sources and sound propagation in electrical machines. Figure adapted from [Yang 1981].

Most studies deals with the electromagnetic noise and, specifically, with the sound generated by the Maxwell forces on the stator, as far as this noise is one of the most intense and annoying in most of the machines; so its study is of great practical interest.

This thesis deals with the electromagnetic noise caused by Maxwell forces whose genesis process is summarized in Figure 2.12.

The complete acoustic study can be divided into different parts: the first one corresponds to the electromagnetic force calculus, the second one to the structural natural vibration modes (i.e., the specific vibrations patterns and frequencies more easily induced into the structure due to its mass and stiffness) and the third one to the vibratory and acoustic behaviour of the structure due to the applied forces. The electromagnetic force calculus was briefly introduced in 2.2.1.2 while the vibration modes estimation and the machine acoustic behaviour are explained in Chapter 6.

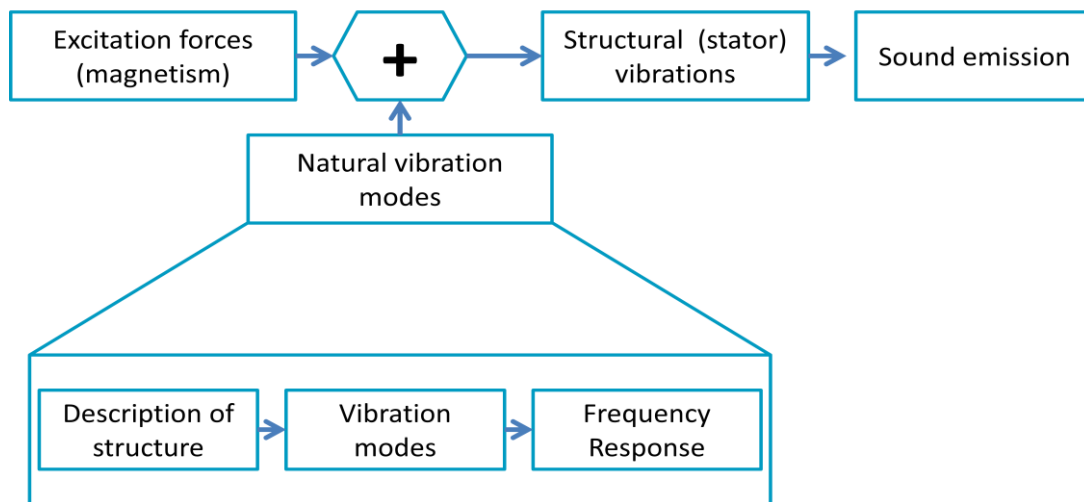


Figure 2.12. Electromagnetic sound genesis in electrical machines.

Both, natural vibration modes and stator vibration and sound response can be calculated by means of numerical methods (FEM and BEM) or analytically. In theory, it is also possible to develop lumped models but these approaches are rarely found in the literature devoted to the subject.

The advantages and drawbacks of the numerical methods are the same exposed in the electromagnetic and thermal models: they are much more accurate than analytic ones but are very time consuming and require a complete knowledge not only of the machine dimensions but also of the stator-housing interface, the house fins and the structure anchoring points. Much of this information is not available during the design stage process and the accuracy of numerical methods decrease dramatically.

Analytical, vibratory and acoustic models show low accuracy, especially compared with electromagnetic and even thermal analytical models. However, they have the advantage of fast calculus and they are capable to correctly estimate the main

vibration frequencies emitted by the machine and to establish a good comparison between candidate designs.

As it was introduced, a natural vibration mode is a specific spatial oscillation pattern; in radial machines the most important ones are the radial modes which present a sinusoidal θ dependence, i.e. the second radial mode is associated with a spatial displacement $k(t) \sin(\theta)$, where t is the time and $k(t)$ is a parameter dependant on the magnitude and frequency of the excitation forces and the stator structural features. Examples of different modes caused by temporal static forces are shown in Figure 2.13.

It is important to notice that every spatial mode has an associated natural frequency, defined as the excitation force frequency which generate an infinite displacement (i.e. $k(t)|_{\max} \rightarrow \infty$) in absence of damping. In real motors, where the deformation is usually of some μm , the damping limits the vibration amplitude. In spite of this fact, the natural frequencies are especially dangerous because if the stator is excited with a force of a frequency close to the natural frequency of this mode resonance will occur and the vibrations and the sound would be very high.

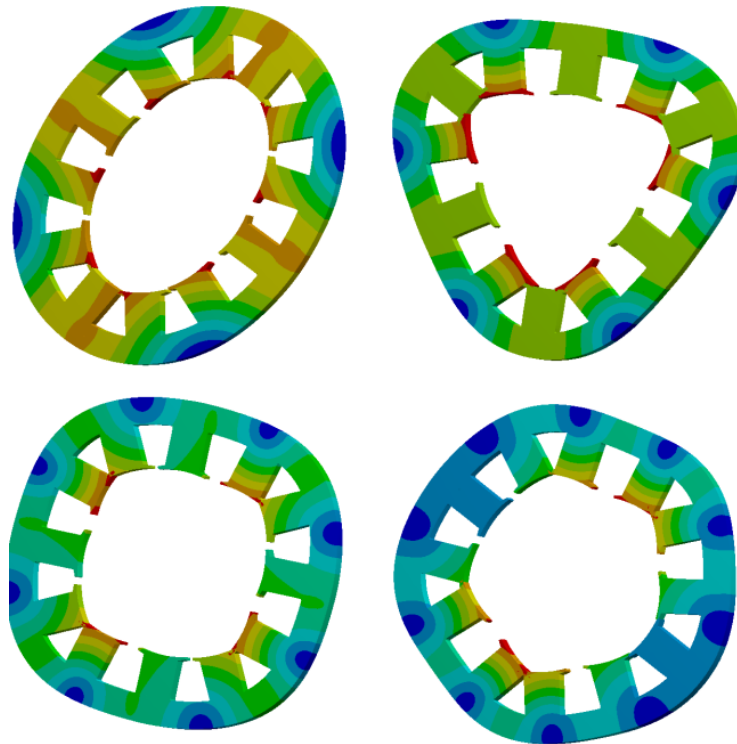


Figure 2.13. 2nd to 5th stator radial modes calculated with ANSYS®. Deflections have been scaled for visual purposes.

Thus, once the structural modes and its natural frequencies are obtained, the excitation forces will be expressed in a mathematical basis conformed by the structural vibration modes. The stator will be treated as a linear system where the forces are the inputs and the displacements (vibrations) the output.

Finally, a radiation factor is estimated and the sound power radiated at each frequency is calculated from the surface vibrations (see Figure 2.12).

In the last decades, a lot of effort has been done in order to establish a reliable and accurate method for the estimation of stator natural vibration modes and static displacements (maximum displacement of the structure when a force of the mode under study and frequency 0 Hz is applied).

During the twenties of the last century, first analytical models of a stator were performed and natural frequencies were calculated approximating the stator by a thin ring. In 1950 Jordan published its work, applying the same thin ring approximation but adding the effects of shear, teeth and winding to the model [Jordan 1950]. Jordan's study is still a capital reference and only little advances were done in the analytical calculus of stator natural frequencies in the last sixty years.

In 1979 Girgis and Verma studied and measured the practical effects that teeth and windings have over the thin ring approach [Girgis 1979] concluding that Jordan analytical approximations reasonably match the experimental results. Another two classical books about the subject [Yang 1981, Timar 1989] rewrite Jordan results adding an additional factor that take into account the effects of the teeth and winding in rotating inertia and establish the usual form that these equations can be found in actual literature. A complete review about noise in electric machines [Vijayraghavan 1999] still references Jordan work equations as the most accurate ones and many recent authors use them with minor modifications [Anwar 2000, Schlensook 2008, Islam 2010, Besnerais 2010, Fiedler 2012]. Moreover [Weilharter 2012] compares his analytical results with those calculated by Jordan sixty-two years before.

Other approaches developed in the last years implies calculate the mode features from the identity between kinetic and potential energies during vibration process [Ishibashi 2003] or to estimate the stator vibratory behaviour from its linear properties, obtaining its impulse response from both FEM or experimental measurements [Van der Giet 2010, Torregrossa 2012].

Nowadays, the research efforts seem to be centred in the correct calculus of Maxwell forces from airgap flux density values, especially in cases where these forces are rich in the frequency domain due to both spatial harmonics, caused by winding distribution [Zhu 2010], and temporal harmonics, caused by Pulse Width Modulation (PWM) or control strategies [Besnerais 2010].

[Gieras 2006] offers a complete study that includes most of the recent developments in the calculus of noise emitted by electric machines, including force estimation and aerodynamic and mechanical sources effects.

As far as Jordan results have proved to have enough accuracy for low order modes during decades of use, and due to its easy implementation and low computing time this approach is adopted in the present thesis.

3

Electromagnetic Characterization

3.1 Introduction: Between Mechanical and Electric Power

The main goal of this chapter is to present an analytic model that allows a fast and accurate characterization of a PMSM electromagnetic behaviour, taking into account its electric, magnetic and geometric features. It is important to notice that the model evaluates a specific PMSM whose choice and feasibility must be previously established by the optimization algorithm and its restriction functions.

As it was aforementioned, the model is fully analytical and based on Fourier series, being its main advantages its fastness, modularity and the easiness of integration with the rest of the physical modelling blocks. The different modules within the electromagnetic model are represented in Figure 3.1.

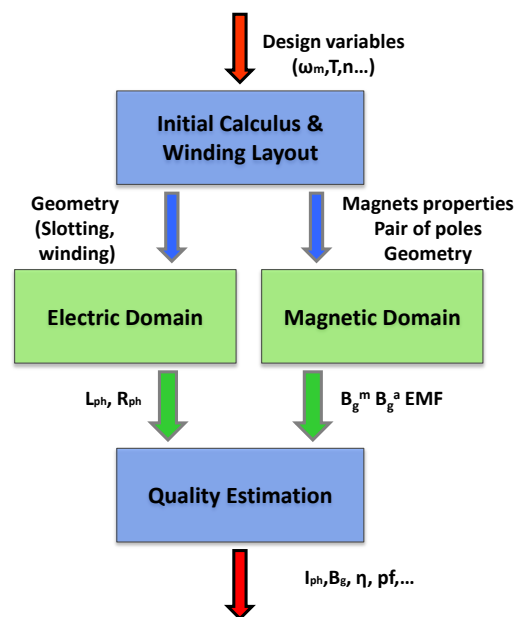


Figure 3.1 Modules within the electromagnetic model block.

The initial calculus, as well as the magnetic and the electric domains, will be further developed in the next sections, while the quality estimation block will be explained in Chapter 4.

3.1.1 Relation between Mechanical and Electrical Domains

The main goal of any rotatory electrical machine is the conversion of electrical energy into mechanical one or vice versa. In this section the links between the machine equivalent electrical circuit and the mechanical motion will be briefly summarized.

There are different approaches in order to explain the above energy conversion; here, two of them will be recalled. A more detailed explanation can be found in [Hanselman 2012].

3.1.1.1 Torque calculus from power identity

From a macroscopic point of view the mechanical and electrical domains are linked through the Faraday's law:

$$E(t) = \frac{d\lambda(t)}{dt} \quad (3.1)$$

where E is the voltage induced in a conductor material embracing a total flux linkage of λ . The sign of the generated voltage is established by applying Lenz's law which states: *"the induced voltage will cause a current to flow in a closed circuit in a direction such that its magnetic effect will oppose the change that produces it"*, i.e. the induced voltage will try to prevent the flux linkage from changing from its present value.

Since the rotor is moving, the amount of magnetic flux embraced will vary with time, so a voltage is induced in the wound coils. As far as a current is flowing through the phases, an electric power will exist.

The expression of the mechanical and the electric instantaneous powers are well known in literature:

$$P_E(t) = E(t)I(t) \quad (3.2)$$

$$P_M(t) = \omega_m(t)T(t) \quad (3.3)$$

where P_E and P_M are the electrical and mechanical powers, I the current intensity flowing through the coils, ω_m the rotor angular speed and T the torque developed by the motor.

In the particular case of a polyphasic PMSM operating like a motor at constant speed it can be established from the identity of mechanical and electrical power at any instant:

$$\sum_{l=1}^m E_l(t)I_l(t) = \omega_m T(t) + P_{\text{loss}}(t) \quad (3.4)$$

where P_{loss} is the sum of the iron and mechanical losses and m is the number of phases. It is supposed that no energy is mechanically stored from one instant to another. Neglecting the losses the torque could be estimated as:

$$T(t) = \frac{\sum_{l=1}^m E_l(t)I_l(t)}{\omega_m} \quad (3.5)$$

This power identity approach is very rough but it permits to obtain a good first approximation of the torque generated, especially if the iron losses are taken into account in an equivalent electric circuit (see Section 3.4). However, in order to obtain a deeper insight in the energy conversion process a more detailed study must be performed.

3.1.1.2 Torque calculus by means of the energy and the coenergy

In a single coil wound around a magnetic core, such as shown in Figure 3.2, the flux linkage can be easily calculated as:

$$\lambda = N\phi = \frac{N^2 i}{R} \quad (3.6)$$

where ϕ is the magnetic flux generated by the coil, N is its number of turns, i is its current and R is the core reluctance. The inductance L is defined as

$$L = \frac{\lambda}{i} = \frac{N^2}{R}. \quad (3.7)$$

From Faraday's law the instantaneous power in a coil can be written as

$$P_{\text{coil}}(t) = i(t) \frac{d\lambda(t)}{dt}, \quad (3.8)$$

and the energy stored in the coil at instant t_1 will be equal to:

$$W = \int_0^{t_1} i(t) \frac{d\lambda(t)}{dt} dt = \int_{\lambda(0)}^{\lambda(t_1)} i d\lambda = \frac{1}{2L} (\lambda^2(t_1) - \lambda^2(0)). \quad (3.9)$$

In a similar way the coenergy is defined as:

$$W_c = \int_{i(0)}^{i(t_1)} \lambda di = \frac{1}{2L} (i^2(t_1) - i^2(0)) \quad (3.10)$$

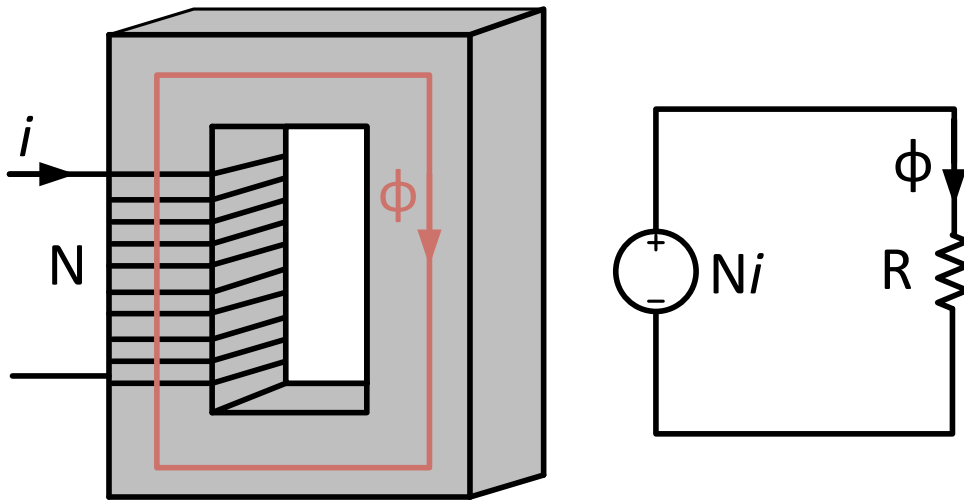


Figure 3.2 Single coil in a magnetic core with equivalent circuit model. Figure adapted from [Hanselman 2012].

If the coil is sharing the core with a magnet, as it is shown in Figure 3.3, an additional source of flux through the coil exists, so its flux linkage is equal to

$$\lambda = \frac{N^2 i}{R} + N\phi_m, \quad (3.11)$$

where ϕ_m is the magnet flux.

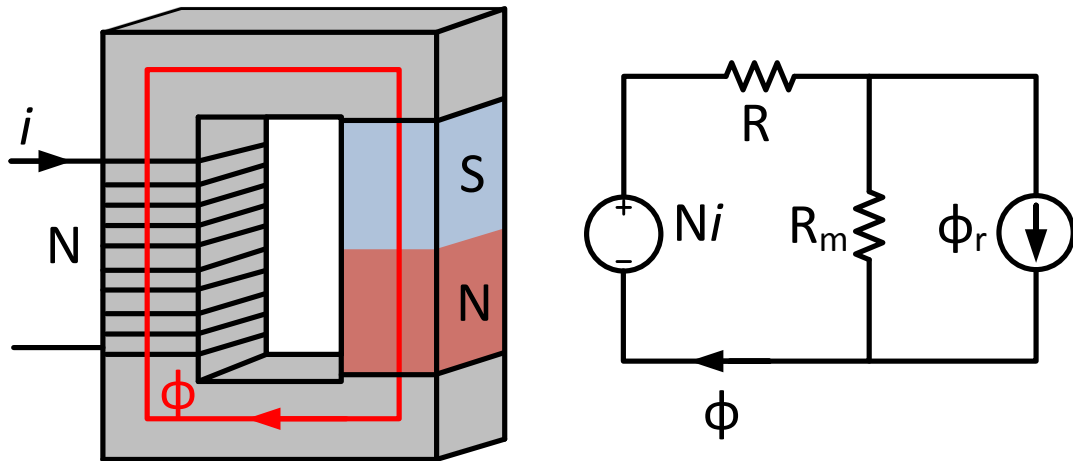


Figure 3.3 Interaction between a coil and a magnet sharing a core. Figure adapted from [Hanselman 2012].

In this case the coenergy is equal to [Hanselman 2012]:

$$W_c = \frac{1}{2}Li^2 + \frac{1}{2}(R + R_m)\phi_m^2 + Ni\phi_m \quad (3.12)$$

where R_m is the magnet equivalent reluctance.

In a rotary machine the torque can be expressed as a function of its angular position by means of [Hanselman 2012]:

$$T(\theta) = \left. \frac{\partial W_c(\theta)}{\partial \theta} \right|_{i=cte} \quad (3.13)$$

The previous formula is applied to the particular case of a torque generated by the interaction of the rotor magnets flux and a current i flowing through a single stator coil with N turns:

$$T(t, \theta) = Ni(t) \frac{d\phi_m(t, \theta)}{d\theta} + \frac{1}{2}i^2(t) \frac{dL(t, \theta)}{d\theta} - \frac{1}{2}\phi_m^2(t, \theta) \frac{dR_g(\theta)}{d\theta} \quad (3.14)$$

where R_g is the airgap reluctance as a function of its angular position and $L(t, \theta)$ the inductance shown by the coil.

In the previous equation it was assumed that the airgap reluctance is not function of time, because it depends only on the stator slotting. As far as the stator is still, no temporal dependence is produced. However, the winding inductance is a function of the relative stator position with respect to the rotor, so it can present both, temporal and angular dependency, as far as the rotor is turning and it could have an angular dependence in some kind of machines (such as IPMSM).

Equation (3.14) has a special relevancy because it classifies the total torque in three components with different behaviours.

The first factor is the electromagnetic torque or mutual torque. It is produced by the interaction between the field produced by the magnets and current flowing in the stator coils. In most electric machines, it is the effective torque.

The second factor is the reluctance torque. It is produced by the electromagnet generated by the stator coils which attract the rotor steel. If the rotor has saliency (i.e. the reluctance seen by the coils is θ dependant) $dL/d\theta$ is not null and a reluctance torque is produced. The SPMSM has little (ideally null) saliency and $dL/d\theta$ is close to zero; hence, in the case under study, reluctance torque can be neglected.

The third factor is known as cogging torque and it was introduced previously. It is based on the same physical principle as reluctance torque. It is caused by the interaction between permanent magnets and stator slotting. In fact, the magnets try to avoid the slots, aligning themselves with the teeth as far as possible.

The reluctance and the cogging torques usually have null mean value and are considered as parasites, so it is a very common practice to try to minimize them. However, some types of motors are capable of taking advantage of the reluctance torque in order to produce effective torque with positive mean value.

The SPMSM has null reluctance torque, so only the mutual and the cogging torques will be studied during the present chapter.

Obviously, the most interesting torque is the mutual one, since it is the cause of the desired motion. In order to calculate it not only a magnetic study but also an electric one is needed. They will be further developed in the next sections.

3.2 Winding Layout: the Star of Slots

The “initial calculus” block obtains the secondary geometrical variables, explained in Section 1.3, and also provides a suitable winding layout design which establishes the coils wound in the available stator slotting. Therefore, in order to obtain an efficient torque production, the phases which are wound in each slot must be chosen, ensuring the design feasibility and a balanced winding spatial distribution.

In technical literature different types of winding layouts are presented:

- As a function of the number of layer (phases wound) in each slot:
 - Single layer winding: when in a slot only one phase coils are wound.
 - Double layer winding: when in a slot two coil sides are wound. In a general way, these sides are part of any phase and are wound in any direction.
- As a function of the number of slots per phase per pole:
 - Integral slot machines: when the number of slots per phase per pole is an integer, i.e. the stator is wound with the same number of spatial periods that pole pairs in the rotor.

- Fractional slot machines: when the number of slots per phase per pole is a fraction, so stator is wound with a number of spatial periods different of the number of pole pairs in the rotor.
- As a function of the winding distribution:
 - Concentrated windings: the coils are wound in consecutive slots, minimizing the end-winding and, thus, the copper losses.
 - Distributed windings: the coils are wound in the more suitable slots in order to obtain the maximum electromotive force (EMF), i.e. the maximum induced voltage.

In a distributed winding layout the main goal is to place the coils having a span such as their midpoints are out of phase 0 electric radians in order to ensure a maximum phase EMF (i.e. place the windings in order to sum in phase their induced voltages). In some simple machines the distribution can be obvious but, in a general manner, the selection of a good winding layout could be a difficult task.

Despite there are different methods that permit to fulfil the previous goal, in this work one of the most popular of them, the star of slots [Bianchi 2006, Almandoz 2008], is implemented.

The star of slots is a generic method based on a graphical representation of the flux phase in each slot. One of its main advantages is that it permits to design automatically any kind of distributed winding, fractional or integral slot machine, single or double layer, in a straightforward way.

A brief description of the method is exposed below.

A parameter q is defined as the number of stator slots per pole and per phase

$$q = \frac{Q}{2pm}, \quad (3.15)$$

where m , p and Q are the number of phases, pole pairs and slots, respectively.

Another important variable is t_p , the winding periodicity: number of the motor periods in the circumferential coordinate. Mathematically, it is defined as the greatest common divisor between Q and p .

$$t_p = \text{GCD}\{Q, p\} \quad (3.16)$$

In the case of an integral slot machine q is an integer and $t_p = p$, but, in a fractional machine, q is fraction and the winding periodicity is different from the number of pole pairs. In fact, the number of pole pairs in a winding periodicity (p') is defined as

$$p' = p/t_p \quad (3.17)$$

In a similar way, Q' is the number of slots within a winding periodicity. Obviously, Q' must be multiple of the number of phases (m), otherwise the winding is not feasible.

$$Q' = Q/t_p \quad (3.18)$$

Two consecutive slots are out of phase between them a number of electric radians

$$\alpha_z = \frac{2\pi p'}{Q'} \quad (3.19)$$

The first step to perform the winding layout is to plot a star of slots with Q' vectors equally spaced. Obviously, the geometrical angle between them will be equal to

$$\alpha_n = \frac{2\pi}{Q'} \quad (3.20)$$

These vectors are numerated from 1 to Q' . One of them is chosen as the initial one and then the others are numerated considering a constant pitch equal to α_z . This number determines the physical slot associated with the selected vector. For example, if the second vector of the star is numerated as eight that means that its physical slot is the 8th within a motor periodicity. See Figure 3.4.

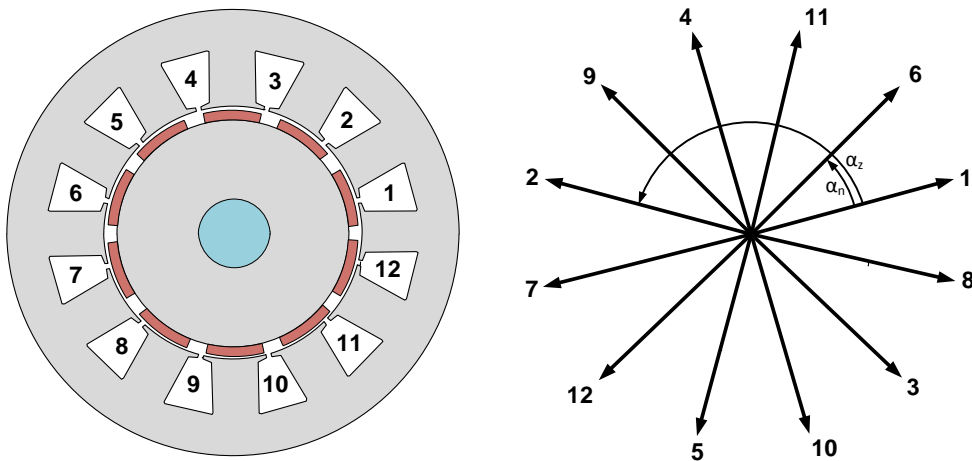


Figure 3.4. Equivalence between a stator slotting and its star of slots.

As it was introduced, the winding layout could be single or double layer. If Q'/m is even a single layer winding is performed. The coils are placed beginning at the first vector and following a fixed sequence. In a three-phase machine, the sequence will be A+C-B+A-C+B-. It must be taken into account that coils of the same phase and direction, if exist, are emplaced-in consecutive vectors.

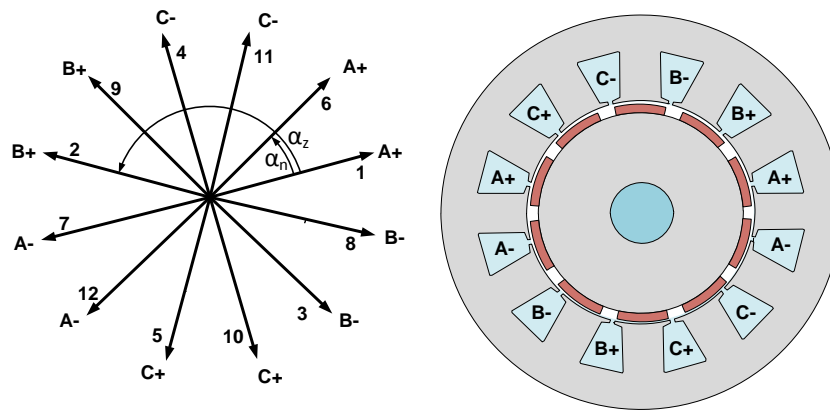
For example, if $Q'=12$ and $m=3$, four slots are assigned to each phase within a motor periodicity. Therefore, the assignation sequence will be A+A+C-C-B+B+A-A-C+C+B-B-.

If Q'/m is odd, a double layer coil distribution is required in order to obtain a feasible winding. The procedure is almost the same as in the single layer case, but two "turns" are needed because there are two coils in each slot. In the first turn an extra

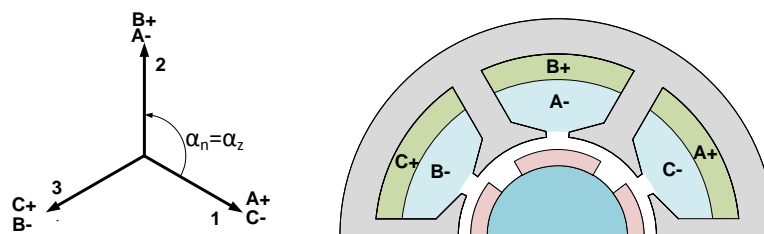
“in direction” coil is wound in each phase, while in the second an extra “out direction” coil is emplaced.

For example, if $Q'=9$ and $m=3$ in the first turn of the wound the sequence will be: A+A+C-B+B+A-C+C+B-, while in the second it will be A+C-C-B+A-A-C+B-B-. Thus, two coils are assigned to each vector.

Once the coils are associated with the vectors, the relation among them and their physical slots are used for a proper winding layout. That is, if vector 2nd is numbered as 12th and contains an A+ coil and a C- coil that means that the 12th real slot is wounded with an A+ and a C- coils. Figure 3.5 shows the final winding layouts for two examples.



Star of slots for a $Q=12$, $p=5$ design. Single layer winding



Star of slots for a $Q=6$, $p=2$ design. Double layer winding

Figure 3.5. Star of slots method applied to a single and a double layer layout.

A program which implements the star of slot method has been developed. Depending on the relation between Q' and m , three different cases are possible.

- Q' is not a multiple of m : it is no possible to find a feasible winding, so the routine aborts it execution and inform on this error.
- Q' is a multiple of $2m$: it is possible to do a single layer winding. The routine returns this winding in form of three vectors: inL, outL and pHL.
- Q' is a multiple of m but not of $2m$: only a double layer winding is possible. The routine returns this winding in form of three vectors: inL, outL and pHL.

The aforementioned vectors are the data returned by the implemented program and should be understood in this way: $\text{inL}(x)$ is the “in slot” (positive direction) of the x coil, $\text{outL}(x)$ is the “out slot” (negative direction) of the same coil, while $\text{phL}(x)$ identifies the phase of the coil. These vectors play a major role in defining the EMF induced in the PMSM and, thus, in its magnetic performance.

Thus, if $\text{inL}=[1,5,3]$, $\text{outL}=[4, 2, 6]$ and $\text{phL}=[1, 2, 3]$, it means that there is a phase A coil which enters through slot 1 and leaves through slot 4, a phase B coil which enters through slot 5 and leaves through slot 2 and, finally, a phase C coil which enters through slot 3 and leaves through slot 6.

It is important to realize that any kind of feasible stator winding can be developed by the methodology proposed, as far as both, the star of slots method and the routine implemented, are completely generic.

3.3 Magnetic Domain

The objective of the magnetic domain is to obtain the values of a group of important status variables, some of them are magnetic ones such as the flux density in different parts of the PMSM (airgap, stator yoke, stator teeth, etc.) and others are directly related with the previous ones such as the EMF or the cogging torque.

An important feature of most of the variables exposed is their periodicity which can be spatial, temporal or both. This is a very important issue since it permits to work with their Fourier Series (FS) coefficients instead of their time domain values. In this work, the FS estimation will be used due to its good features.

Every time a FS is performed it will be clarified whether it is a temporal or a spatial one and, in the second case, which kind of period (electrical period, mechanical period or slot pitch) is taking into account.

3.3.1 Rotor Magnetic Field

In a PMSM the rotor magnetic field is the most common name for the field created by the rotor magnets in the airgap. A first step in its calculus is to solve the canonical magnetic problem shown in Figure 2.6, where three concentric cylinders are considered: the stator, the magnets and the rotor. Due to the problem symmetry it is enough to take into account just a cross-section of the cylinders, simplifying the 3-D formulation into a 2-D one.

Neglecting the effect of the stator slotting, the FS of the airgap flux density can be obtained [Zhu 1993-a].

It should be highlighted that, as far as the angular speed of the rotor is considered as a known constant, it is possible to deduce its magnetic field spatial FS in every

instant of time from its FS at $t=0$. Thus, the spatial FS of the airgap flux density can be expressed at any time as:

$$B_g^m(\theta, 0) = \sum_{k=-\infty}^{\infty} B_{g,k}^m(0) e^{jkp\theta}, \quad (3.21)$$

$$B_g^m(\theta, t_1) = \sum_{k=-\infty}^{\infty} B_{g,k}^m(0) e^{jk(p\theta - \omega_e t_1)}, \quad (3.22)$$

where the rotor is supposed to be turning anticlockwise with an angular speed ω_e . $B_g^m(\theta, t)$ is the rotor magnetic field in the airgap at time "t" and angle "θ", and $B_{g,k}^m(t)$ represents its FS spatial coefficients in t. For the sake of simplicity $B_{g,k}^m(0)$ will be noted as $B_{g,k}^m$. From (3.21) and (3.22) it is concluded that FS coefficients are the same at any time except for an angular delay that can be expressed as

$$B_{g,k}^m(t_1) = B_{g,k}^m e^{-jk\omega_e t_1}. \quad (3.23)$$

In the proposed simplified problem, Maxwell equations can be analytically solved [Zhu 1993-a, Hanselman 2012] in order to obtain the FS coefficients $B_{g,k}^m$.

In a general case, the airgap flux density has both, radial and tangential components and it is dependent not only on the tangential coordinate but also on the radius. In the proposed model only the radial component is taking into account and the radial dependence will be neglected.

In order to carry out the proposed approximations without significant accuracy loss, the airgap flux density is obtained just on the boundary between the airgap and the stator ($r = R_s$), where the radius is fixed and the flux density tangential component is close to zero due to the high permeability of the stator core.

If the ferromagnetic material is unsaturated and the stator slotting effect is neglected it can be demonstrated that the FS coefficients of the flux density are given by [Zhu 1993-a]

$$B_{g,k}^m = 2B_r K_{r,k} \frac{kp}{kp^2 - 1} R_s^{kp-1} \frac{\Gamma_k}{\Delta_k}, \quad (3.24)$$

where

$$\Gamma_k = R_m^{-kp+1} \left((kp - 1)R_m^{2kp} + 2R_r^{kp+1}R_m^{kp-1} - (kp - 1)R_r^{2kp} \right), \quad (3.25)$$

$$\Delta_k = (\mu_r + 1)(R_s^{2kp} - R_r^{2kp}) - (\mu_r - 1) \left(R_m^{2kp} - \left(\frac{R_s R_r}{R_m} \right)^{2kp} \right), \quad (3.26)$$

μ_r is the magnets relative permeability and R_m is the magnets radius (see Figure 2.6).

The previous equations are valid for every k except when $kp = 1$. In fact, equation (3.24) is indeterminate when the fundamental airgap spatial harmonic is calculated in

a one pole pair PMSM. To solve this problem, another equation is proposed for this special case. Thus, when $p = 1$:

$$B_{g,1}^m = B_r K_{r,1} \frac{\left(\frac{R_m}{R_s}\right)^2 - \left(\frac{R_r}{R_s}\right)^2 + 2 \left(\frac{R_r}{R_s}\right)^2 \ln\left(\frac{R_m}{R_r}\right)}{(\mu_r + 1) \left(1 - \left(\frac{R_r}{R_s}\right)^2\right) - (\mu_r - 1) \left(\left(\frac{R_m}{R_s}\right)^2 - \left(\frac{R_r}{R_s}\right)^2\right)} \quad (3.27)$$

In expressions (3.24) and (3.27) $K_{r,k}$ is a factor dependent on the magnetization profile of the magnets and their geometric position in the rotor. The mathematical expression of most of these magnetization profiles can be found in [Hanselman 2012].

The most common magnetization profiles used in superficial magnets PMSM are the radial and the parallel ones; these cases are implemented in the proposed model. As an example, the mathematical expression in the radial case is included:

$$K_{r,k} = \begin{cases} \alpha_m \operatorname{sinc}((k\alpha_m\pi)/2) & \text{for } k \text{ odd} \\ 0 & \text{for } k \text{ even} . \end{cases} \quad (3.28)$$

where α_m is the fraction of the electrical semi-period covered by the magnet, as it is shown in Figure 3.6 and $\operatorname{sinc}(x) = \sin(x)/x$. It is important to notice that a very low value of α_m supposes an inefficient use of the rotor space but a very large one can lead to an important decrease of the flux linkage, as far as many flux lines cross the space between magnets instead of flowing into the stator through the airgap.

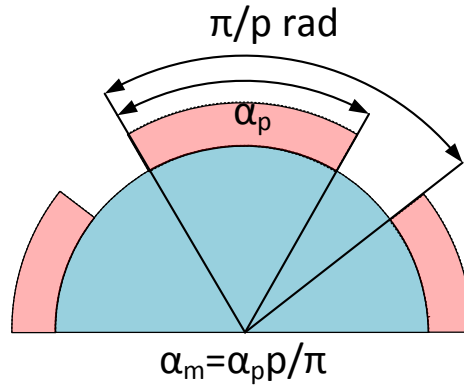


Figure 3.6. Angle covered by a single magnet with respect to the slot pitch.

3.3.2 Slotting Effect: Relative Permeance Function

Once the magnetic flux density in the airgap with smooth stator is obtained the next obvious step is calculate the effect of the slot in its spatial distribution.

Obtaining an analytic solution for this problem could be problematic and the use of a numerical algorithm, like FEM, is not desirable as far as it is very time consuming. Thus, most authors [Zarko 2006, Almandoz 2008, Hanselman 2012] start from the canonical problem solution and define a correction factor $K_{s1}(\theta)$ such that

$$B_{gs}^m(\theta) \approx B_g^m(\theta) K_{sl}(\theta), \quad (3.29)$$

where $B_{gs}^m(\theta)$ is the magnet flux density in the airgap with slotting effect, and B_g^m is the canonical problem solution (with slotless stator).

The factor $K_{sl}(\theta)$ has different names in the literature (slot correction factor in [2012 Hanselman], relative permeance function in [Zarko 2006], etc.). In this work it will be called relative permeance function, since the flux density in the airgap is closely related with its apparent permeance as it will be explained.

A lot of approximations for $K_{sl}(\theta)$ are proposed but all of them are based on the same idea: under a slot opening the apparent length of the airgap (g) is increased, so the length of the airgap is no longer a constant but a variable which depends on the tangential coordinate θ and has a periodicity of $2\pi/Q$ mechanical radians.

As far as the airgap length is variable the reluctance is no longer a constant, since it is increased under the slots. This higher reluctance supposes less flux density under the slots.

Therefore, $K_{sl}(\theta)$ is the relation between the airgap permeance with smooth stator (\wp_g) and the real permeance taking into account the slotting ($\wp_g(\theta)$).

$$K_{sl}(\theta) = \frac{\wp_g(\theta)}{\wp_g} \quad (3.30)$$

The airgap permeance depends on its length and is given by

$$\wp_g = \mu_0 \frac{A_g}{\delta} = \mu_0 \frac{A_g}{g + \frac{l_m}{\mu_r}}, \quad (3.31)$$

where A_g is the cross-sectional area covered by the airgap fraction considered, δ is its effective length and μ_0 is the vacuum magnetic permeability.

It is possible to combine (3.30) and (3.31) to obtain a simple, straightforward relation between $g(\theta)$ and $K_{sl}(\theta)$, namely,

$$K_{sl}(\theta) = \frac{\wp_g(\theta)}{\wp_g} = \frac{\mu_0 A_g / (g(\theta) + \frac{l_m}{\mu_r})}{\mu_0 A_g / (g + \frac{l_m}{\mu_r})} = \frac{g + \frac{l_m}{\mu_r}}{g(\theta) + \frac{l_m}{\mu_r}}. \quad (3.32)$$

A lot of approximations for $g(\theta)$ are available; in this model the equivalence proposed by [Hanselman 2012] is adopted. It is based on the well-known Carter's coefficient in order to estimate the trajectory of the flux in front of a slot opening. Mathematically,

$$g(\theta) = \begin{cases} g & \text{if } |\theta| \leq \theta_t/2 \\ g + \frac{\pi R_s}{2} \left(|\theta| - \frac{\theta_t}{2} \right) & \text{if } |\theta| > \frac{\theta_t}{2}. \end{cases} \quad (3.33)$$

The dimensions and angles used in equation (3.33) are shown in Figure 3.7.

Once the expression of the relative permeance is obtained, it is possible to calculate its spatial FS, taking into account a signal period of $2\pi/Q$ radians.

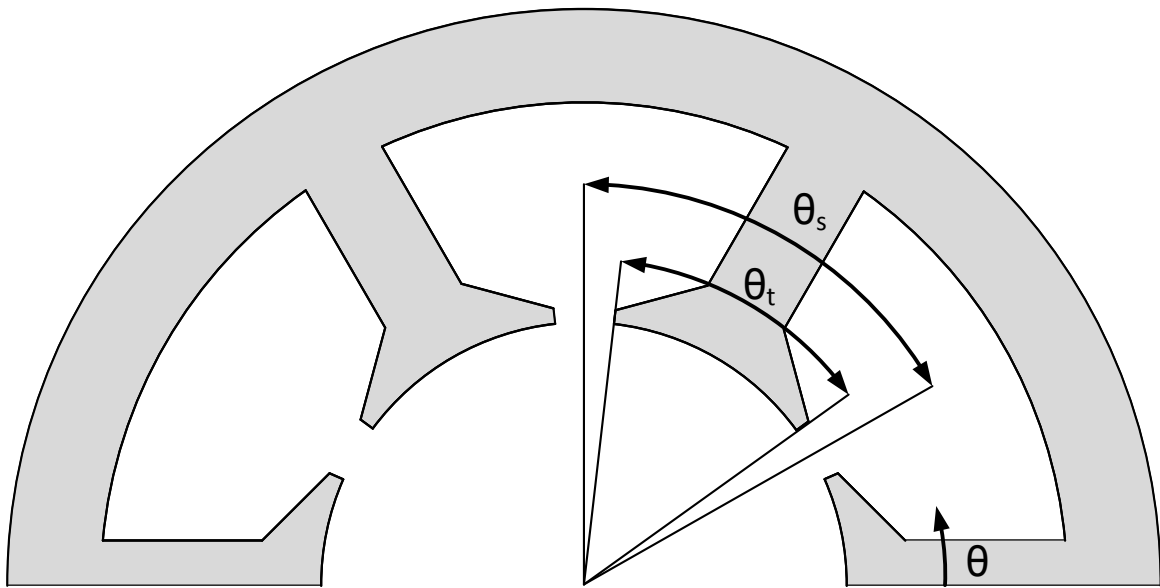


Figure 3.7. Geometry considered for the calculus of the relative permeance function.

3.3.2.1 Relative Permeance Function Limitations

Although the use of the relative permeance function suppose an elegant, straightforward and quite accurate solution which can model the effect of stator slotting in an electric machine, it has some drawbacks that should be corrected.

Two of the most important disadvantages and its possible corrections will be explained. For the sake of clarity, Figure 3.8 is included; it shows the flux density in the airgap calculated both, with the analytical model and using the FEM software FLUX®.

Two main characteristics are shown in Figure 3.8: the first one is that the magnetic field analytically estimated seems to be not solenoidal and the second one is that flux density enhances at both sides of a slot opening. Both effects and its main implications will be widely commented.

About the first problem it can be deduced that, for an odd relations of Q/t_p , the flux density estimated by the analytical approach is not solenoidal, i.e., the rotor acts

like a source or like a sink of field lines. In the shown example, the rotor at the chosen instant is a source because there is a slot in front of the magnet south pole but none in front of the north pole.

As far as the total magnetic flux density leaving a close region is not null its divergence is different from zero and one of the Maxwell equations is not fulfilled.

This important error is a direct cause of equation (3.29). Obviously, the canonical solution ($B_g^m(\theta)$) is solenoidal because it is obtained by direct resolution of Maxwell equations, but the estimated one with the slotting effect ($B_{gs}^m(\theta)$) is no longer solenoidal when there are an odd number of slots in a winding periodicity because of the asymmetry of the relative permeance function.

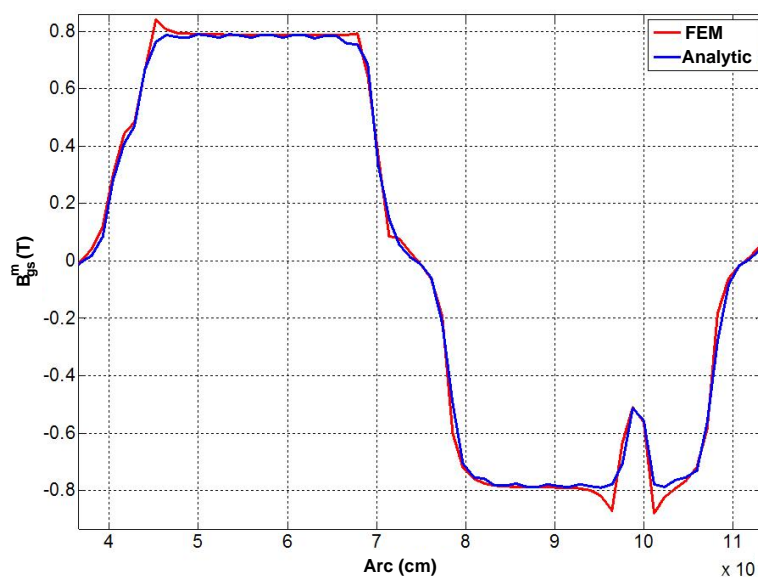


Figure 3.8. Radial component of the magnet flux density in the airgap. The PMSM simulated is a Q3p1 (3 slots and just one pole pair)

The direct consequence of this error is that the total sum of the magnetic flux which goes through each tooth is not equal to zero, so a correct estimation of all the parameters which depends on that flux, such as the electromagnetic force (EMF) or power losses, is impossible.

It is desired to keep the same $K_{sl}(\theta)$ approximation since it is capable to predict the flux density quite accurately. A correction based on the study of the spectrum of the magnet flux in the teeth has been implemented with good results. This approach has proved to be very suitable as far as it corrects the previous error. Its development will be explained later in this section.

The second problem is the flux density “peaks” emplaced at both sides of a slot opening. The approximation used is incapable of modelling such phenomenon because its main assumption is that the flux is completely radial under the teeth but it neglects additional effects occurring at their ends, due to the flux lines concentration.

As can be seen in Figure 3.9 the flux is nearly radial under the teeth but it is not in the proximities of a slot opening, because it curves in order to avoid the opening and enters into the tooth following the minimum reluctance path. This effect leads to a higher flux density in the tooth tips near the slot opening, as predicted by FEM simulations.

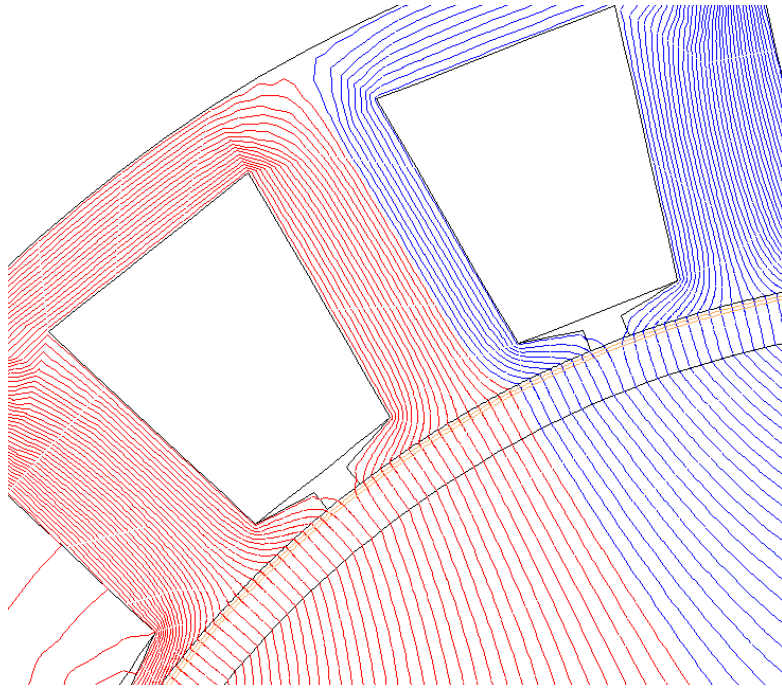


Figure 3.9. Flux paths simulated in FEM with FLUX2D®.

In most cases, this effect has little influence in the subsequent calculus of the flux and the EMF, so only two possible solutions are briefly presented but none of them have been implemented yet.

One of them is the use of an equivalent reluctance circuit. The main drawback of this type of solution is that it requires a computational effort much higher than the analytical algorithms.

Another interesting approach for the relative permeance function is proposed by [Zarko 2006] who used the conformal transformation in order to calculate $K_{s1}(\theta)$ in a more suitable domain. Its method is a good candidate to be implemented in a later version of the magnetic model because it permits to solve in a straightforward manner the two problems addressed here: the possible non-solenoidal field and the increment of the flux density in the proximities of a slot opening.

3.3.3 Electro-Motive Force and Stator Flux Induced by the Magnets

One of the main variables in any electric machine is the EMF generated in the coils, because through this voltage the magnetic energy is converted into electrical one.

In this section the calculus of the flux densities in the stator core of a PMSM will be explained, as well as the method to obtain the EMF once the fluxes are known.

3.3.3.1 Magnet Flux Density in the Stator Teeth

The magnetic flux induced in the stator teeth by the magnets has a great interest not only for the estimation of the core possible saturation level but also for its direct influence in the generation of the EMF.

In [Hanselman 2012] a mathematical procedure in order to obtain this flux (ϕ_t^m) as a function of the angular misalignment between a magnet centre and a tooth centre (α) is proposed. Obviously, the α offset is time dependent because the teeth have a fixed angular position but the magnets turn with constant angular speed ω_m .

In the next equations all the angles are expressed in mechanical radians except otherwise specified.

$$\phi_t^m(\alpha) = \frac{1}{p} \int_{-L_e/2}^{L_e/2} \int_{-\theta_s/2}^{\theta_s/2} K_{sl}(\theta) B_g^m(\theta + \alpha) R_s d\theta dz = \frac{L_e R_s}{p} \int_{-\theta_s/2}^{\theta_s/2} K_{sl}(\theta) B_g^m(\theta + \alpha) d\theta \quad (3.34)$$

where L_e is the PMSM active length and θ_s is the tooth pitch in mechanical radians.

As it is known, B_g^m and K_{sl} can be expressed as their respective FS, but their period difference must be taken into account. B_g^m has a period of $2\pi/p$ radians while K_{sl} has a $2\pi/Q$ radians periodicity.

Having these features in mind it is possible to prove that:

$$\phi_t^m(\alpha) = \frac{2\pi L_e R_s}{Q} \sum_{k=-\infty}^{\infty} \sum_{n=-\infty}^{\infty} B_{g,k}^m K_{sl,n} \text{sinc}\left(\left(n + \frac{kp}{Q}\right)\pi\right) e^{jk\alpha}. \quad (3.35)$$

From (3.35) it is possible to obtain the FS of ϕ_t^m with respect to α :

$$\phi_{t,k}^m = \frac{2\pi L_e R_s}{Q} B_{g,k}^m \sum_{n=-\infty}^{\infty} K_{sl,n} \text{sinc}\left(\left(n + \frac{kp}{Q}\right)\pi\right). \quad (3.36)$$

It is very important to notice that the spatial FS with respect to α , with a period of $2\pi/p$ mechanical radians, is exactly the same as the conjugate temporal FS with a periodicity equal to $1/f_e$, being f_e the electrical frequency. That is why the magnets (and, therefore the offset α) pass through an entire period in a time equal to $1/f_e$, hence,

$$\alpha = -\omega_e t, \quad (3.37)$$

$$\phi_t^m(t) = \sum_{k=-\infty}^{\infty} \phi_{t,k}^m e^{jk\alpha} = \sum_{k=-\infty}^{\infty} \phi_{t,k}^m e^{-jk\omega_e t} = \sum_{k=-\infty}^{\infty} \phi_{t,k}^m e^{jk\omega_e t}. \quad (3.38)$$

Using the properties of the FS it is possible to prove that the temporal FS coefficients are equal to the conjugate of the spatial FS coefficients with respect to α . Due to its physical meaning only the temporal coefficients $\phi_{t,k}^m$ will be used.

With the previous equations the flux in a specific tooth is obtained. The flux in any other tooth will be the same except for a delay. If the first tooth is the reference, the n^{th} one will have FS coefficients given by

$$\phi_{tk,nk}^m = \phi_{tk,1k}^m e^{-j(n-1)kp\theta_s}. \quad (3.39)$$

As it will be explained in 3.3.2.1 an anomalous case exists if Q/t_p is odd, condition that only fractional slot machines satisfy.

As it was introduced, in this case the presence of $K_{s1}(\theta)$ causes that the magnetic flux density calculated in the airgap is not solenoidal, unfulfilling Maxwell equations. It is necessary to correct that error in order to obtain a suitable approximation of important variables, such as the EMF. It is possible to correct this problem carrying out a detailed analysis of the temporal harmonics of the magnet tooth flux.

The flux in each tooth is calculated by means of equation (3.39). The sum all over a spatial periodicity must be null for any instant of time in order to fulfil Maxwell equations, so

$$\sum_{n=1}^{Q/t_p} \sum_{k=-\infty}^{\infty} \phi_{t,1k}^m e^{j\omega_e t} e^{-j(n-1)k 2\pi p/Q} = 0 \quad \forall t. \quad (3.40)$$

A necessary, but not sufficient, condition to ensure that the summation is null is that all temporal harmonics of order $k = sQ/p \quad \forall s \in \mathbb{Z}$ are null.

The proof is trivial: if any $\phi_{t,1sQ/p}^m$ were not null, the total sQ/p harmonic amplitude would be equal to Q times the amplitude of $\phi_{t,1sQ/p}^m$, because every tooth flux will be summing in phase. As far as $\phi_{t,1sQ/p}^m$ can adopt any value, the summation is not null and the flux density could not be solenoidal.

In several simulations, it has been observed that the only difference between the cases when Q/t_p is odd and the others is that the FS in the tooth flux has no null terms when k is multiple of Q/t_p . This is a particular case of the ones when k is multiple of Q/p .

Although a mathematical demonstration has not been obtained yet, it could be deduced by direct comparison with FEM simulations that it is possible to perform a correct calculus of the EMF and the rest of motor variables just correcting the

temporal Fourier Transform of the tooth flux annulling all terms with k multiple of Q/t_p , i.e.:

$$\Phi_{t,sQ/t_p}^m = 0 \quad s \in \mathbb{Z} \quad (3.41)$$

Once the magnet flux in the teeth is obtained and corrected, it is possible to obtain its magnetic induction (B_t^m) assuming that the flux is uniform on a cross-section of them:

$$B_t^m(t) = \frac{\Phi_t^m(t)}{L_e w_t}, \quad (3.42)$$

$$B_{t,k}^m = \frac{\Phi_{t,k}^m}{L_e w_t}, \quad (3.43)$$

where w_t is the teeth width.

3.3.3.2 Magnet Flux Density in the Stator Yoke

The magnetic flux induced by the magnets in the stator yoke is less important than the one induced in the teeth, because it has no direct influence in EMF generation, not in the conversion of electric into mechanical energy.

However, the magnet flux density in stator yoke must be taken into account in order to avoid the saturation of the iron core. In most design procedures this induction determines yoke height and, therefore, the stator external radius.

In order to estimate the magnetic induction in the stator yoke [Hanselman 2012] proposed a direct and straightforward model based on a reduced reluctance circuit. The main assumptions used in this approach are:

- Teeth are modelled as a flux source of value $\Phi_{t,n}^m$.
- The stator yoke portion between two teeth is established as a reluctance of constant value R .
- Indirectly, the model supposes that the flux lines are normal to the rz -plane at each point.

Figure 3.10 shows the reluctance circuit in which the model is based.

Obviously, the presented approach is far from being as accurate as the teeth flux calculus, since it is much simpler and its assumptions are more rough. However, its accuracy is enough to obtain a suitable approximation of the maximum magnetic induction in the stator yoke, which is the only important parameter in order to estimate the magnetic saturation.

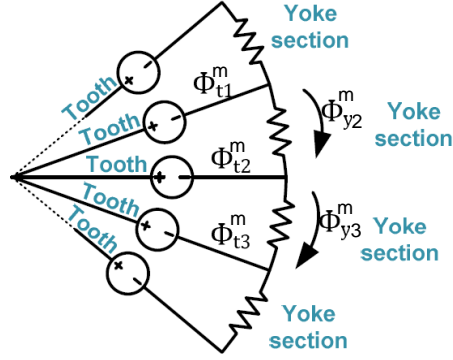


Figure 3.10. Equivalent reluctance circuit for stator yoke magnetic flux calculus.

More precisely, the model presented is especially rough for the magnetic induction calculus in region numbered as two in Figure 3.10 because in that zone the flux is quite far from being normal to the rz -plane, as far as the lines are curved in order to change from a radial direction into a tangential one.

The magnetic flux can be calculated as:

$$\phi_{s,2}^m(t) = \frac{1}{Q} \sum_{n=1}^Q (Q-n) \phi_{t,n+1}^m(t) = \frac{t_p}{Q} \sum_{n=1}^{Q/t_p} (Q-n) \phi_{t,n+1}^m(t) \quad (3.44)$$

Where $\phi_{s,2}^m(t)$ is the stator yoke flux between the first and the second tooth. The general form of this notation establishes that $\phi_{s,n}^m(t)$ is the stator yoke flux between the n^{th} and the $(n-1)^{\text{th}}$ teeth. It should be noticed that the summation is limited to just a winding period due to the stator symmetry.

It is quite simple to modify equation (3.44) in order to obtain the temporal FS coefficients of the yoke flux from the teeth flux temporal FS. If the superposition principle is applied it is obtained

$$\phi_{s,2k}^m = \frac{t_p}{Q} \sum_{n=1}^{Q/t_p} (Q-n) \phi_{t,(n+1)k}^m \quad (3.45)$$

From the fluxes, the magnetic induction in the stator yoke can be obtained in a direct way from

$$B_{s,2}^m(t) = \frac{\phi_{s,2}^m(t)}{L_e w_{sy}}, \quad (3.46)$$

$$B_{s,2k}^m = \frac{\phi_{s,2k}^m}{L_e w_{sy}}, \quad (3.47)$$

where w_{sy} is the yoke height.

Obviously, the fluxes and magnetic induction in any other stator yoke portion can be obtained from the previous equations taking into account the temporal delay with respect to the reference section, just as it is done in teeth flux calculus.

$$\phi_{s,nk}^m(k) = \phi_{s,2k}^m e^{-j(n-2)kp\theta_s} \quad (3.48)$$

3.3.3.3 Induced EMF

The electro-motive force is one of the main variables in a motor design because it is the critical parameter through which energy is converted from the magnetic domain to the electric one, by applying Faraday’s law. Many calculus methods to obtain this variable are proposed in technical literature.

Several authors [Almandoz 2008, Pyrhönen 2008] proposed a model which will be referred to as the classical approach. This approach is based on the calculus of a winding factor (ξ_n), which establishes an equivalence between the back EMF created by one coil (with just an “in” slot and an “out” one) and the back EMF of all coils winding in the stator core. This factor takes into account the coil offset angles and the effect of coil pitch.

The classical method is very suitable when the coil back EMF was assumed to have a sinusoidal dependence with respect to time or when the current harmonics are negligible. However, since the design methodology proposed is general and the current can contain temporal harmonics the interest of the classical approach is very low [Hanselman 2012]. Thus, a different approach proposed by [Hanselman 2012] will be implemented.

The basis of this method consists in obtaining the total magnet flux linked by a phase winding. In order to do so m “scale factor” vectors (one for each phase, noted S_l) are defined. Their length is Q/t_p , i.e. the number of teeth contained in a winding periodicity.

The n^{th} position within vector S_1 defines the number of phase A coils that are linked by the n^{th} tooth and its sign (positive or negative according to the “right-hand rule”). For example, for the phase winding shown in Figure 3.11 the S_1 vector will be:

Table 3.1. Scale factor for the example shown in Figure 3.11

Tooth	1	2	3	4	5	6	7	8	9	10	11	12	13	14	15
S_1	1	1	1	0	-1	-1	-1	1	2	2	1	-1	-1	-1	1

Once vectors S_l have been established the total flux linked by phase A ($\phi_{lKA}^m(t)$) in a spatial periodicity is

$$\Phi_{lkA}^m(t) = \sum_{n=1}^{Q/t_p} S_{1n} \Phi_{t,n}^m(t). \quad (3.49)$$

As it has been proved, the flux induced by the magnets is the same in every tooth, except for a temporal delay, so the FS coefficients of the above summation can be write as

$$\Phi_{lkA,k}^m = \Phi_{t,k}^m \sum_{n=1}^{Q/t_p} S_{1n} e^{-jk(n-1)p\theta_s}. \quad (3.50)$$

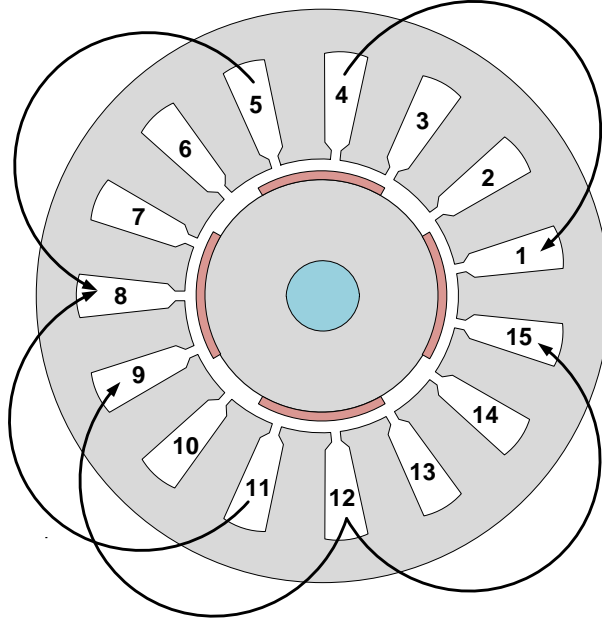


Figure 3.11. Example of phase A winding in a fractional slot machine.

Faraday's law establishes that the voltage induced is equal to:

$$E_{Ap}(t) = Z \frac{d\Phi_{lkA}^m(t)}{dt}, \quad (3.51)$$

where $E_{Ap}(t)$ is the EMF induced in phase A and Z the number of coils per slot per phase. Equation (3.51) can be expressed in the spectral domain as follows:

$$E_{Ap}(t) = Z \sum_{k=-\infty}^{\infty} \Phi_{t,k}^m \frac{de^{jk\omega_e t}}{dt} \sum_{n=1}^{Q/t_p} S_{1n} e^{-jk(n-1)p\theta_s}. \quad (3.52)$$

Therefore, the induced electro-motive force FS is equal to:

$$E_{Ap,k} = jZ\omega_e k \Phi_{t,k}^m \sum_{n=1}^{Q/t_p} S_{1n} e^{-jk(n-1)p\theta_s} \quad (3.53)$$

The sign of the voltage will be established according to Lenz's law. Thus, the positive voltage reference is in the "out" winding slot as can be seen in Figure 3.11.

It is very important to notice that, through the developed procedure, the EMF corresponding to a winding periodicity has been obtained. If we assumed that all the coils in one phase are connected in series the total EMF will be t_p times higher:

$$E_{At,k} = jZ t_p \omega_e k \Phi_{t,k}^m \sum_{n=1}^{Q/t_p} S_{1n} e^{-jk(n-1)p\theta_s}. \quad (3.54)$$

This case is the most common in electric machines [Hanselman 2012] but other connections are available. The total EMF will depend on the particular combination of series and parallel connections of the windings periodicities. For a generic connection the EMF induced will be

$$E_{At,k} = jZ \frac{t_p}{N_{para}} \omega_e k \Phi_{t,k}^m \sum_{n=1}^{Q/t_p} S_{1n} e^{-jk(n-1)p\theta_s}. \quad (3.55)$$

where N_{para} is the number of groups connected in parallel.

The same procedure can be performed in order to obtain the EMF induced in other phases, but it is not necessary as far as the PMSM is supposed to have a balanced winding distribution and the induced EMF in the phases must be equal except for a phase difference of $360^\circ/m$ degrees.

3.3.4 Armature Reaction and Total Magnetic Field

The flux density induced by the stator coils current is known as "armature reaction". The armature reaction is of minor importance in the global behaviour of a PMSM, because it is usually an order of magnitude lower than the magnet induction. In spite of this fact, it is useful to obtain it because it is added to the magnet flux density, so it can have an influence in the losses, and in the non-linearities associated with the core saturation level and the electromagnetic force calculus.

3.3.4.1 Armature Reaction in the Airgap

The literature offers different methods for the analytic calculus of the armature reaction in the airgap [Zhu 1993-b, Almandoz 2008]. Most of them have the main assumption that the ferromagnetic materials can be supposed to be infinitely permeable, so the flux density can be considered as radial, both in the airgap and in the stator core. Figure 3.12 shows the flux lines caused by just one stator coil.

The armature reaction model implemented is based on the estimation of the flux density spatial FS from the stator winding distribution [Almandoz 2008]. In a first stage

the magneto motive force (MMF) generated by just one coil is calculated; its spatial FS can be defined as

$$\frac{\text{MMF}(\theta, t)}{I(t)} = F(\theta) = \sum_{k=-\infty}^{\infty} F_k e^{jkt_p\theta}, \quad (3.56)$$

where $F(\theta)$ is the magneto motive force induced per current unit.

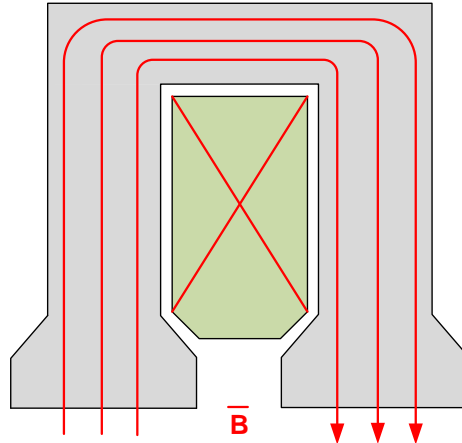


Figure 3.12. Armature reaction caused by one coil in the adjacent teeth.

The spatial waveform of the armature reaction caused by a single coil can be characterized by three parameters: its pitch angle β , its central angle ϕ and its slot opening α (see Figure 3.13).

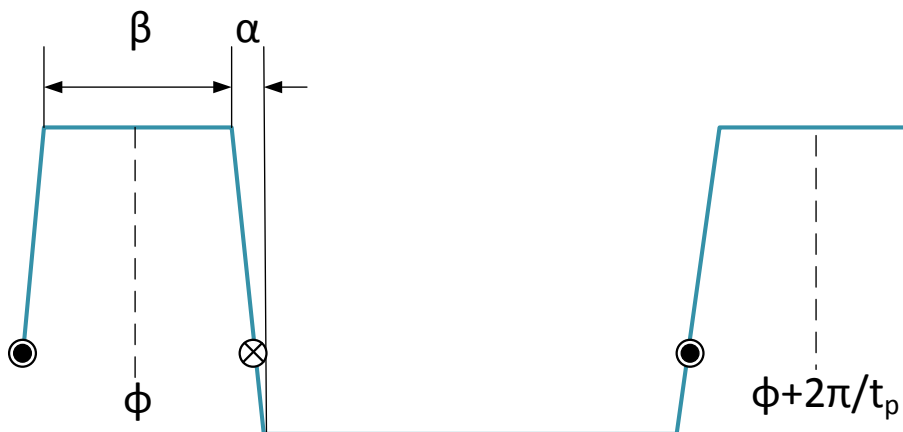


Figure 3.13. Spatial distribution of the MMF per current unit caused by a single coil.
Example from [Almandoz 2008].

It is possible to obtain the three aforementioned parameters for a particular coil from its “in” and “out” slots, i.e. for coil “ n ”:

$$\phi_n = \pi \frac{\text{out}L(n) + \text{in}L(n) - 3}{Q}, \quad (3.57)$$

$$\alpha_n = \frac{w_0}{R_s}, \quad (3.58)$$

$$\beta_n = \frac{2\pi}{Q} (\text{outL}(n) - \text{inL}(n)) - \alpha, \quad (3.59)$$

where w_0 is the slot opening measured in mechanical radian, and outL and inL are the “out” and “in” vector established during the winding layout. In the previous equations the 0 rad reference is at the centre of the first tooth, situated anticlockwise adjacent to the first slot, i.e., a coil which enters by the first slot and leaves by the second is centred in $\phi = 0$ rad.

With the previous values obtained from the coil configuration it is possible to perform the spatial FS of the trapezoidal form adopted by the armature reaction:

$$F_{nk} = \frac{Z}{t_p \alpha_n \pi k^2} \left[\cos \left(kt_p \frac{\beta_n}{2} \right) - \cos \left(kt_p \left(\frac{\beta_n}{2} + \alpha \right) \right) \right] e^{-jkt_p \phi_n}. \quad (3.60)$$

Once all the armature reactions of the coils are obtained individually it is possible to calculate the armature reaction caused by one phase, adding all the individual contributions:

$$F_{A,k} = \sum_{n=1}^{QN_{\text{lay}}/(2m)} F_{nk}. \quad (3.61)$$

where N_{lay} is the number of layers in a single slot (usually one or two) and n is an index which numerates every coil in phase A. Figure 3.14 shows a typical armature reaction of a phase with two coils at an instant of time.

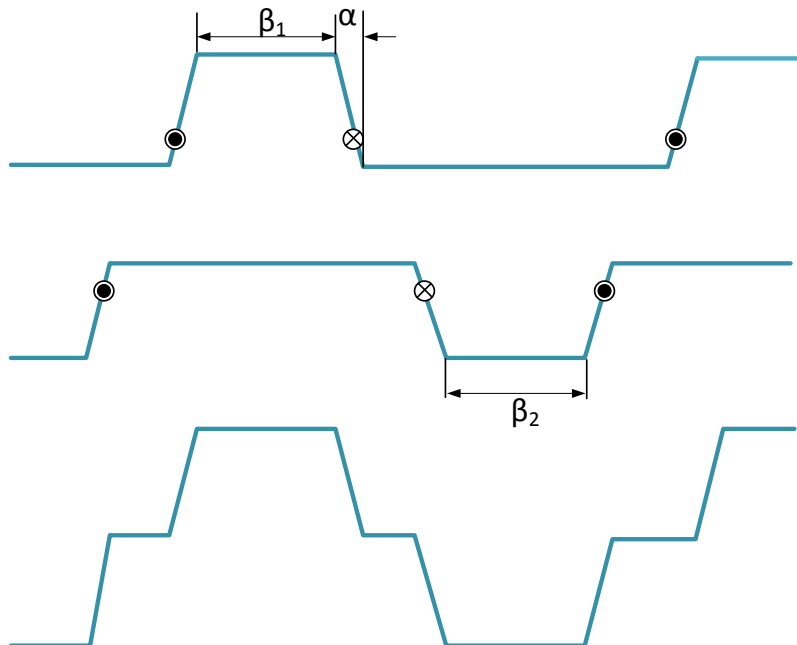


Figure 3.14. Spatial distribution of the MMF per current unit caused by a phase conformed by two coils. Example from [Almandoz 2008].

As far as the PMSM modelled has a spatial balanced winding, all the phases have the same armature reaction waveform up to a phase difference of $2\pi/(mp)$

mechanical radians with respect to the previous phase; hence, the calculus of just one phase armature reaction is enough. The complete magneto-motive force will be

$$\text{MMF}_k^a(t) = \sum_{s=0}^{m-1} F_{A,k} e^{-\frac{j2\pi sk}{m}} I_s(t), \quad (3.62)$$

where index s represents the phase, and $I_s(t)$ is the current flowing through the s phase at instant t .

Once the magneto-motive force is obtained the armature reaction in the airgap ($B_{g,k}^a(t)$) is

$$B_{g,k}^a(t) = \frac{\mu_0 \text{MMF}_k^a(t)}{\delta}. \quad (3.63)$$

A very important feature of that model is that, as far as the temporal and spatial variables are independent, it is possible to perform a double FS with respect to both magnitudes. Thus, the final expression of the coefficients of the double FS of the armature reaction in the airgap will be:

$$B_g^a(\theta, t) = \frac{\mu_0}{\delta} \sum_{s=0}^{m-1} \sum_{k=-\infty}^{\infty} \sum_{l=-\infty}^{\infty} e^{-j2\pi s(k+l)} F_{A,k} I_{A,l} e^{j(kt_p\theta + l\omega_e t)}, \quad (3.64)$$

which, by means of the equilibrate winding distribution and the balance, is equal to

$$B_g^a(\theta, t) = \frac{\mu_0}{\delta} \sum_{k=-\infty}^{\infty} \sum_{l=-\infty}^{\infty} (1 + 2\cos(2\pi(k+l)/m)) F_{A,k} I_{A,l} e^{j(kt_p\theta + l\omega_e t)} \quad (3.65)$$

or, in the spectral domain,

$$B_{g,kl}^a = \frac{\mu_0(1 + 2\cos(2\pi(k+l)/m))}{\delta} F_{A,k} I_{A,l}. \quad (3.66)$$

3.3.4.2 Armature Reaction in the Stator Core

Once the flux density in the airgap is obtained it is possible to calculate its value both in the stator teeth and in the stator yoke. In order to achieve these results it is possible to apply a procedure quite similar to that exposed in 3.3.3.1. The flux caused by the stator coils in the teeth will be equal to

$$\Phi_t^a(t) = \frac{1}{p} \int_{-L_e/2}^{L_e/2} \int_{-\theta_s/2}^{\theta_s/2} K_{s1}(\theta) B_g^a(\theta, t) R_s d\theta dz. \quad (3.67)$$

It is interesting to notice that, for a fixed tooth, the armature reaction $B_g^a(\theta, t)$ can be considered as constant, approximating its trapezoidal form for a rectangular one. Thus, (3.67) can be expressed as:

$$\phi_{t,1}^a(t) = \frac{L_e R_s}{p} B_g^a(t) \int_{-\theta_s/2}^{\theta_s/2} K_{sl}(\theta) d\theta, \quad (3.68)$$

which leads to a temporal FS equal to given by

$$\phi_{t,1k}^a = \frac{L_e R_s}{p} B_{g,k}^a \sum_{n=-\infty}^{\infty} K_{sl,n} \text{sinc}(n\pi). \quad (3.69)$$

For any other tooth the same procedure is applied, establishing the proper limit in the integral along θ . It is very important to realize that, in contrast to what happens with the magnets flux, the flux induced by the armature reaction is not equal in every tooth. In fact, as far as the scale factors S are different for each tooth it is quite possible that some of them have a flux waveform quite different from the others.

From the armature reaction of the teeth it is quite simple to obtain the flux in the stator yoke by using the equations proposed in section 3.3.3.2, just replacing the variable $\phi_{t,nk}^m$ by $\phi_{t,nk}^a$. The final results of that Section are repeated for sake of completeness.

$$\phi_{s,2k}^a = \frac{t_p}{Q} \sum_{n=1}^{Q/t_p} (Q - n) \phi_{t,(n+1)k}^a, \quad (3.70)$$

so, the magnetic induction in the stator yoke can be approximated by:

$$B_{s,2}^a(t) = \frac{\phi_{s,2}^a(t)}{L_e W_{SY}}. \quad (3.71)$$

Magnetic fluxes and inductions in any other stator yoke section can be obtained from the previous equations. In practice, calculating these values will be more time consuming than in the case of the magnet fluxes, because the teeth fluxes are no longer equal in the case of the armature reaction.

The armature reaction for a generic stator yoke section will be

$$\phi_{s,lk}^a = \frac{t_p}{Q} \sum_{n=1}^{Q/t_p} (Q - n) \phi_{t,\text{mod}(n+l, Q/t_p)k}^a, \quad (3.72)$$

where $\text{mod}(x,y)$ is the remainder in the integer division x/y .

3.3.4.3 Total Magnetic Field in the Stator Core

An accurate expression of the total magnetic field, both in the airgap and in the stator core, is needed in order to obtain some physical variables that are of main relevance for the calculus of the efficiency and the thermal and vibratory behaviour of the PMSM.

More precisely, the magnetic field in the airgap causes electromagnetic forces that produce vibrations in the stator cores, vibrations that are transmitted through the housing and are propagated into the air producing undesirable noise. On the other hand, total flux density in the stator core causes iron losses which are critical in the calculus of the overall machine efficiency and its temperature. Moreover, an excessive magnetic induction can cause the ferromagnetic material saturation, worsening its electromagnetic behaviour and entailing an important loss of accuracy in the analytical model implemented.

In some studies the influence of the armature reaction is neglected because it is estimated that, in most occasions, its value is an order of magnitude lower compared with the magnet flux. In spite of this fact, complete magnetic induction estimation is preferred as far as, during this work, it has been proved that the forces and iron losses are notably modified by the armature reaction.

It is important to notice that as far as both armature reaction and magnet flux are vectorial magnitudes they should be added as vectors. Nevertheless, they are supposed to be perfectly radial in the airgap and in the stator teeth, while they are tangential in the stator yoke. Under these assumptions, they can be added in a scalar sense with a minimum accuracy loss.

In first place, the induced flux in a stator tooth will be calculated. Due to the fact that both individual contributions have been obtained previously it is enough to sum its values:

$$\phi_{t,nk}(k) = \phi_{t,nk}^a + \phi_{t,nk}^m \quad (3.73)$$

Thus, the total n^{th} tooth flux expressed in term of its temporal FS coefficients will be equal to:

$$\phi_{t,nk} = L_e R_s \left(\frac{1}{p} B_{g,k}^a \sum_{n=-\infty}^{\infty} K_{sl,n} + \frac{2\pi}{Q} B_{g,k}^m \sum_{n=-\infty}^{\infty} K_{sl,n} \text{sinc} \left(\left(n + \frac{kp}{Q} \right) \pi \right) \right) \quad (3.74)$$

Finally the total flux density of the n -th tooth will be

$$B_{t,nk} = \frac{(\phi_{t,nk}^m + \phi_{t,nk}^a)}{L_e w_t} \quad (3.75)$$

It is important to notice that, while $B_{g,k}^m$ is the same for all teeth except for a temporal delay, it is not the case of $B_{g,k}^a$ which can be different for each tooth depending on the particular stator winding.

Despite of this fact, for the saturation and losses estimation, it will be considered that all the stator teeth have the same armature reaction (i.e., the same $B_{g,k}^a$) equal to the maximum tooth flux calculated. Hence, it is not necessary the exhaustive calculus of the total flux density in each part of the stator core. This simplification is quite time saving and permits to establish a security factor in the iron losses.

The stator yoke total flux can be estimated in a similar fashion, the FS coefficients are given by

$$\phi_{s,lk} = \frac{t_p}{Q} \sum_{n=1}^{Q/t_p} (Q - n) \phi_{t, \text{mod}\left(n+l, \frac{Q}{t_p}\right) k} \quad (3.76)$$

$$B_{s,lk} = \phi_{s,lk} / (L_e w_{sy}). \quad (3.77)$$

In this case, in order to calculate the ferromagnetic losses in the stator yoke, the same approximations as those applied for the teeth will be used. Thus, it will be considered that $\phi_{s,lk}$ is equal in every yoke region.

3.3.4.4 Total Magnetic Field in the Airgap

The total magnetic field in the airgap is an important variable, on one hand because it establishes the flux in the stator core, on the other hand because the radial magnetic forces are proportional to its square value.

The double (temporal and spatial) FS of the magnet airgap flux in a slotless motor can be expressed as

$$B_g^m(\theta, t) = \sum_{k=-\infty}^{\infty} B_{g,k}^m e^{jk(p\theta - \omega_e t)}. \quad (3.78)$$

While the FS of the armature reaction in the airgap is equal to

$$B_g^a(\theta, t) = \frac{\mu_0}{\delta} \sum_{k=-\infty}^{\infty} \sum_{l=-\infty}^{\infty} (1 + 2\cos(2\pi(k+l)/m)) F_{A,k} I_{A,l} e^{j(k t_p \theta + l \omega_e t)}. \quad (3.79)$$

Thus, double FS of the total airgap induction in a slotless motor is equal to their sum

$$B_g(\theta, t) = \sum_{k=-\infty}^{\infty} \left(B_{g,k}^m e^{jk(p\theta - \omega_e t)} + \sum_{l=-\infty}^{\infty} \frac{\mu_0}{\delta} \left(1 + 2\cos\left(\frac{2\pi(k+l)}{m}\right) \right) F_{A,k} I_{A,l} e^{j(k t_p \theta + l \omega_e t)} \right). \quad (3.80)$$

The most direct form of including the effect of the stator slotting is using the relative permeance factor. Thus, the total magnetic induction, taking into account the slots effect will be.

$$B_{gr}(\theta, t) = K_{sl}(\theta) \left(B_g^m(\theta, t) + B_g^a(\theta, t) \right). \quad (3.81)$$

This is the magnetic induction value that will be used by the methodology in order to estimate the radial forces.

3.3.5 Radial Stator Force and Cogging Torque Calculus

The presence of a magnetic field in the boundary between the airgap and the stator ferromagnetic core generates a superficial force due to the material abrupt change. These forces are produced by the interaction of the rotor magnetic fields caused by the magnets and the stator fields caused by the currents flowing through the coils. As it was explained during the torque calculus, these magnets and electromagnets are attracted to each other (generating mutual torque) and to the ferromagnetic cores (producing the cogging and reluctance torques). The magnetic field and the forces on the stator core are represented in Figure 3.15.

There exists a great controversial about the best form of estimate the electromagnetic forces, so many approaches haven been proposed and implemented in order to perform this calculus. All the aforementioned methods are encompassed in two main categories; the virtual power principle [Sanchez 2006, Bossavit 2014] and the Maxwell stress tensor method [Bermúdez de Castro 2014]. Comparisons between them have been carried out [Bossavit 2011].

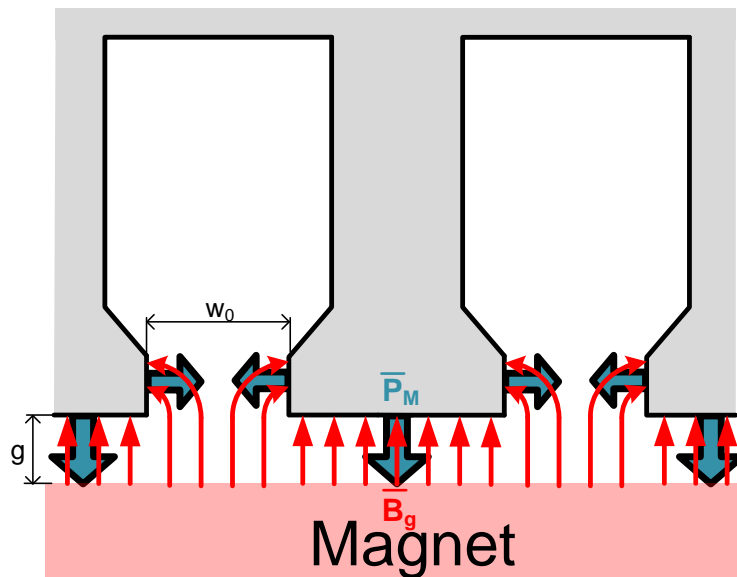


Figure 3.15. Spatial distribution of the radial magnetic field and the generated force density in the stator boundaries.

It is known that, in a general form, the Maxwell stress tensor can be formulated as [Bermúdez de Castro 2014]:

$$\mathcal{T} = \mathbf{E} \otimes \mathbf{D} + \mathbf{B} \otimes \mathbf{H} - \frac{1}{2}(\mathbf{E} \cdot \mathbf{D} + \mathbf{B} \cdot \mathbf{H})\mathbf{I} \quad (3.82)$$

where \mathcal{T} is the Maxwell tensor, \mathbf{I} the identity tensor, \mathbf{E} and \mathbf{D} are the electric field and the electric flux density vectors, and \mathbf{H} and \mathbf{B} the magnetic field intensity and the magnetic flux density vectors.

In the particular case of a PMSM the electric field and the forces caused by it can be neglected respect to the magnetic ones and (3.82) is simplified to:

$$\mathcal{T} = \mathbf{B} \otimes \mathbf{H} - \frac{1}{2}(\mathbf{B} \cdot \mathbf{H})\mathbf{I} \quad (3.83)$$

The electromagnetic force is given by the divergence of the Maxwell electromagnetic stress tensor:

$$\mathbf{f} = \mathbf{div} \mathcal{T} \quad (3.84)$$

It can be proved that this divergence is null all over the stator except just in its boundary with the airgap. According with the magnetostatic theory the force in the boundary between the stator core and the airgap is equal to:

$$\langle \mathbf{f}, \gamma \rangle = - \int_S \left([\mathbf{H} \cdot \mathbf{nB}] - \frac{1}{2}[(\mathbf{B} \cdot \mathbf{H})\mathbf{n}] \right) \cdot \gamma \, dS \quad (3.85)$$

where \mathbf{n} is the normal surface vector (see Figure 3.15), and γ is any smooth enough vector field. The convention adopted for $[\mathbf{a}]$ is

$$[\mathbf{a}] = \mathbf{a}_{\mathbf{Fe}} + \mathbf{a}_{\mathbf{g}}, \quad (3.86)$$

where \mathbf{a} is a vector field which adopts a value $\mathbf{a}_{\mathbf{Fe}}$ in the stator core and a value $\mathbf{a}_{\mathbf{g}}$ in the airgap.

It is important to notice that the divergence operator must be understood in the sense of distributions, because the magnetic fields present discontinuities on boundary S , so a function γ is necessary in order to define the force.

It must be taken into account that the boundary between the stator core and the airgap is free of surface currents what implies that, in order to fulfil Maxwell equations, the normal component of the density flux and the tangential component of the magnetic intensity must be equal at both sides of the boundary.

$$H_{\mathbf{Fe}}^t = H_{\mathbf{Fe}}^t \quad (3.87)$$

$$B_{\mathbf{Fe}}^n = B_{\mathbf{g}}^n \quad (3.88)$$

where superscript t and subscript n refer to the tangential and normal component of the field, respectively. Taking this fact into account, it can be calculated:

$$[\mathbf{H} \cdot \mathbf{nB}] = |\mathbf{B}_{\mathbf{Fe}} \mathbf{n}_{\mathbf{Fe}}|^2 \mathbf{n}_{\mathbf{Fe}} \left(\frac{1}{\mu_{\mathbf{Fe}}} - \frac{1}{\mu_{\mathbf{g}}} \right) \quad (3.89)$$

$$[(\mathbf{B} \cdot \mathbf{H})\mathbf{n}] = |\mathbf{B}_{\mathbf{Fe}} \mathbf{n}_{\mathbf{Fe}}|^2 \mathbf{n}_{\mathbf{Fe}} \left(\frac{1}{\mu_{\mathbf{Fe}}} - \frac{1}{\mu_{\mathbf{g}}} \right) + \mathbf{n}_{\mathbf{Fe}} |\mathbf{H}^t|^2 (\mu_{\mathbf{Fe}} - \mu_{\mathbf{g}}) \quad (3.90)$$

Assuming that the ferromagnetic material is infinitely permeable equations (3.89) and (3.90) yield

$$[\mathbf{H} \cdot \mathbf{nB}] = \frac{-|\mathbf{B}_{\text{Fe}} \mathbf{n}_{\text{Fe}}|^2}{\mu_g} \mathbf{n}_{\text{Fe}} = \frac{-|\mathbf{B}_{\text{Fe}}^{\text{n}}|^2}{\mu_0} \mathbf{n}_{\text{Fe}}, \quad (3.91)$$

$$[(\mathbf{B} \cdot \mathbf{H})\mathbf{n}] = \frac{-|\mathbf{B}_{\text{Fe}} \mathbf{n}_{\text{Fe}}|^2}{\mu_g} \mathbf{n}_{\text{Fe}} = \frac{-|\mathbf{B}_{\text{g}}^{\text{n}}|^2}{\mu_0} \mathbf{n}_{\text{Fe}}, \quad (3.92)$$

where it is taken into account that \mathbf{H} is null in the ferromagnetic core, because of its high permeability.

Thus, the final expression of the integral (3.85) will be

$$\langle \mathbf{f}, \gamma \rangle = \int_S \frac{|\mathbf{B}_{\text{g}}^{\text{n}}|^2}{2\mu_0} \mathbf{n}_{\text{Fe}} \cdot \gamma \, dS. \quad (3.93)$$

Using the localization theorem it is deduced that the force density is equal to

$$d\mathbf{f}(\theta, t) = P_{\text{M}}(\theta, t) = \frac{|\mathbf{B}_{\text{g}}^{\text{n}}(\theta, t)|^2}{2\mu_0}. \quad (3.94)$$

where P_{M} is the Maxwell magnetic pressure in the direction of \mathbf{n}_{Fe} , i.e. of the outward normal with respect to the stator core.

This is the expression of the force density at each point and time that can be used to calculate both, the stator vibrations and the cogging torque.

As it can be seen, the magnetic pressure is applied in two directions, causing different effects.

- If it is applied on the tooth top, generating a radial force that is transmitted to the air through the housing and causes vibration and noise.
- If it is applied on the tooth shoes, i.e. on the boundaries of a slot opening, the forces cause a torque that, by mean of the second Newton's law, is reflected over the rotor generating the so called cogging torque.

Many authors try to link both phenomena as far as they are consequence of the same cause, i.e. the electromagnetic forces. The aim of these studies is to predict the machine vibratory behaviour from its cogging torque. However, recent studies have demonstrated that a higher amount of cogging torque is not directly associated with a worse vibratory behaviour [Gieras 2007, Islam 2010], so the two phenomena must to be studied separately in order to achieve a proper PMSM design.

3.3.5.1 Radial forces

Radial Maxwell forces calculated with (3.93) present a temporal and a spatial dependence, so a double FS with respect to both, the space and the time, can be performed:

$$P_M(\theta, t) = \frac{|\mathbf{B}_n^g(\theta, t)|^2}{2\mu_0} = \sum_{k=-\infty}^{\infty} \sum_{l=-\infty}^{\infty} P_{M,kl} e^{jk\omega_e t} e^{jlt_p\theta}. \quad (3.95)$$

The spatial component of the FS is associated with the radial mode excited in the stator structure, while its temporal component provide the excitation frequency. The vibratory effect caused by the force will be further developed. Figure 3.16 shows the Maxwell pressure over a tooth during an electric period, magnets and armature reactions contribution can be observed.

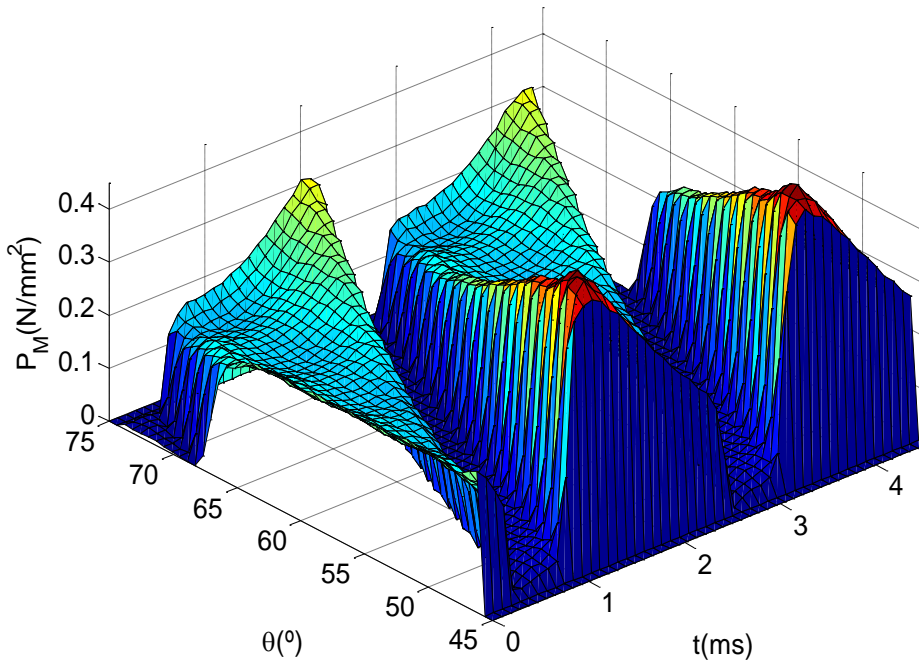


Figure 3.16. Radial force density over a tooth during an electrical period.

3.3.5.2 Cogging torque

The cogging torque also has an important influence in the motor performance, since an excessive torque ripple can cause important mechanical faults depending on the final applications, such as hard disk drives or industrial elevators.

There are many methods in order to calculate the cogging torque, the simplest one being to apply a direct integration in order to obtain the torque caused by just one slot and then to extrapolate it to the complete machine. Despite its accuracy limitations, the direct integration approach has been selected in the developed model because of its simplicity and easiness of implementation once the rotor density flux is estimated. The strategy is used by many authors [Zhu 1992, Proca 2003, Almandoz 2008] who propose several variations to the basic method in order to improve its accuracy maintaining its easiness. It is assumed that the magnetic induction caused by the rotor magnets follows a circumferential arc into the slot openings, causing a tangential force and, thus a cogging torque (see Figure 3.17).

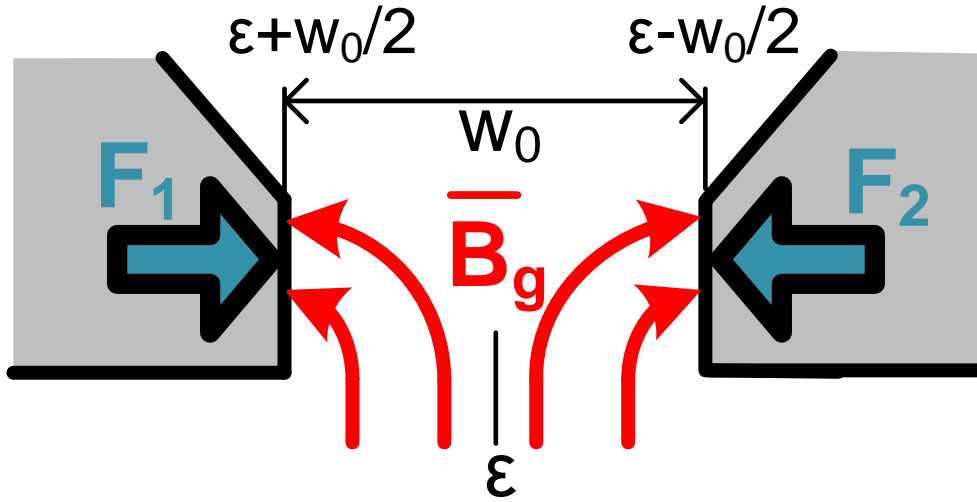


Figure 3.17. Detail of the slot opening surfaces where the forces are applied. Adapted from [Almendoz 2008].

The total cogging torque caused by the two faces of the slots opening can be approached by

$$T_{cs}(t) = -R_s^2 \int_{\epsilon-w_0/2}^{\epsilon+w_0/2} \int_{-L_e/2}^{L_e/2} P_M^m(\theta, t) \cdot \mathbf{n}_{Fe} dz d\theta. \quad (3.96)$$

where $P_M^m(\theta, t)$ is the magnetic pressure caused by the magnets, i.e. the pressure in no-load conditions. It should be noticed that the minus sign is applied from the Newton second law.

Equation (3.96) can be expressed as:

$$T_{cs}(t) = \frac{-R_s^2 L_e}{2\mu_0} \left[\int_{\epsilon-w_0/2}^{\epsilon} B_g^{m2}(t, \theta) K_{sl}^2(\theta) d\theta - \int_{\epsilon}^{\epsilon+w_0/2} B_g^{m2}(t, \theta) K_{sl}^2(\theta) d\theta \right] \quad (3.97)$$

Obviously, $K_{sl}^2(\theta)$ takes into account the effect of the stator slotting which, in fact, causes the cogging torque. In order to obtain the global cogging torque as a function of time it is necessary to solve the integral in θ for each instant.

A lot of computational effort could be saved if equation (3.97) is solved in the spectral domain, using the spatial FS of the magnetic induction and the relative permeance function, both squared. Namely,

$$B_g^{m2}(t, \theta) = \sum_{k=-\infty}^{\infty} B_{g,k}^{m'} e^{j2pk(\theta-\omega_m t)}, \quad (3.98)$$

$$K_{sl}^2(\theta) = \sum_{z=-\infty}^{\infty} K'_{sl,z} e^{jQz\theta}. \quad (3.99)$$

It should be noticed that the spatial period of $K_{s1}^2(\theta)$ is $2\pi/Q$ rad while the spatial period of $B_g^{m^2}(t, \theta)$ is half of the electric period, due to the $B_g^m(t, \theta)$ symmetry.

Applying (3.98) and (3.99) in (3.97) and solving the integral we get

$$T_{cs}(t) = \frac{-R_s^2 L_e}{2\mu_0} \sum_{k=-\infty}^{\infty} B_{g,k}^{m'} e^{-j2pk\omega_m t} \sum_{z=-\infty}^{\infty} K'_{sl,z} \frac{4e^{j\epsilon(2pk+Qz)} \sin^2\left(\frac{\theta_0}{4}(2pk+Qz)\right)}{j(2pk+Qz)} \quad (3.100)$$

By direct inspection the FS temporal coefficients of $T_s(t)$ are equal to:

$$T_{cs}(t) = \sum_{k=-\infty}^{\infty} T_{cs,k}^* e^{-jk2p\omega_m t} = \sum_{k=-\infty}^{\infty} T_{cs,k} e^{jk2p\omega_m t}, \quad (3.101)$$

$$T_{cs,k} = \frac{-R_s^2 L_e}{2\mu_0} B_{g,k}^{m'} \sum_{z=-\infty}^{\infty} K'_{sl,z} \frac{4e^{j\epsilon(2pk+Qz)} \sin^2\left(\frac{\theta_0}{4}(2pk+Qz)\right)}{j(2pk+Qz)}. \quad (3.102)$$

Once the temporal FS of a single slot torque is obtained it is possible to apply the superposition principle and calculate the total cogging torque. All the slots have the same torque except for a known delay, so its sum is given by

$$T_{c,k} = T_{cs,k} \sum_{n=1}^Q e^{-j(n-1)2pk\theta_s} = T_{cs,k} t_p \sum_{n=1}^{Q/t_p} e^{-j(n-1)2pk\theta_s}, \quad (3.103)$$

where θ_s is the slot pitch measured in radians. Due to the properties of the exponential, this sum will be non-null only for those k multiple of Q , so only these harmonics should be calculated.

Applying the previous expression the cogging torque is calculated and its value can be used in an optimization algorithm. If its temporal expression is required it is enough to perform the inverse FS.

3.4 Electric Domain

From an electrical point of view a PMSM can be seen as an EMF voltage connected in series with an equivalent impedance, as it is shown in Figure 3.18. The aim of the electric model is to calculate the impedance values in order to solve the circuit and obtain the interaction variables between the PMSM and its power supply converter, i.e. power factor, consumed power, efficiency, etc.

The combined effect of the grid and the power converter is approximated by a current source with known current value $I_{ph}(t)$, as far as a detailed study of the power interface between the grid and the machine is beyond this work aims.

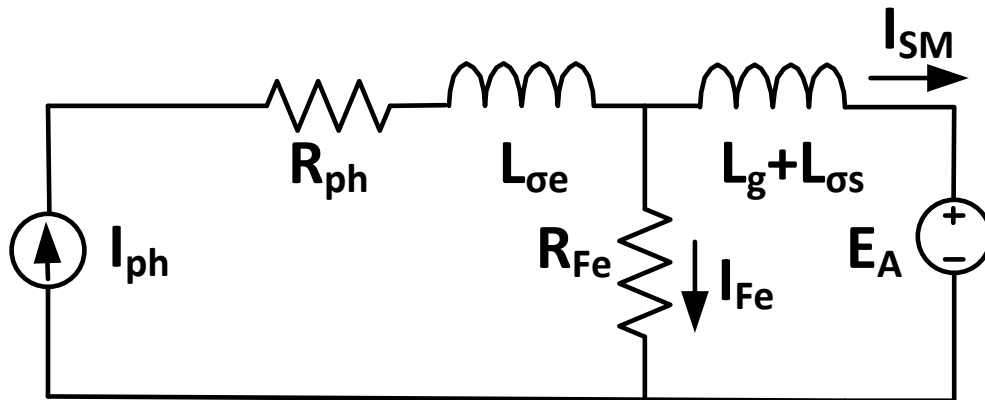


Figure 3.18. Phase A PMSM electric model including iron losses effect.

As it was mentioned, EMF can be calculated using the proposed magnetic model, while the estimation of the impedance values is the main goal in the electric domain. The impedance has three main components:

- Inductance. It is the physical inductance presented by the stator coils, by means of its ability to store magnetic energy.
- Copper resistance. It is the electrical resistance that the stator coils oppose to the current flowing through it.
- Iron resistance. It is a fictitious parallel resistance that represents the losses in the ferromagnetic cores. It is just an equivalent impedance used in order to include all the losses in the proposed circuit.

In the next sections the calculus of the different impedance elements will be explained in detail. In order to do so it will be supposed, without loss of generality, that all the winding periodicities are connected in series.

3.4.1 PMSM Coil Inductance

The stator structure consists of a core of ferromagnetic material and copper coils wound around it. therefore it is obvious that a PMSM behaves as an inductance in series with a voltage source (the EMF). The calculus of this inductance is not an easy task as far as many geometrical features must be considered. Traditionally, the calculus of an electrical machine inductance is subdivided according to the physical region where the magnetic energy is stored: the airgap inductance, the slot inductance and the end-winding inductance.

Figure 3.19 shows an example of magnetic energy stored in the slots and the airgap by means of the armature reactions. As it can be seen, the slots openings and the airgap store most of the energy, so their contribution to the total inductance will be high.

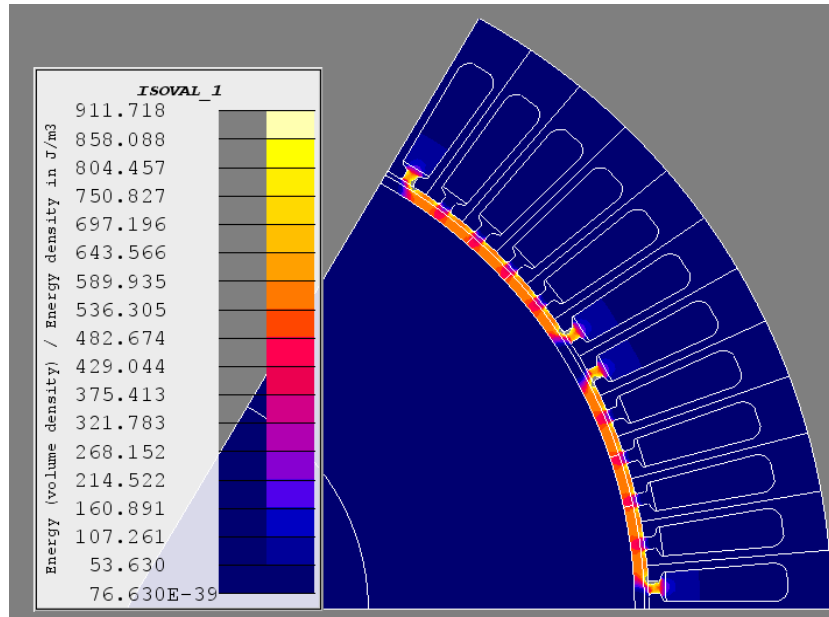


Figure 3.19. Magnetic energy stored in a PMSM due to the armature reaction. FEM simulation in FLUX®.

3.4.1.1 Airgap Inductance

The airgap is one of the main regions where magnetic energy induced by the armature reaction is stored. This is logical as far as the main flux path flows through the airgap in order to perform energy conversion.

In the literature, several airgap inductance estimation methods have been developed, a comparative study of them is included in [Rodríguez 2013]. In the present work an improvement of the approach done by [Hanselman 2012] is applied.

It is very important to notice that the airgap is shared by coils of m phases. Due to this fact, each phase undergoes not only an inductance due to its own flux (the so called self-inductance) but an inductance due to the flux induced by the other phases (the mutual inductance).

For a PMSM with m phases without neutral, the sum of all currents must be 0 and it can be shown that

$$L_g = L_g^A - M_g, \quad (3.104)$$

where L_g is the airgap total inductance, L_g^A the airgap self inductance and M_g the mutual inductance.

Using the concept of scale factor (S_l) a reluctance equivalent circuit is defined (see Figure 3.20).

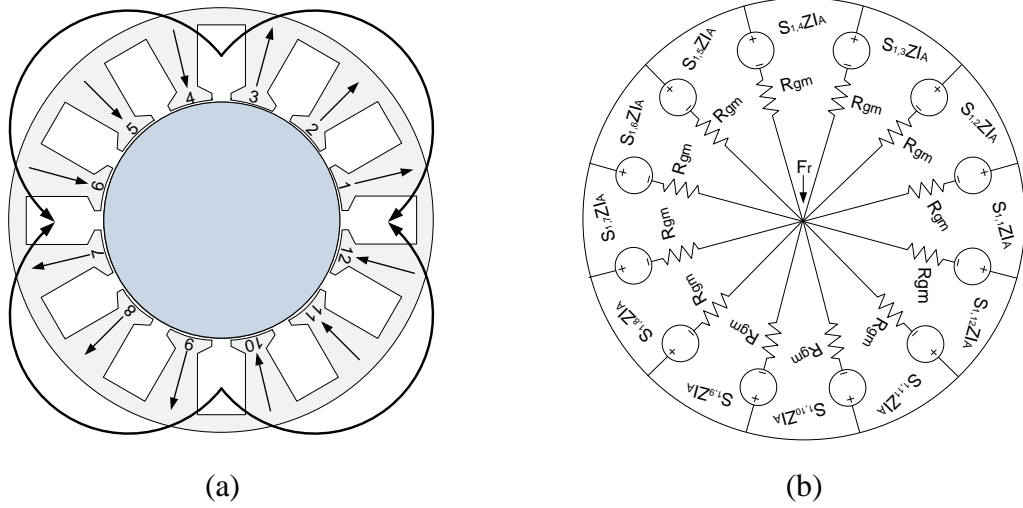


Figure 3.20. (a) Example of phase A winding for a Q12p2 machine, (b) equivalent reluctance circuit.

The proposed reluctance circuit has one branch for each tooth within a spatial periodicity (t_p). R_{gm} is the sum of the airgap and the magnet reluctances seen by each tooth. The solution of the above magnetic circuit for one phase (i.e. phase A) is

$$\text{MMF}_{A,n}(t) = Z(S_{1n} + F_r)I_A(t) = Z\left(S_{1n} - \frac{1}{Q}\sum_{l=1}^Q S_{1l}\right)I_A(t), \quad (3.105)$$

where $\text{MMF}_{A,n}$ is the MMF generated by phase A in tooth n , $I_A(t)$ is the phase A current and F_r is the fictitious MMF at the centre of the machine.

Once $\text{MMF}_{A,n}$ is known, it is possible to calculate the magnetic flux density and the flux in each tooth:

$$\phi_{gA,n}^a(t) = \frac{\mu_0}{\delta} \text{MMF}_{A,n}(t) \frac{L_e 2\pi R_s}{Q}. \quad (3.106)$$

The airgap self-inductance is defined as the flux $\phi_{gA,n}^a(t)$ linked by phase A divided by its current $I_A(t)$.

$$L_g^a = Z \sum_{n=1}^Q S_{1n} \frac{\phi_{gA,n}^a(t)}{I_A(t)} = Z^2 \frac{\mu_0 L_e 2\pi R_s}{\delta} \sum_{n=1}^Q S_{1n} \left(S_{1n} - \frac{1}{Q} \sum_{l=1}^Q S_{1l} \right). \quad (3.107)$$

It is possible to generalize the result obtained in order to calculate the flux generated by phase A and linked by any other phase, obtaining the mutual inductance. In this case, the mutual inductance is equal to

$$M_g = Z \sum_{n=1}^Q S_{2n} \frac{\phi_{gA,n}^a(t)}{I_A(t)} = Z^2 \frac{\mu_0 L_e 2\pi R_s}{\delta} \sum_{n=1}^Q S_{2n} \left(S_{1n} - \frac{1}{Q} \sum_{l=1}^Q S_{1l} \right). \quad (3.108)$$

Thus, the total airgap inductance is

$$L_g = Z \sum_{n=1}^Q (S_{1n} - S_{2n}) \frac{\phi_{gA,n}^a(t)}{I_A(t)} = Z^2 \frac{\mu_0 L_e 2\pi R_s}{\delta} \sum_{n=1}^Q (S_{1n} - S_{2n}) \left(S_{1n} - \frac{1}{Q} \sum_{l=1}^Q S_{1l} \right). \quad (3.109)$$

The method introduced above assumes that the airgap effective length (δ) is constant along the tangential direction. However, δ depends on the tangential coordinate θ due to the existence of stator slotting. In many PMSM the effect of the slots in the airgap inductance cannot be neglected without considerable accuracy loss.

In [Rodríguez 2013] the slot correction factor defined in (3.33) is used in order to take into account that dependence. Therefore $\delta(\theta)$ is defined as

$$\delta(\theta) = g(\theta) + \frac{l_m}{\mu_r} \quad (3.110)$$

and (3.109) can be rewritten as

$$L_g = Z \sum_{n=1}^Q (S_{1n} - S_{2n}) \frac{\phi_{gA,n}^a(t)}{I_A(t)} = Z^2 \frac{\mu_0 L_e 2\pi R_s}{Q} \int_{-\theta_s}^{\theta_s} \frac{1}{\delta(\theta)} d\theta \sum_{n=1}^Q (S_{1n} - S_{2n}) \left(S_{1n} - \frac{1}{Q} \sum_{l=1}^Q S_{1l} \right). \quad (3.111)$$

Due to the better results achieved and the negligible increase in the computation time, (3.111) is preferred to (3.109), so it will be used in the present work.

3.4.1.2 Slot Inductance

The coils generate a magnetic field not only in the airgap and in the ferromagnetic cores but also in the same slots where they are wound. Since a magnetic field exists in the slots air and copper, a non-negligible inductance will appear, especially in the slots openings which offers a low reluctance flux path.

This inductance presents a high dependence of the winding type, single or double layer, so the two configurations will be separately studied. Figure 3.21 shows the typical slot for both winding options.

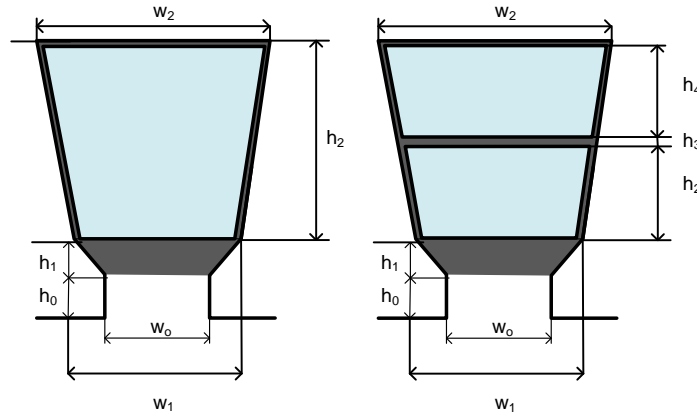


Figure 3.21. Example of the two main cases of slot windings types.

An analytic model could be performed assuming the next approximations:

- It is supposed linear slot geometry (uniform slot), so the radial coordinate will be assimilated to the x-axis, and the tangential one will be projected on the y-axis (see Figure 3.21).
- It is supposed that the magnetic intensity field (\mathbf{H}) only has y-directed component but it only varies with x.
- As far as the ferromagnetic material is infinitely permeable, the flux lines are straight and perpendicular to the slots edges. \mathbf{H} is considered to be null inside the ferromagnetic core.

Taking these approaches into account the magnetic field intensity vector in a single layer slot is equal to:

$$H_y(x) = \begin{cases} \frac{ZI}{w_s} \frac{x}{h_2} & x \leq h_2 \\ \frac{ZI}{w_s + (w_0 - w_s)(x - h_2)/h_1} & h_2 \leq x \leq h_1 + h_2 \\ \frac{ZI}{w_0} & h_1 + h_2 \leq x \leq h_0 + h_1 + h_2 \end{cases} \quad (3.112)$$

where H_y is the y-directed component of \mathbf{H} , w_s is the slot width, w_0 is the slot opening (in meters), h_2 the effective slot height, h_1 and h_0 the slots opening heights and I the current flowing through it.

The inductance can be calculated using its relation with the magnetic energy stored in the slot:

$$\frac{1}{2} L_s I^2 = \frac{1}{2} \mu_0 \int_V H(x)^2 dV \quad (3.113)$$

where L_s is the inductance due to a single slot and V is the slot total volume. Equation (3.113) yields

$$L_s = \mu_0 Z^2 L_{Fe} \left[\frac{h_2}{3w_s} + \frac{h_1}{w_s - w_0} \ln \left(\frac{w_s}{w_0} \right) + \frac{h_0}{w_0} \right]. \quad (3.114)$$

It should be noticed that the main component of L_s is generally provided by the slot opening, due to the low value of w_0 .

The same calculus can be performed in a double layer configuration. In the simple case shown in Figure 3.21 H_y will be given by:

$$H_y(x) = \begin{cases} \frac{ZI_u}{w_s} \frac{x}{h_4} & x \leq h_4 \\ \frac{ZI_u}{w_s} & h_4 \leq x \leq \sum_{i=3}^4 h_i \\ \frac{ZI_u}{w_s} + \frac{ZI_d}{w_s} \frac{(x - \sum_{i=3}^4 h_i)}{h_2} & \sum_{i=3}^4 h_i \leq x \leq \sum_{i=2}^4 h_i \\ \frac{Z(I_u + I_d)}{w_s + (w_0 - w_s)(x - \sum_{i=2}^4 h_i)/h_1} & \sum_{i=2}^4 h_i \leq x \leq \sum_{i=1}^4 h_i \\ \frac{Z(I_u + I_d)}{w_0} & \sum_{i=1}^4 h_i \leq x \leq \sum_{i=0}^4 h_i \end{cases} \quad (3.115)$$

where I_u and I_d are the current flowing through the coils in the “up” and in the “down” positions. A typical $H_y(x)$ form when $I_u = I_d$ is shown in Figure 3.22.

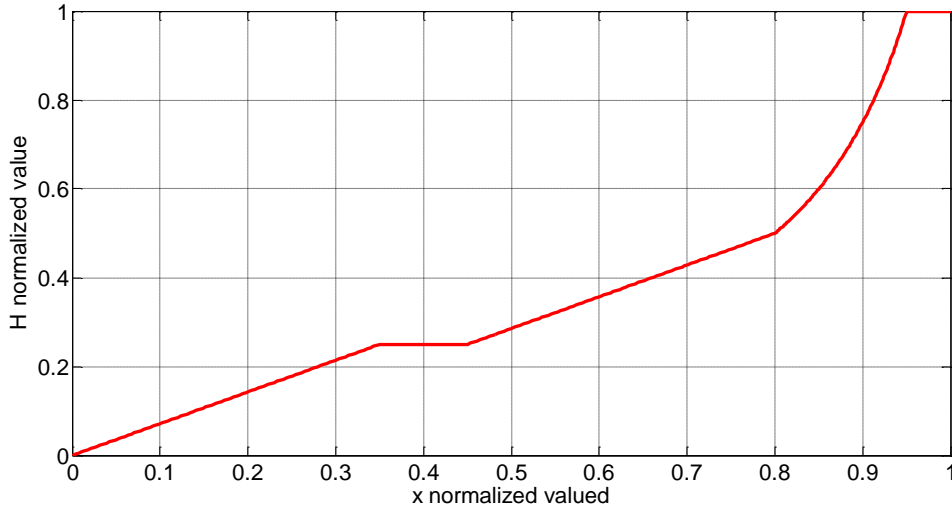


Figure 3.22. Example of magnetic field intensity due to armature reaction.

It is clear that, as far as two different coils are wound in the same slot not one but three different inductances will appear: the self-inductance of the “up” coil (L_{su}), the self-inductance of the “down” coil (L_{sd}) and the mutual inductance (L_{sm}). It is important to notice that these self-inductances are not equal, as far as the geometrical situation of the coils is not the same.

The three inductances can be deduced from a magnetic energy balance:

$$\frac{1}{2}L_{su}I_u^2 + \frac{1}{2}L_{sd}I_d^2 + L_{sm}I_uI_d = \frac{1}{2}\mu_0 \int_V H(x)^2 dV. \quad (3.116)$$

Replacing equation (3.115) in (3.116) the following expressions are obtained:

$$L_{su} = \mu_0 L_{Fe} Z^2 \left(\frac{h_4}{3w_s} + \frac{h_2+h_3}{w_s} + \frac{h_1}{w_s - w_0} \ln \left(\frac{w_s}{w_0} \right) + \frac{h_0}{w_0} \right), \quad (3.117)$$

$$L_{sd} = \mu_0 L_{Fe} Z^2 \left(\frac{h_2}{3w_s} + \frac{h_1}{w_s - w_0} \ln \left(\frac{w_s}{w_0} \right) + \frac{h_0}{w_0} \right), \quad (3.118)$$

$$L_{sm} = \left(\frac{h_2}{2w_s} + \frac{h_1}{w_s - w_0} \ln \left(\frac{w_s}{w_0} \right) + \frac{h_0}{w_0} \right). \quad (3.119)$$

There exists a huge amount of slot geometries with their own analytical approximations, the most important are included in [Pyrhönen 2008]. Since the most common slot geometry is the non-uniform one (a slot which area increases with the radius), Table 3.2 is included in order to show the associated slot inductance for the main slot geometries.

Once a single slot inductance has been obtained the total slot inductance in the PMSM ($L_{\sigma s}$) should be deduced. In the case of a single layer machine it is quite straightforward to deduce

$$L_{\sigma s} = \frac{Q}{m} L_s, \quad (3.120)$$

where L_s is chosen depending on the slot geometry (see Table 3.3).

The case of a double layer machine can be much more complicated since the number of slots shared with the other phases and the slot region occupied by the phase coils must be taken into account in order to obtain $L_{\sigma s}$. Thus, each case has to be analyzed independently.

However, in the particular case of a three-phase machine wound in the star of slots it is possible to find an empirical rule in order to obtain $L_{\sigma s}$. As far as this type of winding is the most common, this approach will be used.

It should be noticed that, in every winding periodicity there are exactly three slots in which two different phase coils are employed. Moreover, these slots are equally spaced and wound according to Table 3.2.

Table 3.2. Two phases slots distribution in a thriphasic PMSM

	Slot 1	Slot 2	Slot 3
Up region	Phase A ⁺	Phase B ⁺	Phase C ⁺
Down region	Phase C ⁻	Phase A ⁻	Phase B ⁻

Table 3.3. Classification of the PMSM design proposals found in the literature.

Type	Geometry	Inductance
Single layer, uniform		$L_s = \mu_0 Z^2 L_{Fe} \left[\frac{h_2}{3w_s} + \frac{h_1}{w_s - w_0} \ln \left(\frac{w_s}{w_0} \right) + \frac{h_0}{w_0} \right] \quad (3.121)$
Single layer, no-uniform		$L_s = \mu_0 Z^2 L_{Fe} \left[\frac{h_2 K_w}{3w_2} + \frac{h_1}{w_2 - w_0} \ln \left(\frac{w_2}{w_0} \right) + \frac{h_0}{w_0} \right] \quad (3.122)$ $K_w = 3 \frac{4c^2 - c^4(3 - 4 \ln(c)) - 1}{4(c^2 - 1)^2(c - 1)} \quad (3.123)$ $c = w_1/w_2 \quad (3.124)$
Double layer, uniform		$L_{su} = \mu_0 L_{Fe} Z^2 \left(\frac{h_4}{3w_s} + \frac{h_2 + h_3}{w_s} + \frac{h_1}{w_s - w_0} \ln \left(\frac{w_s}{w_0} \right) + \frac{h_0}{w_0} \right) \quad (3.125)$ $L_{sd} = \mu_0 L_{Fe} Z^2 \left(\frac{h_2}{3w_s} + \frac{h_1}{w_s - w_0} \ln \left(\frac{w_s}{w_0} \right) + \frac{h_0}{w_0} \right) \quad (3.126)$ $L_{sm} = \left(\frac{h_2}{2w_s} + \frac{h_1}{w_s - w_0} \ln \left(\frac{w_s}{w_0} \right) + \frac{h_0}{w_0} \right) \quad (3.127)$
Double layer, no-uniform		$L_{su} = \mu_0 L_{Fe} Z^2 \left(\frac{h_4 K_{wu}}{3w_3} + \frac{h_2 + h_3}{w_2} + \frac{h_1}{w_2 - w_0} \ln \left(\frac{w_2}{w_0} \right) + \frac{h_0}{w_0} \right) \quad (3.128)$ $L_{sd} = \mu_0 L_{Fe} Z^2 \left(\frac{h_2 K_{wd}}{3w_2} + \frac{h_1}{w_2 - w_0} \ln \left(\frac{w_2}{w_0} \right) + \frac{h_0}{w_0} \right) \quad (3.129)$ $L_{sm} = \left(\frac{h_2 K_{wd}}{2w_2} + \frac{h_1}{w_2 - w_0} \ln \left(\frac{w_2}{w_0} \right) + \frac{h_0}{w_0} \right) \quad (3.130)$ $K_{wu} = 3 \frac{4c_u^2 - c_u^4(3 - 4 \ln(c_u)) - 1}{4(c_u^2 - 1)^2(c_u - 1)} \quad (3.131)$ $K_{wd} = 3 \frac{4c_d^2 - c_d^4(3 - 4 \ln(c_d)) - 1}{4(c_d^2 - 1)^2(c_d - 1)} \quad (3.132)$ $c_u = w_2/w_3 \quad (3.133)$ $c_d = w_1/w_2 \quad (3.134)$

An important advantage of that configuration is that all the phases see the same inductance, as far as they have the same number of coils wound in the upper and in the lower region of the slot.

Thus, taking this fact into account the total inductance will be given by

$$L_{\sigma s} = \left(\frac{2Q}{3} - 2t_p \right) L_s + t_p (L_{su} + L_{sd} + L_{sm}), \quad (3.135)$$

where L_s is chosen from $L_{\sigma s}$ depending on the slot geometry.

3.4.1.3 End-Winding Inductance

The coils have a part that goes through the core following its axial direction, this region is where the EMF is generated. In order to do so, another coil region is necessary to connect an axial section with the next one, this region is called the end-winding. Figure 3.23 shows the end-winding in yellow, while the stator core is painted in red.

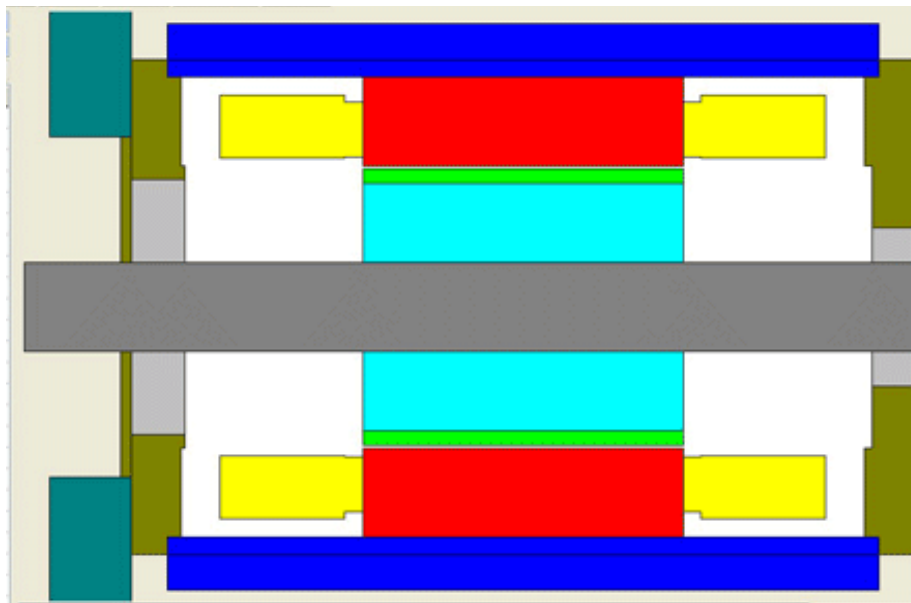


Figure 3.23. Axial cut of a PMSM generated with MotorCAD®.

The end-winding region presents its own inductance as far as a flux is generated by the current flowing through it, see Figure 3.24 (a).

The real end-winding geometry is unknown due to the uncertainties related with its real form and the randomness of the wires distribution, emplaced during the manufacturing process. In this context, the estimation of the end-winding induction is a very difficult task. Fortunately, as far as the end-winding region is formed by non-magnetic materials, the inductance is generally one order of magnitude below the slot and airgap ones, so a very rough estimation is enough in order to perform an initial design sizing.

In order to model the end-winding geometry, some authors approximate the coil by a straight line linked with the stator by two arcs [Almandoz 2008, Pyrhönen 2008], while others authors model the end-winding like a single circumferential arc [Hanselman 2012]. In this work, the model proposed by [Hanselman 2012] will be used and the coil geometry shown in Figure 3.24 (b) will be adopted.

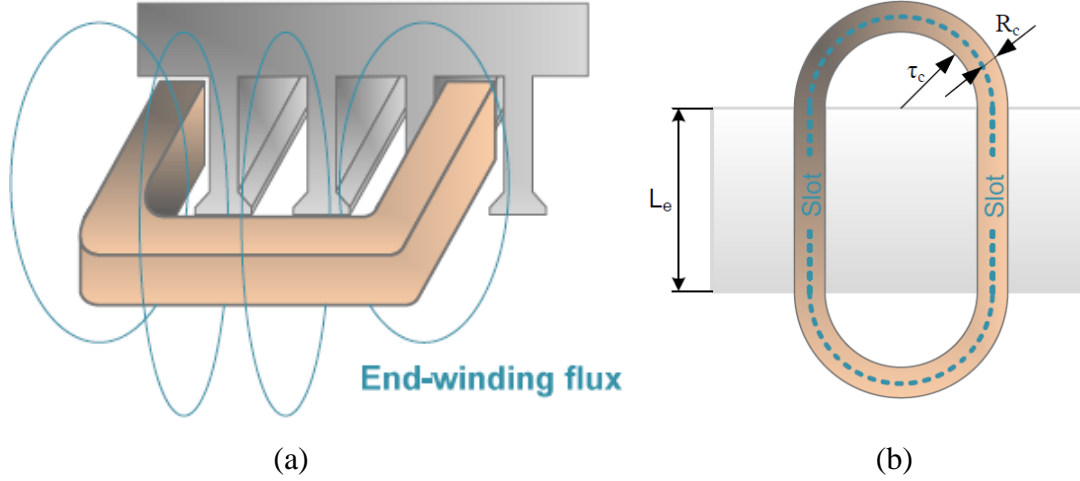


Figure 3.24. (a) Flux generated in the end-winding region, (b) Top view of a coil inserted in the stator slots.

The coils crossing the end-winding from a slot to another are modelled like a single wire with radius R_c following a circumference with radius τ_c (see Figure 3.24 (b)). R_c is estimated from the copper area of an individual wire (A_{Cu}) by

$$R_c = \sqrt{\frac{Z A_{Cu}}{\pi}} = \sqrt{\frac{A_s F_f}{\pi N_{lay}}}, \quad (3.136)$$

where A_s is the slot cross-sectional area and F_f is the fill factor, defined as the ratio between A_s and the total copper area in a slot. Generally the fill factor is imposed by manufacturing limitations and geometric reasons, as far as a rectangular slot cannot be completely filled with circular wires. F_f typical values are about 0.4 or 0.5.

The inductance L generated by a straight wire of finite length (l) and radius R_c could be approximated by [Hanselman 2012]:

$$L = \frac{\mu_0 l Z^2}{2\pi} \ln\left(\frac{l/\pi}{R_c}\right). \quad (3.137)$$

In the proposed problem l is equal to $\pi\tau_c$ with τ_c equal to half the mean coil pitch (τ_{cp})

$$\tau_c = \tau_{cp}/2, \quad (3.138)$$

so the total end-winding inductance is

$$L_{\sigma e} = \frac{QN_{lay}}{m} \frac{\mu_0 \tau_{cp} Z^2}{4} \ln\left(\frac{\tau_{cp}}{2R_c}\right), \quad (3.139)$$

where the factor QN_{lay}/m represents the total end-winding coils in one phase.

It is important to notice the meaning of τ_{cp} as the mean coil pitch. It can be calculated as

$$\tau_{cp} = \frac{1}{QN_{lay}} \sum_{l=1}^{QN_{lay}} |inL(l) - outL(l)| \theta_s R_s. \quad (3.140)$$

The aforementioned estimations are very rough as far as they are based in geometrical approximations that could be quite far from the real end-winding distribution. Moreover, between different phases magnetic coupling can arise, generating mutual inductances which value strongly depends on the random coil distribution. In spite of that it is supposed that the proposed calculus is enough accurate in order to estimate an approximate value of the end-winding inductance.

3.4.2 PMSM resistance

3.4.2.1 Copper resistance

Every material presents an opposition to the current flowing through it; this physical property is called electrical resistance. Conducting materials, such as copper and silver, present a low resistance. The copper resistance in an electrical machine is generally undesired, because it generates losses proportional to the squared flowing current.

In this section the total winding resistance will be estimated taking into account the resistance behaviour with respect to both thermal and frequency phenomena.

The copper wire area can be estimated as

$$A_{Cu} = \frac{F_r A_r}{Z N_{lay}}. \quad (3.141)$$

If the wires have circular section, their diameter is

$$d_{Cu} = 2 \sqrt{\frac{A_{Cu}}{\pi}} = 2 \sqrt{\frac{F_r A_r}{Z N_{lay} \pi}}. \quad (3.142)$$

The mean wire length per turn in a phase can be estimated from the total stator axial length (L_{Fe}) and the mean coil pitch in the end-winding (τ_{cp}):

$$L_{wire} = 2(L_{Fe} + \pi \tau_{cp}/2), \quad (3.143)$$

so the total wire length in a phase is the mean wire length per turn multiplied by the number of turns:

$$L_{phase} = Z \frac{Q N_{lay}}{2m} L_{wire}. \quad (3.144)$$

Therefore, the resistance seen by the circuit represented in Figure 3.18 by a direct current (DC) at 20°C is

$$R_{DC,20^\circ} = \rho_{Cu,20^\circ} \frac{L_{phase}}{A_{Cu}}, \quad (3.145)$$

where $\rho_{Cu,20^\circ}$ is the copper resistivity at 20°C.

It is typical to assume that the resistivity has a lineal dependence with the temperature on a wide range of temperatures:

$$\rho_{Cu} = \rho_{Cu,20^\circ}(1 + \alpha_t(T_{Cu} - 293.15K)), \quad (3.146)$$

$$R_{DC} = R_{DC,20^\circ}(1 + \alpha_t(T_{Cu} - 293.15K)). \quad (3.147)$$

where ρ_{Cu} is the copper resistivity at temperature T_{Cu} measured in Kelvin degrees while α_t is the copper thermal coefficient generally assumed to be $\alpha_t = 0.0039K^{-1}$.

Another important resistance dependence is with respect to the current frequency. Two physical phenomena cause resistance variation with frequency: the skin effect and the proximity effect.

- The skin effect is caused by the Faraday's law, if the currents have high frequency, the temporal derivative of the magnetic field generated is high, so a voltage which opposes that change will appear inside the wire. This voltage directs the current to the conductor surface, avoiding its centre. The global effect is that the effective conductor cross-section is smaller than the physical one and, therefore, its resistance is higher.
- The proximity effect is equally caused by the Faraday's law but, in this case, the magnetic field is generated by a wire in the neighbourhood of the considered one. If both coils have currents flowing in opposite directions the density current is higher close to the other conductor, while if the current is flowing in the same directions the density current is higher in the surface far from the other wire.

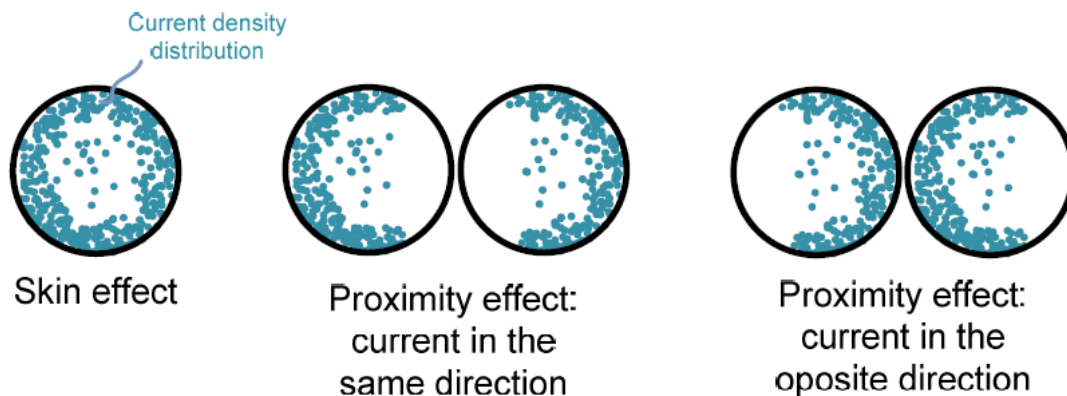


Figure 3.25. Graphic representations of the skin effect and the proximity effect.

The frequency effects in coils have been widely studied in both, rotatory and static electrical machines [Villar 2010, Hanselman 2012] here the main results will be presented.

Within a slot, the wire distribution shown in Figure 3.26 is supposed, where n_d is the number of coils uprightly distributed (in the case shown in Figure 3.26 $n_d = 4$).

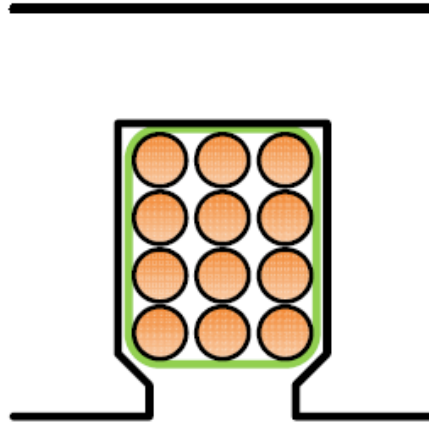


Figure 3.26. Wires distribution within a slot.

For each positive frequency the skin depth δ_k , is defined as the distance where the density current is reduced at a 37% of its maximum value

$$\delta_k = \sqrt{\frac{2\rho_{Cu}}{k\omega_e\mu_{Cu}}} \quad (3.148)$$

μ_{Cu} being the copper magnetic permeance.

The resistance for each harmonic is defined as

$$R_{ph,k} = R_{DC} \left[\Delta_k F(\Delta_k) + \frac{2}{3} (n_d^2 - 1) \Delta_k G(\Delta_k) \right], \quad (3.149)$$

where $F(\Delta)$ models the skin effect and $G(\Delta)$ the proximity one. These functions are given by

$$\Delta_k = \frac{d_{Cu}}{\delta_k}, \quad (3.150)$$

$$F(\Delta) = \frac{\sinh(2\Delta_k) + \sin(2\Delta_k)}{\cosh(2\Delta_k) - \cos(2\Delta_k)}, \quad (3.151)$$

$$G(\Delta) = \frac{\sinh(\Delta_k) - \sin(\Delta_k)}{\cosh(\Delta_k) + \cos(\Delta_k)}. \quad (3.152)$$

It is important to notice that the resistance obtained is not a single value but an array with one element for each current harmonic. This must be taken into account in order to calculate the copper losses, as far as the feed current could be contaminated by non-negligible harmonics.

3.4.2.2 Iron resistance

As it was aforementioned the iron resistance is a fictitious quantity in order to take into account the magnetic iron losses in the circuit shown in Figure 3.18. This

technique is the most popular in order to include the magnetic losses in the electric analysis.

It is supposed that the temporal FS of the feed current is known, i.e. the inverter behaves as an ideal current source.

From an electric point of view all the magnetic losses, from both the ferromagnetic core and the magnets, are dissipated in R_{Fe} . Thus, the circuit can be solved as

$$R_{Fe} = \frac{m}{2(P_{Fe} + P_{mag})} \sum_{k=1}^{\infty} \left(2E_{A,k} + 2I_{SM,k}j\omega_e k(L_{\sigma s} + L_g) \right)^2, \quad (3.153)$$

where P_{Fe} and P_{mag} are, respectively, the ferromagnetic core and magnets losses, and $E_{A,k}$ and $I_{SM,k}$ are the k^{th} harmonic of the voltages and currents represented in Figure 3.18.

From the R_{Fe} value it is possible to estimate $I_{SM,k}$ as

$$I_{SM,k} = \frac{R_{Fe}I_{ph,k} - E_{A,k}}{R_{Fe} + j\omega_e k(L_{\sigma s} + L_g)}. \quad (3.154)$$

In order to solve the previous equations an iterative solution is needed, as far as the calculus of R_{Fe} requires to know the magnetic losses (P_{Fe} and P_{mag}) and these losses are I_{SM} dependant. Thus the value of R_{Fe} is needed in order to obtain them.

The proposed iterative loop is shown in Figure 3.27.

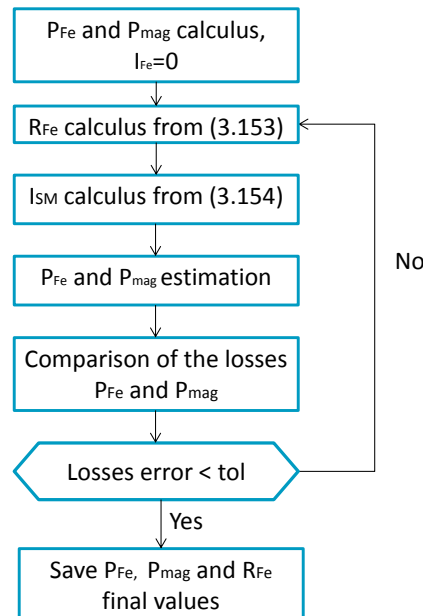


Figure 3.27. Flowchart of the R_{Fe} calculus algorithm.

If an adequate tolerance (tol) value is used (e.g. with 1% maximum error) the above algorithm converges in very few iterations as far as the initial iteration point, where the losses are estimated supposing $R_{Fe} \rightarrow \infty$ is close to the final solution.

Once R_{Fe} is obtained a complete electrical model is achieved. The calculated circuit will be used in the next chapter in order to estimate the efficiency, losses and other important parameters related with the machine behaviour and its interaction with the inverter and the supply grid.

3.5 Results and Conclusions

In order to validate the results, to reach conclusions and to evaluate the accuracy of the method, a tool based on the presented models has been programmed in Matlab® and a single layer, fractional slot, concentrate winding SPMSM design has been tested. The studied PMSM is a three-phase AC machine without neutral and presents a balanced winding spatial distribution designed according to the star of slots method. PMSM main characteristics are shown in Table 3.4. This same machine will be used in the tests for the thermal and vibratory models presented in the next chapters.

Table 3.4. PMSM main parameters.

PARAMETER	VALUE
Number of stator slots, Q	12
Number of rotor poles, $2p$	10
Number of phases, m	3
Rotational speed, n	2650 rpm
Number of conductors per slot, Z	75
Phase rms current, I_{rms}	15 A _{eff}
Rated output power, P_{out}	29.2 kW
Effective length, L_e	120 mm
Stator exterior radius, R_{se}	155.0 mm
Stator inner radius, R_s	90.0 mm
Shaft radius, R_{shaft}	35.6 mm
Airgap length, g	1.0 mm
Magnets height, l_m	6.0 mm
Tooth height, h_t	36.7 mm
Tooth width, w_t	32.0 mm
Tooth-tip height, h_0	2.5 mm
Slots opening, w_0	3.8 mm
Magnets pitch, α_p	0.15π rad

Figure 3.27, Figure 3.28 and Figure 3.29 show the magnetic flux density in the airgap caused by the rotor magnets, the armature reaction and the sum of both contributions. A comparison between the developed analytical model and commercial FEM software (Flux2D®) has been included.

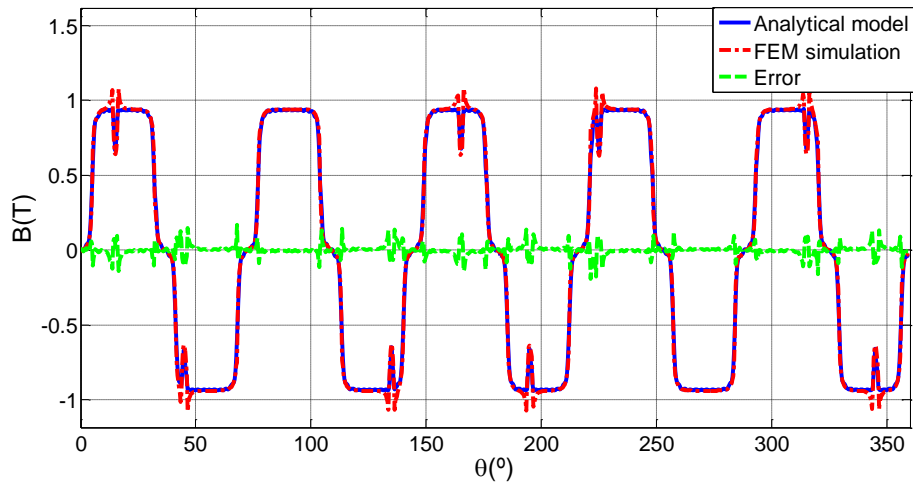


Figure 3.28. Rotor flux density in the airgap at a time instant.

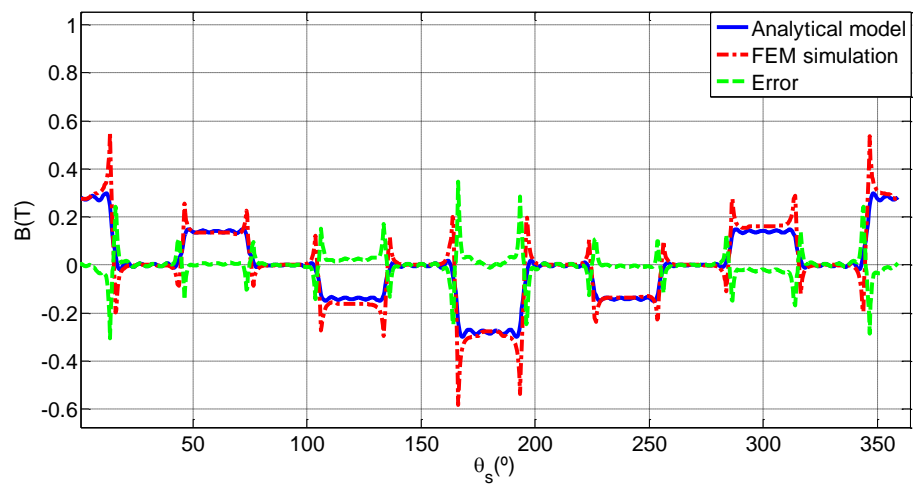


Figure 3.29. Armature reaction in the airgap at a time instant.

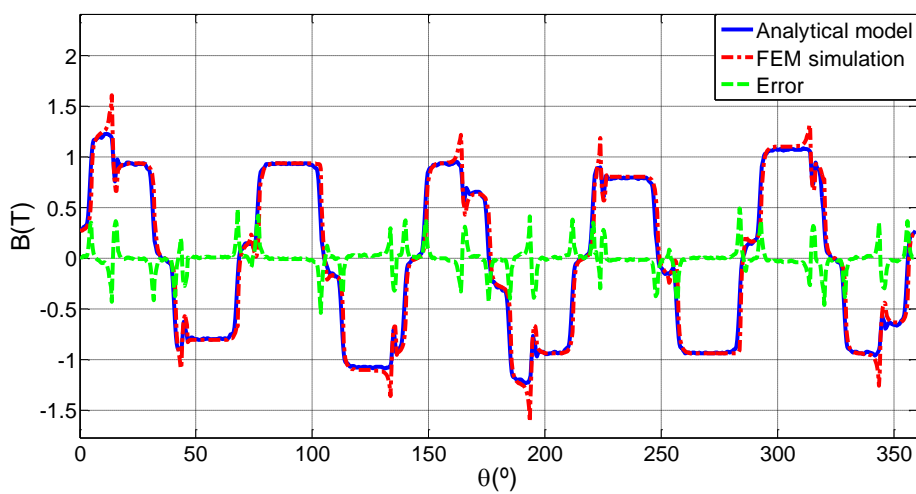


Figure 3.30. Total flux density in the airgap at a time instant.

Some important conclusions can be achieved from the previous graphics; the most important one is the high accuracy of the proposed model when the magnetic cores

are unsaturated; the only distorting effect is produced at both sides of a slot opening, due to the concentration of flux in this concrete regions. The chosen model does not take into account this phenomenon so it is incapable to model it properly.

These slight errors are not critical since the integral calculus nature of the EMF and the electromagnetic torque greatly reduce them, as it is shown in Figure 3.31 and Figure 3.32. Moreover, the mean mutual torque (i.e. the PMSM effective torque) is equal to 108.37 Nm in both, the analytical models and the FEM simulation.

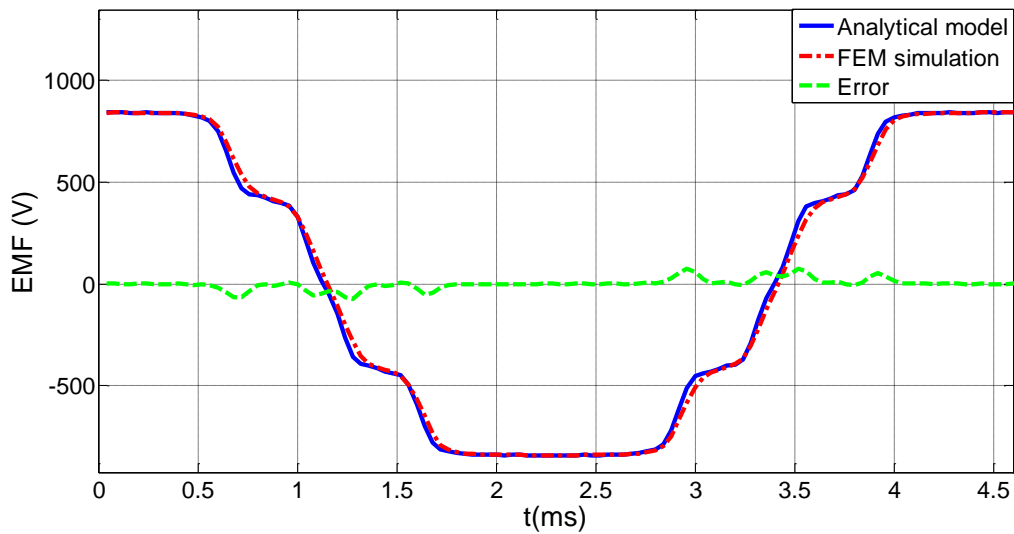


Figure 3.31. EMF induced by the magnets in phase A.

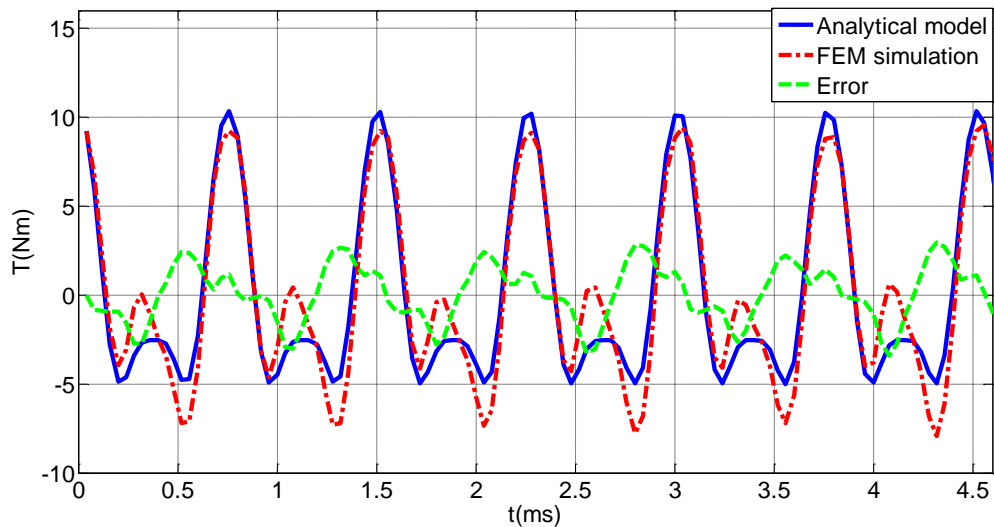


Figure 3.32. Mutual torque ripple

The cogging torque calculated by the analytical model is also very similar to the one simulated by FEM but, since the estimation was rougher, the error is higher than in the flux and EMF calculus.

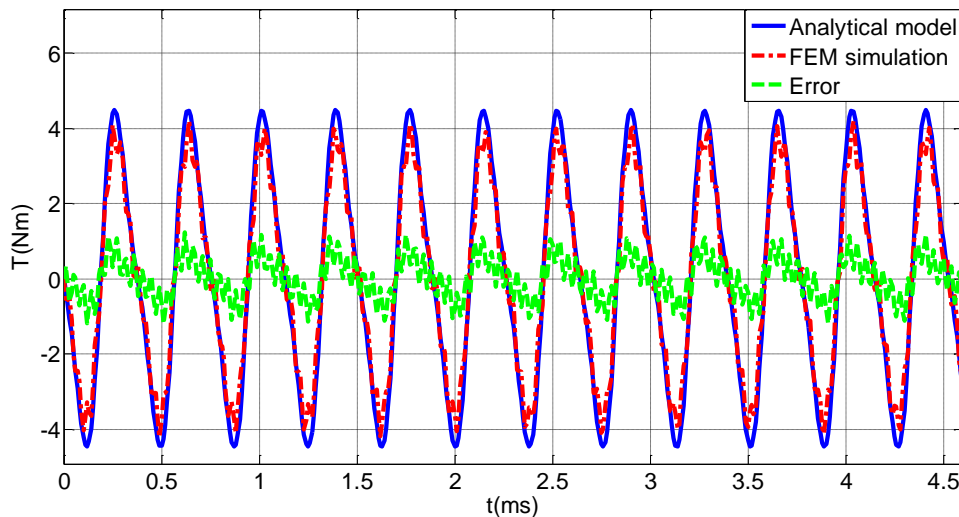


Figure 3.33. Cogging torque

The airgap and the slot inductance calculus can be validated by FEM, by means of an estimation of the inductance from the FEM-simulated energy stored in the airgap and in the slots. However, the resistance and the end-winding inductance cannot be obtained from FEM simulations, since the end-winding regions geometry still unknown and practical measured are necessary in order to obtain these data in a specific machine prototype. The achieved results are included in Table 3.5.

Table 3.5. PMSM calculated resistance and inductance

PARAMETER	ANALYTICAL MODEL	FEM RESULTS
Self airgap inductance, L_g^a	10.9 mH	12.5 mH
Mutual airgap inductance, M_g	0.0 mH	0.0 mH
Slot inductance, $L_{\sigma s}$	5.1 mH	6.3 mH
End-winding inductance, $L_{\sigma e}$	0.4 mH	-
Copper DC resistance, R_{DC}	0.71 Ω	-
Iron resistance, R_{Fe}	1270 Ω	-

The main conclusion that can be achieved is the high accuracy and speed of computation of the magnetic models. The electric ones are able to provide a first approximation of the inductance value but with less accuracy than the magnetic ones, may be due to the more rough geometrical approximations.

The shown results prove the suitability of those models for the development of a fast, accurate, modular and optimized design methodology.

4

Efficiency and Losses Estimation

In this chapter the circuit shown in Figure 3.18 will be solved and the PMSM losses estimated in order to obtain the PMSM figures of merit, such as its efficiency, power factor, electric loading or the total electrical and mechanical power.

4.1 Copper and Iron Losses

In order to obtain the copper losses, the converter and the grid are modelled as an ideal current source, whose temporal FS is equal to:

$$I_{ph}(t) = \sum_{k=-\infty}^{\infty} I_{ph,k} e^{jk\omega_e t}. \quad (4.1)$$

Applying the superposition principle, the mean copper losses due to the Joule effect will be equal to:

$$P_{Cu} = 2m \sum_{k=1}^{\infty} |I_{ph,k}|^2 R_{ph,k}, \quad (4.2)$$

where $R_{ph,k}$ is calculated according to (3.149).

The iron losses are induced by the temporal dependence of the magnetic field in the ferromagnetic core. An accurate estimation of these losses is not an easy task, as far as they are caused by many physical phenomena within the microscopic ferromagnetic core structure.

It is well known that the rotor iron losses are negligible in PMSM, because the magnetic field is rotating in synchronism with the rotor [Hanselman 2012], so the rotor core sees a quasi-steady magnetic field and the losses generated are neglected for the sake of calculus efficiency. However, rotor losses can play a major role in the magnets heating so their consequences will be studied in a subsequent section.

The stator losses will be estimated using the classical Bertotti's approach [Bertotti 1988] which classifies them in three main contributions:

- **Eddy current losses:** due to the voltages induced in the iron by means of the Faraday's law. The voltages generate Foucault (or eddy) currents causing losses in the ferromagnetic material.
- **Hysteresis losses:** due to the energy necessary to orientate the magnetic domains within the core. They are associated with the material hysteresis loop, as far as the amount of energy needed to magnetize a material is proportional to the area enclosed by its BH curve.
- **Additional losses (or excess eddy current losses):** extra losses generated in the material due to the magnetic intensity temporal variation. Some authors propose that they are caused by new magnetic fields induced by the eddy currents.

An integrated formula taking into account all these phenomena in a laminated core for sinusoidal magnetic excitation is introduced in [Chen 2002].

$$P_{Fe} = M_{Fe} \left(k_h f_e B_{pk}^{\alpha_h} + k_e f_e^2 B_{pk}^2 + k_a f_e^{1.5} B_{pk}^{1.5} \right), \quad (4.3)$$

where P_{Fe} are the total iron losses, M_{Fe} the ferromagnetic material weight, f_e the magnetic field frequency (i.e. the electrical frequency) and B_{pk} is the flux density peak value. Coefficients α_h , k_h , k_e and k_a depend on the core material. In the presented model they are calculated from the manufacturer datasheet by the least square method. In (4.3) the first term represents the hysteresis losses, the second the eddy current ones and the third the additional ones.

It is possible to extend (4.3) for a generic flux density waveform:

$$P_{Fe} = M_{Fe} \left(k_h f_e B_{pk}^{\alpha_h} + \frac{k_e}{2\pi^2} \left\langle \left| \frac{dB}{dt} \right|^2 \right\rangle + \frac{k_a}{8.763} \left\langle \left| \frac{dB}{dt} \right|^{1.5} \right\rangle \right), \quad (4.4)$$

where $\langle A \rangle$ denotes the mean value of the variable A during a period.

In order to perform the iron losses, the stator core is divided in two regions: the teeth and the yoke, the density flux in these regions have been previously calculated, the expressions of their temporal FS were presented in equations (3.75) and (3.77), respectively. The iron losses are equal to:

$$P_{Fet} = M_{Fet} \left(k_h f_e B_{tpk}^{\alpha_h} + \frac{k_e}{2\pi^2} \left\langle \left| \frac{dB_t}{dt} \right|^2 \right\rangle + \frac{k_a}{8.763} \left\langle \left| \frac{dB_t}{dt} \right|^{1.5} \right\rangle \right), \quad (4.5)$$

$$P_{Fey} = M_{Fey} \left(k_h f_e B_{ypk}^{\alpha_h} + \frac{k_e}{2\pi^2} \left\langle \left| \frac{dB_y}{dt} \right|^2 \right\rangle + \frac{k_a}{8.763} \left\langle \left| \frac{dB_y}{dt} \right|^{1.5} \right\rangle \right), \quad (4.6)$$

$$P_{Fe} = P_{Fet} + P_{Fey}, \quad (4.7)$$

where B_t and B_y are the magnetic fields in the teeth and in the yoke, respectively. It is important to notice that the amplitude of these fields, and even their waveforms, change in each stator teeth and yoke section, due the armature reaction. In spite of that fact, these variations are neglected and the iron losses are estimated from the calculus of the most saturated teeth and yoke section.

The teeth and yoke total mass (M_{Fet} and M_{Fey}) are calculated from the stator geometrical dimensions:

$$M_{Fet} = \Delta_{Fe} Q h_t w_t L_e \quad (4.8)$$

$$M_{Fey} = \Delta_{Fe} L_e w_{sy} \pi (2R_{se} - w_{sy}) \quad (4.9)$$

where Δ_{Fe} is the stator core density and R_{se} the external stator radius.

4.2 Magnet losses

As it was previously introduced the rotor losses are not important in terms of the total energy consumption, so they can be neglected in the efficiency calculus. However, an important part of these losses are concentrated in the magnets, causing their heating and, in most severe cases, leading to permanent demagnetization.

In this section an approach in order to take into account the magnet losses caused by the MMF temporal and spatial harmonics will be presented. A more detailed study, including the stator slotting effect and a validation example was previously presented in [Rodríguez 2014-b].

In the proposed model, in addition to the general approximations explained in 1.3, the following assumptions are made:

1. The PMSM is a polyphase AC machine with balanced winding distribution.
2. For the sake of simplicity, only the radial component of the magnetic induction in the magnets is taken into account. The induction is supposed to be constant along the radial dimension of the magnet, so the eddy currents too. This leads to a simple model without significant loss of accuracy in most of the PMSMs of practical interest.
3. The problem is considered resistance-limited; i.e. the magnetic reaction of eddy current is neglected.
4. Magnets end-effect is supposed to be negligible in the problem formulation. It will be taken into account in the final result with a 2-D to 3-D correction factor.
5. The magnets are supposed to be homogenous and isotropic with electrical conductivity σ_m and relative magnetic permeability μ_r .

4.2.1 Eddy Current Loss Estimation Method

The study starts with Faraday's equation and the Ohm's law:

$$\nabla \times \mathbf{E} = -\frac{\partial \mathbf{B}}{\partial t}, \quad (4.10)$$

$$\mathbf{J} = \sigma_m \mathbf{E}, \quad (4.11)$$

where \mathbf{B} , \mathbf{E} and \mathbf{J} are the magnetic flux density, electric field strength and current density vectors, respectively. A graphical representation of the basic study geometry is shown in Figure 4.1.

If the PMSM axial dimension (in the z-axis) is much longer than its magnet pitch (the magnet radius by the magnet arch, $R_m \cdot \alpha_p$), i.e. the length of the magnet is much higher than its width, a 2-D approximation can be used and the Stoke's theorem leads to

$$\int_{z=0}^{l_m} \mathbf{E} \, dr = - \int_{\theta_R=\theta_0}^{\theta_0+\alpha_p} \int_{z=0}^{l_m} \frac{\partial B_g^a(t, \theta_R)}{\partial t} r d\theta_R dr \quad (4.12)$$

where r , z and θ_R are the radial, the axial and the circumferential coordinates of the cylindrical system with respect to the rotor frame, l_m is one magnet axial length, and θ_0 is an arbitrary rotor position where a magnet are emplaced for $t = 0$.

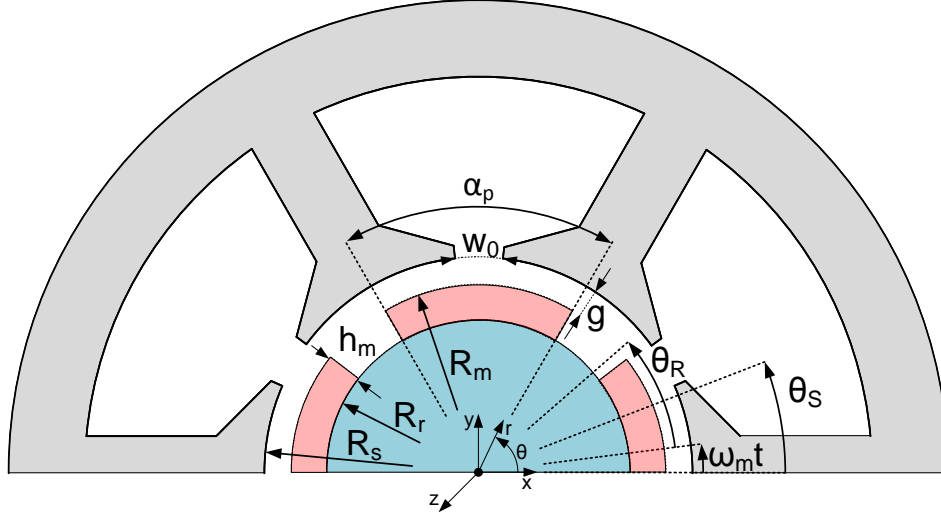


Figure 4.1. 2-D section of the PMSM geometry under study. Both angular references respect to the stator and the rotor have been included.

If the simplified magnet geometry shown in Figure 4.2 is assumed together with the approximations previously made, equations (4.11) and (4.12) can be combined leading to [Madina 2011]:

$$J_z(t, \theta_R) = -\sigma_m \int_{\theta_R} \frac{\partial B_g^a(t, \theta_R)}{\partial t} r \, d\theta_R + C(t), \quad (4.13)$$

where J_z is the axial component of the eddy current (the only considered not negligible), $B_g^a(t, \theta_R)$ is the radial component of the armature reaction with respect to the rotor frame (thus, the main cause of rotor losses) and $C(t)$ is an integration constant which ensures that the total current in a magnet is 0 at any moment, i.e.:

$$\int_{\theta_R=\theta_0}^{\theta_0+\alpha_p} J_z(t, \theta_R) r \, d\theta_R = 0 \quad \forall t. \quad (4.14)$$

Once the current have been obtained the next step is to calculate the mean power dissipated in the magnets which is

$$P_{\text{mag}} = 2 f_e K_{3D} l_m \int_{t=0}^{p/f_e} \int_{\theta_R=\theta_0}^{\theta_0+\alpha_p} \int_{r=R_r}^{R_m} \frac{J_z^2(t, \theta_R)}{\sigma_m} r \, dr \, d\theta_R dt. \quad (4.15)$$

where P_{mag} is the main power dissipated by the magnets and K_{3D} is a correction factor proposed by [Ruoho 2009] which takes into account the end-effects and the axial segmentation of the magnets:

$$K_{3D} = N_{\text{mag}} \frac{3}{4} \frac{l_m^2}{w^2 + l_m^2}, \quad (4.16)$$

where N_{mag} is the number of magnet slices in the axial direction and w is the equivalent width of the magnet, i.e.:

$$N_{\text{mag}} = L_{\text{Fe}}/l_m, \quad (4.17)$$

$$w = \alpha_p(R_m + R_r)/2, \quad (4.18)$$

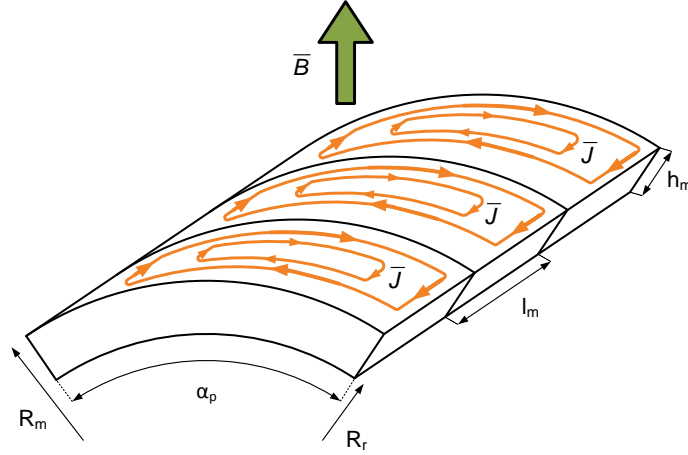


Figure 4.2. One pole geometry with three axial slices, eddy current paths are represented.

Equations (4.13)-(4.16) completely describe the calculus of eddy current losses, only two variables need to be obtained in order to fulfil the analysis. The first one is the derivative of the magnetic induction with respect to time and mainly depends on the armature reaction MMF; the second one is the integration constant which mainly depends on the magnet pitch.

The full process implemented in order to obtain these two critical variables is described below.

4.2.2 Magnetic Induction in the Rotor Frame

It is well known that the main cause of eddy-current losses in the magnets is the MMF spatial and temporal harmonics which are not in synchronism with the rotor. An expression for $B_g^a(t, \theta)$ referred to the stator frame was previously obtained in (3.64), the final results will be included for the sake of clarity.

$$B_g^a(\theta, t) = \frac{\mu_0}{\delta} \sum_{k=-\infty}^{\infty} \sum_{l=-\infty}^{\infty} \left(1 + 2 \cos\left(\frac{2\pi(k+l)}{m}\right) \right) F_{A,k} I_{A,l} e^{j(kt_p\theta + l\omega_e t)}, \quad (4.19)$$

where phase A is assumed to be the temporal angular reference so its angle is taken equal to 0 rad. It is important to notice that the harmonics in (4.19) are only different from 0 when the sum $k + l$ is a multiple of m .

It is quite clear that, in the rotor frame, the circumferential coordinate θ is given by

$$\theta = \theta_R + \omega_m t, \quad (4.20)$$

where θ_R is the tangential coordinate referred to the rotor frame and ω_m the mechanical angular speed, related with the electrical pulsation by

$$\omega_m = \omega_e / p. \quad (4.21)$$

It is quite straightforward to refer the armature reaction to the rotor frame by replacing (4.21) in (4.19):

$$B_g^a(\theta_R, t) = \frac{\mu_0}{\delta} \sum_{k=-\infty}^{\infty} \sum_{l=-\infty}^{\infty} (1 + 2\cos(2\pi(k+l)/m)) e^{j(kt_p\theta_R)} F_{A,k} I_{A,l} e^{j\omega_m t(kt_p+lp)}, \quad (4.22)$$

where $B_g^a(\theta_R, t)$ is the radial component of the armature reaction with respect to the rotor frame. The temporal derivative of the armature reaction can be obtained from (4.22) as

$$\frac{\partial B_g^a(\theta_R, t)}{\partial t} = j\omega_m \sum_{k=-\infty}^{\infty} \sum_{l=-\infty}^{\infty} (kt_p + lp) B_{g,kl}^a e^{j\omega_m t(kt_p+lp)}, \quad (4.23)$$

where $B_{g,kl}^a$ is seen as a multivariable Fourier coefficient given by

$$B_{g,kl}^a = \frac{\mu_0}{\delta} j\omega_m (1 + 2\cos(2\pi(k+l)/m)) e^{j(kt_p\theta_R)} F_{A,k} I_{A,l}. \quad (4.24)$$

This general formulation allows us a simple, precise calculus of the temporal derivative of the armature reaction field in the rotor. An especially important case arises when the PMSM current is considered perfectly sinusoidal, i.e.

$$I_{A,l} = 0 \Leftrightarrow l \neq \pm 1 \quad (4.25)$$

This assumption yields a great simplification of (4.22) into

$$B_g^a(\theta_R, t) = \frac{3\mu_0}{2\delta} I_{A,1} \left(\sum_{k=[\dots-1,2,4,\dots]}^{\infty} F_{A,k} e^{jkt_p\theta_R} e^{j\omega_m t(kt_p+p)} + \sum_{k=[\dots-2,1,4,\dots]}^{\infty} F_{A,k} e^{jkt_p\theta_R} e^{j\omega_m t(kt_p-p)} \right), \quad (4.26)$$

where $I_{A,1}$ is the only term in the current temporal Fourier series and it is equal to the half of the peak value of phase A feed current. The transformation of (4.22) into (4.26) and its implications are fully included in [Rodríguez 2014-b].

4.2.3 Total Current Density in the Magnets

Once the temporal derivative of the magnetic induction has been estimated, the next step is the calculus of the total current density in the magnets, where from (4.13) and (4.14)

$$\int_{-\alpha_p/2}^{\alpha_p/2} \left(-\sigma_m \int_{\theta_R} \frac{\partial B_g^a(t, \theta_R)}{\partial t} R_m d\theta_R + C(t) \right) d\theta_R = 0. \quad (4.27)$$

Direct inspection of (4.23) shows that the derivative term can be expressed as a spatial Fourier series with respect to the rotor angular coordinate θ_R as follows:

$$\frac{\partial B_g^a(t, \theta_R)}{\partial t} = \sum_{k=-\infty}^{\infty} B'_k(t) e^{jk\theta_R}, \quad (4.28)$$

where $B'_k(t)$ is a t dependent spatial Fourier index given by

$$B'_k(t) = j\omega_m \sum_{l=-\infty}^{\infty} (kt_p + lp) j\omega_m \left(1 + 2 \cos\left(\frac{2\pi(k+l)}{m}\right) \right) F_{A,k} I_{A,l} e^{j\omega_m t(kt_p + lp)}. \quad (4.29)$$

By direct integration of (4.27) we get

$$C(t) = -\frac{\sigma_m R_m}{\alpha_p} 2 \sum_{k=-\infty}^{\infty} j \frac{B'_k(t)}{k^2} \sin(k\alpha_p/2). \quad (4.30)$$

Thus, the complete expression of the current density in the magnets is

$$J_z(t, \theta_R) = \sigma_m R_m j \sum_{k=-\infty}^{\infty} \frac{B'_k(t)}{k} \left(e^{jk\theta_R} - \text{sinc}(k\alpha_p/2) \right). \quad (4.31)$$

These calculations can be directly used in (4.15) in order to obtain the mean power dissipated in the magnets. Notice that the properties of the Fourier series can be applied in the resolution of the temporal integral, while the spatial one (with respect to θ_R) can be solved numerically. Figure 4.3 shows a typical eddy current distribution over a magnet; the numerical simulation was made with the commercial software FLUX2D®.

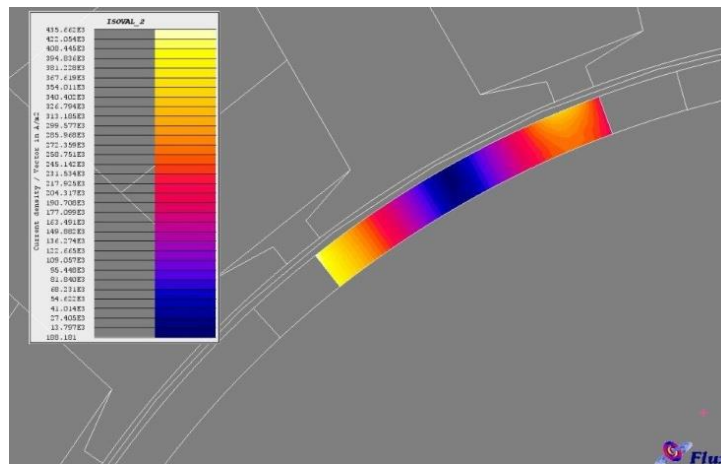


Figure 4.3. Current density in one of the magnets. Current is nearly constant in r

4.3 Efficiency and other Quality Parameters

In order to accurately estimate the efficiency and other critical quality parameters, such as power factor, the equivalent PMSM circuit must be solved. For the sake of completeness, the circuit schematic is included in Figure 4.4.

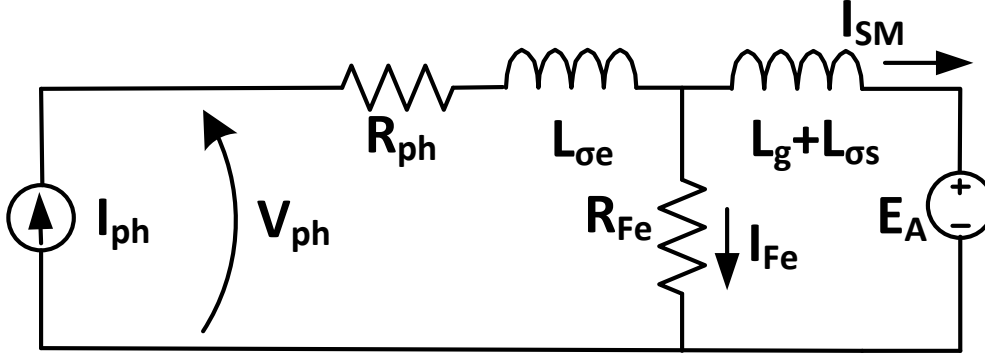


Figure 4.4. Phase A PMSM electric model.

The impedance value was calculated in Chapter 3, while I_{ph} is considered as a sinusoid, polluted with harmonics, but with a known amplitude and delay with respect to the EMF (E_A), i.e. it is supposed that the PMSM control system is fast and accurate enough for correctly provide the needed current supply.

Thus, in order to solve the circuit, the values of V_{ph} and I_{SM} should be obtained. It must be taken into account that the circuit values are frequency dependant so a phasor analysis will be performed.

The temporal FS of V_{ph} and I_{SM} are respectively given by

$$I_{SM,k} = \frac{I_{ph,k} R_{Fe} + E_{A,k}}{jk\omega_e(L_g + L_{\sigma s}) + R_{Fe}}, \quad (4.32)$$

$$V_{ph,k} = (R_{ph} + jk\omega_e L_{\sigma e})I_{ph,k} + jk\omega_e(L_g + L_{\sigma s})I_{SM,k} + E_{A,k}. \quad (4.33)$$

The study below will be perform, without loss of generality, supposing PMSM generator operation.

4.3.1 Power, Torque and Efficiency

The mean electrical output power is

$$P_{elec} = 2m \sum_{k=1}^{\infty} \text{real}(V_{ph,k} I_{ph,k}^*), \quad (4.34)$$

where $I_{ph,1}^*$ denotes the conjugate of $I_{ph,1}$. The total mechanical power in the shaft is

$$P_{mec} = \omega_m \bar{T}, \quad (4.35)$$

where \bar{T} is the mean torque developed by the PMSM.

From a power balance it is possible to obtain the temporal values of the torque, namely,

$$T(t) = \sum_{s=1}^m E_{A,s}(t)I_{SM,s}(t) + P_{ad}, \quad (4.36)$$

where $T(t)$ is the instantaneous torque, $E_{A,s}(t)$ and $I_{SM,s}(t)$ are the EMF and machine current in phase s and P_{ad} is an estimation of the mechanical losses caused by the friction in the bearings and other moving parts. In [Almandoz 2008] these losses are estimated as

$$P_{ad} = K_{ad}M_{rotor}\omega, \quad (4.37)$$

where ω is the rotation speed in revolutions per minute, M_{rotor} the total rotor mass and K_{ad} is an experimental coefficient which value is close to $1.5 \cdot 10^{-3}$.

Thus, the efficiency (η) will be defined as

$$\eta = \frac{P_{elec}}{P_{mec}} \quad (4.38)$$

or, equivalently,

$$\eta = \frac{P_{elec}}{P_{elec} + P_{Fe} + P_{Cu} + P_{ad}}. \quad (4.39)$$

4.3.2 Electric Quality Parameters

Other important quality parameters are related with the power factor (pf), i.e. the delay between the main harmonics of the feed voltage and the feed current.

$$pf = \cos(\varphi) \quad (4.40)$$

where φ is the leading angle of the voltage with respect to the current. A high power factor absolute value is generally preferred, since it permits to generate the same amount of power with less current flowing through the wires, leading to a saving of both, losses and copper material.

The pf calculus in the phasor theory requires the definition of the concepts of real, apparent and reactive powers. The apparent power provided by the grid (S) is defined as

$$S = 2mV_{ph,1}I_{ph,1}^*. \quad (4.41)$$

The real (P_s) and the reactive (Q_s) power are defined as the real and the imaginary part of S , respectively, i.e.

$$P_s = 2m \operatorname{real}(V_{ph,1}I_{ph,1}^*), \quad (4.42)$$

$$Q_s = 2m \operatorname{imag}(V_{ph,1}I_{ph,1}^*). \quad (4.43)$$

It is important to notice that P_s is just the mean power provided by the main harmonic of the electric supply. Once S is defined, the pf is obtained as

$$\text{pf} = \frac{P_s}{|S|}. \quad (4.44)$$

Other interesting quality parameter is the electrical load (q_e), which relates the machine heating in relation with the copper losses. This value is useful in a first part of the design stage in order to obtain a rough estimation of the machine dimensions. The electrical load is equal to

$$q_e = \frac{N_{\text{lay}} Q Z |I_{\text{ph},1}|}{2 \pi R_s}. \quad (4.45)$$

It should be noticed that both, the power factor and the electric load, are interesting figures of merit in order to be included as restrictions in the optimization loop.

4.4 Results and Conclusions

Previous equations will be used in order to obtain the efficiency and other quality parameters of the test PMSM.

Unfortunately circuit resolution cannot be compared with FEM results, as far as many of its parameters, such as end-winding inductance and copper resistance, cannot be accurately estimated in FEM simulations, not even in a 3D one. Thus, many parameters, such as efficiency or power factor are only calculated by the presented analytical model, Table 4.1 shows the achieved results.

Table 4.1. PMSM quality parameters

PARAMETER	ANALYTICAL MODEL	FEM RESULTS
Stator teeth losses $P_{\text{Fe,t}}$	770 W	771 W
Stator yoke losses, $P_{\text{Fe,y}}$	558 W	549 W
Copper losses, P_{Cu}	478 W	-
Mechanical losses, P_{ad}	81 W	-
Input mechanical power, P_{mec}	31.10 kW	-
Output electrical power, P_{elec}	29.21 kW	-
Power factor, pf	-0.88	-
Electrical load, q_e	93.93%	-

The results previously presented are expected to have high accuracy but experimental measures are necessary in order to validate it. A complete comparison with measured data will be included in the final version of this thesis.

5

Thermal Approach

As it was aforementioned, a proper thermal modelling of the PMSM is critical because of the great influence of the temperature on the machine performance and its operation life. The losses generated in both, the ferromagnetic cores and the stator winding give rise to heat, this heat is transfer to the housing and, through it, to the ambient surrounding the machine. A steady state temperature is reached when the amount of heat generated by the losses is in equilibrium with the thermal energy transferred to the ambient.

In an electrical machine, the generated heat is critical since a high temperature can shorten its operation life or even cause irreversible damage in the wires insulation or in the magnets. Thus, during the design stage, it is mandatory to obtain a reliable thermal model in order to predict both, the PMSM thermal behaviour and the coupling between the thermal and electromagnetic models. A complete small lumped thermal circuit is proposed and fully explained in the present chapter, including its correct coupling with the electromagnetic models.

5.1 Heat Transfer: Basic Principles

As it is well known the heat is transferred from hot to cold bodies, in opposite direction to thermal gradient. Three physical heat transfer modes are well established and studied: conduction, convection and radiation.

A complete thermal model should take into account these three processes. In this section a brief introduction to them and their major implication will be presented. For a more detailed description many undergraduate handbooks, such as [John 2003], are available.

5.1.1 Conduction

Conduction is a heat transfer mechanism consisting in the propagation of kinetic energy from warm molecules (which vibrate fast) to cool ones (with slower vibrations). The random collisions between fast and slow molecules cause kinetic energy transmission and tend to equalize their temperatures.

Conduction is produced in solid, liquid and gaseous materials, but it is especially important in the former since it is the state of matter where the molecules are closer to each other, so their collisions are more frequent and the heat transmission faster. In fluids this heat propagation is slower due to their more disperse molecular configurations.

The equation governing conduction heat transfer is the Fourier's law which states: *"The heat flux resulting from thermal conduction is proportional to the magnitude of the temperature gradient and opposite to its sign"*. Thus, from the energy conservation principle it is possible to deduce the following partial differential equation:

$$\rho c \frac{\partial T}{\partial t} = \frac{\partial}{\partial x} \left(\lambda_x \frac{\partial T}{\partial x} \right) + \frac{\partial}{\partial y} \left(\lambda_y \frac{\partial T}{\partial y} \right) + \frac{\partial}{\partial z} \left(\lambda_z \frac{\partial T}{\partial z} \right) + Q \quad (5.1)$$

where T is the temperature, t is the time, (x, y, z) are the Cartesian coordinates, $(\lambda_x, \lambda_y, \lambda_z)$ are the material thermal conductivities along the three coordinate directions, Q is the rate of heat density dissipated in the medium, c is the material specific heat capacity and ρ is its density.

In many practical cases only the steady state is of interest and the heat transfer is produced just in a spatial direction, in this case (5.1) yields [John 2003]:

$$q = \lambda_x \frac{\partial T}{\partial x} \quad (5.2)$$

where q is the amount of heat flux surface density through the propagation direction x , measured in W/m^2 .

Assuming that the temperature varies linearly, (5.2) is equivalent to

$$\Delta T = \frac{P \Delta x}{\lambda_x A} \quad (5.3)$$

where P is the transmitted power, Δx the element length, ΔT the temperature difference and A the heat path cross-sectional area.

The proposed simplification is of great practical importance since it permits to perform an analogy between the electric and the thermal worlds, defining an equivalent thermal resistance (R_{th}) as

$$R_{th} = \frac{\Delta x}{\lambda_x A} \quad (5.4)$$

which yields

$$\Delta T = R_{th} P. \quad (5.5)$$

Equations (5.4) and (5.5) establish the analogy between electric and thermal circuits, where the transmitted power is seen as a current, the temperature as the voltage and the thermal resistance as the electric one.

Another important characteristic is that the defined thermal resistance is not temperature-dependant in many materials of practical interest, since in most solids λ is constant in a wide temperature range. However, the thermal conductivity of gases exhibits a remarkable temperature dependence.

5.1.2 Convection

Convection is the heat transfer through the motion of the particles of the medium. Thus, it is only produced in fluids where the particles can change their position with relative easiness.

One of the most common cases of practical interest is produced when a fluid flows over a solid at higher temperature. The heat is transferred from the solid to the surrounding fluid (or coolant) and the heated coolant is removed from the solid surface and replaced by cold fluid which restarts the process.

The fluid replacement can be caused by a natural physical process (i.e. hot air has less density than cold air, so it tends to rise and to be replaced by colder air) or it can be forced by a pump or fan. The first case is called natural convection while the second is known as forced convection.

In both cases it is supposed that, in steady state, the heat transfer from the solid to the fluid is proportional to the temperature differences between them. This empirical law is known as the Newton 's law of cooling [John 2003]:

$$q = \alpha(T_w - T_\infty), \quad (5.6)$$

where q is the amount of transmitted power by surface unit, T_w and T_∞ are the solid and the coolant temperatures, respectively, and α is the proportionality coefficient known as convection equivalent conduction coefficient. Parameter α depends on many variables, such as the system geometry, the fluid flow pattern near the solid surface, its physical features, its speed, the nature of the convection (natural or forced), etc.

The numerical values of α are usually established by empirical methods or extrapolated from previous measured prototypes. In order to apply them properly, various dimensionless parameters such as the Reynold's, Prandtl's or Nusselt's numbers are used.

From equation (5.6) it is possible to define the convection thermal resistance as:

$$R_{th} = \frac{1}{\alpha A} \quad (5.7)$$

where A is the total surface area.

5.1.3 Radiation

Because of its temperature, a physical body emits energy due to an electromagnetic radiation process. Even if the studied material is in the vacuum it emits, absorbs and transmits thermal radiation according to the Stefan-Boltzmann law, which governs the radiation heat transfer:

$$q = \sigma \varepsilon T_w^4, \quad (5.8)$$

where T_w is the body temperature, ε is the emissivity of the radiative surface (1 in the case of an ideal black body), q is the radiated power per surface unit and σ is the Stefan-Boltzmann constant ($\sigma = 5.67 \cdot 10^{-8} \text{ W}/(\text{m}^2\text{K}^4)$).

It is usually considered that, if the radiative body is surrounded by a non-participating fluid at temperature T_∞ the radiated energy radiated is given by

$$q = \sigma \varepsilon (T_w^4 - T_\infty^4). \quad (5.9)$$

In this case, the equivalent thermal resistance associated with the radiation process is given by

$$R_{th} = \frac{T_w - T_\infty}{\sigma \varepsilon (T_w^4 - T_\infty^4) A}. \quad (5.10)$$

As it can be seen, the defined thermal resistance has high temperature dependence so its proper application in an equivalent thermal circuit could be more complicated than in simpler cases, such as convection and conduction.

It must be highlighted that, in general, the radiation plays a minor role in machine heat transfer, except when the housing achieves high temperatures.

5.2 Introduction to Lumped Thermal Models

The lumped thermal model is the selected approach in order to study and implement the thermal behaviour of a PMSM. This theory is based in the division of the body under study into thermal basic elements with physical and practical relevance. Each element is represented by one or more nodes linked among them by thermal resistances. These elements are part of a grid quite similar to an electric circuit, as can be seen in Figure 5.1.

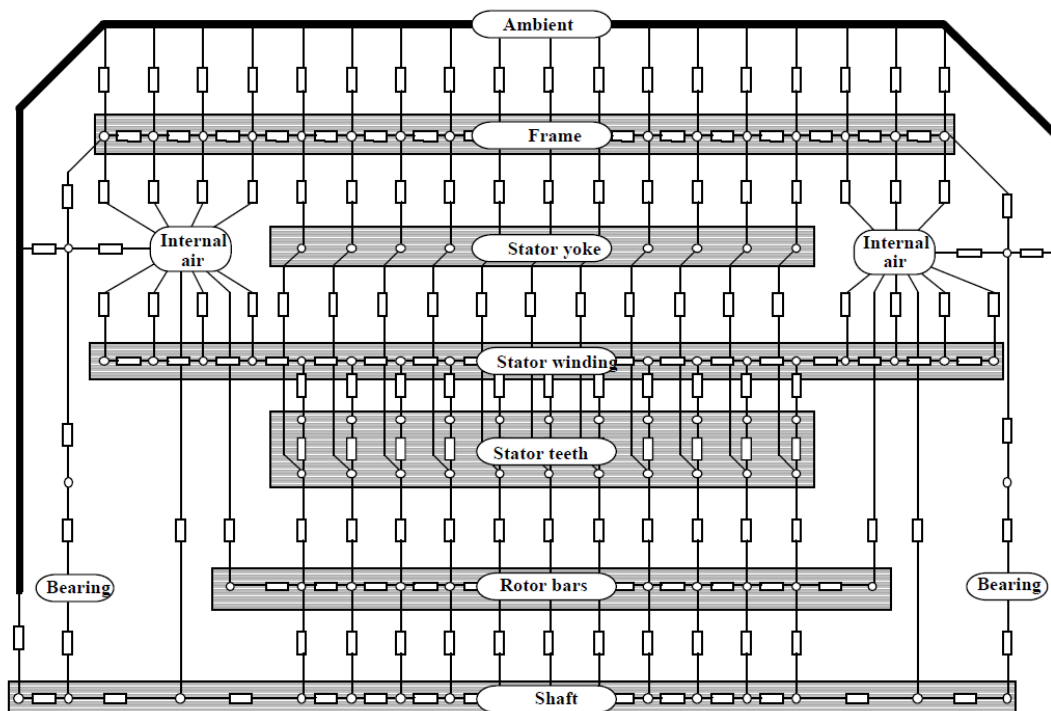


Figure 5.1. Example of an electrical machine thermal network [Kylander 1995].

The analogy between thermal and electrical circuit is shown in Table 5.1.

Table 5.1. Analogy between electrical and thermal circuit

Electrical circuit	Thermal circuit
Electric resistance (Ω)	Thermal resistance (K/W)
Current intensity (A)	Power (W)
Voltage (V)	Temperature (K)

Applying (5.5) and the Kirchhoff's current law it can be deduced that, in steady state:

$$P_i = \frac{T_i - T_{amb}}{R_{i,i}} + \sum_{j=1}^n \frac{T_i - T_j}{R_{i,j}} ; \forall i = 1, \dots, n, \quad (5.11)$$

where P_i is the power dissipated at the i -th node, T_i is its temperature, $R_{i,j}$ is the thermal resistance between nodes i and j , $R_{i,i}$ is the thermal resistance between node i and the ambient and T_{amb} is the ambient temperature selected as a reference.

It is possible to express (5.11) in matrix form:

$$\mathbf{P} = \mathbf{G}\boldsymbol{\theta}, \quad (5.12)$$

where \mathbf{P} is the dissipated power matrix, $\boldsymbol{\theta}$ is the relative temperatures matrix and \mathbf{G} is a thermal conductance matrix, i.e. in an n nodes configuration:

$$\begin{bmatrix} P_1 \\ P_2 \\ \vdots \\ P_n \end{bmatrix} = \begin{bmatrix} \sum_{i=1}^n \frac{1}{R_{1,i}} & \frac{-1}{R_{1,2}} & \dots & \frac{-1}{R_{1,n}} \\ \frac{-1}{R_{2,1}} & \sum_{i=1}^n \frac{1}{R_{2,i}} & & \frac{-1}{R_{2,n}} \\ & \vdots & \ddots & \vdots \\ \frac{-1}{R_{n,1}} & \frac{-1}{R_{n,2}} & \dots & \sum_{i=1}^n \frac{1}{R_{n,i}} \end{bmatrix} \begin{bmatrix} \theta_1 \\ \theta_2 \\ \vdots \\ \theta_n \end{bmatrix}, \quad (5.13)$$

where θ_i is the node temperature referred to the ambient, i.e.,

$$\theta_i = T_i - T_{amb}, \quad \forall i = 1, \dots, n. \quad (5.14)$$

Finally, since the dissipated power is a known variable, the system is solved just inverting the conductance matrix:

$$\boldsymbol{\theta} = \mathbf{G}^{-1}\mathbf{T}. \quad (5.15)$$

Thus, applying (5.15) it is possible to obtain the temperatures in the selected nodes from the dissipated power.

5.3 Simplified Thermal Network for a SPMSM

There exist two different approaches lumped thermal modelling of electric machines: the small or simplified thermal networks and the complete ones. Its main difference is that, in small networks, many points with similar temperatures and physical behaviour are assimilated to the same node, i.e. all teeth are represented by just one node. On the other hand, in a complete network each physical component is usually represented by several nodes in order to characterize the temperature evolution through it. A good example of complete network is shown in Figure 5.1.

Obviously, complete networks offer more information than simplified ones, but they are more time consuming and usually requires data that are not available during the design stage. Meanwhile, simplified thermal models suppose a reliable, effective and short-time consuming thermal approach [Bogglieti 2009] whose accuracy, in most cases, will be enough to estimate the temperature in some critical points of the PMSM. Many authors have proposed, with good results, a small thermal network as a suitable compromise between computation speed and accuracy [Mellor 1991, Lindström 1999].

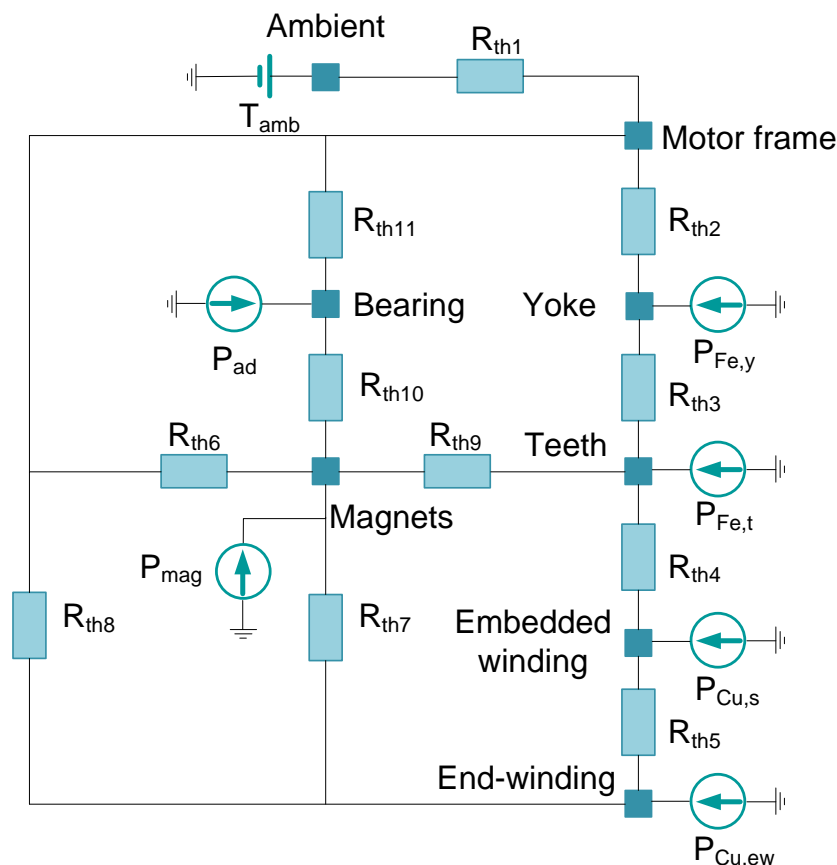


Figure 5.2. SPMSM small thermal network model proposed.

As far as it was investigated, Mellor et al. proposed the first electrical machine simplified thermal network in a foundational paper [Mellor 1991] that was used by [Kylander 1995] in order to perform two induction machine lumped thermal models: a

complete and a simplified one. Lindström particularized and complemented Kylander's model for a SPMSM [Lindström 1999], proposing the eight-node thermal network shown in Figure 5.2.

The simplified thermal network used in the present thesis is a slight modification of that proposed by [Lindström 1999], so both share the same thermal circuit shown in Figure 5.2. In this section the thermal resistance calculus proposed by [Lindström 1999] will be explained, completing its work with more recent publications where needed. The power losses, which are the thermal model main input, are obtained according to the estimations presented in Chapter 4.

It should be highlighted that the implemented thermal model is based on the main assumption that the PMSM can be seen as a group of concentric cylinders (the shaft, the magnets and the stator) through which heating is flowing in both, their axial and radial directions. The equivalent thermal resistances of the different regions will be included below.

5.3.1 Housing and Stator Yoke

The housing and the stator yoke are two of the most important elements in thermal modelling, as far as all the evacuated heat must flow through them in order to be transmitted into the surrounding air. Therefore, it is a major concern of the designer to achieve a low thermal resistance in those elements.

It is important to remark that the resistances concerning the housing and the stator yoke (R_{th1} and R_{th2} in Figure 5.2) are very difficult to estimate and rough approximations or empirical measurements are needed in order to obtain their values.

More precisely, two thermal resistances model the housing thermal behaviour: the conduction resistance and the contact resistance between the housing and the surroundings.

The contact resistance is one of the most critical in electrical machine thermal design and it strongly depends on the cooling system (natural convection, forced air, water jacket, etc.), on the specific housing and on its fins geometry (see Figure 5.3). All these complex dependences suppose that a correct estimation is very troublesome, so experimental measurements are usually required [Kylander 1995].

In [Boglietti 2008] it is proposed a "root mean squared" empirical rule in order to obtain the contact resistance between the housing and the ambient (R_0), taking into account both, natural convention and radiation processes:

$$R_0 = \frac{0.167}{A_S^{1.039}}, \quad (5.16)$$

where A_S is the total housing surface area, i.e. the sum of its lateral surfaces, the two end caps and the fins.

The experiments leading to (5.16) are made for induction motors commercial housings in a power range from 4 to 55 kW. Therefore, it can only be used as a rough estimation over this set of motor powers and sizes. The contact thermal resistance R_0 is much smaller if forced convection is used, especially if a coolant better than air (such as water) is used. In those cases a completely different approximation of R_0 is needed.

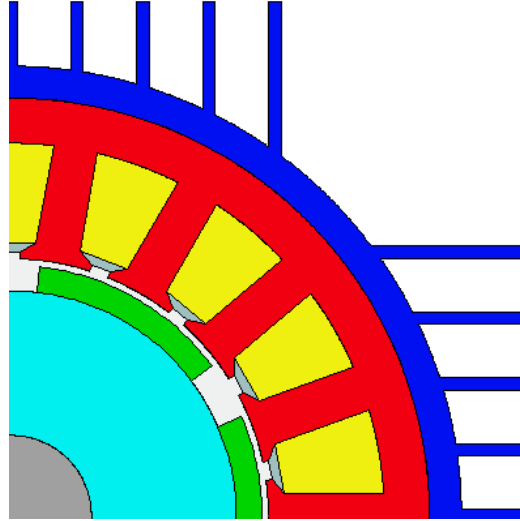


Figure 5.3. Motor 2-D section geometry. Figure from Motor-CAD®

It is supposed that the heat is transmitted radially through the housing and the stator yoke. Their conduction resistances are, generally, of small value and both are well studied since the conduction process is easier to model than the convection one.

The housing is considered as a thin cylinder with a diameter much longer than its thickness, its radial thermal resistance (R_{thfr}) can be estimated as

$$R_{thfr} = \frac{h_{fr}}{2\pi R_{se}(L_{Fe} + 2L_{ew})\lambda_{Al}}, \quad (5.17)$$

where h_{fr} is the stator thickness, L_{ew} is the end-winding length, R_{se} is the external stator radius and λ_{Al} is the thermal conductivity of the housing material, generally aluminium.

In a similar fashion, the stator yoke is modelled as a cylindrical section of a ferromagnetic material where the heat is only flowing along its radial direction. This is a good approximation since the ferromagnetic core insulation layers (used in order to limit the iron losses) are both good electric and good thermal insulator. The expression of the stator yoke thermal resistance (R_{thsy}) in the radial direction is approximated by

$$R_{thsy} = \frac{\ln(R_{se}/R_{ss})}{2\pi L_e \lambda_{Fe}}, \quad (5.18)$$

where λ_{Fe} is the ferromagnetic material conductivity, and R_{ss} the radius defined by the upper part of the stator teeth, i.e.,

$$R_{ss} = R_{se} - w_{sy}. \quad (5.19)$$

There exists a fourth resistance defining the heat flow through the stator yoke and housing: the contact resistance between these two elements (R_{thcy}). This resistance is

not null since the contact between the two surfaces is not perfect and air pockets exist. It can play a major role when R_0 has a small value due to a good refrigeration system.

Parameter R_{thcy} is very difficult to estimate, because it depends on parameters with high manufacture tolerances, such as the pressure between yoke and housing and the smoothness of their surfaces. A common approach consists in the definition of a fictitious equivalent airgap length between the two elements (g_e). Some studies estimate that the airgap is between 30 and 75 μ m in PMSM between 1.5 and 250 kW [Lindström 1999] ; [Boglietti 2008] offers a look-up table for g_e mean values.

Once a reliable approach of g_e is obtained, the equivalent R_{thcy} is given by

$$R_{thcy} = \frac{g_e}{2\pi R_{se}(L_{Fe} + 2L_{ew})\lambda_{air}} \quad (5.20)$$

where λ_{air} is the air thermal conductivity.

With the previous values calculated, the thermal resistance between the mid-point of the machine housing and the surroundings (R_{th1}) and between the housing and the mid-point of the stator yoke (R_{th2}) are given by

$$R_{th1} = \frac{R_{thfr}}{2} + R_0, \quad (5.21)$$

$$R_{th2} = \frac{R_{thys}}{2} + R_{thcy} + \frac{R_{thfr}}{2}. \quad (5.22)$$

5.3.2 Stator Teeth

All the stator teeth are represented with just one node, virtually situated in the mid-point of any of them. The total conduction thermal resistance in the radial direction is supposed to be the parallel configuration of every teeth resistance. Axial heat flow is neglected due to the low thermal conductivity of the core insulation layers.

The thermal resistance of the stator tooth (R_{tht}) is calculated by direct integration along the stator radial dimension (see Figure 5.4):

$$R_{tht} = \frac{1}{Q} \int_0^{h_s} \frac{1}{\lambda_{Fe} L_e w_t(y)} dy, \quad (5.23)$$

where y is the radial dimension variable, $w_t(y)$ is the tooth width and h_s is the total tooth height. According to the dimensions shown in Figure 5.4 the previous integral can be solved:

$$R_{tht} = \frac{1}{Q \lambda_{Fe} L_e} \left(\frac{h_0}{w_{st}} + \frac{h_2}{w_t} + \frac{h_1}{w_{st} - w_t} \ln \left(\frac{w_t}{x_{d2}} \right) \right). \quad (5.24)$$

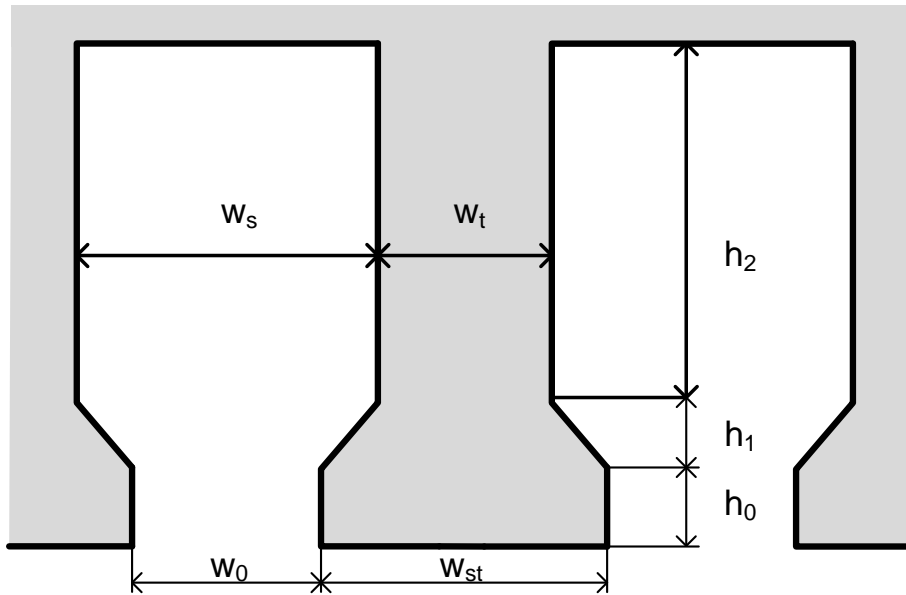


Figure 5.4. Stator teeth and slots typical geometry.

Assuming a homogeneous heat flux from the embedded coils it is possible to represent the thermal resistance between the stator yoke and the teeth midpoints (R_{th3}) as

$$R_{th3} = \frac{1}{2}(R_{tht} + R_{thsy}). \quad (5.25)$$

5.3.3 Stator Coils

The conduction resistance of the stator coils is much more difficult to model than the teeth one, because the heat flows in the three spatial directions: axial, tangential and radial. Moreover, the slot material is not isotropic, as the axial heat flux is mainly transferred through the copper to the end-winding, while the other spatial directions see an inhomogeneous material made of copper and insulation with a lower thermal conductivity.

It is quite straightforward to see that the axial heat flux is due to the heat exchange between the embedded coils and the end-windings, while the radial and tangential fluxes are related to the heat transfer to the stator yoke through the teeth. Since the wires are one of the hot spots within the machine, and due to the high dependence of their expected life with their temperature, special care is needed in order to perform a suitable thermal model.

5.3.3.1 Radial Resistance between Embedded Coils and Teeth

Most authors estimate the slot radial thermal resistance (i.e. the resistance between the slots and the teeth) through a homogenization process, i.e. supposing that the sum of the copper and the insulation behaves like a homogeneous media with a constant thermal conductivity in the radial direction (λ_{slot}).

There exist a great controversial on the accurate estimation of λ_{slot} . Most of authors try to achieve a correlation between its value and the physical thermal conductivity of the insulation material (λ_{imp}). As far as it was investigated in the literature, the first estimation of that relation appears in [Mellor 1991], which established that

$$\lambda_{\text{slot}} = 2.5\lambda_{\text{imp}} . \quad (5.26)$$

However, other authors investigated the strongly dependence between this ratio and the manufacture process used, concluding that both, the winding technique and the slot fill factor (F_f) have a great influence in this relation. [Kylander 1995] proposed the ratio between λ_{slot} and λ_{imp} shown in Figure 5.5, while a more recent publication [Boglietti 2008] estimates λ_{slot} value from experimental data regression as

$$\lambda_{\text{slot}} = 0.2425[(1 - F_f)A_s L_e]^{-0.427}, \quad (5.27)$$

where A_s is the slot cross-sectional area.

In most practical designs F_f is very close to 0.5, value where the three approaches are very close to each other. Thus, for its great simplicity, equation (5.27) will be used in this thesis.

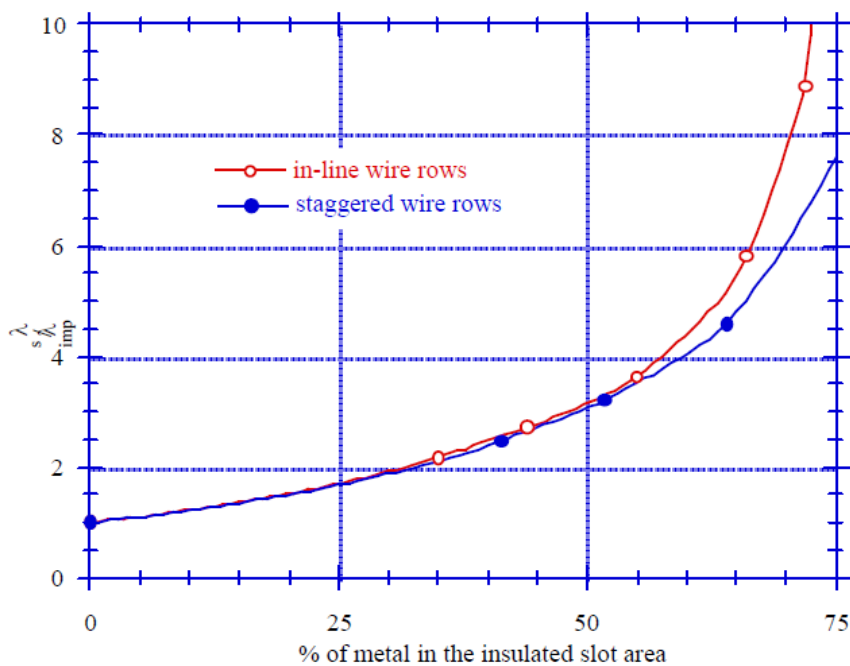


Figure 5.5. Relation between λ_{slot} and λ_{imp} as a function of the slot fill factor and the manufacture technique [Kylander 1995].

Once the equivalent slot thermal conductivity is obtained a two-dimensional heat transfer must be modelled in order to estimate the total resistance between the slot centre and the stator. The exact solution to this problem is complex and cannot be easily implemented but, if it is supposed that the heat flux in one direction is independent from the heat flux in the other direction, a separated thermal resistance in each dimension can be established. The equivalent slot geometry shown in Figure 5.6 is used in order to perform the calculus.

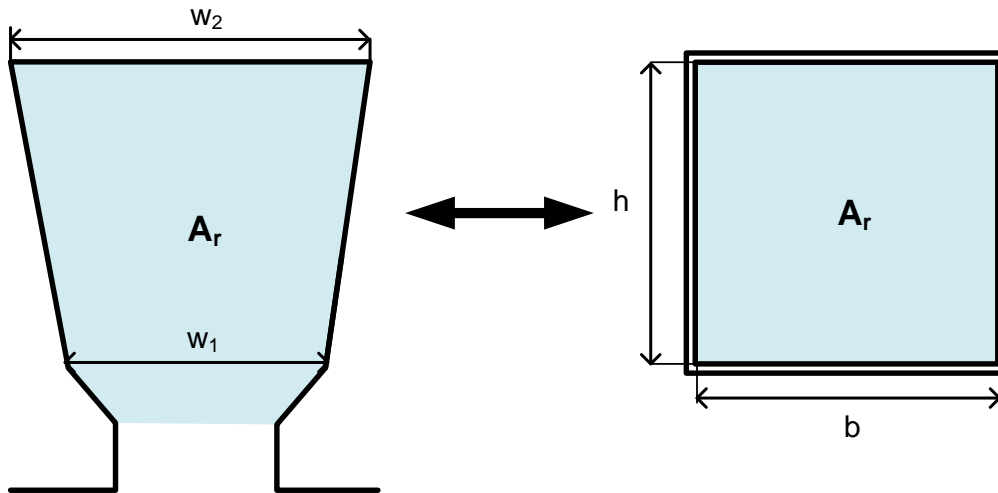


Figure 5.6. Slot geometry equivalence used in the thermal modelling [Lindström 1999].

The slot radial thermal resistance in both coordinate directions (R_{x0} and R_{y0}) is estimated as:

$$R_{x0} = \frac{b}{h\lambda_{\text{slot}}}, \quad (5.28)$$

$$R_{y0} = \frac{h}{b\lambda_{\text{slot}}}, \quad (5.29)$$

where b and h are obtained from the slot real dimensions as (see Figure 5.4):

$$b = \frac{w_1 + w_2}{2}, \quad (5.30)$$

$$h = \frac{2A_r}{w_1 + w_2}. \quad (5.31)$$

Another important contribution to the thermal resistance is the insulation layer placed between the slot and the stator. This material is an important obstacle in the heat flux path. Moreover, within the insulation, air pockets exist, so the equivalent thermal resistance in both dimensions (R_{xi} and R_{yi}) can be estimated as

$$R_{xi} = \frac{h_3}{h\lambda_{\text{imp}}} + \frac{d_{\text{air}}}{h\lambda_{\text{air}}} \quad (5.32)$$

$$R_{yi} = \frac{h_3}{b\lambda_{\text{imp}}} + \frac{d_{\text{air}}}{b\lambda_{\text{air}}} \quad (5.33)$$

where h_3 is the insulation width and d_{air} the equivalent air pocket length.

It is very difficult to obtain a reliable value of d_{air} , as it depends on random events during the manufacturing process. In [Kylander 1995] values of some tenths of millimetre (from 0.2 to 0.3 mm) are proposed.

Once the two contributions are obtained, the total thermal resistance in both directions (R_x and R_y) is calculated as

$$R_x = \frac{1}{2} \left(R_{xi} + \frac{R_{x0}}{6} \right), \quad (5.34)$$

$$R_y = \frac{1}{2} \left(R_{yi} + \frac{R_{y0}}{6} \right). \quad (5.35)$$

Finally, the total resistance between the slots and the stator teeth is estimated as [Lindström 1999]:

$$R_{th4} = \frac{R_x R_y}{Q L_e (R_x + R_y)} \left(1 - \frac{R_{x0} R_{y0}}{720 R_x R_y} \right). \quad (5.36)$$

5.3.3.2 Axial Resistance between the Embedded Coils and the End-Winding

The heat flows in the axial direction through the copper wires, since the copper is not only a good electrical conductor but also a good thermal one. The thermal connection between the midpoint of an embedded coil and the midpoint of the endwinding is represented in Figure 5.7.

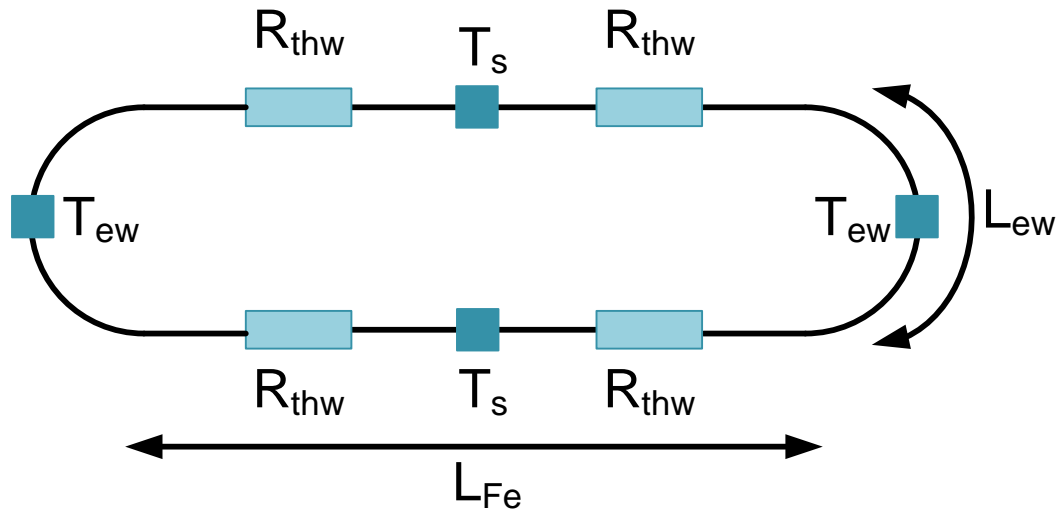


Figure 5.7. Thermal model of a coil. Adapted from [Lindström 1999].

The wire conduction resistance (R_{thw}) will be given by

$$R_{thw} = \frac{L_{Fe} + L_{ew}}{2A_{Cu}\lambda_{Cu}} = \frac{L_{Fe} + L_{ew}}{2A_s F_f \lambda_{Cu}}. \quad (5.37)$$

Supposing that all the end-windings can be represented by a single node, it can be concluded that there exists a total of $2Q$ heat flow paths between the embedded and the end-windings points, as it is graphically shown Figure 5.8.

Thus, the total thermal resistance linking the embedded coils and the end-windings is given by

$$R_{th5} = \frac{R_{thw}}{2Q}. \quad (5.38)$$

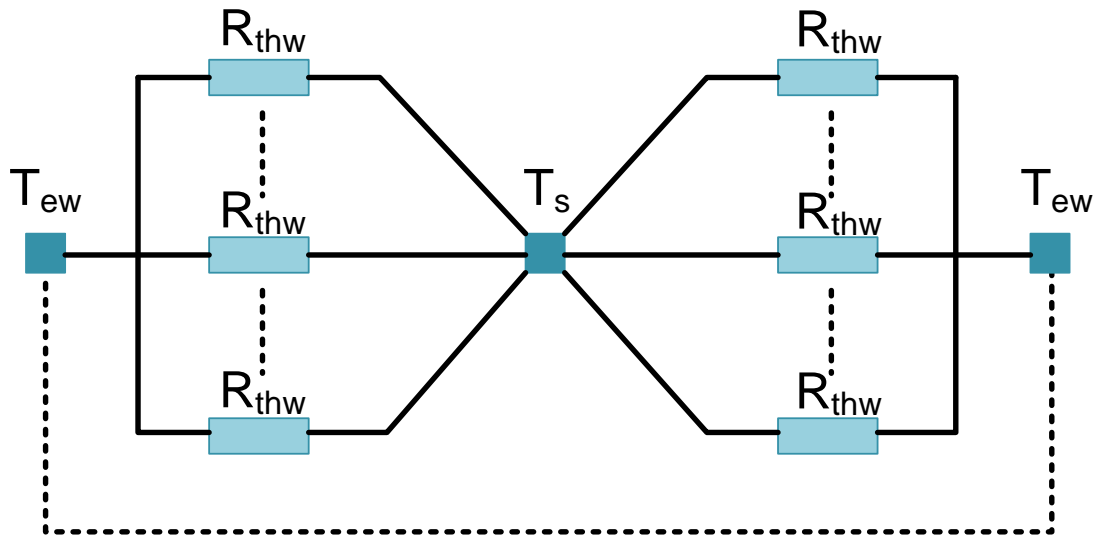


Figure 5.8. Global thermal resistance between embedded coils and end-winding Adapted from [Lindström 1999].

5.3.4 End-Winding Region

Heat transfer in the end-winding regions involves complex convection and radiation process between four main actors: the end-caps (a part of the housing), the rotor, the wires and the internal air, see Figure 5.9.

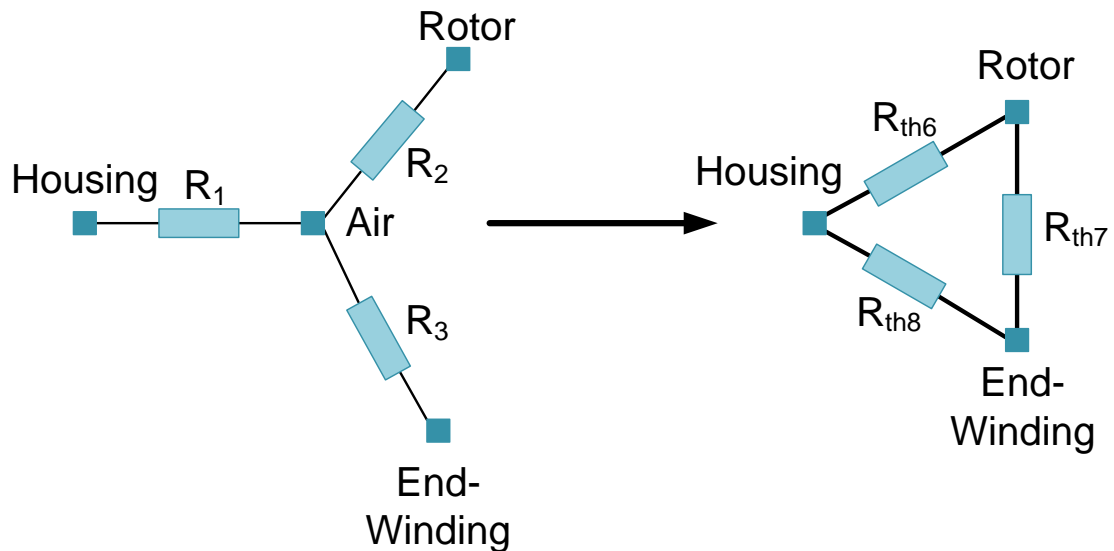


Figure 5.9. Equivalent end-wind thermal network in its Y and Δ forms. [Kylander 1995].

Since the temperatures in this region are close enough, the radiation process is neglected and only the convective terms must be taken into account. In spite of this fact, their calculation is not an easy task, because the precise geometry and the heat flux paths are still unknown. In order to calculate these coefficients the Newton's heating law is applied:

$$R_x = \frac{1}{\alpha_x A_x}, \quad (5.39)$$

where x is an index equal to 1, 2 or 3 identifying the specific thermal resistance shown in Figure 5.9, A_x is the equivalent body external surface and α_x is its convection coefficient.

A lot of works have been published in order to estimate the correct values of α_x and A_x [Mellor 1991, Kylander 1995, Saari 1998, Lindström 1999, Boglietti 2008], but the complexity and uncertainties of the geometry, the rotor motion effect and the random air flux in the end-winding region cause that only rough approximations are available. In this work the approach proposed by [Lindström 1999] will be used.

The end cap convection surface (A_1) and its convection coefficient (α_1) are approximated by

$$A_1 = 2(\pi R_{se}^2 + 2\pi R_{se} L_{ew}), \quad (5.40)$$

$$\alpha_1 = 15 + 6.75(\omega_m R_m)^{0.65}, \quad (5.41)$$

respectively, where A_1 includes all the end-winding internal housing surface, with the end-cap. It should be noticed that the $\omega_m R_r$ term is related to the rotor linear speed making the internal air flows and causing a forced convection.

The rotor and the internal end-winding air present a convection surface (A_2) and transfer coefficient (α_2) equal to:

$$A_2 = 2\pi R_r^2, \quad (5.42)$$

$$\alpha_2 = 16.5(\omega_m R_m)^{0.65}. \quad (5.43)$$

The end winding wires convection surface (A_3) is estimated as

$$A_3 = \pi L_{ew} 2(R_s + h/2), \quad (5.44)$$

where h is the total slots height. The convection heat transfer coefficient (α_3) is approximated by

$$\alpha_3 = 6.5 + 5.25(\omega_m R_m)^{0.6}. \quad (5.45)$$

Once these parameters are calculated, (5.39) is applied in order to obtain the equivalent thermal resistances.

Since the enclosed air is just a heat exchanger between other components (rotor, wires and housing), and its temperature has not real relevance, it is a common practice to eliminate its associated node through a Y- Δ conversion. This conversion is necessary in order to obtain the thermal circuit shown in Figure 5.2; the Y- Δ conversion can be found in any electric undergraduate book. The obtained resistances between the end caps, rotor and end-windings (see Figure 5.9) are equal to

$$R_{th6} = R_1 + R_2 + \frac{R_1 R_2}{R_3}, \quad (5.46)$$

$$R_{th7} = R_2 + R_3 + \frac{R_2 R_3}{R_1}, \quad (5.47)$$

$$R_{th8} = R_1 + R_3 + \frac{R_1 R_3}{R_2}. \quad (5.48)$$

5.3.5 Airgap

The airgap is the natural interface between rotor and stator both in magnetic and thermal aspects. The heating is transferred through the airgap mainly by conduction and convection processes. Usually the radiation plays a minor role in heat propagation since the rotor and the stator temperatures are relatively close to each other.

The heat transfer is quite different whether the air flux through the airgap is laminar or turbulent. In the first case the air motion is distributed in radial layers, with a decreasing speed as they approach the stator. Notice that, in a gas, heat transfer by conduction is relatively small; on the contrary, a turbulent flow supposes a forced convection process and the heat flux is enhanced.

Assuming smooth rotor and stator surfaces the critical transition between laminar and turbulent air flow is determined by Taylor's number (Ta), defined as

$$Ta = \frac{\omega_m R_s g^3}{\nu^2}, \quad (5.49)$$

where the product $\omega_m R_s$ is the peripheral air speed and ν the air kinematic viscosity.

It is generally considered that the air flow is turbulent if Ta is above a threshold of 1740 [Kylander 1995]. Following an empirical law, the Nusselt number (Nu) is obtained as

$$Nu = \begin{cases} 2 & \text{if } Ta_m < 1740 \\ 0.409 Ta_m^{0.241} - 137 Ta_m^{-0.75} & \text{if } Ta_m \geq 1740 \end{cases} \quad (5.50)$$

The heat transfer coefficient is estimated from the Nusselt number:

$$\alpha_g = \frac{Nu \lambda_{air}}{2g}. \quad (5.51)$$

Taking into account that the airgap axial heat transfer is neglected due to its low influence in the heat propagation for most of the PMSM (except for those rotating at very high speeds) the airgap thermal resistance is given by

$$R_{thg} = \frac{1}{\alpha_g 2\pi R_s L_{Fe}}. \quad (5.52)$$

5.3.6 Rotor

From a thermal point of view the rotor can be subdivided into different parts: the magnets, the ferromagnetic core, the shaft and the bearings. The most important are

the magnets, since an excessive heating can lead not only to a lower machine performance but also to their permanent demagnetization.

5.3.6.1 Magnets and ferromagnetic core

The heat flux through the magnets and the core is supposed to be completely radial, since the insulation layers greatly limit the axial flux. The conduction thermal resistance is obtained in a very similar way of that of the stator.

The core resistance is approximated by:

$$R_{thr} = \frac{\ln(R_r/R_{shaft})}{2\pi L_e \lambda_{Fe}}, \quad (5.53)$$

where R_{shaft} is the shaft radius. If the machine under study is a SPMSM the magnets thermal resistance can be modelled as a cylindrical section:

$$R_{thmag} = \frac{\ln(R_m/R_r)}{2\pi \alpha_m L_{Fe} \lambda_{mag}}, \quad (5.54)$$

where λ_{mag} is the magnets thermal conductivity and α_m is the fraction of the total cylindrical crown covered by the magnets.

Therefore, the thermal resistance between the stator teeth midpoints and the magnets midpoints (R_{th9}) is given by

$$R_{th9} = \frac{1}{2} (R_{thmag} + R_{tht}) + R_{thg}. \quad (5.55)$$

5.3.6.2 Shaft and bearings

The shaft is supposed to transmit the heat in the axial direction with a homogeneous thermal distribution, so its thermal resistance is approximated by

$$R_{thsh} = \frac{L_b}{\pi R_{shaft}^2 \lambda_{shaft}}, \quad (5.56)$$

where L_b is the distance between the shaft midpoint and the bearings and λ_{shaft} is the shaft material thermal conductivity.

The contact resistance between the shaft and the rotor (R_{thcr}) is very difficult to estimate, so it is usually neglected.

Once the heat reaches the bearings the thermal transfer is produced through the bearing balls and their contact with the internal and external races.

The bearings thermal resistance depends on their dimensions and angular speed. [Kylander 1995] proposes an empiric approach for this resistance:

$$R_{thb} = 0.45(0.12 - d_b)(33 - \omega_m d_b), \quad (5.57)$$

where d_b is the bearings diameter. The coefficients used in (5.57) are estimated from empirical measurements in two induction motors of 15 kW and 4 kW power, but significant differences may appear in other prototypes.

Two bearings (one at each end) link the housing and the bearings, so the total thermal resistance between their midpoints is given by

$$R_{th11} = \frac{R_{thb}}{4} + \frac{R_{thfr}}{2}. \quad (5.58)$$

Finally, the last thermal resistance of the lumped circuit (Figure 5.2) which is still unknown is the one linking magnets and bearings (R_{th10}). This resistance is the sum of the individual contributions of the magnets, the rotor core, the shaft and the bearings, so it can be calculated as

$$R_{th10} = \frac{R_{thmag}}{2} + R_{thr} + \frac{R_{thsh}}{2} + \frac{R_{thb}}{4}. \quad (5.59)$$

With the previous data the proposed thermal circuit can be correctly solved and the PMSM temperatures obtained. However, as it will be explained, not only the temperatures depend on the losses through the thermal circuit introduced in this chapter; reciprocally, these losses depend on the temperatures because of the thermal dependence of material physical parameters. The linked problem is solved in the next section.

5.4 Thermal-Electromagnetic Coupling

Between the many physical couplings existing in an electrical machine one of the most important is the electromagnetic-thermal one. In fact, the temperature plays a major role in two physical parameters variation: the copper resistivity and the magnet residual induction.

As it was aforementioned in 3.4.2, the copper resistivity varies with temperature according to the formula

$$\rho_{Cu} = \rho_{Cu,20^\circ} (1 + \alpha_t (T_{Cu} - 293.15K)). \quad (5.60)$$

As far as the thermal dependence is considered linear in a wide temperature range, α_t is taken as a constant equal to $\alpha_t = 0.0039 \text{ K}^{-1}$, with $\rho_{Cu,20^\circ} = 1.71 \cdot 10^{-8} \Omega m$.

In a similar way, the temperature dependence in the magnet residual induction is supposed to be linear, so it is approximated by

$$B_r = B_{r,20^\circ} (1 + \alpha_{mag} (T_{mag} - 293.15K)), \quad (5.61)$$

where $B_{r,20^\circ}$ is the magnet residual inductance at 20°C , T_{mag} is the magnet temperature and α_{mag} is the magnet thermal coefficient. $B_{r,20^\circ}$ and α_{mag} depend on the specific magnet material selected, e.g. the neodymium-boron N27H material has $\alpha_{mag} = -1.25 \cdot 10^{-3} \text{ K}^{-1}$ and $B_{r,20^\circ} = 1.04 \text{ T}$.

It is quite straight forward that the change in these physical variables directly affects the machine losses and, therefore, the temperatures.

More precisely, the copper resistance increases linearly with temperature while the current through it, determined by an external controller, is nearly constant. Hence, at high temperatures the Joule losses are incremented, enhancing the temperatures and, therefore, the electrical resistance in a vicious circle that can even damage the wires insulation.

On the other hand, higher temperatures in the magnets causes a decrease of the rotor magnetic field in the stator, decreasing both, the motor performance, the iron losses and even the magnetic forces on the cores. But, the most important thermal effect in the magnets is their possible permanent demagnetization if the Curie's temperature is reached.

The aforementioned effects have two important implications: the first one is the need to perform a carefully thermal design in order to avoid coils and magnet damage due to high temperatures. The second one is the coupling between the thermal and the electromagnetic models, as far as temperatures strongly depend on the losses and losses are a function of temperature.

In order to solve this bidirectional coupling the iterative loop shown in Figure 5.10 is used:

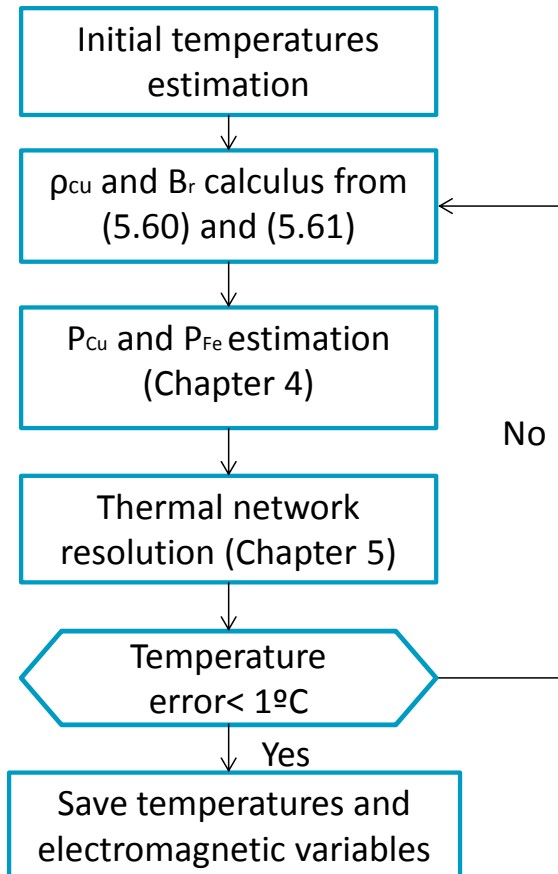


Figure 5.10. Electromagnetic-thermal coupling algorithm flowchart.

With the proposed tolerance (1°C) an accurate result and very fast convergence are achieved, usually after less than three iterations if a good initial temperature guess is selected, e.g. $T_{\text{Cu}} = 373\text{K}$ and $T_{\text{mag}} = 353\text{K}$.

5.5 Results and Conclusions

The proposed thermal network was used in order to estimate the steady state temperatures in the test PMSM.

The results obtained with this small lumped parameter model were compared with those calculated by Motor-CAD[®], a commercial software based on a complete thermal network with more nodes and an extensive library of thermal coefficients obtained during decades of experimental tests for many electrical machine technologies.

The equivalent model used by Motor-CAD[®] can be seen in Figure 5.11, and the results obtained with both approaches are in Table 5.2.

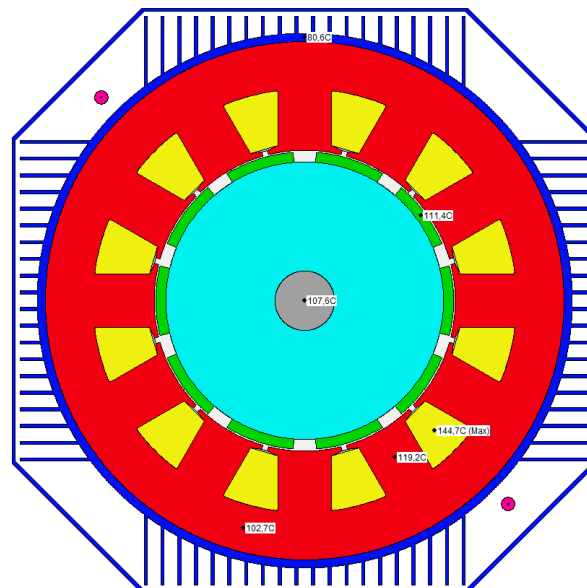


Figure 5.11. PMSM temperatures calculated by Motor-CAD[®].

Table 5.2. Estimated PMSM temperatures

MOTOR REGION	ANALYTICAL MODEL ($^{\circ}\text{C}$)	MOTOR-CAD RESULTS ($^{\circ}\text{C}$)
Ambient, T_{amb}	40.0	40.0
Frame, T_{fr}	86.6	80.6
Stator yoke, T_{sy}	98.6	102.7
Stator teeth, T_{st}	114.2	119.2
Embedded coils, T_{s}	155.4	144.7
End-winding, T_{ew}	156.1	146.2
Magnets, T_{mag}	107.4	111.4
Rotor shaft, T_{shaft}	101.3	107.6

The agreement between the commercial software and the obtained results is very good, with an error less than 11°C in all measures and a mean error of 6.5°C. It must be highlighted that, in spite of the fact that experimental measured are not available yet, Motor-CAD® are tested and recognized as a very reliable approximation to the real temperatures achieved by the PMSM during its operation.

It can be concluded that, at this stage of motor design, the proposed lumped thermal model is a fast and accurate solution, that permits to quickly compare the thermal performance of different designs and to establish safety limits to the temperature in PMSM most critical regions, such as the magnets and the end-windings. A complete comparison with measured data will be included in the final version of this thesis.

6

Structural and Vibratory Behaviour

As it was previously introduced, the PMSM vibratory and acoustic study is mandatory in order to ensure technical standards fulfilment and a reduced noise emission. So, it is not surprising that complete analytical models of electrical machine vibratory behaviour have been carried out since the fifties [Jordan 1950].

In this thesis work the modal analytical approach exposed in [Yang 1981, Timar 1989, Gieras 2006] will be adopted due to its lower computing time and good features, such as its simpler boundary conditions respect to FEM simulations.

As it was exposed in 2.2.3, the complete acoustic study can be divided into different parts: the electromagnetic force calculus, the structural natural vibration modes and, finally, the vibratory and acoustic behaviour of the structure due to the applied forces.

Several assumptions are necessary in order to develop a suitable acoustic model; the most important is that the stator and frame of an electrical machine can be seen as cylindrical shells. Due to their enclosure, the rotor vibrations can be neglected, and only the external parts of the motor (i.e. the stator and the frame) will be taken into account.

The magnetic excitation pressure is assumed to be completely radial and it is considered time and θ -dependant, so it can be expressed by a 2D-Fourier Series as:

$$\overline{P}_M(\theta, t) = \sum_{k=-\infty}^{\infty} \sum_{l=-\infty}^{\infty} P_{M,kl} e^{jk\omega_e t} e^{jl\theta} \bar{r}. \quad (6.1)$$

Due to the curvature of the stator shell geometry the vibrations in the radial, axial and tangential axis are coupled to each other, so an excitation in one direction would cause vibrations in all directions. In spite of that fact, several authors consider that only the radial vibrations are of importance in noise emission, especially for short machines [Hubert 2001], this approximation will be adopted.

The aforementioned assumptions implied that a radial modal basis can be used in order to express the stresses, elongations and speeds of the stator particles, so a modal approach will be used in order to characterise the stator vibrations. Figure 2.13 shows graphically some of these modal basis functions.

As far as the forces are known and were previously calculated in 3.3.5, the chapter will study the estimation of the stator structural and vibratory features. First vibratory basic principles will be explained and applied to a shell structure in cylindrical coordinates and then the particularities of the stator will be modelled.

6.1 Classic Vibratory Theory: d'Alembert Principle and Hooke Law

In order to calculate the internal displacements (i.e. the vibrations) in a body it is necessary to establish a force balance and a mathematical relation between the

aforementioned forces and displacements. The first requirement is satisfied through the d'Alembert principle which states: "Defining the inertial force as the minus product of the mass and acceleration, the sum of all the forces (contact, volumetric and inertial) acting on a body vanished, i.e. they are an equilibrate force system."

Mathematically d'Alembert principle can be expressed in its discrete form as:

$$\sum_{i=1}^n F_i - m_i a_i = 0 \quad (6.2)$$

where the system under study is divided in a finite number of particles (n), where the particle i is characterized by its mass (m_i), acceleration (a_i) and the force acting on it (F_i).

It is possible to define a stress tensor (σ) which matrix form is equal to:

$$\sigma = \begin{bmatrix} \sigma_{11} & \sigma_{12} & \sigma_{13} \\ \sigma_{21} & \sigma_{22} & \sigma_{23} \\ \sigma_{31} & \sigma_{32} & \sigma_{33} \end{bmatrix}, \quad (6.3)$$

where σ_{ij} is the stress applied in the i -axis direction on a surface which its normal vector oriented in the j -axis direction, i.e. the tension vector ($\bar{\sigma}$) applied in a point on a surface which normal vector in this point is (\bar{n}) is equal to:

$$\bar{\sigma} = \sigma \bar{n}. \quad (6.4)$$

An important feature of the stress tensor is that it must be symmetric in order to ensure that the total momentum is null, so it is defined by just six scalar values.

It is possible to apply the d'Alembert principle in 2D-cylindrical coordinates, defining a differential element at position (r, θ) , with a force density $\bar{f} = f_r \bar{r} + f_\theta \bar{\theta}$ acting on it and a total displacement $\bar{u} = u_r \bar{r} + u_\theta \bar{\theta}$ [Timoshenko 1951]. Figure 6.1 represents the element stresses.

In the radial direction the force equilibrium implies:

$$\begin{aligned} f_r dr d\theta = & [(\sigma_{rr}r)_1 - (\sigma_{rr}r)_3] d\theta - [(\sigma_{\theta\theta})_2 + (\sigma_{\theta\theta})_4] \sin\left(\frac{d\theta}{2}\right) dr \\ & + [(\sigma_{r\theta})_2 - (\sigma_{r\theta})_4] \cos\left(\frac{d\theta}{2}\right) dr - \frac{\partial^2 u_r}{\partial t^2} \rho r dr d\theta, \end{aligned} \quad (6.5)$$

where the numeric subindex represents the element face where the stress is applied, u_r is the element radial displacement and ρ is its density.

If (6.5) is divided by $dr d\theta$ and the element dimensions tends to zero (i.e. $dr \rightarrow 0$, $d\theta \rightarrow 0$) it becomes:

$$f_r = \frac{\partial \sigma_{rr}}{\partial r} r + \sigma_{rr} - \sigma_{\theta\theta} - \frac{\partial \sigma_{r\theta}}{\partial \theta} - \frac{\partial^2 u_r}{\partial t^2} \rho r. \quad (6.6)$$

The same procedure can be applied in the θ -axis, obtaining:

$$\begin{aligned}
 f_{\theta} dr d\theta = & [(\sigma_{\theta\theta})_2 - (\sigma_{\theta\theta})_4] \cos\left(\frac{d\theta}{2}\right) dr - [(\sigma_{\theta r})_1 r_1 - (\sigma_{\theta r})_3 r_3] d\theta \\
 & + [(\sigma_{r\theta})_2 + (\sigma_{r\theta})_4] \sin\left(\frac{d\theta}{2}\right) dr - \frac{\partial^2 u_{\theta}}{\partial t^2} \rho r dr d\theta.
 \end{aligned} \quad (6.7)$$

Equation (6.7) can be reformulated in a similar way than (6.5) , i.e. dividing by $dr d\theta$ and making the differentials tends to zero (i.e. $dr \rightarrow 0, d\theta \rightarrow 0$) :

$$f_{\theta} = -\frac{\partial \sigma_{\theta\theta}}{\partial \theta} + \frac{\partial \sigma_{\theta r}}{\partial r} r + 2\sigma_{\theta r} - \frac{\partial^2 u_{\theta}}{\partial t^2} \rho r. \quad (6.8)$$

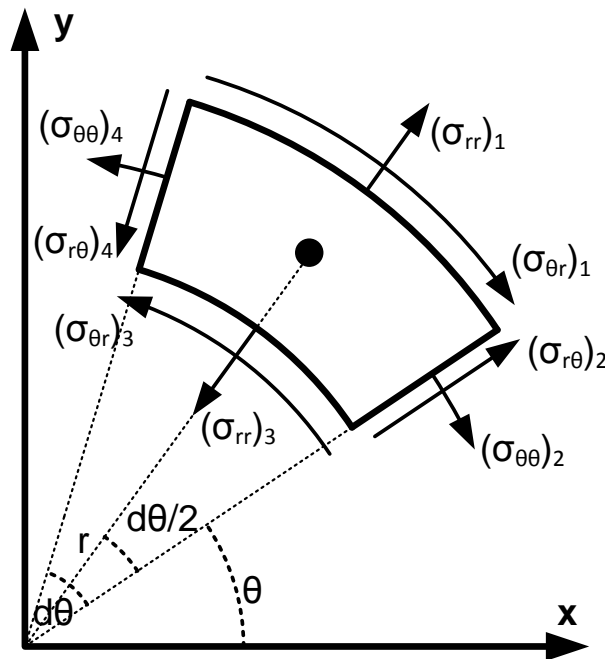


Figure 6.1. Stresses on a differential element in polar coordinates. Figure adapted from [Timoshenko 1951].

Once the internal stresses are estimated a relation between them and the body deformation must be established. It is supposed that the stator is an elastic medium, characterized by its Young module (E) and its Poisson coefficient (ν).

The body deformation is measured by the strain tensor, which establishes the body deformation respect to its original configuration. Mathematically it can be defined as:

$$\varepsilon_{ij} = \frac{1}{2} \left(\frac{\partial u_i}{\partial x_j} + \frac{\partial u_j}{\partial x_i} \right), \quad (6.9)$$

where ε_{ij} represents the differential elongation in the i -axis direction respect to a infinitesimal displacement in the j -axis. u_i is an infinitesimal particle displacement in the i -axis and x_i is the i^{th} coordinate. Equivalently:

$$\boldsymbol{\varepsilon} = \nabla \mathbf{u} + (\nabla \mathbf{u})^T, \quad (6.10)$$

where $\boldsymbol{\varepsilon}$ is the strain tensor, $\nabla \mathbf{u}$ is the displacements field gradient and $(\nabla \mathbf{u})^T$ is its transposed tensor. ε_{ii} represents compression or traction deformations, while ε_{ij} with $i \neq j$ is a shear deformation.

In its matrix form $\boldsymbol{\varepsilon}$ is equal to:

$$\boldsymbol{\varepsilon} = \begin{bmatrix} \varepsilon_{11} & \varepsilon_{12} & \varepsilon_{13} \\ \varepsilon_{12} & \varepsilon_{22} & \varepsilon_{23} \\ \varepsilon_{13} & \varepsilon_{23} & \varepsilon_{33} \end{bmatrix}. \quad (6.11)$$

Strain tensor is symmetric by definition, as far as the anti-symmetric part of the displacements field gradient does not describe a deformation movement but a rotational or translational one. Another important feature of the strain tensor is that, as far as the displacement is small in most of real elastic bodies, it has small values.

An elastic, isotropic body presents a linear relation between its stress and strain tensors defined by the Hooke law, i.e. it is possible to define a tensor \mathbf{C} such as:

$$\boldsymbol{\sigma} = \mathbf{C}\boldsymbol{\varepsilon}, \quad (6.12)$$

A straightforward form to represent the relation between both tensors in an elastic, isotropic body is through the material Young modulus and Poisson coefficient. In a 2D-geometry it can be represented as:

$$\begin{bmatrix} \varepsilon_{xx} \\ \varepsilon_{yy} \\ \varepsilon_{xy} \end{bmatrix} = \frac{1}{E} \begin{bmatrix} 1 & -\nu & 0 \\ -\nu & 1 & 0 \\ 0 & 0 & 2(1 + \nu) \end{bmatrix} \begin{bmatrix} \sigma_{xx} \\ \sigma_{yy} \\ \sigma_{xy} \end{bmatrix}. \quad (6.13)$$

The relations established by Hooke's law (6.13) and d'Alembert principle (6.6), (6.8) in the case of an elastic, linear material in polar coordinates will be used in the next sections in order to estimate the vibratory behaviour of a PMSM stator.

6.2 Dynamic of a Thin Ring

A non-clamped stator structure can be modelled as a thin ring, so a 2D-study could be carried out. In a first step this model will be performed and then the main results will be extended to the PMSM stator case.

In order to perform this study the following assumptions are made:

- A 2D-approximation is accurate enough, stresses in the z-axis are supposed to be null.
- A modular base will be defined. As far as, in most practical cases, the radial modes have a leading vibratory and acoustic interest, only these modes will be included in the base.
- Two types of radial modes are studied: Mode 0 (the breathing mode or extension mode) and the bending modes without elongation (modes 1 onwards).

6.2.1 Breathing Mode

The breathing mode is characterized by the expansion and contraction of the ring; changing its radius but preserving its circular geometry (see Figure 6.2). Figure 6.3 shows a tangential differential element, with its strains and stresses.

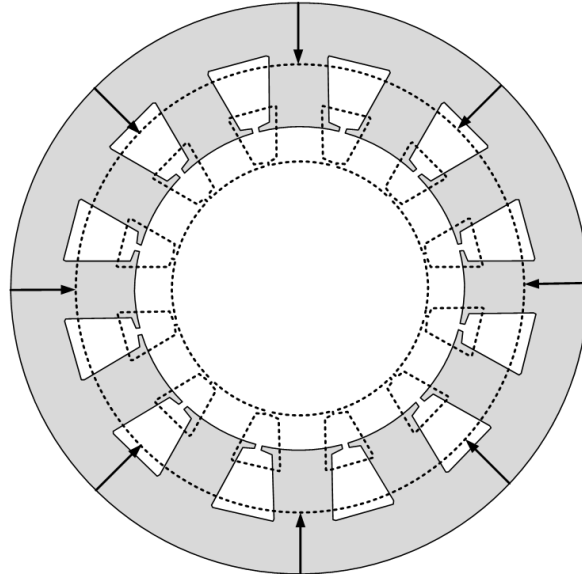


Figure 6.2. Example of a stator breathing mode.

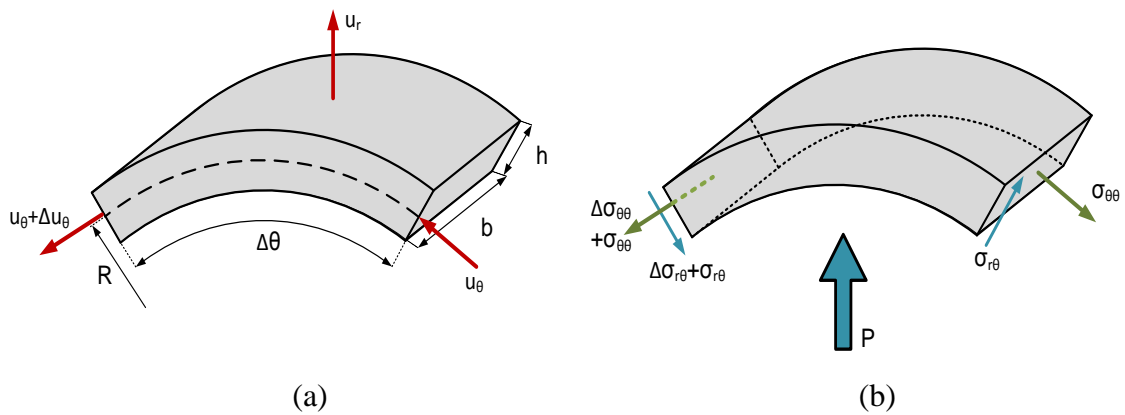


Figure 6.3. (a) Strain and dimensions in a ring element (b) stresses in a ring.

It is supposed that no external forces exist and the only significant deformation is in the tangential direction, i.e. the only non null component of the strain tensor is $\epsilon_{\theta\theta}$. By definition it is equal to:

$$\epsilon_{\theta\theta} = \lim_{\Delta\theta \rightarrow 0} \frac{\Delta u_{\theta} + (R + u_r)\Delta\theta - R\Delta\theta}{R\Delta\theta} = \frac{1}{R} \left(\frac{\partial u_{\theta}}{\partial \theta} + u_r \right), \quad (6.14)$$

by using the Hooke's law:

$$\sigma_{\theta\theta} = \frac{E}{R} \left(\frac{\partial u_{\theta}}{\partial \theta} + u_r \right), \quad (6.15)$$

where E is the material Young modulus and R the ring radius. Equations (6.6) and (6.8) can be particularized:

$$\frac{E}{R} \left(\frac{\partial u_\theta}{\partial \theta} + u_r \right) + \frac{\partial^2 u_r}{\partial t^2} \rho R = 0 \quad (6.16)$$

$$\frac{E}{R} \left(\frac{\partial^2 u_\theta}{\partial \theta^2} + \frac{\partial u_r}{\partial \theta} \right) + \frac{\partial^2 u_\theta}{\partial t^2} \rho R = 0 \quad (6.17)$$

It is supposed that the solution can be expressed in a FS base, i.e:

$$u_\theta = \sum_{n=-\infty}^{\infty} U_{\theta,n} e^{j(n\theta + \omega_n t)} \quad (6.18)$$

$$u_r = \sum_{n=-\infty}^{\infty} U_{r,n} e^{j(n\theta + \omega_n t)} \quad (6.19)$$

where ω_n is the pulsation of the mode.

It can be deduced that the previous equations implies an additional relation between u_θ and u_r [Hubert 2001]:

$$u_\theta = -\frac{\partial u_r}{\partial \theta} \quad (6.20)$$

substituting (6.20) in (6.16):

$$\frac{E}{R} \left(\frac{\partial^2 u_r}{\partial \theta^2} - u_r \right) - \frac{\partial^2 u_r}{\partial t^2} \rho R = 0 \quad (6.21)$$

u_r can be divided in two parts:

$$u_r = V_r(\theta) \Phi_r(t) \quad (6.22)$$

From (6.21):

$$\frac{E}{R^2} \frac{V_r''(\theta) - V_r(\theta)}{V_r(\theta)} = \rho \frac{\ddot{\Phi}_r(t)}{\Phi_r(t)} \quad (6.23)$$

where V_r' denotes the spatial derivative of V_r and $\ddot{\Phi}_r$ the temporal derivative of Φ_r .

For each spatial index, n , there exists one frequency that fulfils (6.23) with a non-trivial solution. This frequency is known as the resonant or natural frequency of the n^{th} mode, and in the breathing mode it is equal to:

$$f_n = \frac{1}{2\pi R} \sqrt{\frac{E(n^2 + 1)}{\rho}} \quad (6.24)$$

The so called breathing mode only presents one important spatial harmonic, when $n = 0$ with a resonant pulsation equal to:

$$\omega_0 = \frac{1}{R} \sqrt{\frac{E}{\rho}} \quad (6.25)$$

If a continuous external pressure P and pulsation ω_f is applied, it will generate a radial displacement u_r of the same order and frequency, i.e.:

$$P = F_r e^{j\omega_f t} \quad (6.26)$$

$$u_r = U_r e^{j\omega_f t} \quad (6.27)$$

The differential equation that must be fulfilled is:

$$\frac{E}{R} \left(\frac{\partial^2 u_r}{\partial \theta^2} - u_r \right) A d\theta - \frac{\partial^2 u_r}{\partial t^2} \rho R A d\theta = P b R d\theta \quad (6.28)$$

where A is the ring cross-sectional area and b is its length (see Figure 6.3). It could be deduced:

$$P = u_r \left[\frac{E}{\rho R^2} (n^2 + 1) \rho h - \omega_f^2 \rho h \right] = u_r \rho h [\omega_n^2 - \omega_f^2] \quad (6.29)$$

where h is the ring thickness. Taking into account that $n=0$ it is possible to deduce:

$$u_r = \frac{F_r e^{j\omega_f t}}{\rho h [\omega_n^2 - \omega_f^2]} \quad (6.30)$$

An important concept in vibratory study is the static displacements (Y_n), defined as the amplitude of the radial displacement per unit of static pressure (i.e. with a continuous exciting force). The static displacement could be obtained from (6.30) when $\omega_f = 0$.

$$Y_0 = \frac{1}{\rho h [\omega_n^2]} = \frac{R^2}{hE} \quad (6.31)$$

6.2.2 Bending Modes without Elongation

General equations (6.6) and (6.8) can be particularized for the bending modes [Hubert 2001].

$$\sigma_{\theta\theta} + \frac{\partial \sigma_{r\theta}}{\partial \theta} + \frac{\partial^2 u_r}{\partial t^2} \rho R = 0, \quad (6.32)$$

$$\frac{\partial \sigma_{\theta\theta}}{\partial \theta} - \sigma_{\theta r} + \frac{\partial^2 u_\theta}{\partial t^2} \rho R = 0. \quad (6.33)$$

Two additional equations are necessary in order to obtain the radial displacements as a function of the force mode and frequency, (6.34) describes the bending moment

and (6.35) imposes the no extension of the ring central line (i.e. a mode without elongation).

$$\frac{\partial M}{\partial \theta} + \sigma_{\theta r} R A = 0 \quad (6.34)$$

$$u_r = -\frac{\partial u_{\theta}}{\partial \theta} \quad (6.35)$$

where M is the ring bending moment and R its initial radius. Forces and moments acting on a differential section of the ring are shown in Figure 6.3.

In a deformed thin ring it is possible to establish a relation between the bending moment (M) and the radial displacements (u_r) [Timoshenko 1976-a, 1976-b]:

$$M = \frac{I_z E}{R^2} \left(\frac{\partial^2 u_r}{\partial \theta^2} + u_r \right) \quad (6.36)$$

where I_z is the moment of inertia respect to the ring neutral axis, i.e:

$$I_z = \int_{z=-b/2}^{b/2} \int_{r=R-h/2}^{R+h/2} (r - R)^2 dr dz, \quad (6.37)$$

where h is the ring thickness and b its length.

Combining the equations from (6.34) to (6.37) the shear stress on the element is equal to:

$$\sigma_{\theta r} = \frac{I_z E}{AR^3} \left(\frac{\partial^4 u_{\theta}}{\partial \theta^4} + \frac{\partial^2 u_{\theta}}{\partial \theta^2} \right) \quad (6.38)$$

From (6.32) the tangential stress can be deduced:

$$\sigma_{\theta \theta} = -\frac{I_z E}{AR^3} \left(\frac{\partial^5 u_{\theta}}{\partial \theta^5} + \frac{\partial^3 u_{\theta}}{\partial \theta^3} \right) - \rho R \frac{\partial^3 u_{\theta}}{\partial t^2 \partial \theta} \quad (6.39)$$

Substituting (6.38) and (6.39) into (6.33):

$$-\frac{I_z E}{R^4} \left(\frac{\partial^6 u_{\theta}}{\partial \theta^6} + 2 \frac{\partial^4 u_{\theta}}{\partial \theta^4} + \frac{\partial^2 u_{\theta}}{\partial \theta^2} \right) + \rho A \left(\frac{\partial^2 u_{\theta}}{\partial t^2} - \frac{\partial^4 u_{\theta}}{\partial t^2 \partial \theta^2} \right) = 0 \quad (6.40)$$

As it was previously introduced the displacements (both in the θ and in the r -axis), can be expressed as a FS, see equations (6.18) and (6.19). So (6.40) yields to:

$$\frac{I_z E V_{\theta}^{(6)} + 2V_{\theta}^{(4)} + V_{\theta}^{(2)}}{R^4 V_{\theta} - V_{\theta}^{(2)}} = \rho A \frac{\ddot{\Phi}_{\theta}(t)}{\Phi_{\theta}(t)}, \quad (6.41)$$

where $V_{\theta}^{(x)}$ is the x -order derivative of V_{θ} and u_{θ} is divided in the product of two single variable functions, i.e.

$$u_{\theta} = V_{\theta}(\theta) \Phi_{\theta}(t). \quad (6.42)$$

Derivatives calculus in (6.41) leads to:

$$\frac{I_z E n^2 (n^2 - 1)^2}{R^4 (n^2 + 1)} = \rho A \omega_n^2. \quad (6.43)$$

So, the resonant frequency of the n^{th} bending mode is equal to:

$$f_n = \frac{n(n^2 - 1)}{2\pi R^2} \sqrt{\frac{I_z E}{\rho A (n^2 + 1)}}, \quad (6.44)$$

a particular case of great importance in the case of electrical machines is when the ring has a rectangular section, in this case (6.37) can be solved as:

$$I_z = Ah^2/12, \quad (6.45)$$

and (6.44) yields to:

$$f_n = \frac{h}{R^2 2\sqrt{3}} \frac{n(n^2 - 1)}{2\pi} \sqrt{\frac{E}{\rho (n^2 + 1)}} \quad (6.46)$$

If an external radial pressure P of mode n and pulsation ω_f is applied equation (6.32) is rewritten as:

$$-\sigma_{\theta\theta} + \frac{\partial \sigma_{r\theta}}{\partial \theta} + \frac{\partial^2 u_r}{\partial t^2} \rho R = bRP \quad (6.47)$$

the angular displacement and the pressure have a factorial form equal to:

$$P = F_r e^{j(\omega_f t + n\theta)}, \quad (6.48)$$

$$u_\theta = U_\theta e^{j(\omega_f t + n\theta)}. \quad (6.49)$$

So, in this case, the tangential stress can be calculated as:

$$\sigma_{\theta\theta} = -\frac{I_z E}{AR^3} \left(\frac{\partial^5 u_\theta}{\partial \theta^5} + \frac{\partial^3 u_\theta}{\partial \theta^3} \right) - \rho R \frac{\partial^3 u_\theta}{\partial t^2 \partial \theta} - bRP \quad (6.50)$$

and (6.40) yields to:

$$-\frac{I_z E}{R^4} \left(\frac{\partial^6 u_\theta}{\partial \theta^6} + 2 \frac{\partial^4 u_\theta}{\partial \theta^4} + \frac{\partial^2 u_\theta}{\partial \theta^2} \right) - b \frac{\partial P}{\partial \theta} + \rho A \left(\frac{\partial^2 u_\theta}{\partial t^2} - \frac{\partial^4 u_\theta}{\partial t^2 \partial \theta^2} \right) = 0 \quad (6.51)$$

once the derivatives are solved:

$$(\omega_n^2 - \omega_f^2) u_\theta = \frac{jnP}{h\rho(n^2 + 1)}, \quad (6.52)$$

so, the angular displacements field is:

$$u_\theta = \frac{jnP}{h\rho(n^2 + 1)(\omega_n^2 - \omega_f^2)} \quad (6.53)$$

and, the radial one:

$$u_r = \frac{n^2 P}{h \rho (n^2 + 1) (\omega_n^2 - \omega_f^2)} \quad (6.54)$$

Therefore, the static displacement (Y_n) is:

$$Y_n = \frac{n^2}{h \rho (1 + n^2) \omega_n^2} = \frac{12 R^4}{h^3 E (n^2 - 1)^2} \quad (6.55)$$

The previous calculi are a general, simple resolution of the vibratory behaviour of a thin ring, from them a more accurate and complete model of an electrical machine is obtained in the next section.

6.3 Dynamic of a Stator

A complete stator is quite different from a simple 2D-thin ring; so, in order to use the aforementioned analytic results, it is necessary to take into account the major differences between a complete stator and the simplified thin ring model, the most important among them are listed below.

1. The stator is not just a ring, but it is loaded by additional elements such as teeth and coils that modify the mass and the stiffness of the complete body.
2. The stator is in close contact with an external housing which plays the role of a vibratory interface between it and the air.
3. There exists a viscous damping as far as the kinetic energy is dissipated into heath during the vibration process.
4. The internal forces are not applied on the medium radius of the external ring, but on the internal stator radius, this must be taken into account in order to estimate the static and dynamic displacements. (see Figure 6.4).
5. The PMSM is nestled by its foot and its shaft, so its vibratory behaviour is not exactly the same in each axial slash, for this reason some non-negligible axial modes could appear.

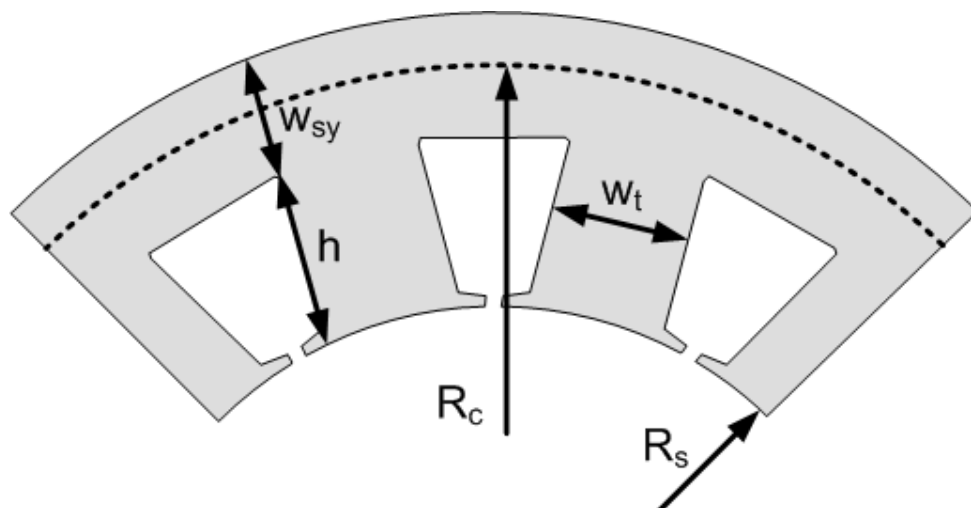


Figure 6.4. Stator seen as a ring (mean radius R_c and thickness h) loaded with teeth.

In order to take into account the aforementioned features the resonance pulsation and the static displacements of the breathing mode are corrected [Yang 1981, Gieras 2006]:

$$\omega_0 = \frac{1}{R_c} \sqrt{\frac{E_{Fe}}{\rho_{Fe} \Delta}}, \quad (6.56)$$

$$Y_0 = \frac{R_s R_c}{w_{sy} E_{Fe}}, \quad (6.57)$$

where R_c is the mean stator yoke radius, R_s the internal stator radius, w_{sy} the stator yoke height, E_{Fe} the core material Young modulus, ρ_{Fe} the core material density and Δ the mass addition factor due to the teeth and winding, i.e:

$$\Delta = \frac{M_{sy} + M_{th} + M_{Cu}}{M_{sy}}. \quad (6.58)$$

where M_{sy} is the stator yoke total mass, M_{th} the total teeth mass and M_{Cu} the total coil weigh.

It is important to notice that the teeth and the winding add an additional mass term in (6.56) but its stiffness is neglected as far as the teeth stiffness contribution is greatly decreased by the coils.

From the static displacement it is possible to obtain the dynamic one; in this case equation (6.30) cannot be directly applied as far as the core material presents a viscous damping which tends to decrease the oscillations amplitude. Therefore, (6.30) leads to [Gieras 2006]:

$$u_{r,k0} = \frac{F_{r,k0} Y_0 \omega_0^2}{\sqrt{(\omega_0^2 - k^2 \omega_e^2)^2 + 4\zeta_0^2 k^2 \omega_e^2 \omega_0^2}}, \quad (6.59)$$

where ω_e is the electrical pulsation, k an index which denotes its temporal harmonic, ζ_0 the damping factor for mode 0, and $F_{r,k0}$ and $u_{r,k0}$ the FS-coefficients of the radial pressure and displacements, respectively, i.e. the total force and radial displacement can be expressed as a sum of its FS-coefficients as:

$$F_r(\theta, t) = \sum_{k=-\infty}^{\infty} \sum_{n=-\infty}^{\infty} F_{r,kn} e^{jk\omega_e t} e^{jn\theta}, \quad (6.60)$$

$$u_r(\theta, t) = \sum_{k=-\infty}^{\infty} \sum_{n=-\infty}^{\infty} u_{r,kn} e^{jk\omega_e t} e^{jn\theta}. \quad (6.61)$$

The damping factor has a mayor importance in equation (6.59), as far as it avoids the theoretical infinite displacement when the stator is excited with a force which has just the resonant frequency of its spatial mode. However, a correct estimation of ζ_n is not an easy task and needs of experimental measure [Gieras 2006]. If measures are

not available an empirical expression proposed by [Yang 1981] can be used for model purposes during the design stage:

$$\zeta_n = \frac{1}{2\pi} (2.76 \cdot 10^{-5} f_n + 0.062). \quad (6.62)$$

where f_n is the n^{th} mode natural frequency.

In a similar way the natural frequencies and the static and dynamic displacements could be calculated for bending modes without elongation as:

$$\omega_n = \frac{w_{sy}}{R_c^2 2\sqrt{3}} n(n^2 - 1) \sqrt{\frac{E_{Fe}}{\rho_{Fe} \Delta (n^2 + 1)}} \phi_n, \quad (6.63)$$

$$Y_n = \frac{12R_s R_c^3}{w_{sy}^3 E_{Fe} (n^2 - 1)^2} \quad (6.64)$$

where ϕ_n is a correction factor which takes into account the teeth rotator inertia [Yang 1981]:

$$\phi_n = \left\{ 1 + \frac{\frac{w_{sy}^2}{12R_c^2} (n^2 - 1) [n^2 (4 + \Delta_{rot}/\Delta) + 3]}{n^2 + 1} \right\}^{-0.5}, \quad (6.65)$$

where Δ_{rot} is the mass addition factor for rotation and it is defined as:

$$\Delta_{rot} = 1 + \frac{Q w_t \frac{M_{th} + M_{Cu}}{M_{th}} h \{4h^2 + 6w_{sy}h + 3w_{sy}^2\}}{2\pi w_{sy}^3 R_c} \quad (6.66)$$

where Q is the teeth number, w_t its width and h its height (see Figure 6.4).

Finally, the dynamic displacement 2D-FS coefficients are equal to:

$$u_{r,kn} = \frac{F_{r,kn} Y_n \omega_n^2}{\sqrt{(\omega_n^2 - k^2 \omega_e^2)^2 + 4\zeta_0^2 k^2 \omega_e^2 \omega_n^2}}, \quad (6.67)$$

With the aforementioned considerations a more realistic PMSM acoustic 2D-model can be performed, however it is convenient to explain some additional considerations about them.

First, the teeth not only add mass and rotational inertia but they can vibrate in a circumferential direction causing additional modes called the “tooth rocking modes”, fortunately these modes are strongly damped by the slot coils and it is assumed that the behaviour of the complete stator is quite similar to a ring (the stator yoke) loaded with an additional mass (teeth plus windings) [Girgis 1979].

Second, the presence of an external housing is usually neglected because of its small thickness compare with the stator yoke, but some authors [Gieras 2006]

proposed a method in order to obtain a global mode estimation taking into account both, stator and housing.

Finally the motor surface is not free during its normal operation, but it is nestled by its feet and shaft. The feet clamping greatly affect the appearance of some radial modes, while the end-bells and the shaft often clamp the machine causing axial modes appearance (see Figure 6.5), these mode are usually neglected as far as they have small relevance, especially in short machines [Hubert 2001].

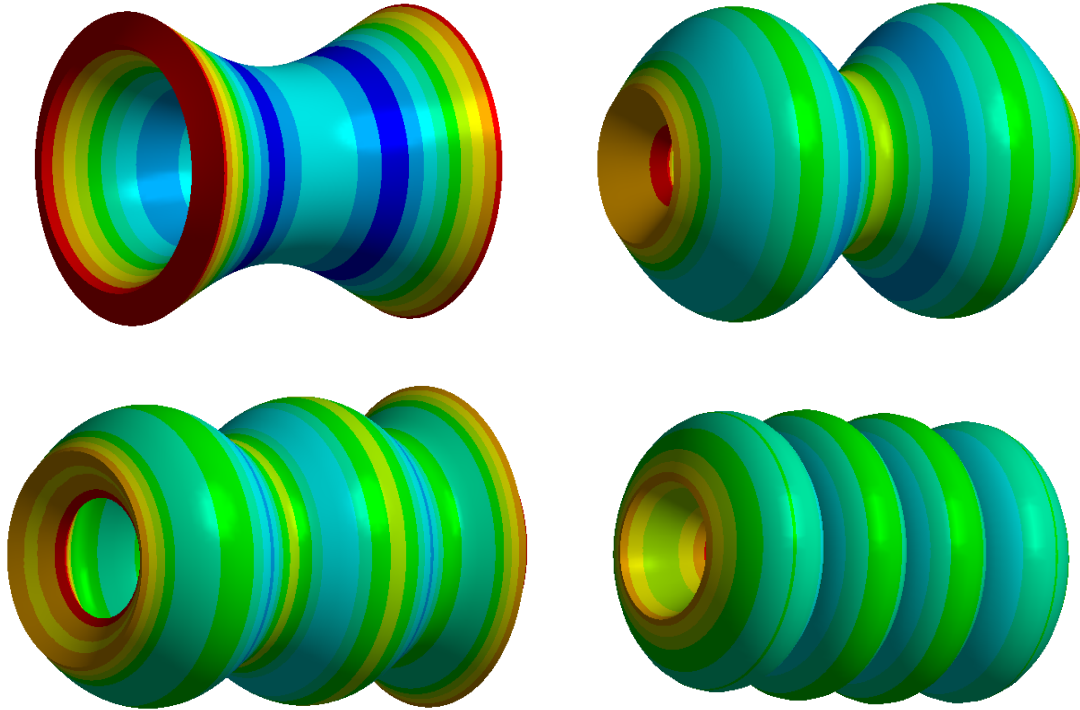


Figure 6.5. 1st to 4th stator axial modes calculated with ANSYS®. Deflections have been scaled for visual purposes.

The acoustic model will be detailed explained in the final thesis document. The total electrical machine radiate sound power can be deduced as [Besnerais 2008]:

$$P_{\text{rad}} = 8200 A_S \sum_{n=-\infty}^{\infty} \sum_{k=-\infty}^{\infty} \frac{u_{r,kn}^2 \sigma_{kn}}{2n+1} (kf_e)^2 \quad (6.68)$$

where A_S is the external machine surface, P_{rad} the sound power radiated and σ_{kn} the noise radiation factor of the machine for mode n at frequency kf_e , that depends of its length [Gieras 2006].

6.4 Results and Conclusions

The implemented analytical model was used in order to estimate the modular vibratory behaviour of the test PMSM.

The results obtained with the analytical model were compared with those calculated by ANSYS®, a commercial FEM software which has a complete structural module with the possibilities of perform both a modal analysis and a random vibration response.

A complete modal analysis was carried out, and the static displacements and natural frequencies of each mode calculated with both approaches. The obtained results can be seen in Table 6.1.

Table 6.1. Simulated and estimated modal static displacements and natural frequencies

MODE	FEM RESULTS (ANSYS®)		ANALYTICAL MODEL		RELATIVE ERROR	
	f_n (Hz)	Y_n (m ³ /N)	f_n (Hz)	Y_n (m ³ /N)	f_n (%)	Y_n (%)
0	4307	2.4 e^{-12}	4128	2.3 e^{-12}	-4.16	-4.17
2	590	91.2 e^{-12}	554	92.5 e^{-12}	-6.10	1.43
3	1535	12.9 e^{-12}	1445	13.0 e^{-12}	-5.86	0.78
4	2638	4.0 e^{-12}	2516	3.7 e^{-12}	-4.63	-7.50
5	3637	1.7 e^{-12}	3671	1.5 e^{-12}	0.93	-11.76

The agreement between the commercial software and the obtained results is quite good, in the five firsts modes the natural frequency error is less than 6% and the static displacement one less than 8%. Superior order modes are usually neglected in acoustic calculus, because its poor radiation factor.

Although the errors may seem high they are perfectly acceptable. Error reasons are the aforementioned neglected effects which cause that the global results of the analytical vibratory study are not as accurate as electromagnetic and even thermal ones. Spite of that fact, a fair comparison between candidate designs can be performed and it is also possible determine the most problematic frequency bands which are the two main objectives in the design process.

It can be concluded that, at this stage of motor design, the proposed analytical acoustic model is a fast and suitable solution, which permits to quickly compare the vibratory behaviour of different designs and to establish the frequencies which should be avoided in the excitation magnetic force.

As a final remark, it must be highlighted that experimental results must be performed in order to validate both, the analytical and FEM calculus, as far as external elements such as feet, shaft or housing have been neglected in both approaches, so the final measured results could be different of the presented ones. A complete comparison with measured data will be included in the final version of this thesis.

7

Optimized Methodology Proposal

7.1 The optimization process: A Global View

As it was previously introduced a complete optimized methodology development implies two different steps: a model definition and an optimization process selection. Previous chapters were devoted to the first aim, while the present briefly outlines the second.

Among the features of the proposed methodology (analytical, fast, modular, multiphysical, complete and optimized), the last two ones are specially related to the optimization process, while the former depends mostly on the modelling.

The correct definition of an optimized methodology (i.e. an optimization problem resolution) involves the following steps:

1. Definition of a set of mathematical or physical models that accurately represents the system behaviour.
2. Selection of a set of design variables (i.e. the input variables) and the state ones.
3. Definition of one or more objective and restriction functions depending on both, the design and the state variables.
4. Selection of a suitable optimization algorithm that matches the problem features.

This chapter is devoted to the last three points, since the first ones were detailed in the previous sections. The mathematical definition of an optimization problem was briefly introduced in 2.1.2.

7.1.1 Design and Status Variables

The selected design variables are presented in Table 7.1. They are defined as the variables that the optimization algorithm directly modifies in order to minimize objective functions. As it can be seen, they are a set of 13 geometric and configuration variables which determine the electromagnetic, thermal and vibratory PMSM behaviour. The rest of parameters that are needed in order to fully describe the machine performance (i.e., the chosen ferromagnetic core material or the selected magnets) are considered as constants, since they are imposed by manufacturer restrictions.

Other important variables are the state variables that are defined as those that are calculated from the design ones and are needed in order to obtain one or more of the objective or restriction functions.

Table 7.2 shows the defined state variables while Figure 7.1 shows the models flowchart and the state variables that couple the different physical domains

Table 7.1. Design variables

DESIGN VARIABLE	UNITS	NATURE	TYPE
Slot number, Q	-	Configuration	Discrete
Pole pair number, p	-	Configuration	Discrete
Number of conductors per slot per layer, Z	-	Configuration	Discrete
Magnet height, I_m	m	Geometric	Continuous
Magnet pitch, α_m	-	Geometric	Continuous
Internal stator radius, R_s	m	Geometric	Continuous
External stator radius, R_{se}	m	Geometric	Continuous
Airgap length, g	m	Geometric	Continuous
Slot height, h_2	m	Geometric	Continuous
Tooth-tip height, h_0	m	Geometric	Continuous
Slot opening, w_0	m	Geometric	Continuous
Tooth width, w_t	m	Geometric	Continuous
Stator length, L_e	m	Geometric	Continuous

Table 7.2. State variables

STATUS VARIABLE	UNITS	NATURE
Winding periodicity, t_p	-	Configuration
Output power, P_{out}	W	Electric/Mechanical
EMF, E	V	Electromagnetic
PMSM phase current, I_{SM}	A	Electric
Input voltage, V_{ph}	V	Electric
Airgap armature reaction, B_g^a	T	Magnetic
Airgap rotor magnetic field, B_g^m	T	Magnetic
Stator yoke flux density, B_t	T	Magnetic
Stator teeth flux density, B_s	T	Magnetic
Electric load, q_e	A/m ²	Electric
Power factor, pf	-	Electric
Copper losses, P_{Cu}	W	Electric
Iron losses, P_{Fe}	W	Magnetic
Mechanical losses, P_{ad}	W	Mechanical
End-winding temperature, T_{ew}	K	Thermal
Magnets temperature, T_{mag}	K	Thermal
Copper total mass, M_{Cu}	kg	-
Iron total mass, M_{Fe}	kg	-
Magnets total mass, M_{mag}	kg	-
Torque ripple, T_{pk-pk}	N.m	Mechanical
Emitted noise level, L_p	dB(A)	Acoustic

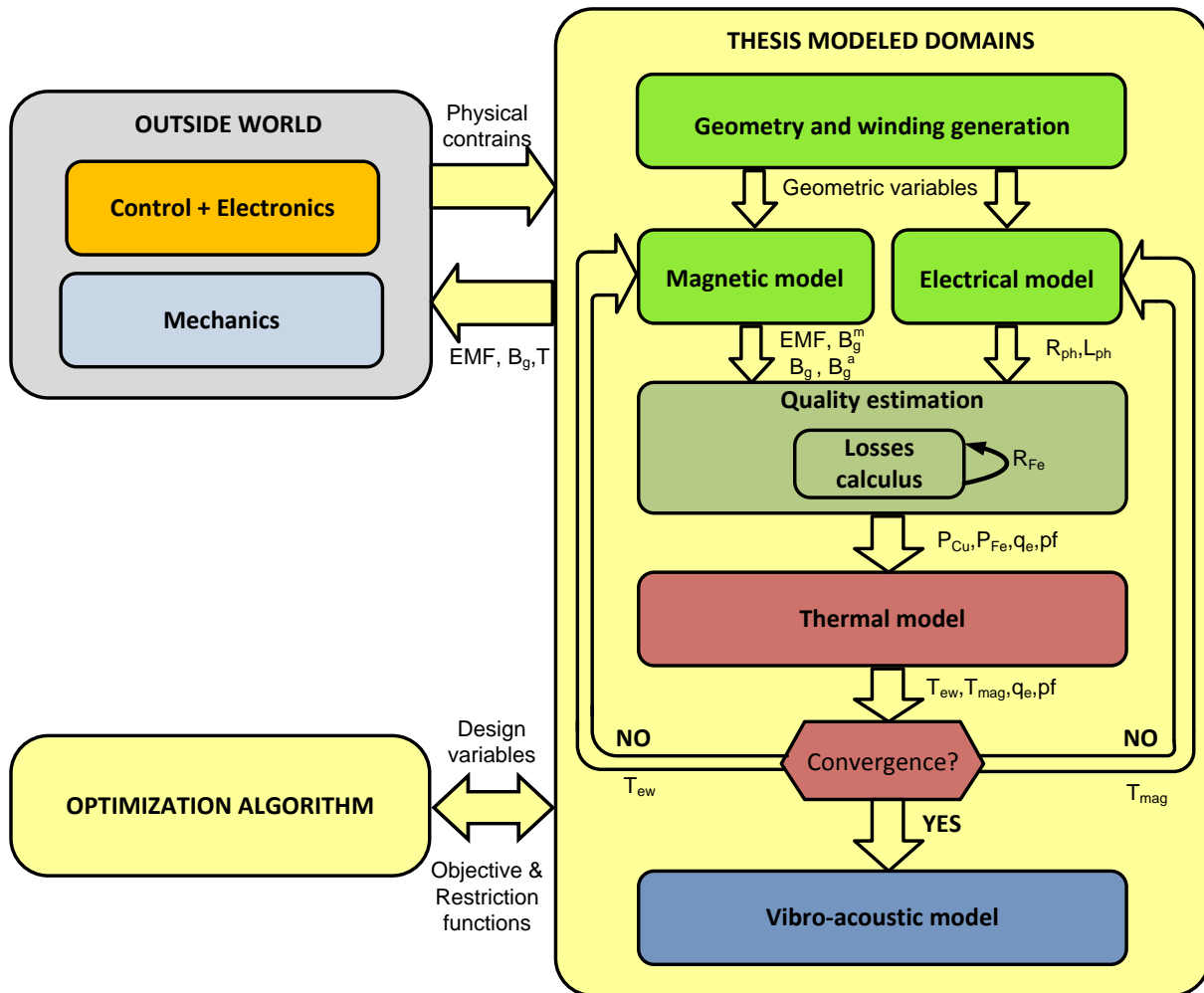


Figure 7.1. PMSM model flowchart.

7.1.2 Objective and restriction functions

As it was aforementioned, an optimization problem consists in the minimization of one or more objective functions, taking into account a set of restrictions. Both, the objective and the restriction functions, should be established in order to achieve a suitable and feasible solution, i.e., a correct PMSM design.

In the proposed thesis work a multi-objective function optimization is proposed. More precisely, the efficiency will be maximized and the materials cost minimized, using a Pareto frontier approach.

The efficiency was defined in Chapter 4 as

$$\eta = \frac{P_{out}}{P_{out} + P_{Fe} + P_{Cu} + P_{ad}}, \quad (7.1)$$

where P_{out} is P_{elec} if the machine is operating as a generator and P_{mec} if it is in motor operation mode.

The material cost is the sum of the prices of the copper, the iron and the magnets, i.e.,

$$\text{Cost} = M_{\text{Cu}} c_{\text{Cu}} + M_{\text{Fe}} c_{\text{Fe}} + M_{\text{mag}} c_{\text{mag}} \quad (7.2)$$

where c_{Cu} , c_{Fe} and c_{mag} are, respectively, the cost of the copper, the ferromagnetic material and the magnets per unit mass.

It is important to notice that the objective functions must be completed with the restriction ones, which will establish features as important as the geometrical feasibility of the design, the output power, the size and the maximum permitted temperature or noise levels. The identified restrictions are included in the next tables and classified according to its nature (geometric, electrical, thermal, etc.).

In the next tables a set of limits and thresholds are included. In order to clearly identify them bold letters are used. They are the minimum rotor radius (\mathbf{R}_{rmin}), the objective output power (\mathbf{P}_{obj}), the maximum active volume ($\mathbf{Vol}_{\text{max}}$), the maximum torque ripple ($\mathbf{T}_{\text{pkmax}}$), the ferromagnetic core saturation threshold (\mathbf{B}_{sat}), the demagnetization flux density ($\mathbf{B}_{\text{demag}}$), the maximum slot current density (\mathbf{J}_{max}), the maximum electric load (\mathbf{q}_{emax}), the maximum input voltage ($\mathbf{V}_{\text{phmax}}$), the minimum power factor (\mathbf{pf}_{min}), the maximum noise emission (\mathbf{Lp}_{max}) and the maximum winding and magnets temperature ($\mathbf{T}_{\text{Cumax}}$ and $\mathbf{T}_{\text{magmax}}$).

Table 7.3. Design restrictions

Restriction	Formulation
Minimum output power	$0.95\mathbf{P}_{\text{obj}} - 0.5 I_{\text{SM}} \text{EMF} \cos(\phi) \leq 0$
Maximum output power	$0.5 I_{\text{SM}} \text{EMF} \cos(\phi) - 1.05\mathbf{P}_{\text{obj}} \leq 0$
Maximum active volume	$\pi R_{\text{se}}^2 L_e - \mathbf{Vol}_{\text{max}} \leq 0$
Maximum torque ripple	$T_{\text{pk-pk}} - \mathbf{T}_{\text{pkmax}} \leq 0$

where the output power is defined in motor operation mode and ϕ is the angle between the fundamental components of EMF and I_{SM} .

Table 7.4. Geometric restrictions

Restriction	Formulation
Stator yoke feasibility	$R_s + h - R_{\text{se}} \leq 0$
Minimum rotor radius	$\mathbf{R}_{\text{rmin}} - (R_s - l_m - g) \leq 0$
Slot opening feasibility	$w_0 - \left(\frac{2\pi R_s}{Q} - w_t\right) \leq 0$
Tooth width feasibility	$w_t - \frac{2\pi R_s}{Q} \leq 0$

Table 7.5. Magnetic restrictions

Restriction	Formulation
Maximum teeth saturation level	$B_t - B_{sat} \leq 0$
Maximum yoke saturation level	$B_s - B_{sat} \leq 0$
Avoid magnets demagnetization	$B_g^a - B_{demag} \leq 0$

Table 7.6. Electric restrictions

Restriction	Formulation
Maximum current density	$\frac{I_{SM}}{F_R h_2 \left(\frac{2\pi R_s}{Q} - w_t \right)} - J_{max} \leq 0$
Maximum electric load	$q_e - q_{emax} \leq 0$
Maximum input voltage	$V_{ph} - V_{phmax} \leq 0$
Minimum power factor	$f_{pmin} - f_p \leq 0$

Table 7.7. Thermal and acoustic restrictions

Restriction	Formulation
Maximum wire temperature	$T_{ew} - T_{Cumax} \leq 0$
Maximum magnet temperature	$T_{mag} - T_{magmax} \leq 0$
Maximum noise emission level	$L_p - L_{pmax} \leq 0$

7.1.3 The DMS Algorithm

The direct multisearch (DMS) algorithm is a novel multiobjective derivative-free heuristic methodology that is based on the search/poll paradigm (i.e., it is closely related with the Hooke and Jeeves method) combined with the Pareto dominance concept. Due to these properties it is selected as the optimization algorithm used in the proposed PMSM design methodology.

The DMS method was first presented in 2011 and a very detailed explanation and convergence study could be found in [Custódio 2011], here just the basic principles are introduced.

Initially a group of feasible solutions (i.e. points with n coordinates, where n is the number of design variables) is selected, each point is associated with a "search step" α . This initial group is called L_0 .

From this initial point a group of iterations is launched, each generating its own solutions group called L_k , where k is the iteration number. In each iteration, the steps are the following:

1. **Selection of an iterative point:** one of the points in L_{k-1} is chosen in order to perform an exploratory step. Many algorithms can be implemented in order to select the most suitable “exploratory point” x_k .
2. **Poll step:** a new group L_{add} is calculated from the exploratory point. Generally α is added and subtracted from each x_k coordinate, i.e. if $x_k = (0.5, 1.5)$ and $\alpha = 1$, a possible value of L_{add} will be $L_{add} = \{(1.5, 1.5), (0.5, 2.5), (-0.5, 1.5), (0.5, 0.5)\}$
3. **Filtering dominated points:** a new set $L_{k-1} \cup L_{add}$ is defined, and all the dominated points are filtered, i.e., if a point "a" is worse in all the objective functions than other point "b", it is said that "a" is dominated by "b" and "a" is eliminated from $L_{k-1} \cup L_{add}$.
Thus, the new solution group will be $L_k = \text{filter}(L_{k-1} \cup L_{add})$
4. **Step size parameter update:** if $L_k \neq L_{k-1}$ the iteration is considered successful and α is usually incremented for the next iteration. Otherwise α is decremented (generally halved) for the next iteration step, in order to search a better solution in a closer region.

More detailed and rigorous explanations of the DMS algorithm, with some concrete examples, are included in [Custódio 2011].

7.2 The Proposed Methodology

The aforementioned models, design variables, objective functions and restriction functions have been integrated in the DMS algorithm in order to obtain a complete and functional methodology which takes into account the complex requirements than real industrial applications impose on a PMSM.

The complete methodology flowchart is shown in Figure 7.2. The different stages will be briefly outlined in this section, while a more complete description will be presented in the thesis final document.

The implemented algorithm can be defined as a “two rounds exploratory” one. It is defined as exploratory because from a small group of solutions (the initial population) a higher number of solutions that conform a Pareto-optimal frontier are obtained.

In the first round, a set of feasible Q and p values are chosen. For each combination and using basic sizing equations, a small initial population is selected (from 1 to 6 initial PMSM) and the DMS algorithms is running N_{iter} times in order to obtain a Pareto-frontier population. In other words, if the number of slots (Q) could be 36 or 72 and the number of pole pairs (p) could be 4, 5 or 6, the DMS algorithms is run a total of six times with a maximum of N_{iter} iterations each, finally six Pareto-frontiers are obtained.

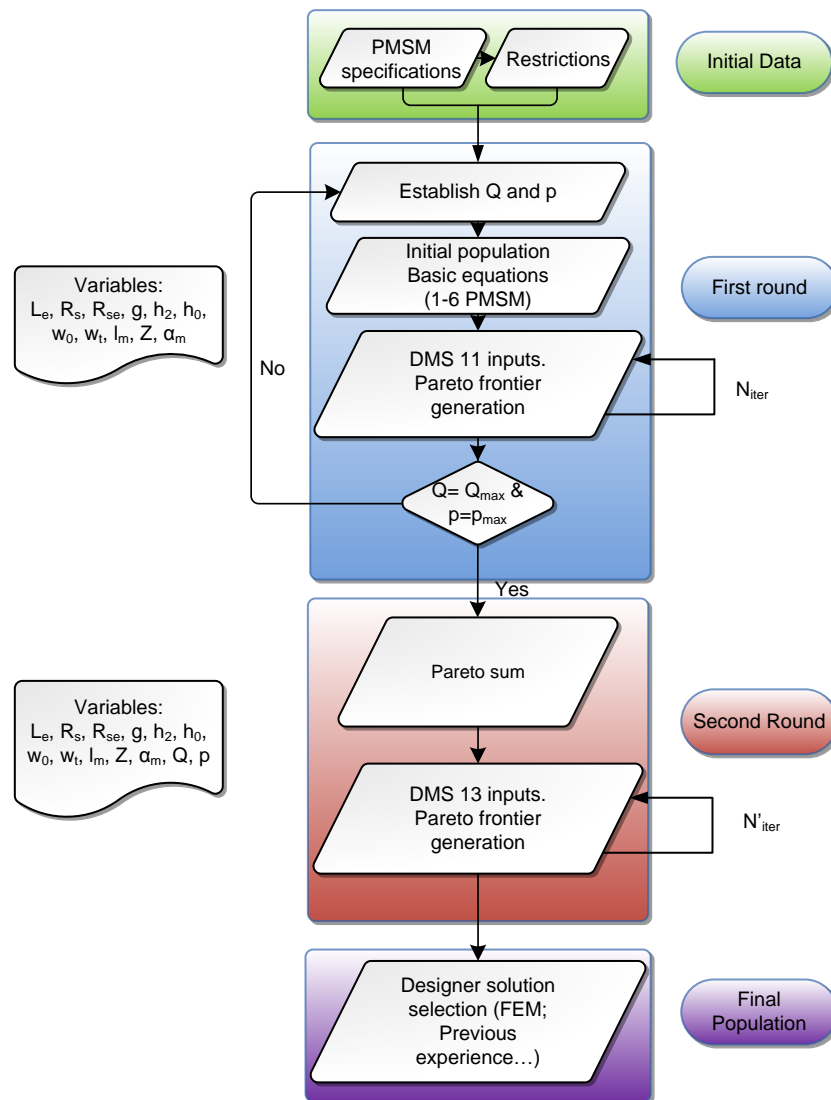


Figure 7.2. PMSM design methodology flowchart.

From the first round a group of preselected solutions is achieved and a new global Pareto is generated from the partial Pareto previously obtained. In the second round the DMS algorithm is run again, but now the initial solution group is the global Pareto aforementioned and the iteration number (N'_{iter}) is higher than N_{iter} .

Moreover, Q and p are considered design variables in this second round, so the DMS will look for the best slot- pole pair configuration, being the final Pareto frontier the final population. Among the proposed solutions the designer can choose the most suitable one.

8

Conclusions and Future Work

8.1 Conclusions

PMSMs have an important and increasing presence in many power applications, such as electric vehicle, railway traction, elevation, power generation, renewable energies and aircraft industry. It is expected that, in next years, this trend becomes even greater and an increasing number of exigent applications demand more efficient and suitable PMSMs in order to fulfil a strict set of specifications at minimum cost. Hence, it is evident that a proper design methodology is needed in order to overcome the proposed challenges.

In the present work the basic principles of a PMSM operation was introduced and a state of the art in its design methodology has been performed. However, nowadays most of the papers devoted to the subject only take into account partial aspects of the global problem, and offers unclear methodologies that are hardly replicable and rely on empirical rules. Only in recent years, more complex design methodologies, which include multiphysical and optimized approaches, have been developed.

In spite of this fact, to the best author's knowledge, a complete, analytical design methodology, covering all the key features of a PMSM design, included electrical, magnetic, thermal and vibratory domains has not been presented yet. Thus, the main aim of this thesis is to fill this gap, introducing a new PMSM design methodology offering a holistic, multiphysics, modular and fast approach.

In order to achieve the proposed goal two different objectives have been defined. The first one is the development of a complete set of PMSM physical models. Thus, a specific state of the art has been performed and, based on its results, a new improved PMSM model has been presented. Its main feature consists in a multiphysical approach which takes into account electrical, magnetic, thermal and vibratory processes coupled together through key variables. Moreover, its complete analytical nature supposes a very high computational speed and an adequate level of integration of the different physical domains.

The present work offers a complete validation process , a concrete 10-poles, 12-slots PMSM design has been fully analysed with both, the developed model and some commercial software. The packages FLUX2D[®], Motor-CAD[®] and ANSYS[®] were used in order to obtain the machine electromagnetic, vibratory and thermal behaviour, respectively.

The high accuracy of the results, as well as the low execution time (the proposed PMSM takes 15 ms in being modelled in an Intel[®] Core i7-3370 @ 3.40 GHz) and the good level of detail achieved in the different domains under study show that the proposed model is a very suitable choice to support multiphysical and optimized design methodologies, which development is the second main objective.

In that sense, the proposed design optimized methodology has been outlined. Another of the contributions of the proposed thesis is the use of the DMS algorithm, a heuristic multi-objective optimization method, in PMSM design.

A completely original design methodology, based on a two rounds strategy, has been proposed and very promising preliminary results have been obtained. Its complete implementation will be included in the final thesis report.

8.2 Future Work

The next steps for the continuation and conclusion of this thesis work are listed below:

- **Improvement of the used models:** related with a more accurate representation of the magnetic saturation effect, the use of the conformal transformation in order to model the stator slotting fringe effect, the representation of the skew, the determination of some thermal model uncertainties and a more complete vibratory model validation.
- **Development of a complete design methodology:** to finish the methodology proposed in Chapter 7, improving the selection of initial suitable points for the DMS algorithm. Once this task be accomplished, this methodology will be used in order to design a complete PMSM.
- **Manufacturing a prototype, experimental measures:** the aforementioned prototype need to be tested in order to validate, not only it proper operation, but also the design methodology. Therefore it will be constructed and an extensive experimental validation will be carried out.

9

Bibliographic references

[Agamloh 2013] Agamloh, E.B.; Cavagnino, A., "High efficiency design of induction machines for industrial applications," Electrical Machines Design Control and Diagnosis (WEMDCD), 2013 IEEE Workshop on , vol., no., pp.33,46, 11-12 March 2013

[Almandoz 2008] Almandoz, G., "Metodología avanzada de diseño para máquinas multipolares de imanes permanentes, orientada a la aplicación" Ph.D. dissertation, Mondragón Goi Eskola Politeknikoa, Mondragón Unibertsitatea 2008

[Amdouni 2012] Amdouni, I.; Amraoui, L.E.; Gillon, F.; Benrejeb, M.; Brochet, P., "Optimal design approach developed for permanent magnet motors," Electrical Machines (ICEM), 2012 XXth International Conference on , vol., no., pp.1374,1379, 2-5 Sept. 2012

[Amrhein 2013] Amrhein, M.; O'Connell, T.C.; Wells, J.R., "An integrated design process for optimized high-performance electrical machines," Electric Machines & Drives Conference (IEMDC), 2013 IEEE International , vol., no., pp.847,854, 12-15 May 2013

[Anwar 2000] Anwar, M. N.; Husain, I., "Radial force calculation and acoustic noise prediction in switched reluctance machines," Industry Applications, IEEE Transactions on , vol.36, no.6, pp.1589,1597, Nov/Dec 2000

[Anyuan 2010] Anyuan Chen; Nilssen, R.; Nysveen, A., "Performance Comparisons Among Radial-Flux, Multistage Axial-Flux, and Three-Phase Transverse-Flux PM Machines for Downhole Applications," Industry Applications, IEEE Transactions on , vol.46, no.2, pp.779,789, March-april 2010

[Atallah 2000] Atallah, K.; Howe, D.; Mellor, P.H.; Stone, D.A., "Rotor loss in permanent-magnet brushless AC machines," Industry Applications, IEEE Transactions on , vol.36, no.6, pp.1612,1618, Nov/Dec 2000

[Bermúdez de Castro 2011] Bermúdez de Castro, A.; Pena, F., "Galerkin lumped parameter methods for transient problems", Numerical methods in Engineering, International Journal for, vol. 87, Issue 10, pp. 943,961, September 2011

[Bermúdez de Castro 2014] Bermúdez de Castro, A.; Salgado, P.; Gómez, D., "Mathematical Models and Numerical Simulation in Electromagnetism". Springer, series: UNITEXT, Vol. 74, 2014

[Bertotti 1988] Bertotti, Giorgio, "General properties of power losses in soft ferromagnetic materials," Magnetics, IEEE Transactions on , vol.24, no.1, pp.621,630, Jan 1988

[Besnerais 2008] Le Besnerais, J., "Réduction du bruit audible d'origine magnétique dans les machines asynchrones alimentées par MLI – règles de conception silencieuse et optimisation multi-objectif–" Ph.D. dissertation, Laboratoire d'Electricité et d'Electronique de Puissance de Lille, École Centrale de Lille, 2008

[Besnerais 2009] Le Besnerais, J.; Lanfranchi, V.; Hecquet, M.; Brochet, P., "Optimal Slot Numbers for Magnetic Noise Reduction in Variable-Speed Induction Motors," *Magnetics, IEEE Transactions on* , vol.45, no.8, pp.3131,3136, Aug. 2009

[Besnerais 2010] Le Besnerais, J.; Lanfranchi, V.; Hecquet, M.; Brochet, P., "Characterization and Reduction of Audible Magnetic Noise Due to PWM Supply in Induction Machines," *Industrial Electronics, IEEE Transactions on* , vol.57, no.4, pp.1288,1295, April 2010

[Bettayeb 2010] Bettayeb, A.; Jannot, X.; Vannier, J. -C, "Analytical calculation of rotor magnet eddy-current losses for high speed IPMSM," *Electrical Machines (ICEM), 2010 XIX International Conference on* , vol., no., pp.1,6, 6-8 Sept. 2010

[Bianchi 2006] Bianchi, N.; Dai Pre, M., "Use of the star of slots in designing fractional-slot single-layer synchronous motors," *Electric Power Applications, IEE Proceedings -* , vol.153, no.3, pp.459,466, 1 May 2006

[Boglietti 2003] Boglietti, A.; Cavagnino, A.; Lazzari, M.; Pastorelli, M., "Predicting iron losses in soft magnetic materials with arbitrary voltage supply: an engineering approach," *Magnetics, IEEE Transactions on* , vol.39, no.2, pp.981,989, Mar 2003

[Boglietti 2008] Boglietti, A.; Cavagnino, A.; Staton, D., "Determination of Critical Parameters in Electrical Machine Thermal Models," *Industry Applications, IEEE Transactions on* , vol.44, no.4, pp.1150,1159, July-aug. 2008

[Boglietti 2009] Boglietti, A.; Cavagnino, A.; Staton, D.; Shanel, Martin; Mueller, M.; Mejuto, C., "Evolution and Modern Approaches for Thermal Analysis of Electrical Machines," *Industrial Electronics, IEEE Transactions on* , vol.56, no.3, pp.871,882, March 2009

[Bossavit 2011] Bossavit, A., "Virtual power principle and Maxwell's tensor: which comes first?" *The International Journal for Computation and Mathematics in Electrical and Electronic Engineering*, Vol. 30 Iss: 6, pp.1804 – 1814, 2011.

[Bossavit 2014] Bossavit, A., "On Forces in Magnetized Matter," *Magnetics, IEEE Transactions on* , vol.50, no.2, pp.229,232, Feb. 2014

[Bracikowski 2012] Bracikowski, N.; Hecquet, M.; Brochet, P.; Shirinskii, S.V., "Multiphysics Modeling of a Permanent Magnet Synchronous Machine by Using Lumped Models," *Industrial Electronics, IEEE Transactions on*, vol.59, no.6, pp.2426,2437, June 2012

[Carlson 2012] Carlson, R.; Wurtz, F.; Voltolini, H., "Sizing and optimization models: Design of a set of two permanent magnet generators," *Electrical Machines (ICEM), 2012 XXth International Conference on*, vol., no., pp.1358,1363, 2-5 Sept. 2012

[Cassimere 2009] Cassimere, B.N.; Sudhoff, S.D., "Population-Based Design of Surface-Mounted Permanent-Magnet Synchronous Machines," *Energy Conversion, IEEE Transactions on*, vol.24, no.2, pp.338,346, June 2009

[Chen 2002] Yicheng Chen; Pillay, P., "An improved formula for lamination core loss calculations in machines operating with high frequency and high flux density excitation," *Industry Applications Conference, 2002. 37th IAS Annual Meeting. Conference Record of the*, vol.2, no., pp.759,766 vol.2, 13-18 Oct. 2002

[Cho 2000] Dong-Hyeok Cho; Hyun-Kyo Jung; Tae-Kyung Chung; Cheol-Gyun Lee, "Design of a short-time rating interior permanent magnet synchronous motor using a niching genetic algorithm," *Magnetics, IEEE Transactions on*, vol.36, no.4, pp.1936,1940, Jul 2000

[Comanescu 2003] Comanescu, Mihai; Keyhani, A.; Min Dai, "Design and analysis of 42-V permanent-magnet generator for automotive applications," *Energy Conversion, IEEE Transactions on*, vol.18, no.1, pp.107,112, Mar 2003

[Custódio 2011] Custódio, A.L.; Madeira, J.F.A.; Vaz A. I. F.; and Vicente, L.N., "Direct multisearch for multiobjective optimization", *SIAM Journal on Optimization*, vol. 21, pp. 1109,1140, 2011

[Dorrell 2006] Dorrell, D.G.; Staton, D.A.; McGilp, M.I., "Design of Brushless Permanent Magnet Motors - A Combined Electromagnetic and Thermal Approach to High Performance Specification," *IEEE Industrial Electronics, IECON 2006 - 32nd Annual Conference on*, vol., no., pp.4853,4858, 6-10 Nov. 2006

[Duan 2013-a] Yao Duan; Ionel, D.M., "A Review of Recent Developments in Electrical Machine Design Optimization Methods With a Permanent-Magnet Synchronous Motor Benchmark Study," *Industry Applications, IEEE Transactions on*, vol.49, no.3, pp.1268,1275, May-June 2013

[Duan 2013-b] Yao Duan; Qin Sun; Ionel, D.M., "Methods for studying the pareto-fronts in multi-objective design optimization problems of electrical machines," Energy Conversion Congress and Exposition (ECCE), 2013 IEEE , vol., no., pp.5013,5018, 15-19 Sept. 2013

[Ede 2007] Ede, J.D.; Atallah, K.; Jewell, G.W.; Wang, J.B.; Howe, D., "Effect of Axial Segmentation of Permanent Magnets on Rotor Loss in Modular Permanent-Magnet Brushless Machines," Industry Applications, IEEE Transactions on , vol.43, no.5, pp.1207,1213, Sept.-oct. 2007

[Elosegui 2008] Elosegui, I.; Egana, I.; Fontan, L.; Garcia Rico, A.; Martinez-Iturralde, M., "Fast sizing and simulation of multipole radial flux permanent magnet synchronous machines," Power Electronics, Electrical Drives, Automation and Motion, 2008. SPEEDAM 2008. International Symposium on , vol., no., pp.1445,1450, 11-13 June 2008

[El-Refaie 2004] EL-Refaie, A.M.; Harris, N.C.; Jahns, T.M.; Rahman, K.M., "Thermal analysis of multibarrier interior PM synchronous Machine using lumped parameter model," Energy Conversion, IEEE Transactions on , vol.19, no.2, pp.303,309, June 2004

[Fadriansyah 2012] Fadriansyah, T.; Strous, T. D.; Polinder, H., "Axial segmentation and magnets losses of SMPM machines using 2D FE method," Electrical Machines (ICEM), 2012 XXth International Conference on , vol., no., pp.577,581, 2-5 Sept. 2012

[Favi 2011] Favi, C.; Germani, M.; Marconi, M.; Mengoni, M.; Tirabassi, A., "EROD: New collaborative design platform for developing energy efficient electric motors," Electric Machines & Drives Conference (IEMDC), 2011 IEEE International , vol., no., pp.59,64, 15-18 May 2011

[Fiedler 2010] Fiedler, J.O.; Kasper, K.A.; De Doncker, R.W., "Calculation of the Acoustic Noise Spectrum of SRM Using Modal Superposition," Industrial Electronics, IEEE Transactions on , vol.57, no.9, pp.2939,2945, Sept. 2010

[García 2014] García, A., "Optimal Design of Medium-Frequency High-Power Converters". Ph.D. dissertation, Université de Lausanne, 2014

[Gieras 2006] Gieras, J., Wang C., Lai J.; "Noise of polyphase electric motors". ,US: CRC Press, 2006

[Ginsberg 1953] Ginsberg, David; Misenheimer, Leo J., "Design Calculations for Permanent-Magnet Generators [includes discussion]," Power Apparatus and Systems, Part III. Transactions of the American Institute of Electrical Engineers , vol.72, no.2, pp.,, Jan. 1953

[Girgis 1979] Girgis, R. S.; Verma, S. P., "Resonant Frequencies and Vibration Behaviour of Stators of Electrical Machines as Affected by Teeth, Windings, Frame and Laminations," Power Apparatus and Systems, IEEE Transactions on , vol.PAS-98, no.4, pp.1446,1455, July 1979

[Giurgea 2008] Giurgea, S.; Fodorean, D.; Cirrincione, G.; Miraoui, A.; Cirrincione, M., "Multimodel Optimization Based on the Response Surface of the Reduced FEM Simulation Model With Application to a PMSM," Magnetics, IEEE Transactions on , vol.44, no.9, pp.2153,2157, Sept. 2008

[Gómez 2014] Gomez, D.J.; Rodriguez, A.L.; Villar, I.; Lopez-de-Heredia, A.; Etxeberria-Otadui, I., "New Improved Lumped Circuit Model for Embedded Magnet Synchronous Machines" Electrical Machines (ICEM), 2014 XXith International Conference on., September 2014. Accepted

[Goss 2013-a] Goss, J.; Wrobel, R.; Mellor, P.; Staton, D., "The design of AC permanent magnet motors for electric vehicles: A design methodology," Electric Machines & Drives Conference (IEMDC), 2013 IEEE International , vol., no., pp.871,878, 12-15 May 2013

[Goss 2013-b] Goss, J.; Staton, D.; Wrobel, R.; Mellor, P., "Brushless AC interior-permanent magnet motor design: Comparison of slot/pole combinations and distributed vs. concentrated windings," Energy Conversion Congress and Exposition (ECCE), 2013 IEEE , vol., no., pp.1213,1219, 15-19 Sept. 2013

[Hafner 2011] Hafner, Martin; Finken, T.; Felden, M.; Hameyer, K., "Automated Virtual Prototyping of Permanent Magnet Synchronous Machines for HEVs," Magnetics, IEEE Transactions on , vol.47, no.5, pp.1018,1021, May 2011

[Hanselman 2012] Hanselman, D.; "Brushless Motors. Magnetic Design, Performance, and Control". US: E-Man Press LLC, 2012

[Hecker 2013] Hecker, Q.; Ccoa, J.A.B.; Meyer, W.; Herzog, H.-G., "Automated design of squirrel-cage induction machines by predefined torque-speed-characteristic," Electric Machines & Drives Conference (IEMDC), 2013 IEEE International , vol., no., pp.1160,1165, 12-15 May 2013

[Hubert 2001] Hubert, A., "Contribution à l' étude des bruits acoustiques générés lors de l'association machines électriques -convertisseurs statiques de puissance. Application à la machine asynchrone" Ph.D. dissertation, Université de Technologie de Compiègne, 2001

[Hwang 2013] Chang-Chou Hwang; Chia-Ming Chang; Cheng-Tsung Liu, "A Fuzzy-Based Taguchi Method for Multiobjective Design of PM Motors," *Magnetics, IEEE Transactions on* , vol.49, no.5, pp.2153,2156, May 2013

[Iles-Klumpner 2004] Iles-Klumpner, D.; Boldea, I., "Comparative optimization design of an interior permanent magnet synchronous motor for an automotive active steering system," *Power Electronics Specialists Conference, 2004. PESC 04. 2004 IEEE 35th Annual* , vol.1, no., pp.369,375 Vol.1, 20-25 June 2004

[Ishak 2005] Ishak, D.; Zhu, Z.Q.; Howe, D., "Eddy-current loss in the rotor magnets of permanent-magnet brushless machines having a fractional number of slots per pole," *Magnetics, IEEE Transactions on* , vol.41, no.9, pp.2462,2469, Sept. 2005

[Ishibashi 2003] Ishibashi, F.; Kamimoto, K.; Noda, S.; Itomi, K., "Natural frequency of stator core of small induction motor," *Electric Power Applications, IEE Proceedings -* , vol.150, no.2, pp.210,214, Mar 2003

[Islam 2009] Islam, M.R., "Cogging torque, torque ripple and radial force analysis of permanent magnet synchronous machines" Ph.D. dissertation, Akron University, 2009

[Islam 2010] Islam, R.; Husain, I., "Analytical Model for Predicting Noise and Vibration in Permanent-Magnet Synchronous Motors," *Industry Applications, IEEE Transactions on* , vol.46, no.6, pp.2346,2354, Nov.-Dec. 2010

[Jannot 2011] Jannot, X.; Vannier, J. -C; Marchand, C.; Gabsi, M.; Saint-Michel, J.; Sadarnac, D., "Multiphysic Modeling of a High-Speed Interior Permanent-Magnet Synchronous Machine for a Multiobjective Optimal Design," *Energy Conversion, IEEE Transactions on* , vol.26, no.2, pp.457,467, June 2011

[John 2003] John H. Lienhard IV, John H. Lienhard V. *A Heat Transfer Textbook*, third edition, Phlogiston Press, 2003

[Jordan 1950] Jordan, H.; "Electric motor silencer- formation and elimination of the noises in the electrical motors". W. Giradet-Essen editor, 1950

[Kazmin 2008-a] Kazmin, E.V.; Lomonova, E.A.; Paulides, J. J H, "Brushless traction PM machines using commercial drive technology, Part I: Design methodology and motor design," *Electrical Machines and Systems, 2008. ICEMS 2008. International Conference on* , vol., no., pp.3801,3809, 17-20 Oct. 2008

[Kazmin 2008-b] Kazmin, E.V.; Lomonova, E.A.; Paulides, J. J H, "Brushless traction PM machines using commercial drive technology, Part II: Comparative study of the motor configurations," *Electrical Machines and Systems*, 2008. ICEMS 2008. International Conference on , vol., no., pp.3772,3780, 17-20 Oct. 2008

[Kolehmainen 2010] Kolehmainen, J., "Optimal Dovetail Permanent Magnet Rotor Solutions for Various Pole Numbers," *Industrial Electronics, IEEE Transactions on* , vol.57, no.1, pp.70,77, Jan. 2010

[Kreuawan 2007] Kreuawan, S.; Gillon, F.; Moussouni, F.; Brisset, S.; Brochet, P., "Optimal design of traction motor in railway propulsion system," *Electrical Machines and Power Electronics*, 2007. ACEMP '07. International Aegean Conference on , vol., no., pp.343,348, 10-12 Sept. 2007

[Kylander 1995] Kylander, G.; "Thermal modelling of small cage induction motors" Department of Electrical Machines and Power Electronics, Chalmers University of Technology, Göteborg, Sweden, Tech. Rep., February 1995

[Lee 2009] Sang-Ho Lee; Jung-Pyo Hong; Sang-Moon Hwang; Woo-Taik Lee; Ji-Young Lee; Young-Kyoun Kim, "Optimal Design for Noise Reduction in Interior Permanent-Magnet Motor," *Industry Applications, IEEE Transactions on* , vol.45, no.6, pp.1954,1960, Nov.-dec. 2009

[Legranger 2008] Legranger, J.; Friedrich, G.; Vivier, S.; Mipo, J.C., "Combination of Finite Element and Analytical Models in the Optimal Multi-Domain Design of Machines: Application to an Interior Permanent Magnet Starter Generator," *Industry Applications Society Annual Meeting*, 2008. IAS '08. IEEE , vol., no., pp.1,6, 5-9 Oct. 2008

[Lindström 1999] Lindström, J.; "Thermal model of a permanent-magnet motor for a hybrid electric vehicle," Department of Electric power Engineering, Chalmers University of Technology, Göteborg, Sweden, Tech. Rep., Apr. 1999

[Liu 2008] Liu, Z.J.; Li, J.T., "Accurate Prediction of Magnetic Field and Magnetic Forces in Permanent Magnet Motors Using an Analytical Solution," *Energy Conversion, IEEE Transactions on* , vol.23, no.3, pp.717,726, Sept. 2008

[Lu 2006] Lu, K.; Rasmussen, P.O.; Ritchie, E., ""An Analytical Equation for Cogging Torque Calculation in Permanent Magnet Motors"". *Electrical Machines*, 2006 International Conference on , Chania, Kreta, Greece, 2006.

[Lu 2013] Xiaomin Lu; Iyer, K.L.V.; Mukherjee, K.; Kar, N.C., "Development of a Novel Magnetic Circuit Model for Design of Premium Efficiency Three-Phase Line Start Permanent Magnet Machines With Improved Starting Performance," *Magnetics, IEEE Transactions on* , vol.49, no.7, pp.3965,3968, July 2013

[Madina 2011] Madina, P.; Poza, J.; Ugalde, G.; Almandoz, G., "Magnet eddy current loss calculation method for segmentation analysis on permanent magnet machines," *Power Electronics and Applications (EPE 2011), Proceedings of the 2011-14th European Conference on* , vol., no., pp.1,9, Aug. 30 2011-Sept. 1 2011

[Makni 2007] Makni, Z.; Besbes, M.; Marchand, C., "Multiphysics Design Methodology of Permanent-Magnet Synchronous Motors," *Vehicular Technology, IEEE Transactions on* , vol.56, no.4, pp.1524,1530, July 2007

[Marignetti 2006] Marignetti, F.; Tomassi, Giovanni; Cancelliere, P.; Delli Colli, V.; Di Stefano, R.; Scarano, Maurizio, "Electromagnetic and Mechanical design of a Fractional-slot-windings Axial-flux PM synchronous machine with Soft Magnetic Compound Stator," *Industry Applications Conference, 2006. 41st IAS Annual Meeting. Conference Record of the 2006 IEEE* , vol.1, no., pp.62,69, 8-12 Oct. 2006

[Markovic 2007] Markovic, M.; Perriard, Y., "An Analytical Determination of Eddy-Current Losses in a Configuration With a Rotating Permanent Magnet," *Magnetics, IEEE Transactions on* , vol.43, no.8, pp.3380,3386, Aug. 2007

[Mellor 1991] Mellor, P.H.; Roberts, D.; Turner, D.R., "Lumped parameter thermal model for electrical machines of TEFC design," *Electric Power Applications, IEE Proceedings B* , vol.138, no.5, pp.205,218, Sep 1991

[Mi 2006] Mi, C.C., "Analytical design of permanent-magnet traction-drive motors," *Magnetics, IEEE Transactions on* , vol.42, no.7, pp.1861,1866, July 2006

[Muetze 2008] Muetze, A., "A neglected stepchild?," *Industry Applications Magazine, IEEE* , vol.14, no.2, pp.14,22, March-April 2008

[Muntenau 2012] Munteanu, A.; Boldea, I.; Tutelea, L., "Novel hybrid design methodology for a surface permanent magnet synchronous motor," *Power Electronics, Electrical Drives, Automation and Motion (SPEEDAM), 2012 International Symposium on* , vol., no., pp.603,608, 20-22 June 2012

[Nerg 2008] Nerg, J.; Rilla, M.; Pyrhonen, J., "Thermal Analysis of Radial-Flux Electrical Machines With a High Power Density," *Industrial Electronics, IEEE Transactions on* , vol.55, no.10, pp.3543,3554, Oct. 2008

[Nipp 1999] Nipp, E., "Permanent Magnet Motor Drives with Switched Stator Windings" Ph.D. dissertation, Royal Institute of Technology Department of Electric Power Engineering Electrical Machines and Drives, Stockholm 1999

[Novotny 1996] Novotny, D.W.; Lipo, T.A.; "Vector Control and Dynamics of AC Drives". Us: Oxford University Press, 1996

[Ombach 2007] Ombach, G.; Junak, J., "Design of PM Brushless Motor Taking into Account Tolerances of Mass Production - Six Sigma Design Method," Industry Applications Conference, 2007. 42nd IAS Annual Meeting. Conference Record of the 2007 IEEE , vol., no., pp.2139,2146, 23-27 Sept. 2007

[Patel 2013] Patel, V.I.; Jiabin Wang; Weiya Wang; Xiao Chen, "Analysis and design of 6-phase fractional slot per pole per phase permanent magnet machines with low space harmonics," Electric Machines & Drives Conference (IEMDC), 2013 IEEE International , vol., no., pp.386,393, 12-15 May 2013

[Pérez 1979] Perez, I.J.; Kassakian J.G., "A stationary thermal model for smooth airgap rotating electrical machines". Electric Machines and Electromechanics 3, p. 285-303. 1979

[Proca 2003] Proca, A.B.; Keyhani, A.; El-Antably, A.; Wenzhe Lu; Min Dai, "Analytical model for permanent magnet motors with surface mounted magnets," Energy Conversion, IEEE Transactions on , vol.18, no.3, pp.386,391, Sept. 2003

[Pyrhönen 2008] Pyrhönen, J., Jokinen T., Hrabovcová V.; "Design of Rotating Electrical Machines". UK. John Wiley & Sons Ltd., 2008

[Pyrhönen 2012] Pyrhonen, J.; Jussila, H.; Alexandrova, Y.; Rafajdus, P.; Nerg, J., "Harmonic Loss Calculation in Rotor Surface Permanent Magnets—New Analytic Approach," Magnetics, IEEE Transactions on , vol.48, no.8, pp.2358,2366, Aug. 2012

[Rahman 2013] Rahman, M.A., "History of interior permanent magnet motors [History]," Industry Applications Magazine, IEEE , vol.19, no.1, pp.10,15, Jan.-Feb. 2013

[Rodríguez 2013] Rodriguez, A.L.; Gomez, D.J.; Villar, I.; Lopez-de-Heredia, A.; Etxeberria-Otadui, I., "New improved estimation method for airgap self and mutual inductance in electric machines," Power Electronics and Applications (EPE), 2013 15th European Conference on , vol., no., pp.1,9, 2-6 Sept. 2013

[Rodríguez 2014-a] Rodríguez, A.L.; Gomez, D.J.; Villar, I.; Lopez-de-Heredia, A.; Etxeberria-Otadui, I., "Improved Analytical Multiphysical Modeling of a Surface PMSM" Electrical Machines (ICEM), 2014 XXlth International Conference on., September 2014. Accepted.

[Rodríguez 2014-b] Rodríguez, A.L.; Gomez, D.J.; Villar, I.; Lopez-de-Heredia, A.; Etxeberria-Otadui, I., "New Analytical Method for PMSM Magnet Losses Estimation based on Fourier Series" Electrical Machines (ICEM), 2014 XXlth International Conference on., September 2014. Accepted.

[Ruoho 2009] Ruoho, S.; Santa-Nokki, T.; Kolehmainen, J.; Arkkio, A., "Modeling Magnet Length In 2-D Finite-Element Analysis of Electric Machines," Magnetics, IEEE Transactions on , vol.45, no.8, pp.3114,3120, Aug. 2009

[Saari 1998] Saari,J., "Thermal analysis of high-spped induction machines" Ph.D. dissertation, Helsinki University of Technology, Laboratory of Electromechanics, 1998

[Saito 2010] Saito, N.; Kijima, R.; Shimomura, S., "The design method to minimize torque ripple in interior permanent magnet synchronous motor with concentrated winding," Power Electronics Conference (IPEC), 2010 International , vol., no., pp.1293,1298, 21-24 June 2010

[Sanchez 2006] Sanchez-Grandia, R.; Vives-Fos, R and Aucejo-Galindo, V., "Magnetostatic Maxwell's tensors in magnetic media applying virtual works method from either energy or co-energy." The European Physical Journal Applied Physics, 35, pp 61-68. 2006

[Sarikhani 2012] Sarikhani, A.; Mohammed, O.A., "HIL-Based Finite-Element Design Optimization Process for the Computational Prototyping of Electric Motor Drives," Energy Conversion, IEEE Transactions on , vol.27, no.3, pp.737,746, Sept. 2012

[Schlensok 2007] Schlensok, C.; Van der Giet, M.; Gracia, M.H.; Van Riesen, D.; Hameyer, K., "Structure-Dynamic Analysis of an Induction Machine depending on Stator-Housing Coupling," Electric Machines & Drives Conference, 2007. IEMDC '07. IEEE International , vol.2, no., pp.1540,1545, 3-5 May 2007

[Semidey 2011] Semidey, S.A.; Yao Duan; Mayor, J.R.; Harley, R.G.; Habetler, T.G., "Optimal Electromagnetic-Thermo-Mechanical Integrated Design Candidate Search and Selection for Surface-Mount Permanent-Magnet Machines Considering Load Profiles," Industry Applications, IEEE Transactions on , vol.47, no.6, pp.2460,2468, Nov.-Dec. 2011

[Sirvent 2012] G. Sirvent. "El mercado de tierras raras: Un mercado estratégico". Instituto Español de asuntos estratégicos. Ministerio de defensa. September 2012. [Available at: <http://www.ieee.es/documentos/areas-tematicas/retos-y-amenazas/2012/detalle/DIEFEO72-2012.html>]

[Tessarolo 2012] Tessarolo, A.; Bortolozzi, M.; Mezzarobba, M., "On the validity of the harmonic superposition principle for computing rotor eddy current losses in permanent magnet machines," Electrical Machines (ICEM), 2012 XXth International Conference on , vol., no., pp.1369,1373, 2-5 Sept. 2012

[Timar 1989] Timar, P.; "Noise and Vibration of Electrical Machines". Amsterdam, The Netherlands: Elsevier, 1989

[Timoshenko 1951] Timoshenko, S. and Goodier J.N., "Theory of Elasticity" McGraw-Hill, second edition 1951

[Timoshenko 1976-a] Timoshenko, "Strength of materials. Part I" Robert E. Krieger Publishing Company, third edition 1976

[Timoshenko 1976-b] Timoshenko, "Strength of materials. Part II" Robert E. Krieger Publishing Company, third edition 1976

[Torregrossa 2012] Torregrossa, D.; Fahimi, B.; Peyraut, F.; Miraoui, A., "Fast Computation of Electromagnetic Vibrations in Electrical Machines via Field Reconstruction Method and Knowledge of Mechanical Impulse Response," Industrial Electronics, IEEE Transactions on , vol.59, no.2, pp.839,847, Feb. 2012

[Tsampouris 2013] Tsampouris, E.M.; Kakosimos, P.E.; Kladas, A.G., "Coupled Computation of Electric Motor Design and Control Parameters Based on Ant Colonies Speed Trajectory Optimization," Magnetics, IEEE Transactions on , vol.49, no.5, pp.2177,2180, May 2013

[Tutelea 2010] Tutelea, L.; Boldea, I., "Surface permanent magnet synchronous motor optimization design: Hooke Jeeves method versus genetic algorithms," Industrial Electronics (ISIE), 2010 IEEE International Symposium on , vol., no., pp.1504,1509, 4-7 July 2010

[Van der Giet 2010] Van der Giet, M.; Franck, D.; Rothe, R.; Hameyer, K., "Fast-and-easy acoustic optimization of PMSM by means of hybrid modeling and FEM-to-measurement transfer functions," Electrical Machines (ICEM), 2010 XIX International Conference on , vol., no., pp.1,6, 6-8 Sept. 2010

[Vese 2010] Vese, I.; Marignetti, F.; Radulescu, M.M., "Multiphysics Approach to Numerical Modeling of a Permanent-Magnet Tubular Linear Motor," *Industrial Electronics, IEEE Transactions on* , vol.57, no.1, pp.320,326, Jan. 2010

[Vijayraghavan 1999] Vijayraghavan, P.; Krishnan, R., "Noise in electric machines: a review," *Industry Applications, IEEE Transactions on* , vol.35, no.5, pp.1007,1013, Sep/Oct 1999

[Villar 2010] Villar, I., "Multiphysical Characterization of Medium-Frequency Power Electronic Transformers" Ph.D. dissertation, Laboratoire d'Électronique Industrielle, École Polytechnique Fédérale de Lausanne, 2010

[Wang 2012] Daohan Wang; Xiuhe Wang; Mun-Kyeom Kim; Sang-Yong Jung, "Integrated Optimization of Two Design Techniques for Cogging Torque Reduction Combined With Analytical Method by a Simple Gradient Descent Method," *Magnetics, IEEE Transactions on* , vol.48, no.8, pp.2265,2276, Aug. 2012

[Wang 2013] Jiabin Wang; Xibo Yuan; Atallah, K., "Design Optimization of a Surface-Mounted Permanent-Magnet Motor With Concentrated Windings for Electric Vehicle Applications," *Vehicular Technology, IEEE Transactions on* , vol.62, no.3, pp.1053,1064, March 2013

[Weidong 2007] Weidong Zhu; Pekarek, S.; Fahimi, B.; Deken, B.J., "Investigation of Force Generation in a Permanent Magnet Synchronous Machine," *Energy Conversion, IEEE Transactions on* , vol.22, no.3, pp.557,565, Sept. 2007

[Weilharter 2012] Weilharter, B.; Biro, O.; Lang, H.; Ofner, G.; Rainer, S., "Validation of a Comprehensive Analytic Noise Computation Method for Induction Machines," *Industrial Electronics, IEEE Transactions on* , vol.59, no.5, pp.2248,2257, May 2012

[Wrobel 2006] Wrobel, R.; Mellor, P.H., "Particle Swarm Optimisation for the Design of Brushless Permanent Magnet Machines," *Industry Applications Conference, 2006. 41st IAS Annual Meeting. Conference Record of the 2006 IEEE* , vol.4, no., pp.1891,1897, 8-12 Oct. 2006

[Wu 2012] Wu, L. J.; Zhu, Z.Q.; Staton, D.; Popescu, M.; Hawkins, D., "Analytical Model for Predicting Magnet Loss of Surface-Mounted Permanent Magnet Machines Accounting for Slotting Effect and Load," *Magnetics, IEEE Transactions on* , vol.48, no.1, pp.107,117, Jan. 2012

[Wu 2014] Wu, L.J.; Zhu, Z.Q, "Analytical Modeling of Surface-Mounted PM Machines Accounting for Magnet Shaping and Varied Magnet Property Distribution," *Magnetics, IEEE Transactions on* . To be published. 2014

[Wurtz 1996] Wurtz, F.; Bignon, J.; Poirson, C., "A methodology and a tool for the computer aided design with constraints of electrical devices," *Magnetics, IEEE Transactions on* , vol.32, no.3, pp.1429,1432, May 1996

[Yang 1981] Yang, S.J.; "Low-Noise Electrical Motors". Oxford: Clarendon Press, 1981

[Zarko 2006] Zarko, D.; Ban, D.; Lipo, T.A., "Analytical calculation of magnetic field distribution in the slotted airgap of a surface permanent-magnet motor using complex relative air-gap permeance," *Magnetics, IEEE Transactions on* , vol.42, no.7, pp.1828,1837, July 2006

[Zarko 2008] Zarko, D.; Ban, D.; Lipo, T.A., "Analytical Solution for Cogging Torque in Surface Permanent-Magnet Motors Using Conformal Mapping," *Magnetics, IEEE Transactions on* , vol.44, no.1, pp.52,65, Jan. 2008

[Zhu 1992] Zhu, Z.Q.; Howe, D., "Analytical prediction of the cogging torque in radial-field permanent magnet brushless motors," *Magnetics, IEEE Transactions on* , vol.28, no.2, pp.1371,1374, Mar 1992

[Zhu 1993-a] Zhu, Z.Q.; Howe, D.; Bolte, E.; Ackermann, B., "Instantaneous magnetic field distribution in brushless permanent magnet DC motors. I. Open-circuit field," *Magnetics, IEEE Transactions on* , vol.29, no.1, pp.124,135, Jan 1993

[Zhu 1993-b] Zhu, Z.Q.; Howe, D., "Instantaneous magnetic field distribution in brushless permanent magnet DC motors. II. Armature-reaction field," *Magnetics, IEEE Transactions on* , vol.29, no.1, pp.136,142, Jan 1993

[Zhu 2004] Zhu, Z.Q.; Ng, K.; Schofield, N.; Howe, D., "Improved analytical modelling of rotor eddy current loss in brushless machines equipped with surface-mounted permanent magnets," *Electric Power Applications, IEE Proceedings -* , vol.151, no.6, pp.641,650, 7 Nov. 2004

[Zhu 2010] Zhu, Z.Q.; Xia, Z.P.; Wu, L. J.; Jewell, G.W., "Analytical Modeling and Finite-Element Computation of Radial Vibration Force in Fractional-Slot Permanent-Magnet Brushless Machines," *Industry Applications, IEEE Transactions on* , vol.46, no.5, pp.1908,1918, Sept.-Oct. 2010